University of Oklahoma

Graduate College

SEARCH FOR VECTOR-LIKE QUARKS AND DARK MATTER IN MONO-TOP EVENTS IN PROTON-PROTON COLLISIONS WITH THE ATLAS DETECTOR

A dissertation

submitted to the Graduate Faculty

in partial fulfillment of the requirements for the

Degree of

DOCTOR OF PHILOSOPHY

By

QING WANG
Norman, Oklahoma
2019

SEARCH FOR VECTOR-LIKE QUARKS AND DARK MATTER IN MONO-TOP EVENTS IN PROTON-PROTON COLLISIONS WITH THE ATLAS DETECTOR

A dissertation approved for the
HOMER L. DODGE DEPARTMENT OF PHYSICS AND ASTRONOMY

BY

Dr. Phillip Gutierrez, Chair

Dr. Michael Strauss

Dr. Chung Kao

Dr. Bruce Mason

Dr. Liangzhong Xiang

Abstract

This dissertation describes a search for events with one top-quark and large missing transverse momentum in the final state. Data collected during 2015 and 2016 by the ATLAS experiment from 13 TeV proton-proton collisions at the LHC corresponding to an integrated luminosity of 36.1 fb^{-1} are used. Two channels are considered, depending on the leptonic or the hadronic decays of the W boson from the top quark. The obtained results are interpreted in the context of simplified models for dark-matter production and for the single production of a vector-like T quark. In the absence of significant deviations from the Standard Model background expectation, 95% confidence-level upper limits on the corresponding production cross-sections are obtained and these limits are translated into constraints on the parameter space of the models considered.

Contents

List of Figures

List of Tables

1

The Standard Model and Beyond

The Standard Model (SM) of particle physics is a quantum field theory that describes the elementary particles and their interactions governed by three of the four fundamental forces. It gives excellent agreement with experimental results such as the properties of the weak neutral current (1, 2), and the W and Z bosons (3, 4, 5), which are well confirmed by tests in the last few decades. The discovery of the Higgs boson (6, 7), the last unveiled part of the SM, makes it a complete theory. Despite its huge successes, it still can not explain phenomena like the asymmetry between matter and anti-matter (8), the existence of dark matter particles implied by cosmological observations (9, 10, 11, 12) and the mass of the neutrinos (13). Therefore, there are physics models proposed to address these problems and they are called physics beyond the SM (BSM).

This chapter is intended to provide a brief introduction of the basic concepts of the SM: The first section introduces the fundamental constituents of the SM and the fundamental interactions. The second section discusses the theoretical foundation of the SM, gauge theories. The limitation of the SM and some new physics models are discussed in the last section, and vector-like quarks and dark matter are introduced.

A deatailed and in-depth discussion of the theory of the SM is beyond the scope of this thesis and the interested reader can refer to the famous book by Peskin and Schroeder (14).

1.1 Particle contents and their interactions

The elementary particles in the SM can be categorized as either fermions or bosons. Fermions are spin-1/2 particles and they are the buliding blocks of matter. They follow the Pauli exclusion principle, which states that no two fermions can occupy the same state at the same time. Bosons are either spin-1 vector bosons (photon, gluon, W and Z) which are the mediators of the interaction forces between fermions, or spin 0-scalar bosons (Higgs) which give mass to fermions and mediator bosons.

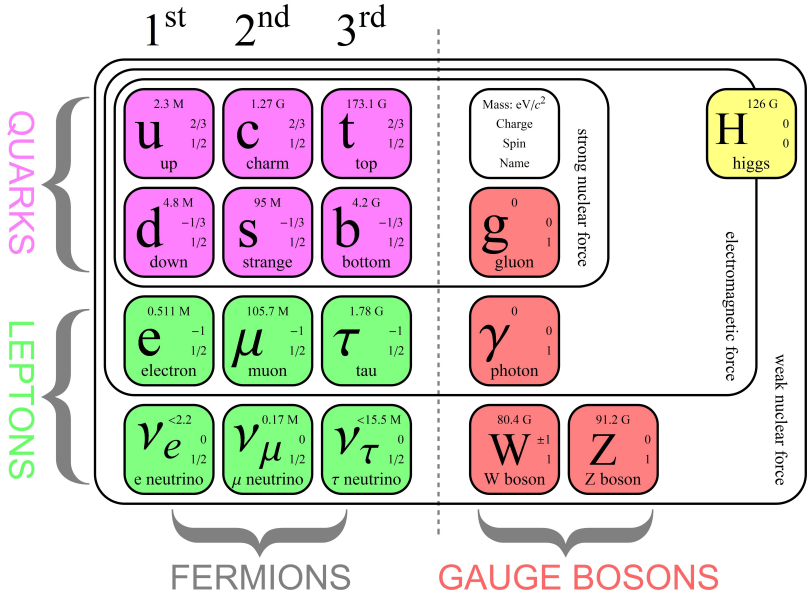

Figure 1.1: Illustration of the elementary particls and their interactions in the SM (15).

Fermions as the building blocks of matter

Fermions are further classified as quarks and leptons. There are six quarks and six leptons and they fall in three generations. There are three different lepton flavors, electron (e), muon (μ) and tau (τ) and they have electric charge of -1. There are also three types of neutrinos matched to their partner lepton. Neutrinos are massless in the SM but experimental observations show they have light masses (13). Neutrinos do not carry any electric charge, and therefore they only interact through weak interaction which makes them hard to detect.

In addition to leptons there are quarks which have six flavors up, down, charm, strange, top and bottom. They carry the color charge which is the charge associated with the strong force. Unlike leptons, there are no free quarks. They only exist in the form of composite particles namely baryons (quark triplets) such as the proton and the neutron, and mesons (quark doublets), which are together called hadrons. Quarks carry a fractional electric charge of either $2/3$ or $-1/3$.

It is also important to note that for each fermion, there exists an antifermion which has the same mass but opposite physicsl charges such as electric charge. When a femion meets its counterpart antifermion, annihilation will happen and generate energy which can be transformed to other particles.

Bosons as mediators of the fundamenta interactions

There are four fundamental interactions that are responsible for all the phenonema in nature: the electromagnetic, the strong, the weak and the gravitational interactions. These interactions are realized by exchanging the corresponding mediator vector bosons

and each interaction has its own effective range. The strong interaction, mediated by the gluons, acts only on the color-charged quarks and gluons and it is only effective in the nucleus range (10^{-15} m). It is called the strong force because of the fact that at this range, it is about 137 times as strong as the electromagnetic force, a million times as strong as the weak interaction and 10^{38} as strong as the gravitational force. The electromagnetic interaction, mediated by the photon, governs the interaction of electrically charged partices. It can be effective very long range and includes both the static electric force and the combined electric and magnetic effects on moving charges. The weak interaction affectes both leptons and quarks and is carried by the massive W and Z bosons. Like the strong interaction, it is only effective in the nucleus range. A well-known example of the weak interaction is the β decay. The gravitational interaction is still beyond the SM description, and its mediator particle, the graviton has not been discovered yet.

1.2 Theoretical framework of the Standard Model

The Standard Model does not merely give an exhaustive list of elementary particles, it also has a supporting theoretical framework formulated as a relativistic quantum field theory, of which the foundation is built up on gauge theories. In a quantum field theory, each particle is represented by discrete excitations of a field $\boldsymbol{\psi(x)}$, and the dynamics of the fields are described by Lagrangians ($\mathcal{L}$), which are functions of the field $\boldsymbol{\psi(x)}$ and its first derivative $\partial^\mu \boldsymbol{\psi(x)}$. By requiring the gauge invariance on the Lagarangian under the fundamental symmetries, the interactions between fermions and bosons will follow automatically.

A fermion is a spin-1/2 particle and thus can be represented by a relativistic spin-1/2 field, which is called a Dirac spinor:

$$\mathcal{L}_{Dirac} = i\bar{\boldsymbol{\psi}}\gamma^\mu \partial_\mu \boldsymbol{\psi} - m\bar{\boldsymbol{\psi}}\boldsymbol{\psi}, \tag{1.1}$$

where $\bar{\boldsymbol{\psi}}$ refers to the field associated to the antifermion, and γ^μ are the Dirac matrices. The Lagrangian is required to be invariant under local pahse transformations, which is known as the gauge transformations:

$$\boldsymbol{\psi(x)} \rightarrow U(x)\boldsymbol{\psi(x)} = e^{i\boldsymbol{\alpha}(x)\cdot\frac{\boldsymbol{\tau}}{2}}\boldsymbol{\psi(x)}, \tag{1.2}$$

where $\boldsymbol{\alpha}(x)$ are the space-time dependent rotation parameters in the symmetry group represented by the Lie group generators $\boldsymbol{\tau}$. In order to keep the Lagrangian invariant, the derivative must be replaced with a covariant derivative,

$$D_\mu = \partial_\mu - ig\frac{\boldsymbol{\tau}}{2}\boldsymbol{A}_\mu, \tag{1.3}$$

where $\boldsymbol{A_\mu}$ are the newly introduced vector gauge fields which interact with the fermion fields with a coupling costant g. The Dirac Lagrangian then becomes

$$\mathcal{L}_{Dirac} = i\bar{\boldsymbol{\psi}}\gamma^\mu \partial_\mu \boldsymbol{\psi} - m\bar{\boldsymbol{\psi}}\boldsymbol{\psi} + g\bar{\boldsymbol{\psi}}\gamma^\mu \frac{\boldsymbol{\tau}}{2}\boldsymbol{\psi}\boldsymbol{A}_\mu, \tag{1.4}$$

with the additional term that describes the interaction beween the fermion fields mediated by the gauge fields $\boldsymbol{A_\mu}$.

The matrix U(x) in Equation (1.2) is defined as a general rotation matrix of the symmetry group SU(N). The three fundamental interactions in the Standard Model can be obtained by requring the Lagrangian to be gauge invariant under the corresponding symmetry groups as illustrated below.

Electroweak theory

The electromagnetic and the weak interactions, which appear to be very different at low energies but can be unified as a single electroweak interaction at an energy scale of the order of 100 GeV, which is known as the electroweak energy scale. The theory can be obtained by requiring gauge invariance under the $\mathrm{U(1)_Y} \times \mathrm{SU(2)}_L$ (14) symmetry group. As a result, one gauge field B_μ is introduced by the $\mathrm{U(1)_Y}$ group and three gauge fields W_μ^α are introduced by the $\mathrm{SU(2)_L}$ group. In addition, two coupling constants, g_1 and g_2, are introduced by $\mathrm{U(1)_Y}$ and $\mathrm{SU(2)_L}$, respectively. The gauge bosons are represented as linear combinations of these fields:

$$A_\mu = \sin\theta_W W_\mu^3 + \cos\theta_W B_\mu, \tag{1.5}$$

$$W_\mu^\pm = \sqrt{\frac{1}{2}}(W_\mu^1 \mp i W_\mu^2), \tag{1.6}$$

$$Z_\mu = \cos\theta_W W_\mu^3 - \sin\theta_W B_\mu, \tag{1.7}$$

where $W_\mu^\pm$ and Z_μ are the $W^\pm$ and Z^0 fields and A_μ is the photon field, and θ_W is defined as $\arctan\frac{g_1}{g_2}$, which is known as the weak mixing angle.

Quantum Chromodynamics (QCD)

The theory of Quantum Chromodynamics, which describes the strong interaction, is obtained by requiring gauge invariance under the symmetry group SU(3) (14). As a result, eight gauge boson fields are introduced associated to this symmetry group, and the corresponding bosons are massless and known as gluons. A unique charasteristic of QCD is called confinement. It states that the strong coupling constant α_s goes to zero eventually at high energies. As a result, the strong force becomes stronger when the distance between quarks and gluons increases. Therefore, the quarks and gluons can not exist on their own, but are confined in color-neutral hadrons. This effect is also know as asymptotic freedom.

So far the resulting Lagrangian including terms representing the three fundamental interactions does not have any mass term, therefore it can not explain where the masses of particles come from. Adding some mass term explicitly to the Lagrangian will break the gauge invariance. Instead, the Higgs mechanism, which introduces a complex scalar doublet ϕ with a non-zero vacuum expectation value (VEV), was proposed to solve this problem. The idea behind such a mechanism is that it realizes a spontaneous symmetry breaking (SSB), which means it does not break the gauge invariance explicitly, but mass

terms arise from the choice of a minimal configuration of the popential of a new field, know as the Higgs field. The Lagrangian of the Higgs field is written as:

$$\mathcal{L}_H = (D^\mu\phi)^\dagger(D_\mu\phi) - V(\phi) \tag{1.8}$$

$$= (D^\mu\phi)^\dagger(D_\mu\phi) - \mu^2\phi^\dagger\phi - \lambda(\phi^\dagger\phi)^2, \tag{1.9}$$

where μ and λ are constants representing a mass parameter and self-interaction strength. When $\mu^2 < 0$ there are infinite choices for the groud state for the potential V and by choosing a ground state and expanding the field around it, the SSB is achieved. As a result, three of the four fields of the scalar doublet are absorbed by the massless vector fields of the weak interaction and this gives masses to the W and Z bosons:

$$m_W = \frac{1}{2}vg_2 \tag{1.10}$$

$$m_Z = \frac{1}{2}v\sqrt{g_1^2 + g_2^2}, \tag{1.11}$$

where g_1 and g_2 are the coupling constants for the fields B_μ and $\boldsymbol{A_\mu}$. The remaining field gives rise to the Higgs boson that has a mass $m_H = \sqrt{2\lambda}v$. The Higgs field does not couple to the A field and the photon is massless.

The fermions acquire their masses in a different way, that is through the Yukawa couplings with the Higgs boson. The Higgs mechanism allows us to insert the following gauge-invariant term in the Lagrangian:

$$\mathcal{L} = -Y^d_{ij}\bar{\psi}_{L,i}\phi\psi_{R,j} - Y^u_{ij}\bar{\psi}_{L,i}\hat{\phi}\psi_{R,j} + h.c, \tag{1.12}$$

where Y_{ij} are the Yukawa matrices and $\hat{\phi} = i\tau_2\phi^*$. The L and R represent left- and right-handed fermions. The hadness, which is also known as chirality, is defined as $\psi_L = \frac{1}{2}(1-\gamma_5)\psi$ for left- and $\psi_R = \frac{1}{2}(1+\gamma_5)\psi$ for right-handed fermions. The fermions aquire thier masses through the Yukawa interactions that describes the couplings of the fermions with the Higgs field. For massive particles, a reference frame which overtakes the spinning particle could always be found, in which case the particle will seem to move backwards, flipping its helicity, which is defined as the sign of projection of the spin vector onto the momentum vector of a particle, left is negative while right is positive.

In summary, the Standard Model is a renormalizable gauge theory, that is based on a symmetry group U(1)× SU(2)× SU(3), where the U(1)× SU(2) describes the electroweak interaction and the SU(3) symmetry group represents QCD. The full Lagrangian of the SM describes the three generations of fermions, the gauge bosons that mediate the three fundamental forces and the Higgs mechanism which gives masses to the particles and introduces the spin-0 massive scalar Higgs boson.

1.3 The limitations and physics beyond the SM

Although the SM is an extremely successful theory and makes many precise predictions that agree with experiments. There are still phenomena that are unexplained and many open questions in modern physics. Here are some of them:

Baryon asymmetry

The Big Bang theory should have produced equal amounts of matter and antimatter. And we know that when particles meet their anti-particle counterparts, annihilation happens, leaving only pure energy existing in the form of photons. However, in the current observable universe, there is a large predominance of matter over antimatter. The charge congugate violation (14) (CP violation), discovered in the weak interaction, could account partially for the matter antimatter asymmetry, but not enough to explain the asymmetry observed today.

The hierarchy problem and vector-like quarks

Another debated question of the standard model is the so-called hierachy problem (14), that is why is there a large gap between the electroweak scale, which is $\mathcal{O}(100)$ GeV, and the Planck scale, the scale at which the gravitational interaction is expected to dominate the other interactions, which is $\mathcal{O}(10^{19})$ GeV. An effect of that large gap between the two scales is that the bare value of the Higgs mass-squared m_H^2 receives large radiative corrections from the fermions interacting with the Higgs field:

$$\Delta m^2 = -\frac{\lambda_f^2}{8\pi^2}\Lambda_{UV}^2, \tag{1.13}$$

where λ_f^2 is the Yukawa coupling of fermions to the Higgs boson, and Λ_{UV} is an energy cutoff until at which the SM is expected to be valid.

If the SM is valid at the Planck scale, then the Higgs mass would be extremely large. Since this is not the case, which means that the parameters of the SM are fine-tuned in such a way that prevents these large corrections or there is new physics at a scale between the electroweak scale and the Plank scale which provides the cancellation.

A popular solution for this problem is via the supersymmetry (SUSY) (14). Supersymmetry could remove the quantratic divergence of the radiative corrections to the Higgs mass as long as the SUSY particles are light enough to satisfy the Barbieri-Giudice criterion.

An alternative approach to solve this so called hierachy problem is to propose a spaontaneously broken global symmetry of the extended theory, with the Higgs boson emerging as a pesudo-Namby-Goldstone boson. Some BSM models that implement this idea are Composite Higgs (18, 19) and Little Higgs models (16, 17). These extended models predict the vector-like quarks, which are color-triplet spin-1/2 fermions whose left- and right-handed chiral components have the same transformation properties under the electroweak symmetry group $\mathrm{SU(2)_L}\times\ \mathrm{U(1)_Y}$. The vector-like quarks could mix with the SM quarks of the same charge, and this kind of mixing could play a crucial role in regulating the divergence in the radiative correction terms in the Higgs mass-squared expression.

In order to preserve gauge invariance, there is only a limited set of possible such quarks, and their electric charge can be +2/3 e (T quark), −1/3 e (B quark), +5/3 e (X quark) or −4/3 e (Y quark), where e is the elementary charge. The channel with

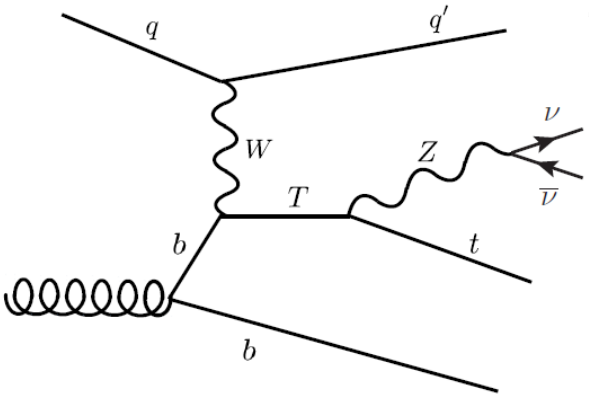

Figure 1.2: Feynman diagram corresponding to the single production of a vector-like T-quark at the LHC (20).

$T \rightarrow Zt \rightarrow \nu\bar{\nu}Wb$ decay is chosen for this analysis beacause it has the same event topology with the channel where we look for dark matter particles, which is introduced in the next section.

Dark matter and dark energy

Many cosmological experiments, such as the measure of the rotational speed of stars in galaxies and the study of gravitational lensing effect, have revealed the existance of non-luminous and mostly non-baryonic matter, which is referred to as dark matter. Surprisingly, the matter we currently know, which consists of the SM quarks and leptons, only accounts for 5% of the content of the universe, with the remaining being 27% dark matter and 68% dark energy. The name dark comes from the fact it does not interact through the electromagnetic force, therefore it does not reflect, absorb or emit light, which makes it very difficult to detect. At the collider experiments, this leads to a significant amount of missing transverse momentum[1]. Both the ATLAS and CMS experiments have performed searches for DM particles (χ) in events produced with jets (28, 29, 30, 31), photons (32, 33), W or Z (34, 35, 36), or Higgs (37, 38, 39, 40) bosons with large amount of missing transverse momentum.

[1]The initial momentum of the protons in the transverse plane is zero and accordring to the law of conservation of momentum, the sum of the momenta of all the final state particles in the transverse plane should also be zero. However, some particles like the dark matter particles will escape the detector without being detected, leaving a negtive vector sum of the transverse momenta of the final state particles and is called the missing transverse momentum and its magnitude is denoted as $E_{\mathrm{T}}^{\mathrm{miss}}$.

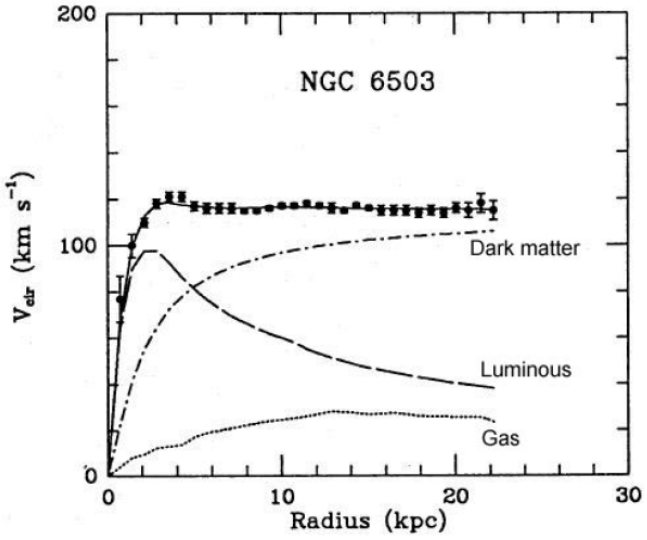

Figure 1.3: Rotation curve of NGC 6503. The dotted, dashed and dash-dotted lines show the contributions from gas, disk, and dark matter, respectively (24).

Evidence of existance

The most direct evidence for the dark matter is the observation of the rotation curces of galaxies, which is the measurement of the circulation velocities of the stars around the galactic center. According to Newtonian dynamics, the velocity is expressed as the function of mass of the galaxy $M(r)$, and the distance between the center of the galaxy and the star:

$$v(r) = \sqrt{\frac{GM(r)}{r}} \tag{1.14}$$

with

$$M(r) = 4\pi \int \rho(r) r^2 dr \tag{1.15}$$

where G is the gravitational constant and $\rho(r)$ is the mass density of the galaxy. As shown in Figure 1.3, it turns out that the rotation curve becomes flat at long distances, implying the universe is filled with some non-luminous matter contributing to $M(r)$ with a density propotional to $\frac{1}{r^2}$.

Another strong evidence of dark matter is observations of gravitational lensing in the universe (25). We learn from Einstein's theory of general relativity that a cluster of galaxies will act as a lens to bend the light between the source, e.g a quasar, and the observer. The more massive the galaxies, the more bended is the light. And from the analysis of distorted images of the sources, the mass of galaxies could be obtained. For example, measurement of the Abell 370 cluster shows that the cluster of galaxies is dominated by dark matter. An image from Abell 370 could be seen in Figure 1.4.

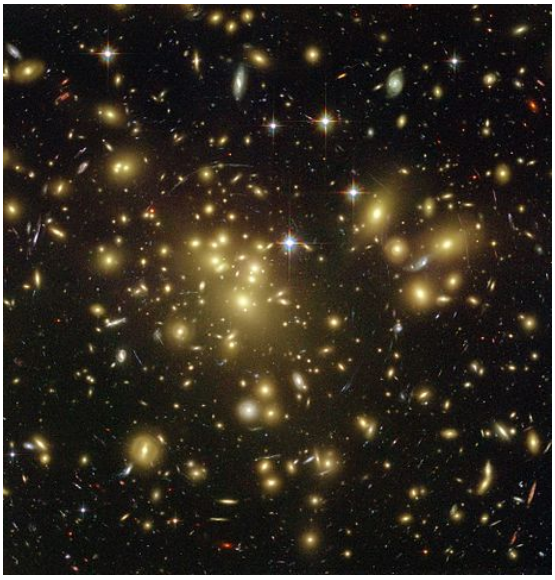

Figure 1.4: Image of the massive galaxy cluster Abell 370 taken by the NASA/ESA Hubble Space Telescope, where giant arcs due to gravitational lensing can be clearly seen (25).

Dark matter models used in this analysis

In this analysis the resonant and non-resonant production of dark matter particles associated with a top-quark are considered. These processes follow a simplified model that is constructed by imposing that the Lagrangian respects the electroweak U(1)× SU(2) gauge symmetry and by requiring minimality in terms of new states to supplement to the SM fields (20, 21, 22). The resonant case, as shown in Figure 1.5(a), corresponds to the production of a colored charge-2/3 scalar (ϕ) decaying into a top-quark and a spin-1/2 dark matter particle (χ) (23). This process is described by the following Lagrangian (20, 26):

$$\mathcal{L}_{\text{int}} = \lambda\phi\bar{d^c}P_{\text{R}}s + y\phi\bar{\chi}P_{\text{R}}t + h.c., \tag{1.16}$$

where the parameters λ and y represent the couplings of the charged scalar to the d- and s-quarks and to the top-quark and the dark matter particle χ, respectively. The term P_{R} is the right-handed chirality projector. The non-resonant case, as shown in Figure 1.5(b) and Figure 1.5(c), corresponds to a flavor changing neutral current interaction, producing a top-quark and a new vector particle V, which in turn decays invisbly to a pair of dark matter particles. This process is described by the following Lagrangian (20, 26):

$$\mathcal{L}_{\text{int}} = aV_\mu\bar{\mu}\gamma^\mu P_{\text{R}}t + g_\chi V_\mu\bar{\chi}\gamma^\mu\chi + h.c., \tag{1.17}$$

where the vector particle V couples to a dark matter particle with a strength of g_χ. The parameter a stands for the coupling constant between the massive vector boson V and the t- and u-quarks, and γ^μ are the Dirac matrices.

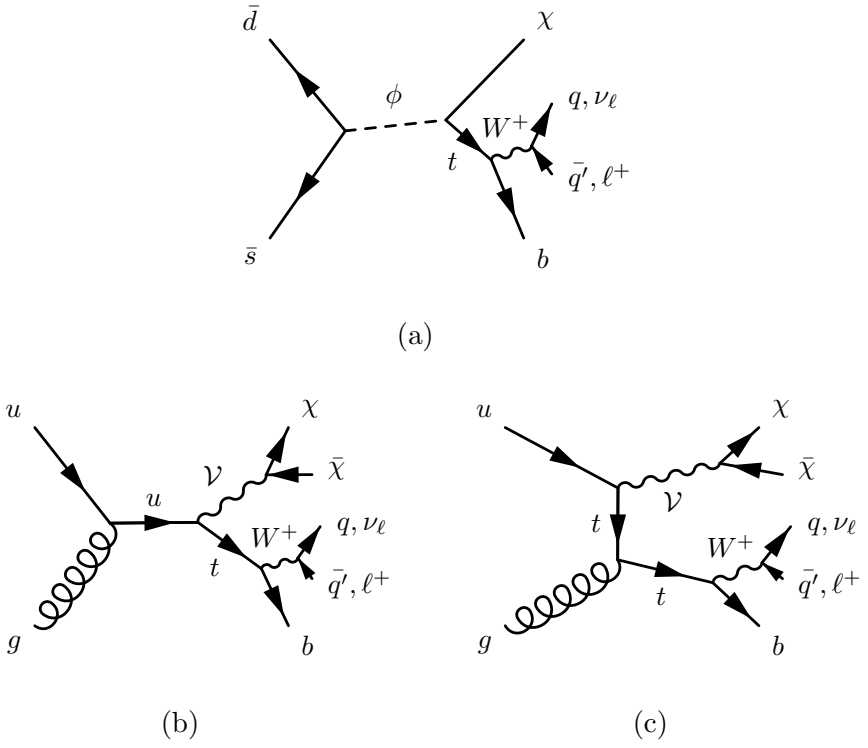

Figure 1.5: Monotop production in the context of an effective dark matter model: the leading order Feynman diagrams for the resonant (a) and non-resonant (s- (b) and t-channels (c)) cases are shown.

2

The Large Hadron Collider

The Large Hadron Collider (LHC) (41) is currently the world's largest and highest-energy particle collider. It is built by the European Orgization for Nuclear Research (CERN[1]). It lies within a tunnel of 27 kilometers (17 miles) in circumference and 175 meters (574 feet) beneath the Franco-Swiss border near Geneva, Switzerland. The LHC is designed for a luminosity of 10^{34} $cm^{-2}s^{-1}$ for proton-proton collisions at an energy of 14 TeV at a collision rate of 40 MHz. The primary focus is to study a range of phenomena, such as the properties of Higgs boson, which was discovered at the LHC in July 2012, supersymmetry and search for dark matter and extra dimensions.

As shown in Figure 2.1, the accelerator complex consists of several parts that successively accelerate the protons. First, protons are extracted from a bottle of ionized hydrogen gas by electric field and accelerated by the linear particle accelerator (Linac 2) to 50 MeV, before being fed to the Proton Synchrotron Booster (PSB). There the protons are pushed to the energy of 1.4 GeV and injected to the Proton Synchrotron (PS), where they are further accelerated up to 25 GeV. Then the Super Proton Synchrotron (SPS) increases the energy to 450 GeV and sends the protons into the circular accelerator, which does the final acceleration of the protons to their peak energy. During Run 1 of the LHC from 2009 to 2013, protons are produced up to 8 TeV collison energy. For Run 2, 2015 through 2018, the energy was 13 TeV. At this energy the protons travel at a speed that is only 3.1 m/s slower than the speed of light.

The protons are divided into 2808 bunches with about 115 billion protons in each bunch rather than in continuous beams. Two beams of protons are accelerated in seperate rings in opposite directions with collisions occurring every 25 ns. Four detectors are installed around four seperate collision points in order to detect the byproducts and analyze them, as shown in Figure 2.1: A Toroidal LHC Apparatus (ATLAS), Compact Muon Solenoid (CMS), Large Hadron Collider beauty (LHCb) and A Large Ion Collider Experiment (Alice). They aim at different regions of study: ATLAS and CMS are designed to search for the Higgs boson and new physics beyond SM including suppersymmetry, dark matter and extral dimmensions; LHCb experiment intends to make precise measurements of bottom quark parameters and find a solution for the

[1]CERN is the abbreviation for its name in French

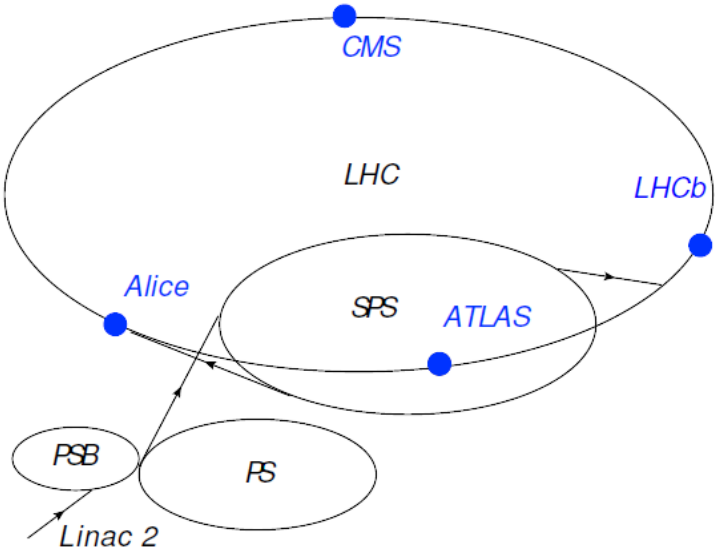

Figure 2.1: A schematic layout for LHC including the accelerator complex and four main detectors.

imblance of matter and antimatter; Alice is optimized to study quark-gluon plasma in heavy ion collisions.

The benchmark of a collider is characterized by the absolute luminosity, $\mathcal{L}$ with:

$$\mathcal{L} = \frac{N_e}{\sigma} = \frac{kN^2 f}{4\pi\sigma_x^*\sigma_y^*} \tag{2.1}$$

where N_e is the event rate, σ is cross section of a certain prosess, k is the number of bunches per steam, N is the number of protons per bunch, f is the beam revolution frequency and σ_x^*, σ_y^* are the horizontal and vertical beam sizes at the collison point, which are 16 μm each. Therefore, in order to produce more events of interest, we need to increase the luminosity. This means storing the number of bunches per beam, and the number of protons per bunch as many as possible. However, a consequence of this is that there will be several proton-proton collisions when two proton bunches cross at the interaction point. For the designed luminosity of LHC, 10^{34} cm^{-2}s^{-1}, there will be an average of 25 collisons at each bunch crossing. This effect is called pileup and will pollute the reconstructed final state. Therefore the LHC is performed up to the maximum value.

The integrated luminosity over time, $\int \mathcal{L}dt$, the unit of which is inverse to that of cross section, e.g fb^{-1}, is often used as the benchmark of the size of collected data in a given period. The cumulative integrated luminosity from 2015 to 2017 is shown in Figure 2.2.

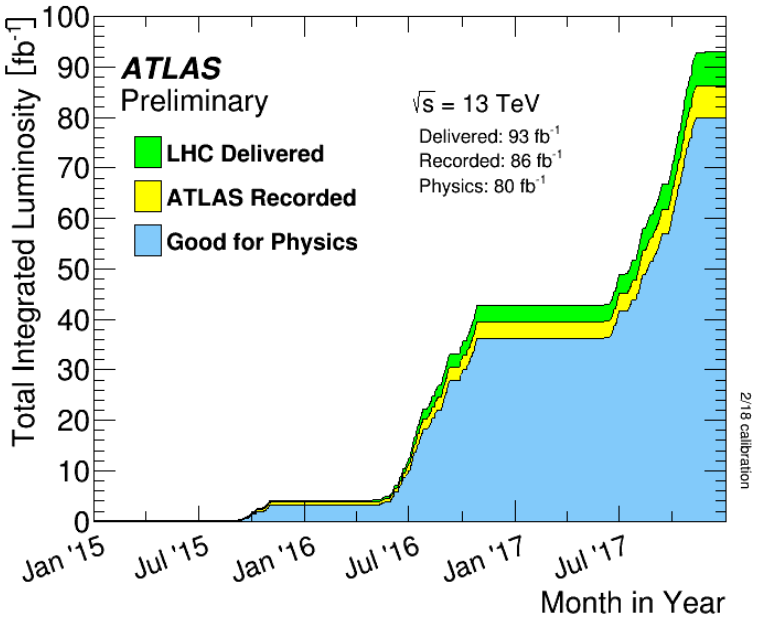

Figure 2.2: Cumulative integrated luminosity from 2015 to 2017. The LHC delivered luminosity is the total luminosity delivered to ATLAS from LHC; The ATLAS recorded luminosity accounts for that the ATLAS actually has recored; And the luminosity good for physics, which is $80 fb^{-1}$, is recorded when ATLAS is performing optimally and will be used for physics analysis (42).

3

The ATLAS Detector

The ATLAS detector at the LHC is a multi-purpose particle detector that is used to make precision measurement of SM processes, as well as search for BSM processes such as dark matter production, production of supersymmetric particles, extral dimensions, etc. These physics goals impose several general requirements on the design of the ATLAS detector:

- A precise tracking system with fast sensor elements and high granularity, that could provide good momentum resolution and reconstruction efficiency.
- Full-coverage calorimeters for energy measurements and particle identification.
- A fine-granularity muon spectrometer with good momentum resolution for efficient identification and reconstruction of muons.
- A highly efficient trigger system to reduce event rate and record physics events of interest.

The ATLAS detector was built following these requirments and was installed in 2008. The layout of the ALTAS detector is illustrated in Figure 3.1. It consists of several sets of subsystems that complement each other. The inner detector, which is closest to the beam pipe, measures trajectories of charged particles used to determine the vertex and momentum and provides information for particle identification, with the high-resolution semiconductor pixel and strip detectors. Outside the inner detector is the solenoid magnet which provides a 2T magnetic field to bend the charged tracks. The particle's charge can be determined by the direction of the curvature and the particle's momentum can be calculated based on the degree of the curvature. The next component is the calorimeter system that includes electromagnetic and hardronic calorimeters, that are used to measure the direction and energy deposit of electrons, photons and hadrons with $|\eta|$ up to 4.9. Beyond the calorimeters stands the muon spectrometer used to mesure the momentum of muons up to $|\eta|$ of 2.7.

In the following, Section 3.1 introduces the coordinate system of the ATLAS detector. Then the magnet system, the inner detector, the calorimeter system and the

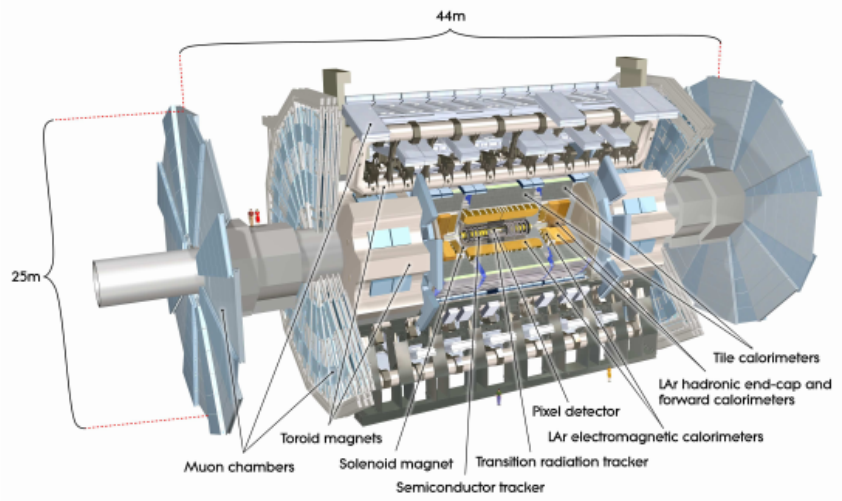

Figure 3.1: Inllustration of the layout of ATLAS (43).

muon spectrometer are briefly summarised in Sections 3.2, 3.3, 3.4 and 3.5. Finally, Section 3.6 desribes the trigger system. The majority of this chapter is based on Reference (43).

3.1 Coordinate system and overview of ATLAS

Geometrically, the ATLAS detector has a cylindrical shape, with forward-backward symmetry in respect to the interaction point. This enables it to have almost 4π coverage around the collision point.

The ATLAS detector uses a right-handed coordinate system with the z axis along the beam line and the origin at the collision point, as shown in Figure 3.2. The x-y plane is transverse to the beam direction. The polar angel θ, being the angle from z axis and azimuthal angel ϕ, measured around z axis, are difined in the same way as in the cylindrical system. In addition, the rapidity

$$y = \frac{1}{2}\ln(\frac{E + p_z}{E - p_z}) \tag{3.1}$$

and pseudorapidity

$$\eta = -\ln\tan(\frac{\theta}{2}) \tag{3.2}$$

are used. The distance ΔR beween two objects is defined as:

$$\Delta R = \sqrt{(\Delta\eta)^2 + (\Delta\phi)^2}. \tag{3.3}$$

The transverse momentum of a particle, $p_{\mathrm{T}} = p\sin\theta$, is the momentum in the transverse plane.

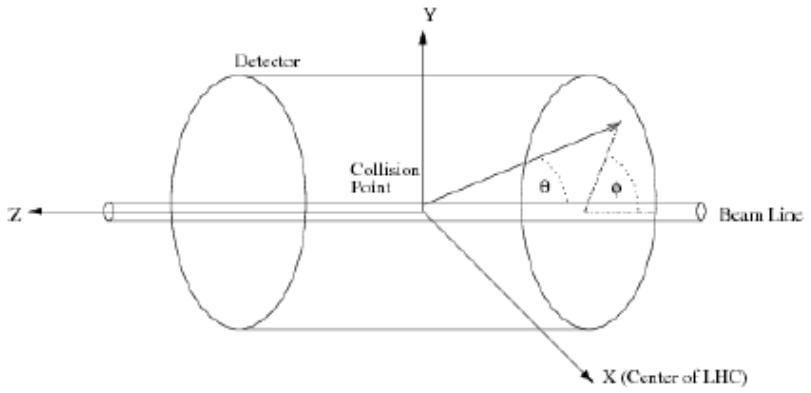

Figure 3.2: Coordinate system of ATLAS (44).

3.2 The magnet system

The magnet system provides the magnetic field to bend the charged particles. It consists of four superconducting magnets, including one solenoid and three toroids (one barrel and two end-caps). They are all operated in the vacuum system with the vaccum environment provided by diffusion pumps for the toriods and the LAr cryogenic system for the solenoid.

The central solenoid, as displayed in Figure 3.3, is designed to provide a 2 T axial field along the beam axis for the inner detector. Its length is 5.8 m and the inner and outer diameters are 2.46 m and 2.56 m. Since the alignment of the solenoid is near the calorimeters, its thickness must be as low as possible in order to get the desired calorimeter performance. As a result, the solenoid assembly has approximately 0.66 radiation lenghths in total.

A barrel toroid and two end-cap toroids are designed to produce a magnetic field of 0.5 T and 1 T for the muon spectrometer in the cental and end-cap regions, respectively. The barrel toroid has a length of 25.3 m, and diameters of 9.4 m and 20.1 m for the inner and outer diameters. The picture of the barrel toroid is shown is Figure 3.4.

3.3 Inner detector

The inner dector (ID) is designed to measure tracks of charged particles, bent by the 2 T magnetic field provided by the soleroid magnet, and provide precise measurement of their momentum and trajectories for the reconstruction of both primary and secondary vertices. It lies at the innermost part and has cylindrical shape with a dimeter of 2.1 m and a length of 6.1 m.

The ID containes three independent sub-detectors: the pixel detector including the Insertable B-Layer (IBL), the SemiConductor Tracker (SCT) and the Transistion Radiation Tracker (TRT), in that order from the beam pipe. Each subdector has sensors arranged in a cylindrical structure in the barrel region and disk-shaped sensors

Figure 3.3: The solenoid magnet of the ATLAS detector (43).

perpendicular to the beam line in the end-cap region. The acceptance is $|\eta| < 2.0$ for the barrel region and $|\eta| > 2.0$ for the end-cap region with a full coverage of $|\eta| < 2.5$.

Pixel detector

The design of the pixel detector utilizes leading-edge technology because of the very stringent requirement of radiation hardness, resolution and occupamcy nearest to the beam pipe. The pixel detector consists of 1744 identical pixel sensors (19×63 mm^2 each) with 47232 pixels on each sensor, with a size of 50×400 μm^2. There are three layers of pixel sensors at the barrel region and 3×2 disks at the end-cap region, as illustrated in Figure 3.5, providing spatial resolutions of 10 μm in the transverse r-ϕ plane and 115 μm in the z direction (barrel) or radial direction (end-caps). The pixel detector has about 80 million of channels which send out the hit information to the readout electronics. The IBL, which contributes to the performance of secondary vertex recosntruction, was working in the innermost layer from 2013 to 2014.

Semiconductor Tracker

As shown in Figure 3.5, the SCT is the intermediate sub-system which has four stereo layers of silicon microstrips in the barrel region and nine discs in each end-cap region. The spatial resolutions are 17 μm in the transverse plane and 580 μm in the z direction and radial direction.

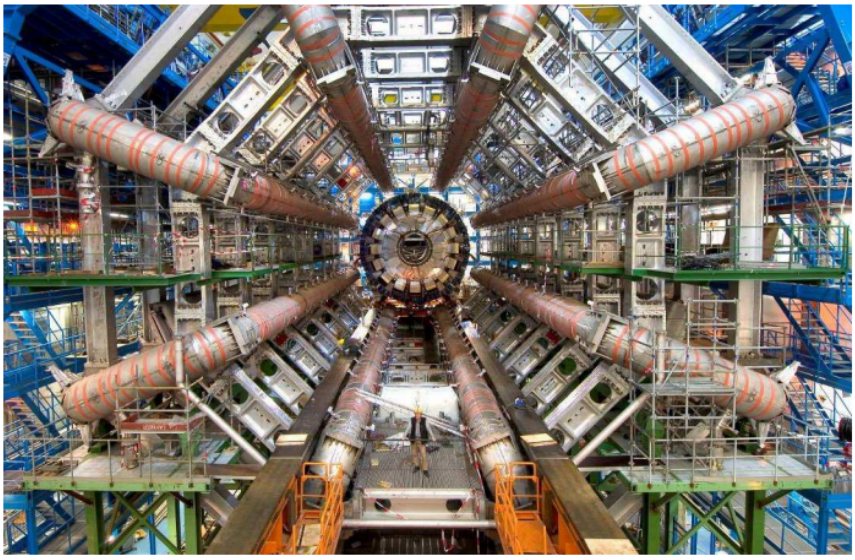

Figure 3.4: The barrel toroid magnet of the ATLAS detector(43).

Transition radiation tracker

TRT is comprised of 4 mm diameter straw tubes filled with a mixture of 70% xenon, 27% carbon dioxide and 3% oxygen. The tubes are arranged parallel to the beam axis in the barrel region while in wheels at the end-caps. TRT has only the spatial resolution of 130 μm in the beam or radial direction based on the allignment. Though with lower resoluton than pixels and SRT, TRT consumes most space of the ID and has the most hits from charged particles, therefore contributes significantly to the measurement of momentum. And due to the fact that it is a transition radiation detector, it helps in the separation of electrons from pions.

3.4 Calorimeteres

The calorimeter system, as shown in Figure 3.6, is located outside the solenoid magnet. It is designed to measure the energy and the position of the resulting particle showers of both charged and neutral particles except for muons and neutrinos, with the pseudo-rapidity coverage up to $|\eta| = 4.9$. In addition, the calorimeters determines the missing transverse momentum, originating from undetected particles such as neutrinos and use particle showering information to identify particles. The calorimeters are segemented into many small cells, the deposited energy of which can be individually read out, in order to achieve good spatial resolution.

All of the calorimeters of the ATLAS detector are sampling calorimeters. They consist of alternating layers of absorber and active materials. The traversing particles interact with the absorber materials, inducing a cascade of particles that result in

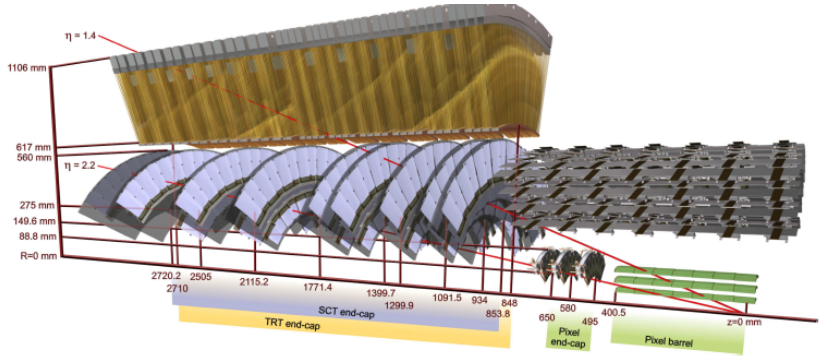

Figure 3.5: A three-dimensional drawing illustrating the structural arrangement of the ID layers in one end-cap region, with their radii and z-axial distance (using the detector center as origin) (43).

particle showers. And the deposited energy of the cascade particles is measured in the active material.

The calorimeter system consists of three subsystems. The innermost part is the electromagnetic calorimeter (EMCal), optimised to measure the electromagnetic showers induced by electrons and photons and is introduced in Section 3.4.1. The outermost part is the hadronic calorimeter (HADCal), optimised to measure the hadronic showers induced by hadronic particles and is described in Section 3.4.2. In addition, in the forward region, a forward calorimeter (FCal) is used and described in Section 3.4.3.

3.4.1 Eletromagnetic calorimeter

The EMCal consists of two half-barrels at the barrel region ($|\eta| < 1.475$) and two coaxial wheels at endcap ($1.375 < |\eta| < 3.2$), covering $1.375 < |\eta| < 2.5$ and $2.5 < |\eta| < 3.2$, respectively. In addition, an accordion geometry is applied in order to have full azimuthal coverage. Both the barrel and endcap EMCal use lead as absorber and liquid argon (LAr) as the active material.

The barrel EMCal is longitudinally divided into three layers, as illustrated in Figure 3.7. The inner layer, the thickness of which is 4.3 X_0 [1], is designed to discriminate between photon and neutral pion decaying to a pair of photons. It consists of strip cells with the size of 0.003 $\times$ 0.1 in $\Delta\eta \times \Delta\phi$. The middle layer, aiming to absorb most of the deposited enegry of the traversing particles, has a thickness of 16 X_0, consists of square cells with a size of 0.025 $\times$ 0.0245 in $\Delta\eta \times \Delta\phi$. The outlayer has a thickness of 2 X_0 and the coarser cells of it has a size of 0.05 $\times$ 0.0245 in $\Delta\eta \times \Delta\phi$.

Each wheel of the endcap EMCal consists of eight modules with cell size up to 0.1 $\times$ 0.1 in $\Delta\eta \times \Delta\phi$. There is a Lar presampler layer installed in front of the barrel and endcap EMCals in order to correct for the energt loss in the upstream materials (The solenoid magnet, the ID, etc).

[1]The radiation length X_0 is defined as the average distance after which the energy of a traversing particle is reduced by a factor of 1/e due to electromagnetic interactions with the detector.

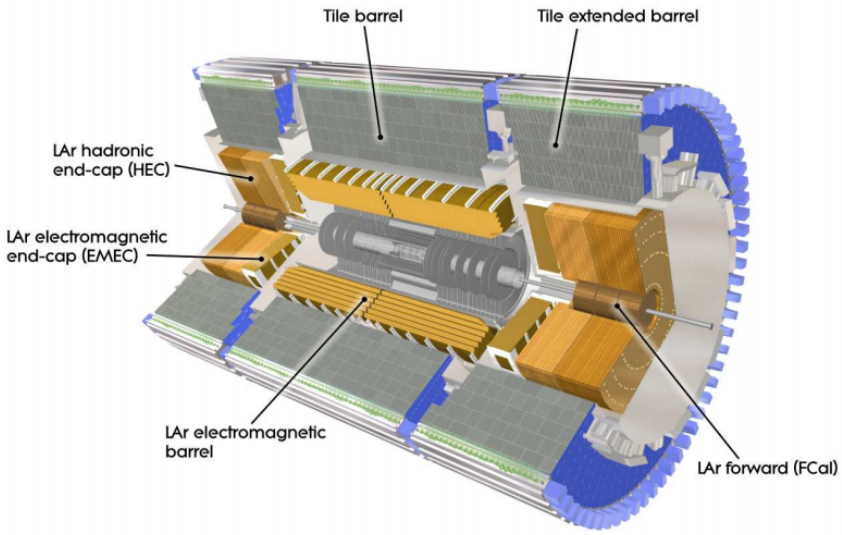

Figure 3.6: Overview of the calorimeter system of the ATLAS detector (43).

The designed energy resolution of the EMCal is $\frac{\sigma_E}{E[GeV]} = \frac{10\%}{\sqrt{E}} \oplus 0.7\%$

3.4.2 Hadronic calorimeter

The HADCal consists of a center barrel within $|\eta| < 1.0$ and two external barrels on each side within $0.8 < |\eta| < 1.7$ in the barrel region, and two adjacent wheels at endcap. The barrel HADCal uses steel as absorber and polystyrene-based scintillators as the active materia while the endcap HADCal uses copper as absorber and LAr as the active material.

The center and two extended barrels of the barrel HADCal are further segmented into three concentric layers. The interaction lenghth of the three layers are 1.5 λ [2], 4.1 λ and 1.8 λ for the center barrel, and 1.5 λ, 2.6 λ and 3.3 λ for the extended barrel, respectively. Each barrel subsystem has 64 modules, and a representive module is illustrated in Figure 3.8. The scintillation light induced by the traversing particles is read by the fibres connected to the photomultiplier tubes (PMTs). By grouping the readout fibres of multiple tiles on the same PMT, a granularity of 0.1×0.1 in $\Delta\eta \times \Delta\phi$ is achieved.

For the endcap HADCal, the granularity is 0.1×0.1 in $\Delta\eta \times \Delta\phi$ within $1.5 < |\eta| < 2.5$ and 0.2×0.2 in $\Delta\eta \times \Delta\phi$ within $2.5 < |\eta| < 3.2$.

The designed energy resolution of the HADCal is $\frac{\sigma_E}{E[GeV]} = \frac{50\%}{\sqrt{E}} \oplus 3\%$.

[2]The interaction length λ is defined as the average distance after which the energy of a traversing particle is reduced by a factor of 1/e due to electromagnetic and strong interactions with the material detector.

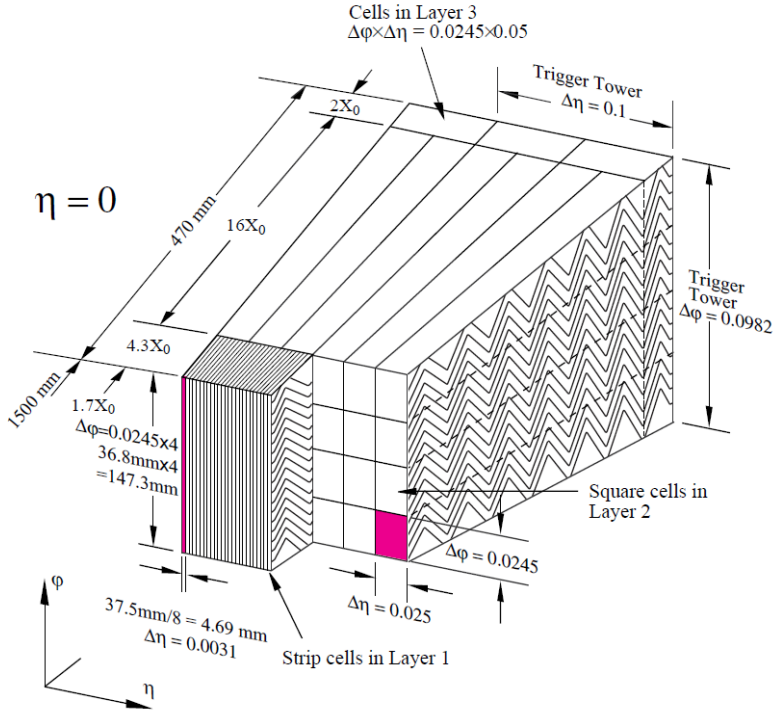

Figure 3.7: Structure of a module in the barrel EMCal (43).

3.4.3 Forward calorimeter

The FCal is integrated into the endcap cryostats, as shown in Figure 3.6, to provide uniformity of the calorimetric coverage and to reduce radiation background levels in the muon spectrometer. The FCal has a thickness of about 10 λ and it consists of the electromagnetic FCal layer and two hadronic layers on each side. The electromagnetic (hadronic) FCal uses copper (tungsten) as absorber and LAr as the active material.

The designed energy resolution of the FCal is $\frac{\sigma_E}{E[GeV]} = \frac{100\%}{\sqrt{E}} \oplus 10\%$.

3.5 Muon spectrometer

Muons are the only detectable particles that can travel through the entire ID and calorimeters without being stopped. Therefore, the muon spectrometer is placed at the outermost radius of ATLAS, aiming at measuring the momentum of muons with $|\eta|$ up to 2.7. In addition, it is also designed to trigger on the muons with time resolution of 1.5 ns to 4 ns.

The muon spectrometer consists of three layers of detectors in the barrel region between the toroid coils, arranged in cylinders around the beam pipe at radii of 5 m, 7.5 m and 10 m and four layers of detectors at endcap in front and behind the

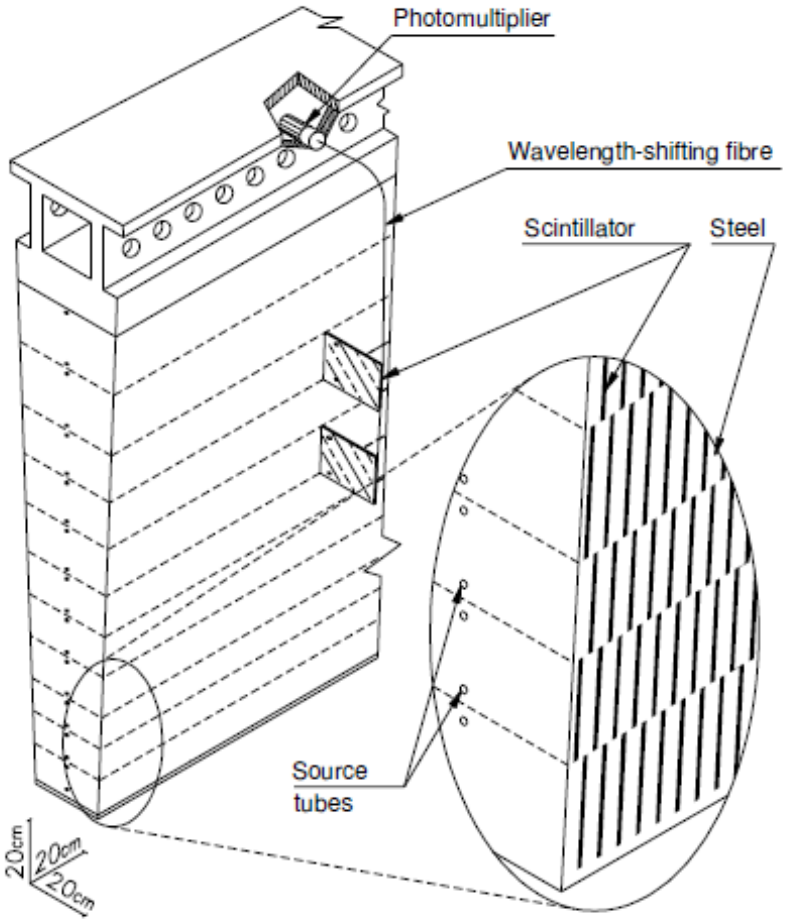

Figure 3.8: Structure of a module of the barrel HADCal with its optical readout (43).

endcap toroids, arranged in wheels at distances from the interaction point of 7.4 m, 10.8 m, 14 m, and 21.5 m. It has four types of tracking detectors. Monitored Drift Tube (MDT) and Cathode Strip Chamber (CSC) are used for high precision tracking while Thin Gap Chamber (TGC) and Resistive Plate Chamber (RPC) are used for muon triggering and supplementary tracking information. The structure of the muon system is shown in Figure 3.9 and the main parameters of the detectors are described in Figure 3.10.

- **MDT** chambers are composed of three to eight layers of cylindrical alumimum drift tubes, which are filled with a mixture of gases and have a central wire at high potential. When the muon passes through the tube, it will ionize the gas creating free charge that will be collected by the wire. The spatial resolution is 35 μm in the z direction with a drift time less than 700 ns.

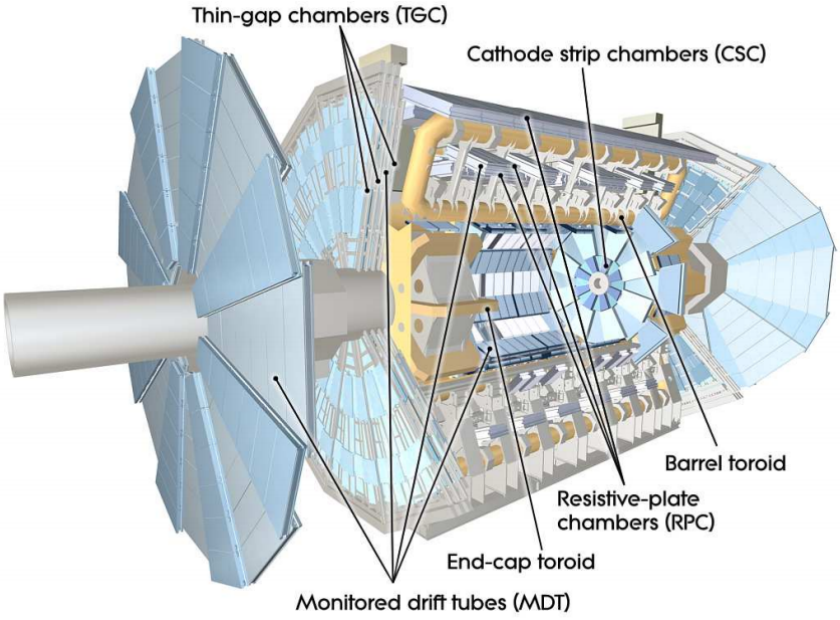

Figure 3.9: Overview of the ATLAS muon spectrometer (43).

		Chamber resolution (RMS) in			Measurements/track		Number of	
Type	Function	z/R	ϕ	time	barrel	end-cap	chambers	channels
MDT	tracking	35 μm (z)	—	—	20	20	1088 (1150)	339k (354k)
CSC	tracking	40 μm (R)	5 mm	7 ns	—	4	32	30.7k
RPC	trigger	10 mm (z)	10 mm	1.5 ns	6	—	544 (606)	359k (373k)
TGC	trigger	2–6 mm (R)	3–7 mm	4 ns	—	9	3588	318k

Figure 3.10: Main parameters of the four types of tracking detectors in the ATLAS muon spectrometer (43).

- **CSC** chambers are multi-wired proportional chambers which are made of a plane of pependicular cathodes strips with multiple anode wires. They are arranged in wheels at the end-caps, as shown in Figure 3.9, covering the region $2.0 < |\eta| < 2.7$. The spatial resolution is 40 μm in the R direction and 5 mm in ϕ-direction, with a drift time less than 40 ns and an intrinsic timing resolution of 7 ns.

- One **RPC** chamber consists of two parallel electrode-plates, which are 2 mm away from each other, with an electric field of 4.7 kV/mm. The RPC chamber is operated in avalanche mode. The spatial resolution is 10 mm in the z direction and 10 mm in the ϕ direction with an intrinsic time resolution of 1.5 ns.

- **TGC** chambers are multiwire proportional chambers filled with a highly quenching gas mixture of carbone dioxide and n-pentane, operated in a quasi-saturated mode due to having the wire-to-wire distance larger than the the wire-to-cathode distance. The spatial resolution is between 2 mm to 6 mm in the R direction and

between 3 mm and 7 mm in the ϕ direction, with an intrinsic timing resolution of 4 ns. The trigger efficiency for muons with $p_{\mathrm{T}} > 20$ GeV is approximately 90%.

The designed momentum resolution of the muon system is $\frac{\sigma_{p_{\mathrm{T}}}}{p_{\mathrm{T}}[GeV]} = 10\%$ at $p_{\mathrm{T}} =$ 1 TeV.

3.6 Trigger system of ATLAS

At the design luminosity of LHC 10^{34} cm^{-2}s^{-1}, the collision between bunches of protons will happen every 25 ns, corresponding to the event rate of 40 MHz. Given the fact that one full event consumes about 1 MB of disk space, it is impossible to store all the events since it means recording 40 TB of data per seond. Besides, we are only interested in events with particular particles in the final state. Therefore ATLAS adopts a two-level trigger system, including the hardware-based level one trigger (L1 trigger) and the software-based high level trigger (HLT), to select the interesting physics events while rejecting the background contamination. The trigger and data aquisition (DAQ) system of Run 2 in shown in Figure 3.11.

In the L1 trigger, the central trigger processor (CTP) receives information of the reconstructed objects (high p_{T} electrons, photons and $E_{\mathrm{T}}^{\mathrm{miss}}$) at trigger-level sent from the ID and calorimeters and determines whether to accept the event in 2.5 μs. If an event is accepted, a L1 accept (L1A) signal is sent to all ATLAS subdetectors to initiate the full readout of the subdetectors data in Regions-of-Interest (RoIs) identified by the L1 trigger. The nominal L1A output rate is 1 KHz, corresponding to a rate reduction factor of 400.

The HLT uses algrithms that are close to the offline reconstruction, which is introduced in chapter 4, to make the final trigger decision based on full granularity information from detectors in the RoI region, which is not available in the L1 trigger. It reduces the event rate further to 1 kHz within 200 ms decision time and then sends the selected events to the data storage.

A new level-1 topological trigger (L1Topo), performing algorithms based on topological or kinematic selections on the reconstructed objects at trigger-level, was commisioned in 2017 (45). But it was not used for the 2015 and 2016 dataset used in this analysis.

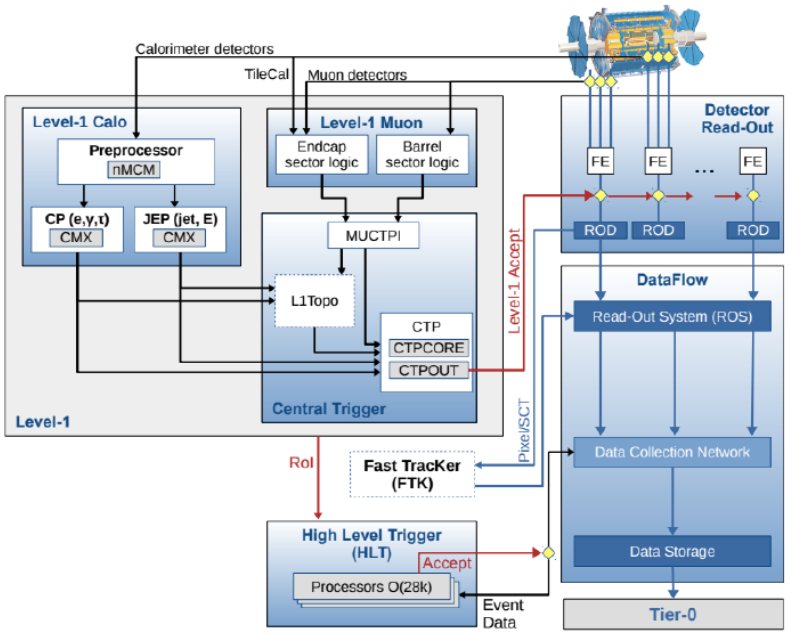

Figure 3.11: Trigger system of ATLAS (43).

4

Object Reconstruction

After passing the online trigger requirements, the data are recorded by the data aquisition system (DAQ) of ATLAS. These data are called raw data and are in terms of energy deposits in the calorimeter cells, hits in the tracking system, etc. These raw data are then reconstructed and identified into physics objects (electrons, muons, jets, etc) in order to be used in the analysis. In the following, the reconstruction and identification criteria of the physics objects used in this analysis are briefly introduced.

4.1 Electrons

Electrons are reconstructed based on the tracks in the inner detector (ID) and energy deposits in the electromagnetic (EM) calorimeter. The main backgrounds come from hadrons and non-prompt electrons originating from photon conversions and heavy flavor hadron decays. Thus identification and isolation criteria are also required to reduce the backgrounds and therefore improve the purity. The reconstruction of electrons in the central region of ATLAS ($|\eta| < 2.47$) follows these steps (74):

Reconstruction

Electron reconstruction starts with the seed-cluster algorithm. First, a sliding window with a size of 3×5 longitudinal towers searches for *seeds* that have total transverse energy (E_{T}) above 2.5 GeV, where a tower spreads 0.025 × 0.025 in the η-ϕ plane, corresponding to the granularity of the EM calorimeter middle layer. Then a clustering algorithm (75) using the seed information it is applied in order to form the clusters and reconstruct their kinematics. The clustering efficiencies range from 95% for E_{T} at 7 GeV, to more than 99% for E_{T} above 15 GeV.

After the seed reconstruction, electron tracks are reconstructed from the track seeds (which have three hits in different layers of the silicon detector) produced by the ID. This reconstruction has two steps, pattern recognition and track fit. The pattern recognition uses the information of the energy loss of the particle through the interaction with the detector material. Two different pattern recognition methods are used in

this process, corresponding to the pion hypothesis and electron hypothesis. The pattern recognition using the pion hypothesis is identical to the standard ATLAS pattern recognition which allows up to 30% energy loss at each intersection, taking into account for possible bremsstrahlung. If a track seed with E_{T} above 1 GeV can not be extended to a full track with at least seven hits and falls in the EM cluster region of interest (RoI), the pion hypothesis is discarded and the electron hypothesis is used instead, which allows for larger energy loss. After the pattern recognition, the track candidates are fitted using the ATLAS Globlal χ^2 Track Fitter (76). Track candidates that pass the electron hypothesis and have significant number of precision hits in the silicon detector (≥ 4) are loosely matched to electron clusters and are refit using an optimized Gaussian Sum Filter (GSF) (77), taking into account the non-linear bremsstrahlung.

The final procedure of the electron reconstruction is the matching of the track candidate to the cluster seed. If several tracks satisfy the matching condition, one track is chosen as the primary track based on the cluster-track distance ΔR calculated with different momentum hypothesis and information from the ID, such as the number of pixel hits (78). If the candidate is found to have no associated hits in the ID, it is considered to be a photon.

For the four momentum of the electron, the energy is given by the final calibrated cluster (79), and the η and ϕ are obtained from the best track matched to the original seed cluster.

In addition for the Run 2 analyses, the combination between the track candidates and the primary vertex is required in order to reduce backgrounds originating from conversions and secondary particles. The following conditions are applied: $d_0/\sigma_{d_0} < 5$ and $\Delta z_0 \sin\theta < 0.5$ mm, where the impact paramter d_0 is the closest distance of the track to the beam line, z_0 is the distance along the beam line between the point where d_0 is measured and the beam spot position, and θ is the polar angle of the track.

Figure 4.1 shows the reconstruction efficiency for electrons using $Z \to ee$ events in both data and MC. There is good agreement of the results obtained from data and MC.

Identification

In order to discriminate the reconstructed electron candidates from backgrounds coming from hadronic jets or converted photons and improve the purity of the real leptons, a likelihood-based (LH) method is used to do the electron identification, which is a multivariate technique combining the variables such as track quality and track-cluster matching. The output discriminant $d_{\mathcal{L}}$ is defined as:

$$d_{\mathcal{L}} = \frac{\mathcal{L}_S}{\mathcal{L}_S + \mathcal{L}_B},\ \mathcal{L}_{S(B)} = \prod P_{S(B)}, \tag{4.1}$$

where $P_{S(B)}$ are the probability density functions (PDFs) of the variables for the signal (background). Three levels of idetification operating points are provided, which are referred to as Loose, Medium and Tight, increasing in background rejection power. Some variables such as the shower shape depends on the E_{T} and the operating points are

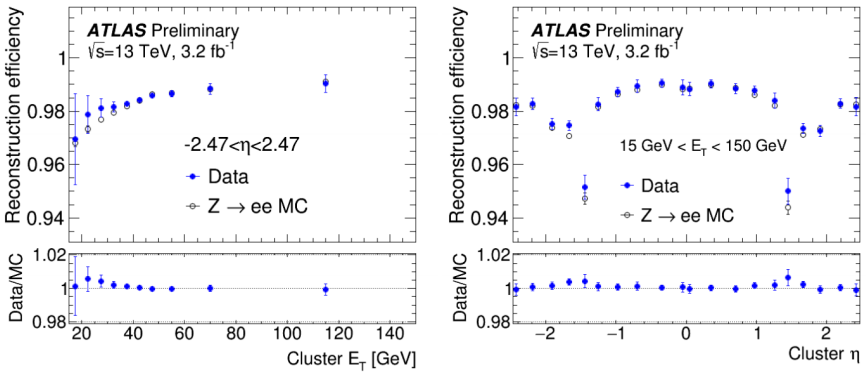

Figure 4.1: Reconstruction efficiencies of electrons as a function of E_{T} (left) and as a fuction of η for 15 GeV $< E_{\mathrm{T}} <$ 150 GeV (right). The uncertainty includes the statistical uncertainty and the systematic uncertainty (74).

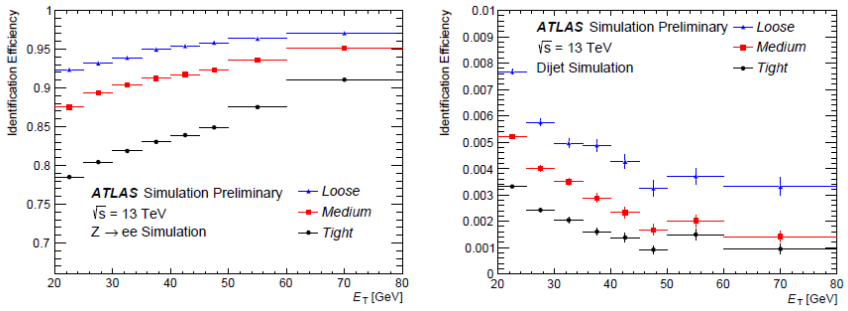

Figure 4.2: The identification efficiency of electrons from simulated $Z \to ee$ events (left) and the efficiency to identify hadrons as electrons from simulated dijet samples (74).

thus optimized in different bins of E_{T}. The performance of the identification algorithm is shown in Figure 4.2.

Isolation

To further discrminate electrons originating from events of interest and background contamination, some isolation criteria is applied in addition to the identification requirement, which uses two discriminating variables. First one is $E_{\mathrm{T}}^{\mathrm{cone0.2}}$ that is defined as the sum of total transverse energies from the calorimeter clusters within a cone of $\Delta R = 0.2$ around the electron candidate cluster. The second one is the track-based $p_{\mathrm{T}}^{\mathrm{varcone0.2}}$ defined as the p_{T} scalar sum of all the tracks in a cone of $\Delta R = \min(0.2, 10\ GeV/E_{\mathrm{T}})$ around the electron candidate track, exluding the electron track itself. These tracks should come from the primary vertex and fulfill the quality requirement. Cuts on these two variables are chosen in order to have a simulated isolation efficiency of 90% for each cut.

Differences between data and MC samples for all the electron reconstruction, identification and isolation are calculated using $Z \to ee$ and $J/\psi \to ee$ events as scale factors and the scale factors are applied to the simulation samples in order to reproduce the efficiencies with data.

4.2 Muons

Similar to the electron reconstruction, the muon reconstruction also includes identification and isolation to reject non-prompt muons coming from semileptonic hadron decays. The reconstruction of muons proceeds through these steps (80):

Reconstruction

The muon tracks are first reconstructed independently in the ID and the Muon Spectrometer (MS), and then combined to form the muon tracks that are used in the physics analysis. In the ID, muons are reconstructed similar to the method described in Section 4.1. While in the MS, the muon reconstruction starts with a search for the hit patterns in each muon chamber to form segments. Then hits from the segments in different layers are fitted together to build the muon track candidates. At least two matching segments are required to build a track except at the barrel-endcap transistion region. Finally, hits associated to each track are fitted using the ALTAS global χ^2 fit.

After the reconstruction in the ID and MS, the combined ID-MS reconstruction is performed based on various algorithms and they define four types of muons.

- **Combined (CB) muons**: A global refit uses both hits in the ID and MS to form a combined muon track and the MS hits might be removed to improve the fit quality. Most muons are reconstructed following the outside-in pattern, in which muons are first reconstructed in the MS and then extrapolated inward to match a track from the ID. The inside-out pattern is also used as a complementary approach.

- **Segment-tagged (ST) muons**: If a track in the ID, when extrapolated to the MS, is associated to at least one local track segment in the MDT or CSC chambers, it is classified as a ST muon. This algorithm aims at increasing the acceptance of muons with low p_{T}.

- **Calorimeter-tagged (CT) muons**: If a track in the ID can be matched to an energy deposit in the calorimeter compatible with a minimum-ionizing particle, it is classified as a CT muon. This algorithm increases the acceptance of muons in the $|\eta| < 0.1$ region of the MS.

- **Extrapolated (ME) muons**: ME muons are reconstructed based only on the MS tracks and a loose requirement on compatibility with the interaction point, they are used to extend the acceptance into the $2.5 < |\eta| < 2.7$ region, which is not covered by the ID.

	$4 < p_{\mathrm{T}} < 20$ GeV		$20 < p_{\mathrm{T}} < 100$ GeV	
Selection	$\epsilon_{\mu}^{\mathrm{MC}}$ [%]	$\epsilon_{\mathrm{Hadrons}}^{\mathrm{MC}}$ [%]	$\epsilon_{\mu}^{\mathrm{MC}}$ [%]	$\epsilon_{\mathrm{Hadrons}}^{\mathrm{MC}}$ [%]
Loose	96.7	0.53	98.1	0.76
Medium	95.5	0.38	96.1	0.17
Tight	89.9	0.19	91.8	0.11
High-p_{T}	78.1	0.26	80.4	0.13

Figure 4.3: Reconstruction efficiencies for promt muons coming from W decays and hadrons identified as prompt muons (80).

Identification

In order to suppress backgrounds mainly from pion and kaon decays, muon identification is performed by applying quality requirements on several variables that have good discriminating power:

- q/p significance, defined as the absolute value of the difference between the ratio of the charge and momentum of the muons measured in the ID and MS;
- $\rho\prime$, defined as the absolute value of the difference between the transverse momentum measurements in the ID and MS;
- normalised χ^2 of the combined track fit.

Theres are four muon identification selections (Medium, Loose, Tight and High-p_{T}) and only tight muons are used in this analysis. The reconstruction efficiencies for muons from W decays and hadrons misidentified as muons are obtained from the $t\bar{t}$ simulation sample, as shown in Figure 4.3. Figure 4.4 shows the muon reconstruction efficiency as a function of η.

Isolation

The isolation variables are the same with those for the electron isolation. The criteria is chosen in this analysis such that the isolation efficiency could reach 95% for $p_{\mathrm{T}} = 25$ GeV and 99% for $p_{\mathrm{T}} = 60$ GeV corresponding to the Gradient Working point.

4.3 Jets

In collision experiments, when high energy partons are produced, these partons will form cones of hadrons through fragmentation and hadronization which are called *jets*, with the total momentum alligned in the direction of the initial partons. The jets used in this analysis are reconstructed using a method called the anti-k_t algorithm (81), which

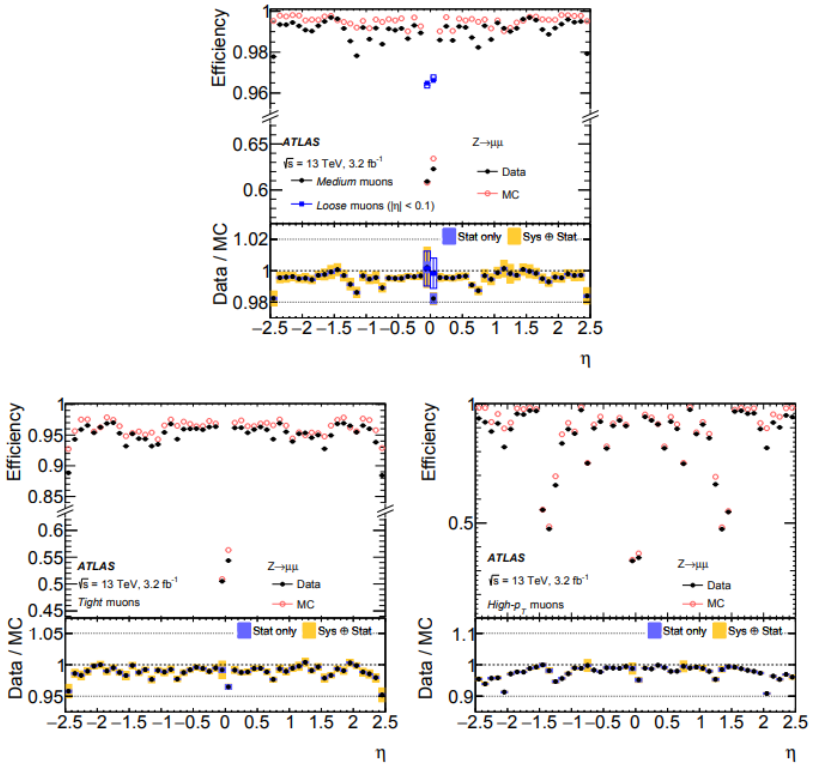

Figure 4.4: Reconstruction efficiency of muons with $p_{\mathrm{T}} > 10$ GeV as a function of η measured using $Z \to \mu\mu$ data and MC events for Medium (top), Tight (bottom left) and High-p_{T} (bottom right) muons (80).

is the standard jet algorithm at ATLAS. The jets will be categorized into calorimeter-based jets or track-based jets depending on the elements used for their reconstruction, enegy deposit clusters in the calorimeter clusters or track clusters from the ID.

The anti-k_t jet clustreing algorithm

The algorithm makes use of two distance measuring parameters, d_{ij} which is distance between two partices and d_{iB} which is the distance between a particle and the beam:

$$d_{ij} = min(\frac{1}{k_{ti}^2}, \frac{1}{k_{tj}^2})\frac{\Delta_{ij}^2}{R^2} \tag{4.2}$$

$$d_{iB} = \frac{1}{k_{ti}^2}. \tag{4.3}$$

The angular distance Δ_{ij}^2 is defined as $\Delta_{ij}^2 = (\eta_i - \eta_j)^2 + (\phi_i - \phi_j)^2$ and k_{ti} is the transverse momentum of particle i. R determines the radius of the cone, e.g. which is 0.4 for the small-R jets including gluon, light quark an b-jets. The functionality of

this algorithm can be understood through a simple example. Consider an event with a hard particle 1 and many soft particles. The distance variable d_{1j} is then exclusively determined by the transverse momentum of particle 1 and Δ_{1j}. Since d_{ij} between soft particles are much larger, soft particles tend to cluster with hard ones long before they cluster among themselves. If there is only one hard particle within $2R$, then all the soft particles in this range will cluster with the hard one and form a jet which is perfectly conical. However, this is not always the case. If another hard particle exists with $R < \Delta_{12} < 2R$, then two jets will be formed. If $k_{t1} \gg k_{t2}$, jet 1 will be perfectly conical while jet 2 is partially conical due to the fact that the overlapping part with particle 1 is removed. And in the case where $k_{t1} \sim k_{t2}$, both jets will be tailored with the boundry b between them defined according to $\Delta R_{1b}/k_{t1} = \Delta R_{2b}/k_{t2}$. The jets reconstructed by the anti-k_t algorithm are required to have a minimum p_{T} of 7 GeV.

4.3.1 Calorimeter-based small-R jets

Reconstruction

For the calorimeter-based jets, the input constituents for the jet reconstruction are the topologically clustered calorimeter cells, which are called topo-clusters. These clusters are formed starting from the seed cells, which should have energy deposits four times greater than the quadratic sum of the measured electronics and pile-up noise, which is denoted as σ and adding neighbour cells with energy deposits over 2σ. Then these topo-clusters are seperated by the cluster splitting algorithm in order to remove overlaps. The topo-clusters used for reconstruction are considerd to be massless and should only have positive energies.

Calibration

The small-R jets refer to the jets reconstructed by the anti-k_t algorithm with cone size $R = 0.4$. These jets are then calibrated to match the truth jets (82), which are reconstructed using anti-k_t clustering of stable final-state particles from MC generation and therefore have the engergy at paticle level. The calibration scheme is illustrated in Figure 4.5

Original correction: First, the four-momentum of the jets are recalculated to point to the hard-scatter primary vertex instead of the detector center, without affecting the jet energy. This correction is used to improve the η resolution of jets, based on the difference between reconstructed and truth jets calculated from MC simulation. As a result, for jets with p_{T} of 20 GeV the η resolution is improved from about 0.06 to 0.045, and for jets with $p_{\mathrm{T}} > 200$ GeV it is improve from 0.03 to below 0.006.

Pile-up correction: Then a two-step pile-up correction is applied to remove the excess energy coming from pile-up. In the first step, an area-based correction removes the per-event contribution to the p_{T} of each jet according to its area. This contribution is derived from the median p_{T} density ρ of jets in the η-ϕ plane, which is calculated using the k_t algorithm (R chosen to be 0.4) with positive-enegy topo-clusters up to $|\eta|$

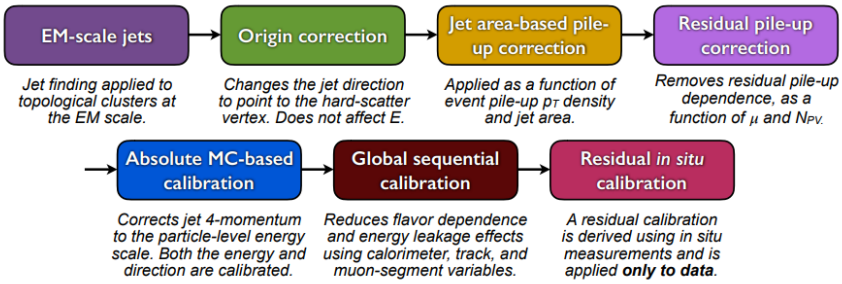

Figure 4.5: Illustration of the sequential procedure to calibrate the energy of the jets at ATLAS (82).

= 2 due to the higher calorimeter occupance in the forward region. ρ is equal to p_{T}/A, where A is the area of the jet, calculated using ghost association. While in the second step, another correction which accounts for the residual p_T dependence on the number of primary vertices, N_{PV} and the average number of pile-up events, μ, is applied. The coefficents of these two variables are extracted from the separate linear fits done in bins of p_{T}^{truth} and $|\eta|$ on MC samples. In summary, the pile-up correction gives the corrected jet p_{T}:

$$p_{\mathrm{T}}^{\mathrm{corr}} = p_{\mathrm{T}}^{\mathrm{reco}} - \rho \times A - \alpha \times (N_{\mathrm{PC}} - 1) - \beta \times \mu \tag{4.4}$$

Jet energy scale (JES) and η calibration: The absolute JES calibration matches the reconstructed jet energy to the particle-level energy scale of the truth jet. The correction factor is derived from the energy response which is derived from a Gaussian fit to the core of $E^{\mathrm{reco}}/E^{\mathrm{truth}}$. The energy response is distributed as a function of eta of the jet pointing to the center of the detector, η_{det}, for different values of E^{truth}, as shown if Figure 4.6. Then a second correction is derived as the difference between the reconstructed η^{reco} and the truth η^{truth}. Jets after this step are considered to be at EM+JES scale.

Global sequential calibration and In-situ calibration: The global sequential calibration is aming at improving the resolution JES against the fluctuations observed in the particle composition and distribution of the energy of the jets. And for the last step, the in-situ calibration uses three well-measured reference objects (Z, γ, and multijet) to correct the difference of jet response between MC and data due to the fact that the detector material and intractions with particles can not be perfectly modelled by the MC simulation.

B-tagging

B-jets are the jets which originate from b quarks. Because the top quark decays to a W boson and a b-quark for almost 100%, it is important for this analysis to successfully identify the b-jets in the final state. The algorithm used to detect b-jets is called b-tagging algorithm and there are basically three different types:

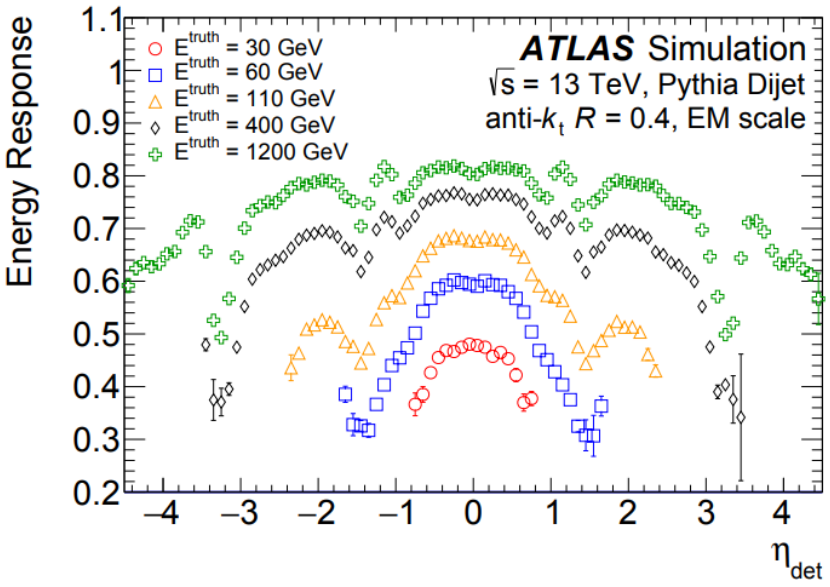

Figure 4.6: The average energy response for the simulated jets as a fuction of the jet η, shown for several values of E^{truth} (82).

Algorithms based on impact parameter (IP2D, IP3D): Since hadrons containing b-quarks have relatively long life time ($c\tau \sim 450$ μm), the tracks corresponding to b-jets have a larger impact parameter than tracks of c- and light flavor jets. IP2D and IP3D algorithms calculate the logarithm of likelihood ratio between b- and other flavor hypothesises, $\log(P_b/P_u)$, in order to discriminate b-jets from other jets. The difference of these two methods is that IP3D uses both the transverse impact parameter (d_0) and the longitudinal impact parameter ($Z_0 \sin\theta$) while IP2D only uses the later one. The performance can be seen in Figure 4.7.

Algorithms using inclusive secondary vertex reconstruction (SV): Given the fact that a b-hadron travels a relatively long distance (~ 450 μm), it will form a displaced secondary vertex from the hard-scatter primary vertex. The SV algorithm recontructs explicitly an inclusive secondary vertex within the jet. Candidate tracks are used to reconstruct the two-track vertex, and if this secondary vertex originates from long-lived particles (K_S, Λ), photon conversion or particles from the hadronic interaction with detector material, it will be discarded. At last, a single vertex is built using the tracks pass the selection.

Algorithms employing decay chain multi-vertex reconstruction (JetFitter): There is another type of b-tagging algorithms which exploits the topological structure of weak b- and c-hadron decays within the jet and reconstruct the full decay chain for PV $\rightarrow$ b-jet $\rightarrow$ c-jet. It assumes these vertices form a line along the flight path of the b-hadron, and this line together with the vertices are found using a Kalman filter.

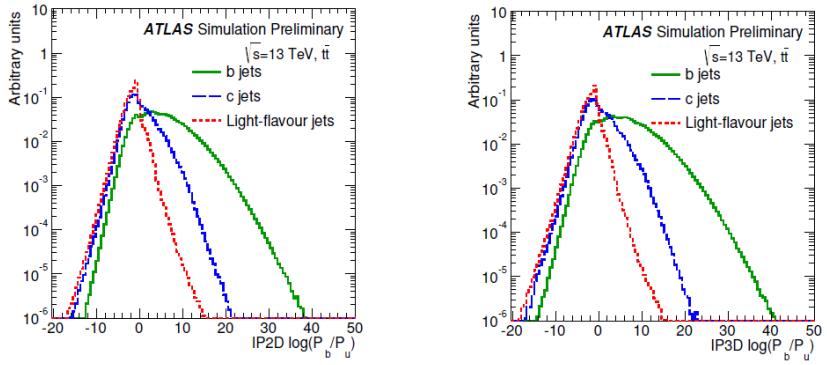

(a) (b)

Figure 4.7: Distribution of the logarithm of likelihood ratio between b- and other flavor hypothesises, $\log(P_b/P_u)$, for b-, c- and light-flavor jets for the IP2D and IP3D algorithms (83).

Finally, a multivariate algorithm based on a boosted decision tree (BDT) which takes the output variables from the above algorithms, which is called MV2c10 and widely used for current analyses. This BDT is trained on 5 million $t\bar{t}$ events and the discriminating performance can be seen in Figure 4.8. The "c10" in the name means that the background in the trainning sample consists of 10% c-jets and 90% light-flavor jets. However, due to the fact most physics analysis are more sensitive to c-jets than the light jets, this fraction in practice can be modified in order to increase the c-jet rejection power. The c-jet fraction is actually 7%.

The b-tagging operating points of MV2c10, corresponding to the cut values on the output of the BDT, are shown in Figure 4.9.

4.3.2 Calorimeter-based large-R jets

When a massive particle, such as the top quark and the Higgs boson, is highly boosted and decays hadronically into quarks, the resulting quarks can be reconstruted as a single large-radius jet. Large-R jets are used in this analysis for the hadronic channel with missing transverse momentum greater than 200 GeV ($E_{\mathrm{T}}^{\mathrm{miss}} > 200$ GeV) to reconstruct the boosted hadronically decaying top quark.

Reconstruction

The large-R jets are reconstructed using also the anti-k_t algorithm, with the cone size R set to be 1.0. And the input elements for the clustering are the topological clusters calibrated using the local calibration weighting (LCW). The large-R jets are then trimmed by first reclustering the input elements of the initial jet into subjects of radius R_{sub} and removing any subject that is less than f_{cut} times the transverse momentum of the parent jet. These two parameters are chosen to be: $R_{\mathrm{sub}} = 0.2$ and

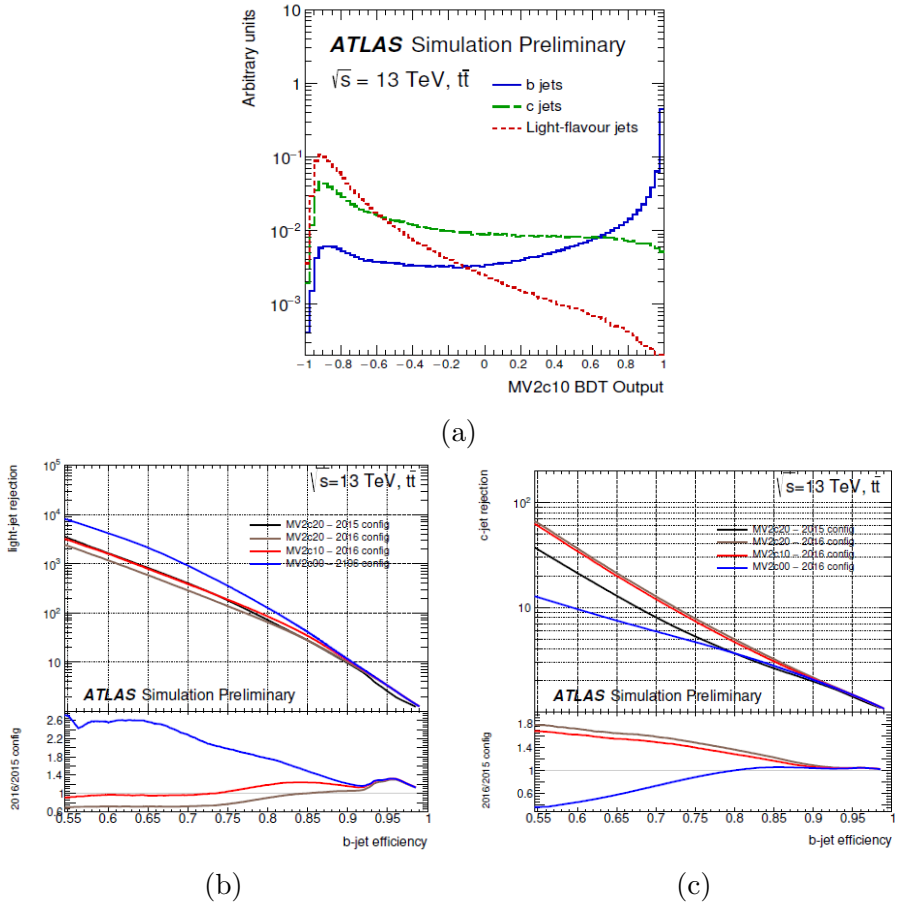

Figure 4.8: MV2c10 b-tagging algorithm output for b-, c- and light flavor jets (a), light flavor jet (b) and c-jet rejection as a function of b-jet efficiency in $t\bar{t}$ events (83).

$f_{\text{cut}} = 5\%$. The remaining consituents add up to the four-momentum of the jet.

Top-tagging

The algorithm used to identify the boosted top quark produced by a massive particle is called top-tagging. It exploits the substructure of the large radius jet and the decay products. There are two variables used in the top-tagging, the calibrated jet mass m_{jet}^{calib} and the N-subjettiness ratio τ_{32}. Selections are made on these variables to get different working points corresponding to different signal efficiencies, i.e 50% and 80%. The signal efficiency is calculated using a mixture of simulated $Z' \rightarrow t\bar{t}$ samples, defined as the fraction of reconstructed jets passing the top-tagging algorithm that match a generator-level jet.

BDT Cut value	b-jet Efficiency [%]	c-jet Rejection	τ-jet Rejection	Light-jet Rejection
0.9349	60	34	184	1538
0.8244	70	12	55	381
0.6459	77	6	22	134
0.1758	85	3.1	8.2	33

Figure 4.9: MV2c10 b-tagging algorithm operating points (83).

4.3.3 Track-based jets

Track-based jets are also used in this analysis for the hadronic channel. They are reconstructed using the anti-k_t algorithm with the radius parameter $R = 0.2$, taking the ID tracks as inputs. The calibration is different from that for the calorimeter jets. The b-tagging of track jets is also based on the multivariate algorithm MV2c10.

4.4 Missing transverse momentum

In the final states of the monotop events considered in this analysis, the dark matter particles or the neutrinos, can not be detected by the ATLAS detector. Therefore it is impossible to directly reconstruct these particles. However, due to the conservation of momentum and the initial transverse momentum of the system is zero, the imblance of transverse momentum, defined as $E_{\mathrm{T}}^{\mathrm{miss}}$, can give us information for the undetectable particles. In the TST MET scheme, $E_{\mathrm{T}}^{\mathrm{miss}}$ is reconstructed using the vectorial sum in the transverse plane for the hard objects plus soft-term which includes the residual visible momenta mainly from soft jets ($p_T < 20$ GeV) and misidentified muons. $E_{\mathrm{T}}^{\mathrm{miss}}$ and its azimuthal angle are given by:

$$E_{\mathrm{T}}^{\mathrm{miss}} = \sqrt{(E_x^{\mathrm{miss}})^2 + (E_y^{\mathrm{miss}})^2} \tag{4.5}$$

$$\phi^{\mathrm{miss}} = \arctan(\frac{E_y^{\mathrm{miss}}}{E_x^{\mathrm{miss}}}) \tag{4.6}$$

5

Data and Monte Carlo samples

5.1 Data samples and triggers

This analysis uses proton-proton collision data collected by the ATLAS detector at a center-of-mass energy of $\sqrt{s} = 13$ TeV, during the years 2015 and 2016 in the periods when the LHC was operationg with a bunch crossing of 25 ns. In addition, we only take the data when all the detector components necessary for this analysis were fully functional, since sometimes the subsystems of the ATLAS detector might have issues and need to be reset. This is achieved by requiring the data events to pass the quality criteria, so-called Good-Run Lists (GRLs). The data GRLs used in this analysis are:

- **2015 Data**: DetStatus-v79-repro20-02_DQDefects-00-02-02_PHYS_StandardGRL_All_Good_25ns
- **2016 Data**: DetStatus-v88-pro20-21_DQDefects-00-02-04_PHYS_StandardGRL_All_Good_25ns

Finally we have a data sample with a total integrated luminosity of 36.1 fb^{-1}.

The data events are also required to pass the triggers described below. For the hadronic channel, events are required to have large missing transverse momentum, and therefore $E_{\mathrm{T}}^{\mathrm{miss}}$ triggers based on the summed up energy deposits reconstructed from calorimeter clusters are apllied on the data. For the leptonic channel, events are require to pass at least one of the single-electron or single-muon triggers. The triggers require a p_{T} of at least 24 GeV(26 GeV) for electrons and 20 GeV(26 GeV) for muons for the 2015(2016) datasets, and also have requirments on the lepton reconstruction and isolation. These are complemented by triggers with higer p_{T} thresholds and relaxed isolation and identification requirements to ensure maximum efficiency at higer lepton p_{T}. In this analysis the following single lepton and $E_{\mathrm{T}}^{\mathrm{miss}}$ unprescaled triggers are used for the single lepton and fully hadronic channels, respectively:

- lepton triggers are based on single-electron and single-muon triggers (see below) which are combined using a logical "or":

  - single electron triggers: HLT_e24_lhmedium_L1EM20VH, HLT_e60_lhmedium, HLT_e120_lhloose for data collected in 2015 and HLT_e26_lhtight_nod0_ivarloose, HLT_e60_lhmedium_nod0, HLT_e140_lhloose_nod0 for 2016 data.
  - single muon triggers: HLT_mu20_iloose_L1MU15, HLT_mu50 for data collected in 2015 and HLT_mu26_ivarmedium, HLT_mu50 for 2016 data.

- $E_{\mathrm{T}}^{\mathrm{miss}}$ triggers are based on the summed up energy depositions reconstructed from calorimeter clusters:
  - For data taken during the 2015 data-taking-period events have to pass :
    * HLT_xe70 trigger.
  - For data taken during the 2016 data-taking-period events have to pass :
    * HLT_noalg_L1J400 OR HLT_xe90_mht_L1XE50 OR HLT_xe100_mht_L1XE50 OR HLT_xe110_mht_L1XE50

5.2 Monte Carlo samples

Monte Carlo simulation samples are generated to evaluate background modeling, signal acceptance, optimization of the event selection and evaluate systematic uncertainties and to build templates for the statistical analysis. These samples are produced with the approved ATLAS event generation procedure and the ATLAS detector is simulated using GEANT4 (46) for a full simulation or AF2 (47) for a fast simulation. The TOPQ1 and EXOT7 derivations are used for the leptonic channel and fully hadronic channel events, respectively. The MC generators, parton distribution functions (PDFs) used for all the MC samples are summarised in Table 5.1. In the following, a brief description of the signal MC samples and the background MC samples is given in Section 5.2.1 and Section 5.2.2, respectively.

5.2.1 Signal samples

Signal samples for both resonant and non-resonant DM models are generated with MadGraph5_ aMC@NLO (48) v2.2.3 at LO using the NNPDF3.0LO PDF set (49). Parton showering and hadronization are handled by the Pythia 8.212 (50) event generator with the A14 tune (51), using the NNPDF2.3LO (52) PDF set. Signal samples for the resonant model are generated assuming a DM mass $m_\chi = 10$ GeV and a range of mediator masses m_ϕ between 1 TeV and 5 TeV. The values of the coupling constants and mixing parameter are chosen following the recommendations of the ATLAS and CMS Dark Matter Forum: $\lambda = 0.2$ and $y = 0.4$. The kinematic distributions predicted by the model are not strongly dependent on the coupling parameters after similar cuts either at the particle level or at the reconstruction level, and thus all the samples are generated using this set of parameters. The remaining kinematic dependence on the different couplings and masses was accounted for by means of a reweighting procedure

Process	Generator	PDFs
$t\bar{t}$	Powheg + Pythia8	A14
$W \to \ell\nu$**+jets**	Sherpa (2.2.1)	NNPDF30NNLO
$Z \to \nu\nu, \ell\ell$**+jets**	Sherpa (2.2.1)	NNPDF30NNLO
Single top		
t-channel	Powheg + Pythia	P2012
s-channel	Powheg + Pythia	P2012
Wt	Powheg + Pythia	P2012
Diboson		
WW	Powheg + Pythia8	CT10
WZ	Powheg + Pythia8	CT10
ZZ	Powheg + Pythia8	CT10
$t\bar{t}$**+X**		
$t\bar{t}$+W	Sherpa (AFII)	NNPDF30NNLO
$t\bar{t}$+Z	Sherpa (AFII)	NNPDF30NNLO
$t\bar{t}$+H	aMcAtNlo + Herwig	UEEE5 + CTEQ6L1 + CT10
QCD		
jj	MadGraph + Pythia8	NNPDF30LO
mono-W/Z signals	MadGraph + Pythia8	A14N23LO
VLT	MadGraph + Pythia8	NNPDF30LO + A14NNPDF23LO

Table 5.1: List of MC generators and parton distribution functions (PDFs) used for the signal and background processes. Details are given in the text.

(The details are described in Section 7.5). Similarly, the MC samples for the non-resonant model are generated for ranges of m_V between 500 GeV and 3 TeV and a benchmark DM mass $m_\chi = 1$ GeV for which this analysis is sensitive. The values of the coupling parameters are set to $a = 0.5$, and $g_\chi = 1.0$. The signal samples are normalised to the theoretical LO cross-sections, that are computed using MadGraph5_aMC@NLO.

The VLT signal samples are generated with MadGraph5_aMC@NLO v2.2.3 at LO using the NNPDF3.0LO PDF set. Parton showering and hadronization are handled by the Pythia 8.212 event generator with the A14 tune, using the NNPDF2.3LO PDF set. The signal samples are generated for VLT masses between 700 GeV and 2 TeV with a benchmark coupling of $\kappa_T = 0.5$ in the WTb production vertex. In order to study the effect of different VLT widths on the kinematic distributions, additional samples are generated by changing κ_T to 0.1 and 1.0. The signal samples are normalised to the NLO cross-section by correcting the LO cross-section calculated using MadGraph5_aMC@NLO for the difference between the NLO and LO cross-sections reported for the neutral single-VLT production process via a ZTt coupling (53).

5.2.2 Background samples

The background samples are generated using different combinations of matrix element (ME) event generators and parton shower and hadronization programs. The $t\bar{t}$ samples are generated with POWHEG-BOX v2 (54, 55, 56, 57, 58, 59, 60) at NLO, interfaced to PYTHIA 8.210 using the A14 tune. The single-top samples are generated with POWHEG-BOX v1 at NLO for the $t-, WT-$ and $s-$channels and with MADGRAPH5_aMC@NLO at LO for the tZq process, interfaced to PYTHIA 6.428 (61). The CT10f4 (CT10) PDF set (62) is used in the matrix element calculations for the $t-$channel ($Wt-$ and $s-$channels). For the parton shower and hadronization, the CTEQ6L1 (63) PDF set and the Perugia 2012 tune (64) are used. The W+jets and Z+jets samples are generated with SHERPA v2.2.1 (65). Matrix elements are calculated for up to two partons at NLO and up to four partons at LO using the COMIX (66) and OPENLOOPS (67) ME generators, and merged with the SHERPA parton shower (68) according to the ME+PS@NLO prescription (69). The NNPDF3.0NNLO PDF set (70) is used together with a SHERPA parton shower tune. The diboson samples are generated with POWHEG-BOX v2 interfaced to PYTHIA 8.186. The CT10nlo PDF set is used for the hadronic process and the CTEQ6L1 PDF set is used for the parton shower. The $t\bar{t}$+X(X = W, Z and H) samples are generated with MADGRAPH5_aMC@NLO v2.3.2 at NLO, interfaced to PYTHIA 8.186. Nonperturbative effects are modelled with the AZNLP tune (71).

The cross-sections for the dominant background processes, $t\bar{t}$ and W/Z+jets. are calculated at NNLO(72, 73). The calculation for the $t\bar{t}$ samples also includes the next-to- next-to-leading logarithmic (NNLL) soft gluon terms.

6

The monotop analysis

As mentioned in the introduction section, this analysis is focused on the search for the resonant and non-resonant production of dark matter particles and the vector-like quark T, in the monotop topology which has a single top quark associated with large missing transverse energy up to the TeV scale, in the final state. The Feynman disgrams for these processes are shown in Figure 6.1. Depending on the decay mode of the top quark, a leptonic or fully hadronic topology can be obtained. Both possibilities are explored in this analysis independently. The first two sections are for the studies done in leptonic channel and hadronic channel respectively, including pre-selection, signal region definition and background estimation in these two channels. The next section describes the sources of systematic uncertainties, which could come from detector-related uncertainties and the modeling of the background processes. The results from the two channels are combined statistically and interpreted for both the DM and VLT scenarios.

6.1 Leptonic channel

6.1.1 Pre-selection

The experimental signature of the leptonic channel is one isolated lepton and one b-jet from the W boson decay, plus large missing transverse momentum due to the undetected neutrino and dark matter particles, and one additional jet in the forward region for VLT production. The TOPQ1 derivation, which is used to produce the data and MC samples, requires the events to have at least one electron or muon with $p_{\mathrm{T}} > 20$ GeV and $|\eta| < 2.5$. Furthermore, these preselected events are required to contain exactly one tight lepton with $p_{\mathrm{T}} > 30$ GeV, one b-jet with $p_{\mathrm{T}} > 30$ GeV, $E_{\mathrm{T}}^{\mathrm{miss}} > 50$ GeV, and m_{T}^{W} [1] $+ E_T^{miss} > 60$ GeV, in order to reduce the QCD contanmination. A so-called charge-asymmetry cut is also applied due to the fact that the non-resonant model favours positive leptons while the resonant model favours the negative ones. Therefore,

[1] The transverse mass of the lepton and missing transverse enegy, is defined as $m_T(l, E_T^{miss}) =$

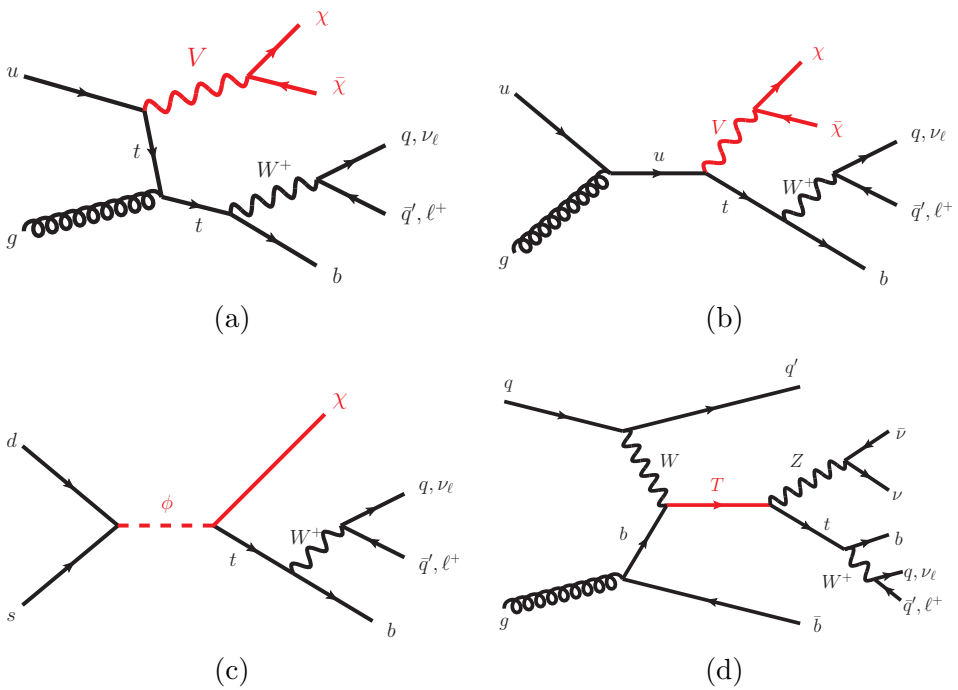

Figure 6.1: Representative leading-order Feynman diagrams corresponding to the signals sought in this paper: non-resonant (a) t-channel and (b) s-channel DM production in association with a top-quark; (c) resonant production of a DM particle (χ) and a top-quark from the decay of a scalar particle (ϕ); and (d) single production of a vector-like T quark decaying into $Zt\,(\rightarrow \nu\bar{\nu}bW)$.

only the events with a positive charged lepton are selected for the non-resonant model and events with a negative charged lepton are selected for the resonant model.

Figure 6.2 and 6.3 show the distributions of some kinematic variables after the pre-selection, for the elctron and muon channels, respectively. Three non-resonant signal modeles with m_V = 200, 500 and 1500 GeV are also included in the plots. The uncertainty bands includes the statistical uncertainty of the MC simulation events and also a 50% normalisation uncertainty for the multijet background, which is derived using data-driven methods.

6.1.2 Signal region definition

As we can see from Figure 6.2 and 6.3, $|\Delta\phi(l,b)|$ and m_{T}^{W} have the most discriminating power of signal over background. The lepton and b-jet are closer to each other if they both come from the decay of a top quark than come from W+jets or multijet backgroud events. In addition, for the signal events, the azimuthal difference between the lepton and $E_{\mathrm{T}}^{\mathrm{miss}}$ is larger than the SM backgrounds, which leads to a larger $m_{\mathrm{T}}(l, E_{\mathrm{T}}^{\mathrm{miss}})$. Therefore, an optimization of the cuts on these two variables is performed by performing a grid search for the best expected limit on the production cross-section. The calculation

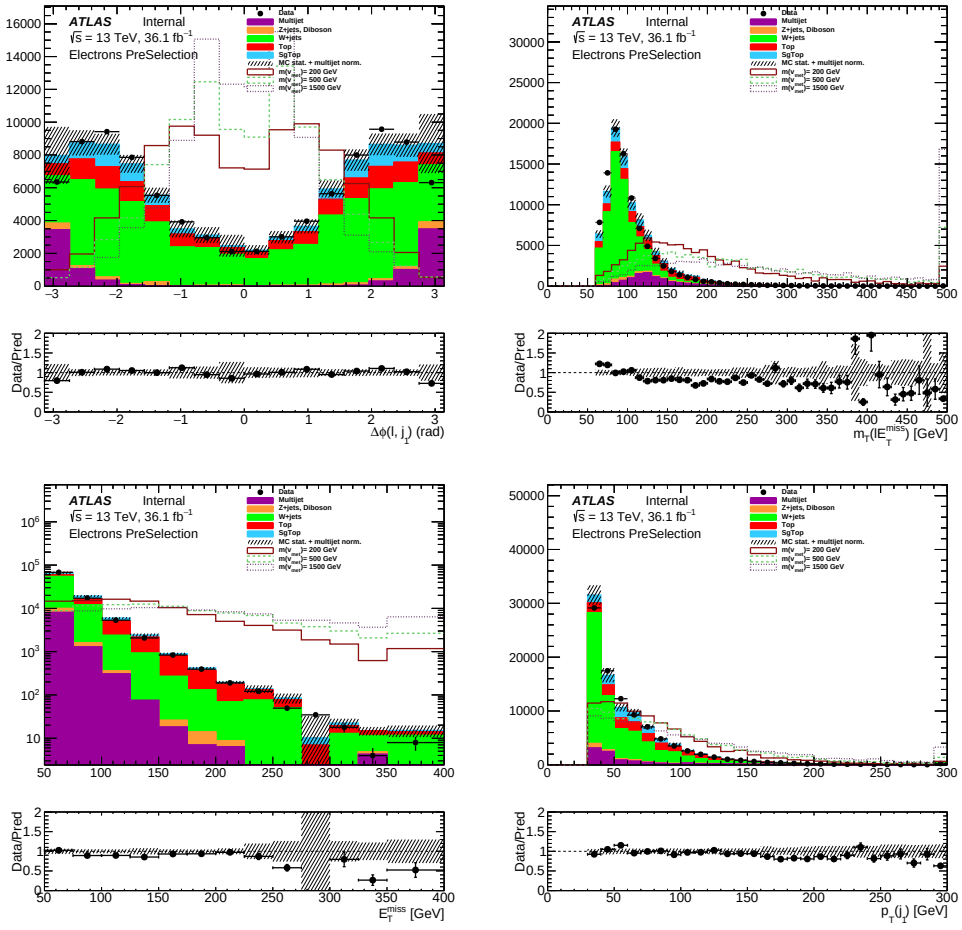

Figure 6.2: Distributions of $\Delta\phi$ between the lepton and the jet with largest p_{T} ($\Delta\phi(l, j_1)$), transverse mass of the lepton and the $E_{\mathrm{T}}^{\mathrm{miss}}$ ($m_{\mathrm{T}}(l, E_{\mathrm{T}}^{\mathrm{miss}})$), the $E_{\mathrm{T}}^{\mathrm{miss}}$ and the p_{T} of the jet with largest p_{T} after preselection for the electron channel. The uncertainty bands includes the statistical uncertainty of the MC simulation events and also a 50% normalisation uncertainty for the multijet background, which is derived using data-driven methods.

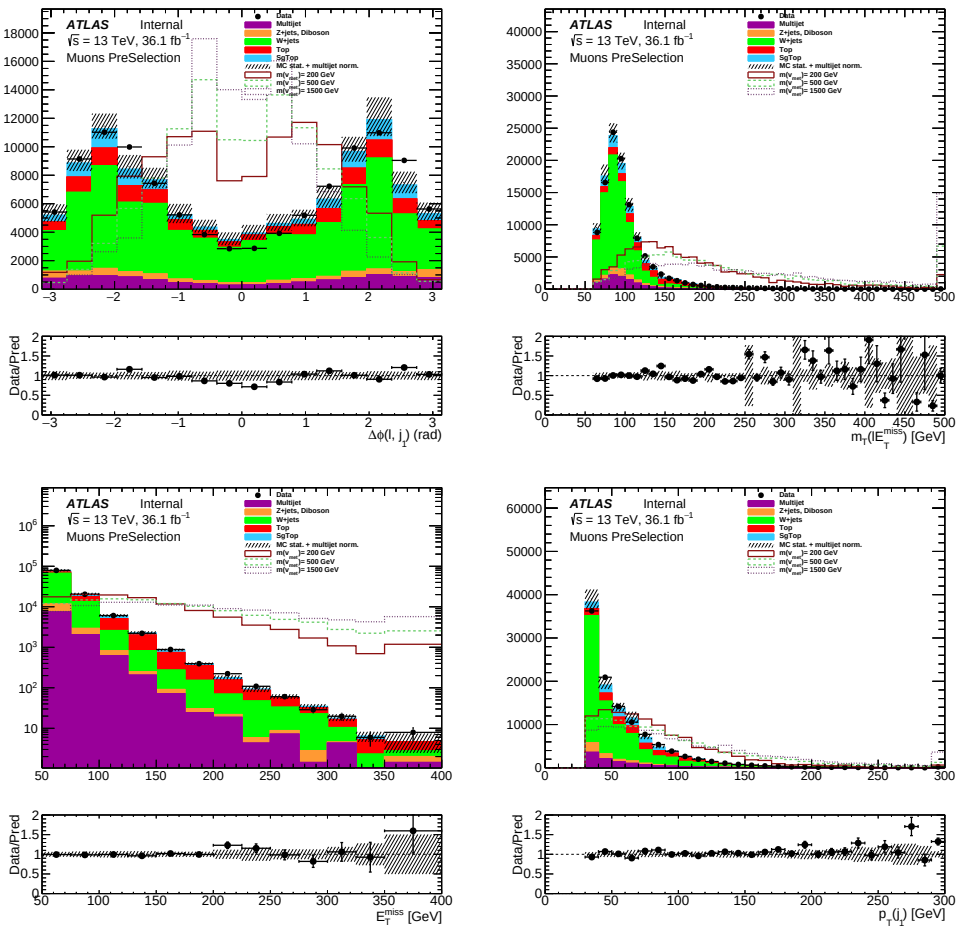

Figure 6.3: Distributions of $\Delta\phi$ between the lepton and the jet with largest p_{T} ($\Delta\phi(l, j_1)$), transverse mass of the lepton and the $E_{\mathrm{T}}^{\mathrm{miss}}$ ($m_{\mathrm{T}}(l, E_{\mathrm{T}}^{\mathrm{miss}})$), the $E_{\mathrm{T}}^{\mathrm{miss}}$ and the p_{T} of the jet with largest p_{T} after the preselection for the muon channel. The uncertainty bands includes the statistical uncertainty of the MC simulation events and also a 50% normalisation uncertainty for the multijet background, which is derived using data-driven methods.

of the expected limit is described in Section 7.1, and it includes all the statistical and systematic uncertainties. The search range for $m_{\mathrm{T}}(l, E_{\mathrm{T}}^{\mathrm{miss}})$ is from 160 to 300 GeV with a step of 20 GeV, and for the $|\Delta\phi(l,b)|$ is from 1.0 to 2.8 in steps of 0.2. The optimazation is done on several non-resonant signal samples with m_V of 500, 750, 1000 and 1500 GeV. The result is show in Figure 6.4, and the expected limit is transformed to the signal strength that is defined as the ratio of the signal cross-section to the theoretical signal cross-section. As a result, cuts of $m_{\mathrm{T}}(l, E_{\mathrm{T}}^{\mathrm{miss}}) > 260$ GeV and $|\Delta\phi(l,b)| < 1.2$ are chosen to define the signal region.

Similar studies are also done for the renonant DM model and the VLT production.

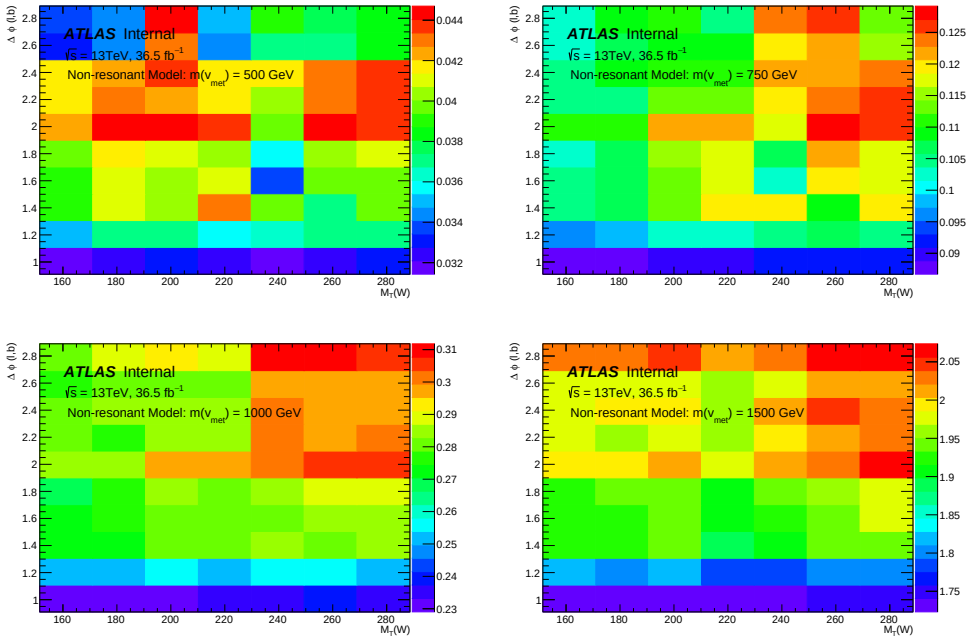

Figure 6.4: Expected excluded signal strength as a function of $|\Delta\phi(l,b)|$ and $m_{\mathrm{T}}(l, E_{\mathrm{T}}^{\mathrm{miss}})$ for non-resonant signal models with $m_V = 500$, 750, 1000 and 1500 GeV, respectively

6.1.3 Background esitimation

We can see from Table 6.2 and 6.3 that the main backgrounds in the signal region are the $t\bar{t}$ and W+jets. In order to check if the kinematic variables in these samples are well modeled, control regions that are othoganal to the signal region and enriched in the background events are defined for these two processes, respectively. These two regions are referred to as the TCR and the WCR. The TCR is required to have 2 b-jets since there is a pair of top quarks. The $m_{\mathrm{T}}(l, E_{\mathrm{T}}^{\mathrm{miss}})$ range is from 60 to 100 GeV, and the $|\Delta\phi(l,b)|$ cut is removed for both control regions. In addition, to correctly account for the normalization of the multijet background in the muon channel, which is estimated using a data-driven method, another control region (MCR) is defined. In the MCR, all

Selections	SR	TCR	WCR	TVR	WVR	MCR
N(tight leptons)	1	1	1	1	1	1
$p_T(\ell)$ [GeV]	> 30	> 30	> 30	> 30	> 30	> 30
charge sign	> 0	> 0	> 0	> 0	> 0	> 0
N (b-jets)	1	2	1	2	1	1
$p_T(b-\text{jets})$ [GeV]	> 30	> 30	> 30	> 30	> 30	> 30
E_T^{miss} [GeV]	> 50	> 50	> 50	> 50	> 50	
$m_T(l, E_T^{miss}) + E_T^{miss}$ [GeV]	> 60	> 60	> 60	> 60	> 60	
$m_T(l, E_T^{miss})$ range [GeV]	> 260	[60,100]	[60,100]	[100,180]	[100,180]	[0,60]
$\lvert\Delta\phi(l,b)\rvert$	< 1.2			< 1.8	< 1.8	

Table 6.1: Summary of the cuts applied in the control, validation and signal regions.

the preselection cuts are removed and the $m_{\mathrm{T}}(l, E_{\mathrm{T}}^{\mathrm{miss}})$ is required to range from 0 to 60 GeV.

Two validation regions, which are called WVR and TVR, are also defined to validate the normalization of W+jets and $t\bar{t}$ and to monitor the extrapolation of the W+jets and $t\bar{t}$ backgrounds to the signal region. Figure 6.5 illustrates, and Table 6.1 summarises the definition of all the signal, control and validation regions.

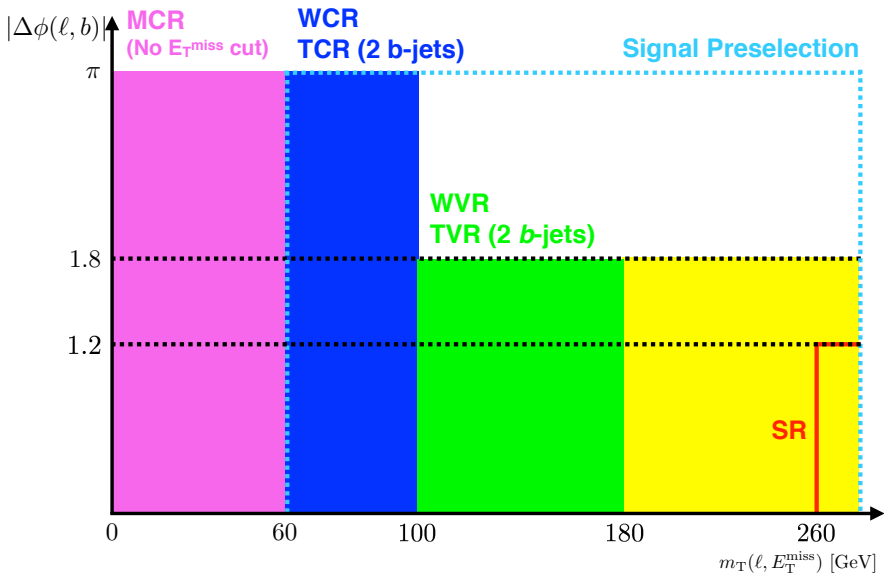

Figure 6.5: Illustation of the control, signal and validation regions in the phase space of $|\Delta\phi(l,b)|$ and $m_{\mathrm{T}}(l, E_{\mathrm{T}}^{\mathrm{miss}})$

Tables 6.2 and 6.3 show the event yields of MC bagrounds and the data samples for all the control and validation regions, in the electron and muon channel respectively. Only the event yields of MC samples is shown in the signal region due to the data

	WCR	TCR	WVR	TVR	SR
NR (v_{met}) = 200 GeV	1644 ± 77	59 ± 23	5703 ± 143	94 ± 30	3194 ± 109
NR (v_{met}) = 500 GeV	111 ± 6	2 ± 1	445 ± 12	10 ± 2	602 ± 15
NR (v_{met}) = 1000 GeV	6 ± 0	0 ± 0	29 ± 1	1 ± 0	64 ± 1
NR (v_{met}) = 1500 GeV	1 ± 0	0 ± 0	4 ± 0	0 ± 0	11 ± 0
SgTop	5797 ± 51	1441 ± 27	1683 ± 30	405 ± 15	35 ± 4
$t\bar{t}$	4218 ± 40	6111 ± 48	4242 ± 40	5318 ± 45	224 ± 10
W+jets	41074 ± 1714	1091 ± 67	7088 ± 705	235 ± 39	15 ± 34
Z+jets, Diboson	1087 ± 182	91 ± 10	169 ± 74	26 ± 4	5 ± 2
Multijet	1147 ± 38	0 ± 8	181 ± 18	0 ± 7	0 ± 2
Total backgrounds	53322 ± 1725	8734 ± 88	13364 ± 711	5985 ± 62	279 ± 35
Data	57273	8440	12825	5595	270

Table 6.2: Event yields for the control, validation and signal regions in the electron channel. The uncertainty accounts for the statistical uncertainty of the MC simulation events.

blinding policy described in Section 6.3.The event yields of the non-resonant signal models with $m(v_{\text{met}})$ = 200, 500, 1000 and 1500 GeV are shown in the tables. The uncertainty in the tables only includes the statistical uncertainty of the MC simulation events.

	WCR	TCR	WVR	TVR	SR
NR (v_{met}) = 200 GeV	2050 ± 88	53 ± 13	6230 ± 151	86 ± 16	2567 ± 91
NR (v_{met}) = 500 GeV	129 ± 7	4 ± 1	479 ± 13	8 ± 2	460 ± 13
NR (v_{met}) = 1000 GeV	7 ± 0	0 ± 0	30 ± 1	1 ± 0	46 ± 1
NR (v_{met}) = 1500 GeV	1 ± 0	0 ± 0	4 ± 0	0 ± 0	8 ± 0
SgTop	6254 ± 55	1461 ± 27	1778 ± 31	417 ± 15	30 ± 3
$t\bar{t}$	4129 ± 38	6071 ± 48	4260 ± 39	5295 ± 45	163 ± 7
W+jets	50097 ± 2109	776 ± 188	8577 ± 878	202 ± 24	19 ± 6
Z+jets, Diboson	3108 ± 211	155 ± 12	692 ± 94	41 ± 9	2 ± 2
Multijet	6026 ± 2319	664 ± 257	1462 ± 564	494 ± 192	10 ± 5
Total backgrounds	69613 ± 3142	9127 ± 323	16769 ± 1049	6448 ± 199	225 ± 12
Data	70014	9222	16017	6039	240

Table 6.3: Event yields for the control, validation and signal regions in the muon channel. The uncertainty accounts for the statistical uncertainty of the MC simulation events.

Figures 6.6, 6.7, 6.8 and 6.9 show the distributions of some kinematic variables in the control regions, for the electron and muon channels separately. Figures 6.10, 6.11, 6.12 and 6.13 show the same distributions in the validation regions. The uncertainty band includes the statistical uncertainty of the MC simulation events and also a 50% normalisation uncertainty for the multijet background. The top quark p_{T} mis-modeling in $t\bar{t}$ events has some impact on these distributions and will be accounted for as a systematic source of uncertainty, as will be described in Section 6.4.2.

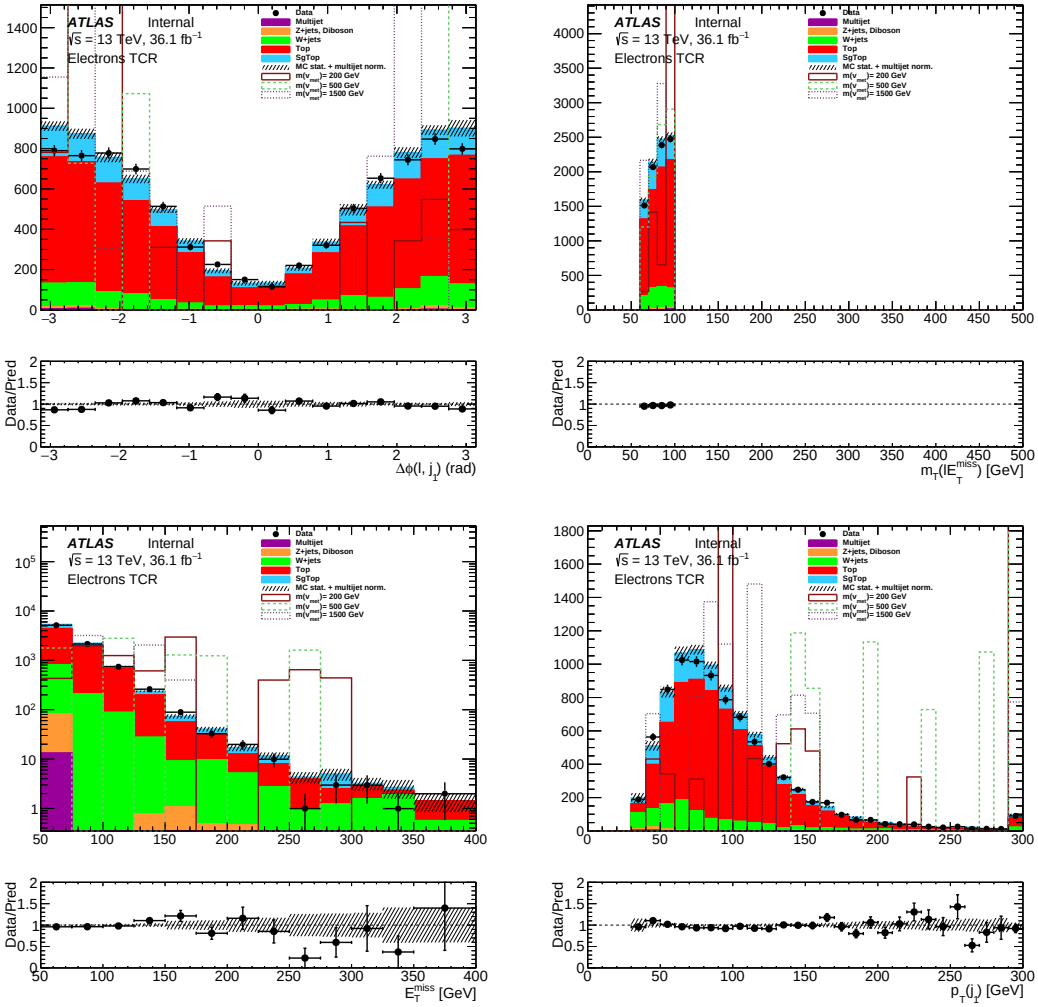

Figure 6.6: Distributions of $\Delta\phi$ between the lepton and the jet with largest p_{T} ($\Delta\phi(l, j_1)$), transverse mass of the lepton and the $E_{\mathrm{T}}^{\mathrm{miss}}$ ($m_{\mathrm{T}}(l, E_{\mathrm{T}}^{\mathrm{miss}})$), the $E_{\mathrm{T}}^{\mathrm{miss}}$ and the p_{T} of the jet with largest p_{T} in the TCR for the electron channel. Three non-resonant signal models with $m(v_{\mathrm{met}}) = 200$, 500 and 1500 GeV are also shown. The uncertainty band includes the statistical uncertainty of the MC simulation events and also a 50% normalisation uncertainty for the multijet background.

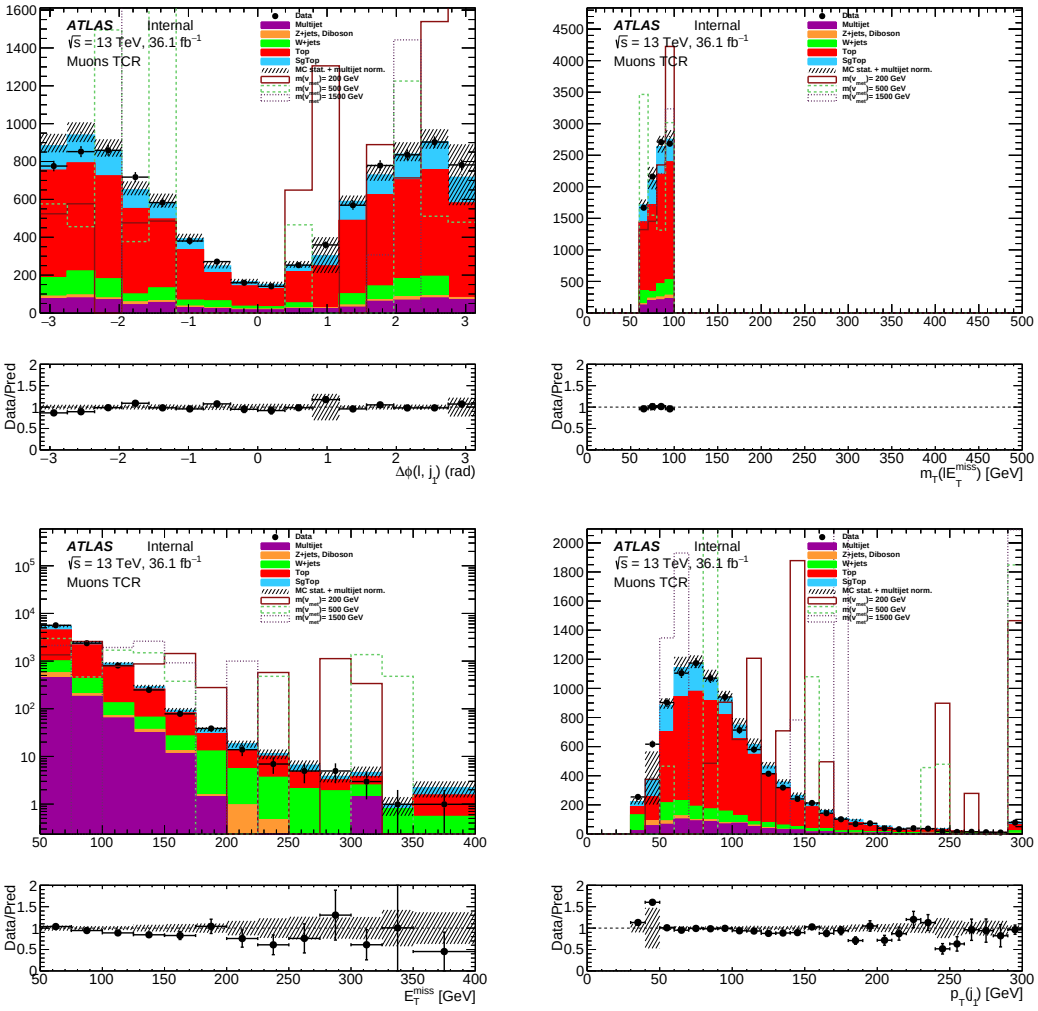

Figure 6.7: Distributions of $\Delta\phi$ between the lepton and the jet with largest p_{T} ($\Delta\phi(l, j_1)$), transverse mass of the lepton and the $E_{\mathrm{T}}^{\mathrm{miss}}$ ($m_{\mathrm{T}}(l, E_{\mathrm{T}}^{\mathrm{miss}})$), the $E_{\mathrm{T}}^{\mathrm{miss}}$ and the p_{T} of the jet with largest p_{T} in the TCR for the muon channel. Three non-resonant signal models with $m(v_{\mathrm{met}}) = 200$, 500 and 1500 GeV are also shown. The uncertainty band includes the statistical uncertainty of the MC simulation events and also a 50% normalisation uncertainty for the multijet background.

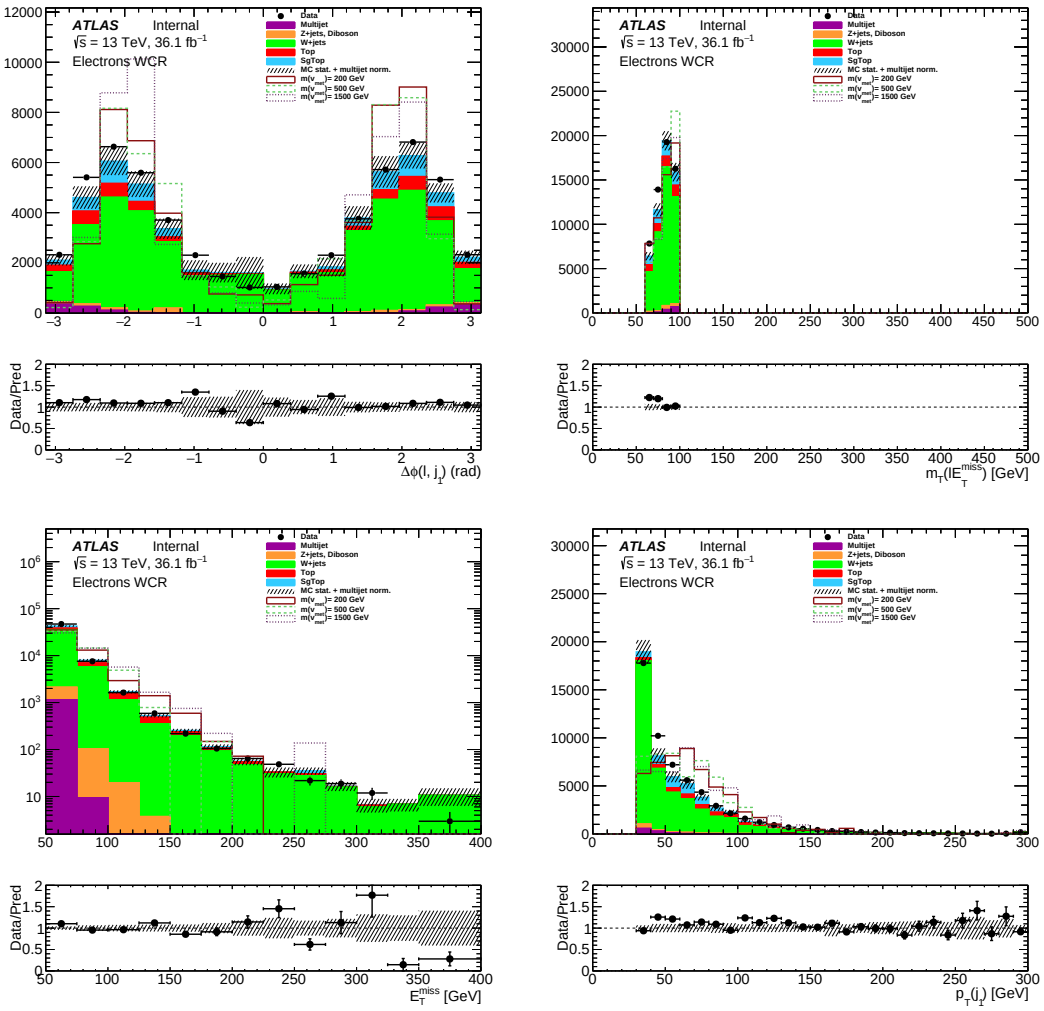

Figure 6.8: Distributions of $\Delta\phi$ between the lepton and the jet with largest p_{T} ($\Delta\phi(l, j_1)$), transverse mass of the lepton and the $E_{\mathrm{T}}^{\mathrm{miss}}$ ($m_{\mathrm{T}}(l, E_{\mathrm{T}}^{\mathrm{miss}})$), the $E_{\mathrm{T}}^{\mathrm{miss}}$ and the p_{T} of the jet with largest p_{T} in the WCR for the electron channel. Three non-resonant signal models with $m(v_{\mathrm{met}}) = 200$, 500 and 1500 GeV are also shown. The uncertainty band includes the statistical uncertainty of the MC simulation events and also a 50% normalisation uncertainty for the multijet background.

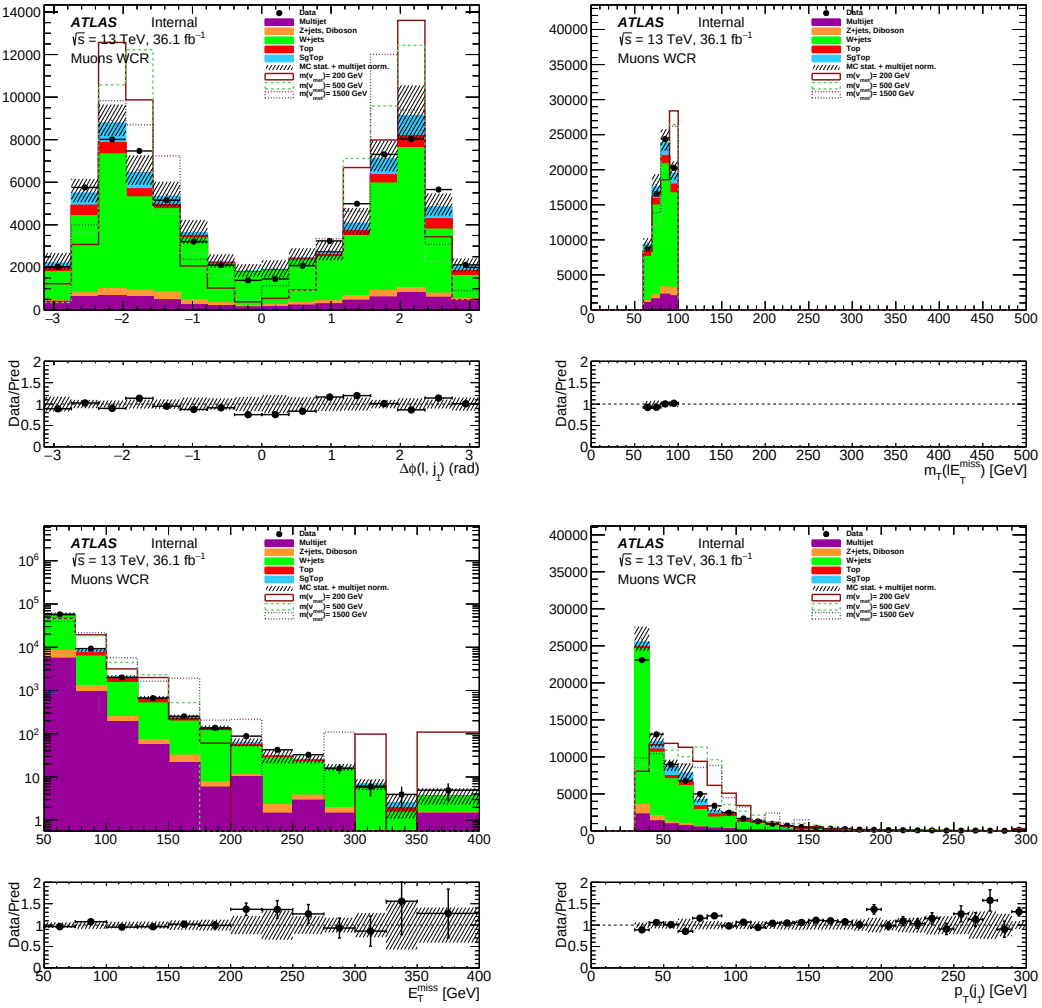

Figure 6.9: Distributions of $\Delta\phi$ between the lepton and the jet with largest p_{T} ($\Delta\phi(l, j_1)$), transverse mass of the lepton and the $E_{\mathrm{T}}^{\mathrm{miss}}$ ($m_{\mathrm{T}}(l, E_{\mathrm{T}}^{\mathrm{miss}})$), the $E_{\mathrm{T}}^{\mathrm{miss}}$ and the p_{T} of the jet with largest p_{T} in the WCR for the muon channel. Three non-resonant signal models with $m(v_{\mathrm{met}}) = 200$, 500 and 1500 GeV are also shown. The uncertainty band includes the statistical uncertainty of the MC simulation events and also a 50% normalisation uncertainty for the multijet background.

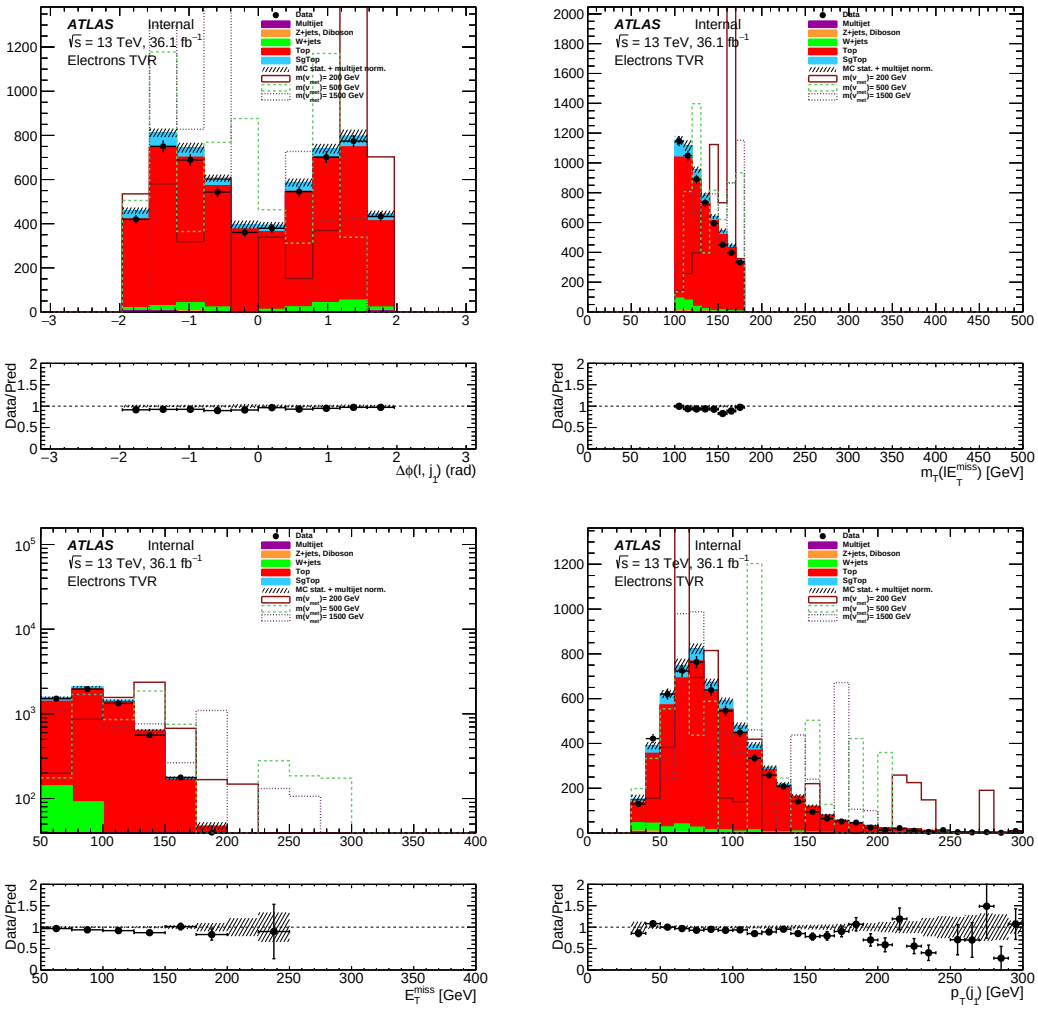

Figure 6.10: Distributions of $\Delta\phi$ between the lepton and the jet with largest p_{T} ($\Delta\phi(l, j_1)$), transverse mass of the lepton and the $E_{\mathrm{T}}^{\mathrm{miss}}$ ($m_{\mathrm{T}}(l, E_{\mathrm{T}}^{\mathrm{miss}})$), the $E_{\mathrm{T}}^{\mathrm{miss}}$ and the p_{T} of the jet with largest p_{T} in the TVR for the electron channel. Three non-resonant signal models with $m(v_{\mathrm{met}}) = 200$, 500 and 1500 GeV are also shown, normalised to the total expected background yields. The scale factors are not applied. The uncertainty band includes the statistical uncertainty of the MC simulation events and also a 50% normalisation uncertainty for the multijet background.

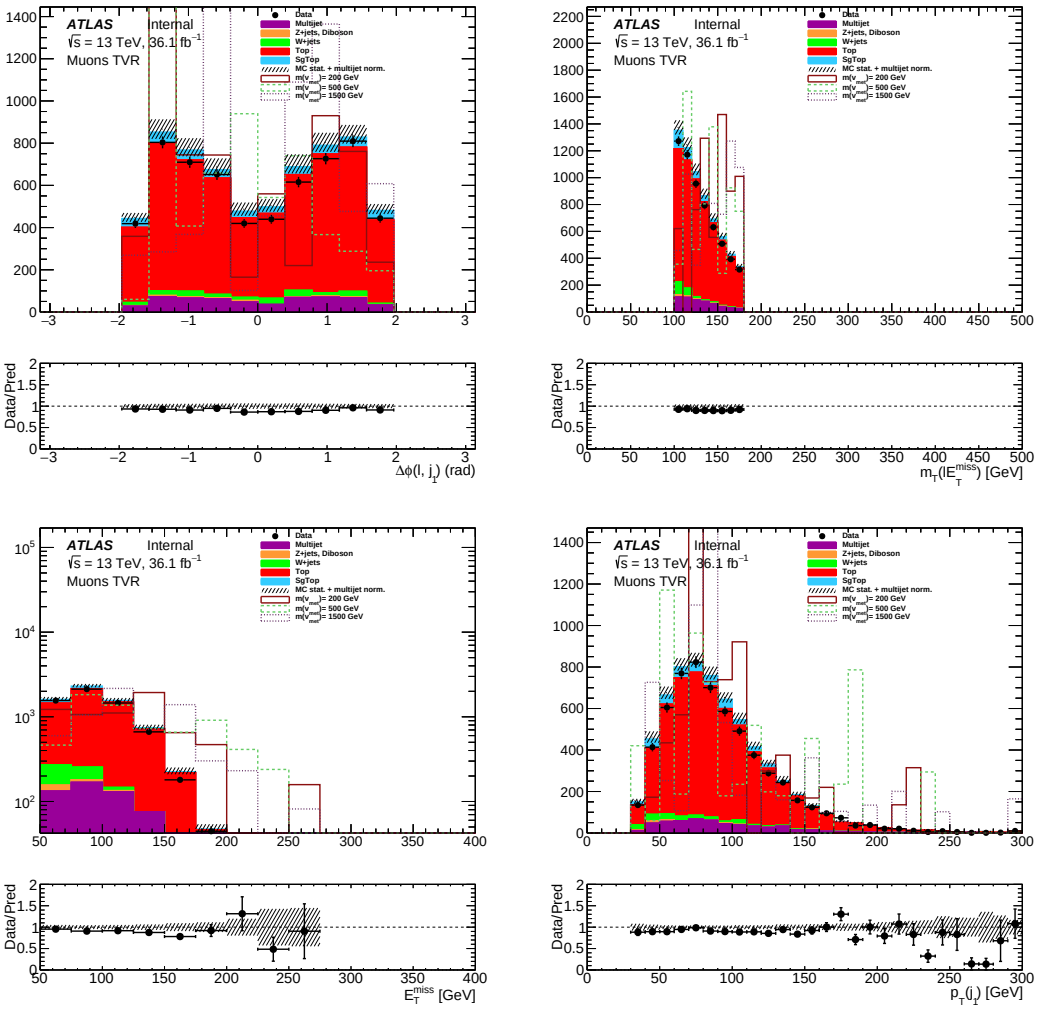

Figure 6.11: Pre-fit distributions of $\Delta\phi$ between the lepton and the jet with largest p_{T} ($\Delta\phi(l, j_1)$), transverse mass of the lepton and the $E_{\mathrm{T}}^{\mathrm{miss}}$ ($m_{\mathrm{T}}(l, E_{\mathrm{T}}^{\mathrm{miss}})$), the $E_{\mathrm{T}}^{\mathrm{miss}}$ and the p_{T} of the jet with largest p_{T} in the TVR for the muon channel. Three non-resonant signal models with $m(v_{\mathrm{met}}) = 200$, 500 and 1500 GeV are also shown, normalised to the total expected background yields. The scale factors are not applied. The uncertainty bands cover the simulation statistics contribution and a 50% normalisation uncertainty for the data-driven multijet background.

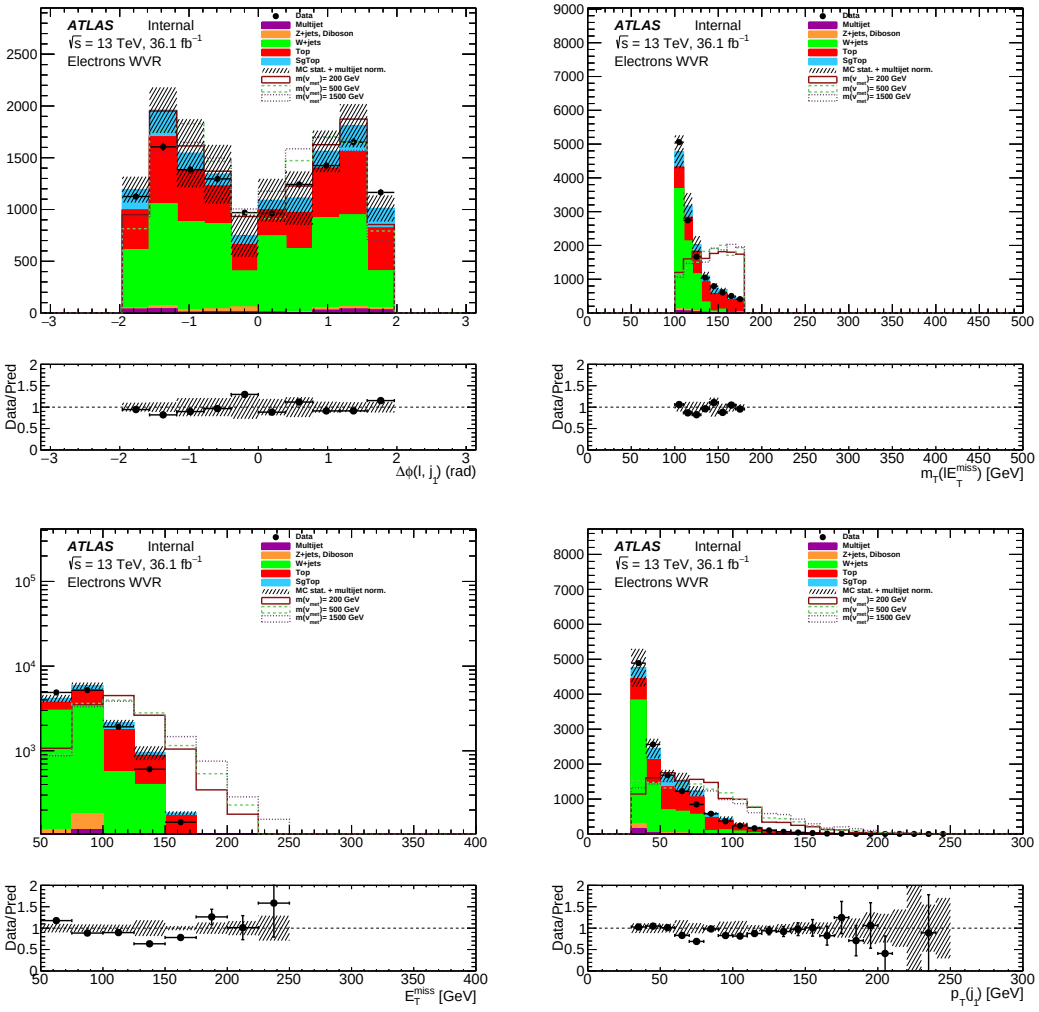

Figure 6.12: Distributions of $\Delta\phi$ between the lepton and the jet with largest p_{T} ($\Delta\phi(l, j_1)$), transverse mass of the lepton and the $E_{\mathrm{T}}^{\mathrm{miss}}$ ($m_{\mathrm{T}}(l, E_{\mathrm{T}}^{\mathrm{miss}})$), the $E_{\mathrm{T}}^{\mathrm{miss}}$ and the p_{T} of the jet with largest p_{T} in the WVR for the electron channel. Three non-resonant signal models with $m(v_{\mathrm{met}}) = 200$, 500 and 1500 GeV are also shown, normalised to the total expected background yields. The scale factors are not applied. The uncertainty bands cover the simulation statistics contribution and a 50% normalisation uncertainty for the data-driven multijet background.

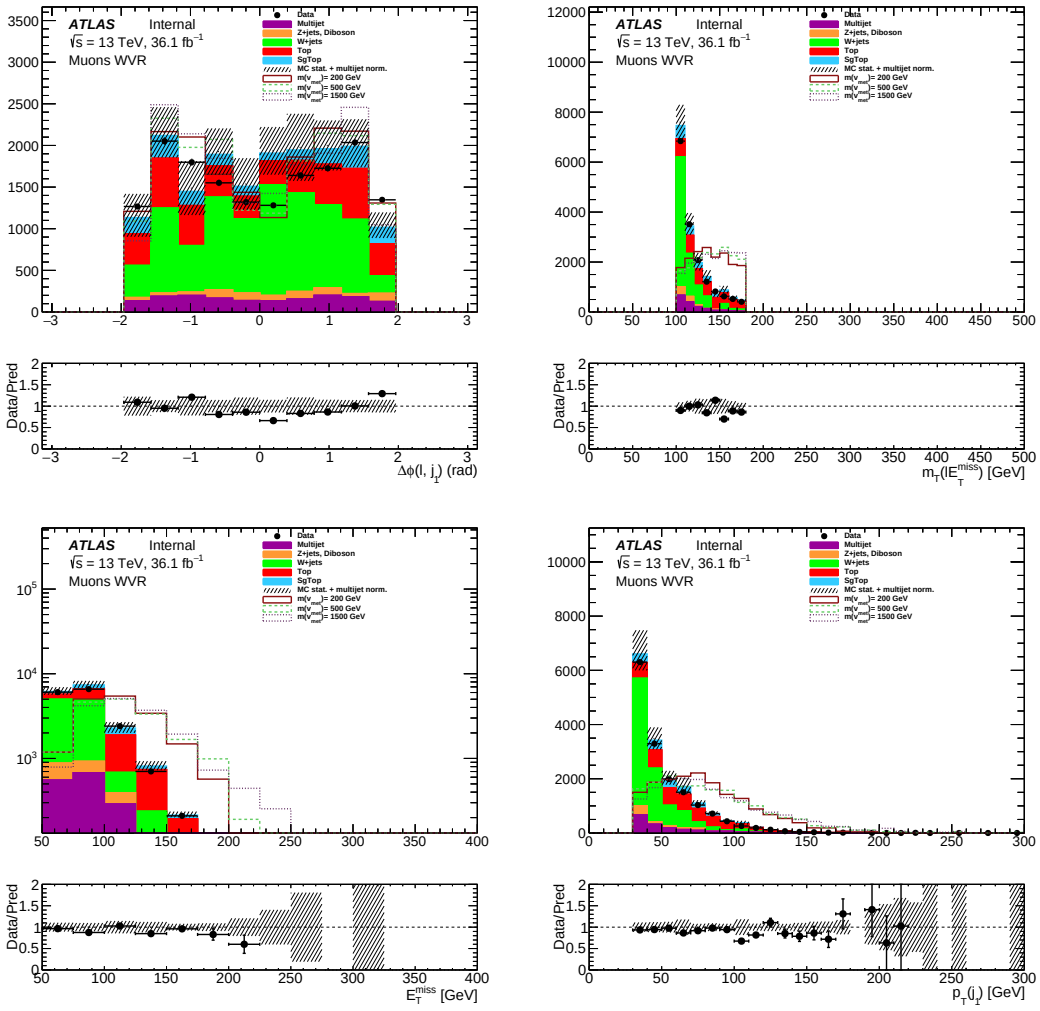

Figure 6.13: Distributions of $\Delta\phi$ between the lepton and the jet with largest p_{T} ($\Delta\phi(l, j_1)$), transverse mass of the lepton and the $E_{\mathrm{T}}^{\mathrm{miss}}$ ($m_{\mathrm{T}}(l, E_{\mathrm{T}}^{\mathrm{miss}})$), the $E_{\mathrm{T}}^{\mathrm{miss}}$ and the p_{T} of the jet with largest p_{T} in the WVR for the muon channel. Three non-resonant signal models with $m(v_{\mathrm{met}}) = 200$, 500 and 1500 GeV are also shown, normalised to the total expected background yields. The scale factors are not applied. The uncertainty bands cover the simulation statistics contribution and a 50% normalisation uncertainty for the data-driven multijet background.

6.1.4 A background-only fit to normalize the backgrounds

We can see from Figures 6.8 and 6.9 that there is a notable discrepancy between the total number of the MC background and data events. For simplification, overall scale factors are calculated for the W+jets and $t\bar{t}$ events by performing a maximum likelihood fit of the MC backgrounds to the data in the two control regions simultaneously, since the signal is negligible in these regions. The background rates are constrained using gaussian priors in the fitting procedure. In addition, a normalization constraint corresponding to the theoretical uncertainty of the production cross-section, is applied in the fit, which is +5.58, -6.11% for the $t\bar{t}$ precess and ±5% for the W+jets. The fit is done independently in the electron and muon channels, and the obtained scale factors are achieved for these two channels. Since these scale factors are not far from 1, they are only applied in the control and validation regions in order to have better agreement of data and MC event yields, but not in the final fit in the signal region.

6.2 Fully Hardronic channel

6.2.1 Pre-Selection

Similar to the pre-selection done in the leptonic channel in Section 6.1.1, a pre-selection is applied in the hadronic channel in order to reduce the amount of events to be processed and increase the speed of the next steps of the analysis chain. The EXOT7 derivation, which is used to produce the data and MC samples in the hadronic channel, requires that the events have one anti-$k_t(R = 1.0)$ jet with $p_{\mathrm{T}} > 200$ GeV and $|\eta| < 2.0$ or at least two anti-$k_t(R = 0.4)$ jets with $p_{\mathrm{T}} > 25$ GeV and $|\eta| < 4.5$. Furthermore, the $E_{\mathrm{T}}^{\mathrm{miss}}$ is required to be above 200 GeV to reduce the multijet contribution, which is hard to model. In addition, a veto on tight, isolated electrons and muons is applied in order to make this channel orthoganal to the leptonic channel. The decay products from the top quark will experience a large Lorentz boost and therefore can be clustered as large radius jet. Consequently, at least one large-R jet with $p_{\mathrm{T}} > 250$ GeV and $|\eta| < 2.0$ is required in each event. Figure 6.14 shows event properties after the pre-selection. Figure 6.15 shows the central jet multiplicity with $|\eta| < 2.5$.

6.2.2 Signal region definition

These selections are applied after the pre-selection:

a) The events are required to contain exactly one top-tagged large-R jet J with 80 % efficiency and $p_{\mathrm{T}} > 250$ GeV.

b) The events are required to contain exactly one b-tagged track jet with 70 % efficiency.

c) The distance between the top-tagged large-R jet and the missing transverse momentum has to fulfill $\Delta\phi(E_{\mathrm{T}}^{\mathrm{miss}}, J) >= \pi/2$.

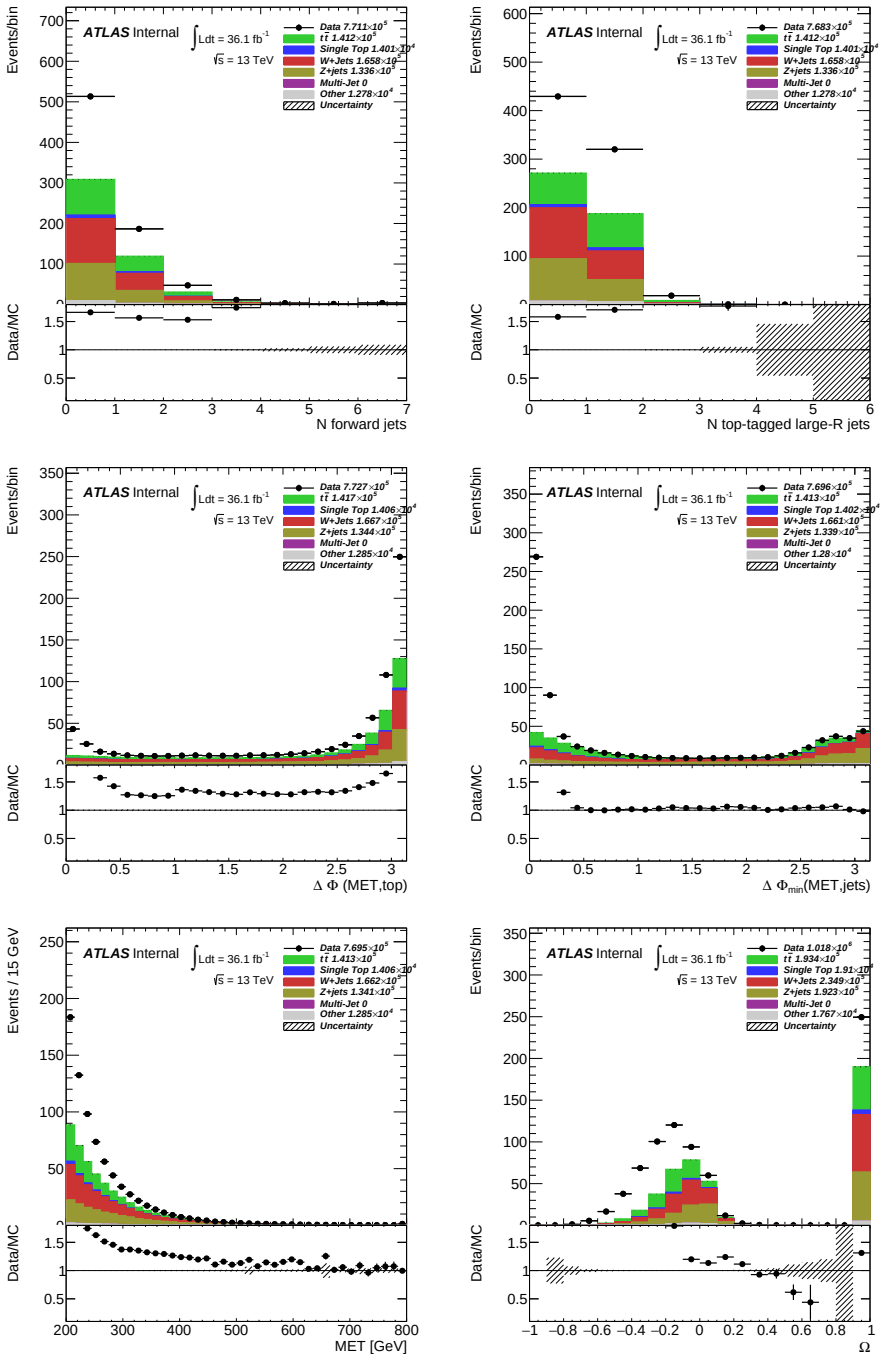

Figure 6.14: Distributions of some variables after the pre-selection. The uncertainty band includes only the statistical uncertainty of the MC simulation events. The disagreement between data and background event yields is mainly caused by the multijet background, which requires a data-driven estimation and is therefore not included at this level.

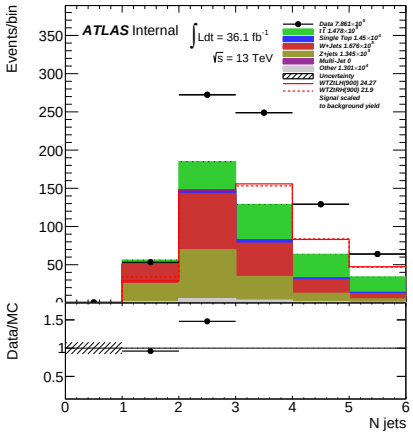

Figure 6.15: Distributions of the number of central jets after the pre-selection. The uncertainty band includes only the statistical uncertainty of the MC simulation events. The disagreement between data and background event yields is mainly caused by the multi-jet background, which requires a data-driven estimation and is therefore not included at this level.

d) The asymmetry between and the p_{T} of the top-tagged large-R jet defined as $\Omega = \frac{E_{\mathrm{T}}^{\mathrm{miss}} - p_{\mathrm{T}}(J)}{E_{\mathrm{T}}^{\mathrm{miss}} + p_{\mathrm{T}}(J)}$ is > -0.3.

e) The minimal distance between the $E_{\mathrm{T}}^{\mathrm{miss}}$ and any jet in the transverse plane is $\Delta\phi_{\mathrm{min}} > 1.0$.

f) The events are required to contain (VLT model only) at least one forward jet with $p_{\mathrm{T}} > 25$ GeV and $2.5 < |\eta| < 4.5$.

Several optimizations are done on these selections in order to get the best expected limit on the signal production cross section. The vector-like top quark signals are used for these optimizations, assuming either an exclusive left- or right-handed coupling to the SM particles at an generated vector-like quark mass of 900 GeV . The expected exclusion limit is calculated by performing a binned maximum likelihood fit, including only the statistical uncertainty, which is described in detail in Chapter 7 to the reconstructed transverse mass of the selected large-R jet J and the $E_{\mathrm{T}}^{\mathrm{miss}}$, which is defined as:

$$m_{\mathrm{T}}(J, E_{\mathrm{T}}^{\mathrm{miss}}) = \sqrt{m(J)^2 + 2 \cdot \left(E_{\mathrm{T}}(J) - p_{\mathrm{T}}(J) \cdot \cos\left(\phi(J) - \phi(J, E_{\mathrm{T}}^{\mathrm{miss}})\right)\right)} \qquad (6.1)$$

Optimization using jet flavor tagging

The events are required to have exactly one large-R top-tagged jet with $p_{\mathrm{T}} > 250$ GeV. The pre-recommended 80 % working point of the top-tagging is used, which is based on a smooth cut on both the mass of the calorimeter based large-R jet and the n-subjettiness ratio τ_{32}^{wta} parameter. The 80 % working point corresponds to a very tight

selection, therefore a lower one, 50 % is tested but does not give a better exclusion limit. Another recommended smooth top-tagging using the mass of the large-R jet, the splitting-scale $\sqrt{d_{12}}$ and the n-subjettiness ratio τ_{32}^{wta} as inputs is also tested but again results give a worse exclusion limit. In addition, requiring a matched b-tagged track jet within the large-R jet radius of $\Delta R < 1.0$ dose not increase the performance, either. The results of these tests on the expected exclusion limits, which are expressed in signal strength, are shown in Table 6.4

	WTZt900LH	WTZt900RH	Res. DM (3TeV)
Pre-rec. top-tagged(loose)	26,687	27,763	0.532
Pre-rec. top-tagged(loose) : top-b-matched	27,426	29,671	0.576
Pre-rec. top-tagged(tight)	30,364	30,441	0.980

Table 6.4: Expected limits on signal strength for different top-taggers and top-tagged jet to b-tagged track jet matching.

Figure 6.16 shows the distribution of the number of top-tagged large-R jets after the pre-selection for the MC signal and backgrounds samples. We can see that most signal events have only one top-tagged large-R jet while most background events have zero or one top-tagged large-R jet.

To further identify the events containing a top quark, only events with exactly one b-tagged track jet are selected. No alignment requirement between the top-tagged large-R jet and b-tagged track jet is required based on the test results shown in Table 6.4. The distribution of the number of b-tagged track jets for signal and background after the pre-selection and the cut on the top-tag multiplicity, is shown in Figure 6.17. We can see that most signal events have one b-tagged track jet as opposed to background events that mostly do not contain one.

Optimization based on spherical deviations

The VLT is produced at rest due to its large mass. As a result, its decay products are likely to be back to back in the transverse direction. In addition, we know that most of the contribution to the missing transverse energy comes from the two neutrinos from the Z boson decay. Therefore a requirement of $\Delta\Phi(E_T^{miss}, J) > \pi/2$ between and the $E_{\mathrm{T}}^{\mathrm{miss}}$ and the top-tagged large-R jet is imposed. Figure 6.18 displays the distribution of $\Delta\phi(E_{\mathrm{T}}^{\mathrm{miss}}, J)$ for the MC signal and background samples before applying this cut. We can see that the signal distribution does indeed have its peak at $\Delta\phi(E_{\mathrm{T}}^{\mathrm{miss}}, J) \approx \pi$ as expected while the background also has a noteworthy contribution in the opposite direction.

Optimization based on transverse energy asymmetry

The distribution of the asymmetry between and the $p_{\mathrm{T}}(J)$ of the top-tagged large-R jet for signal and SM background after the pre-selection and cuts a) - c) is shown in Figure

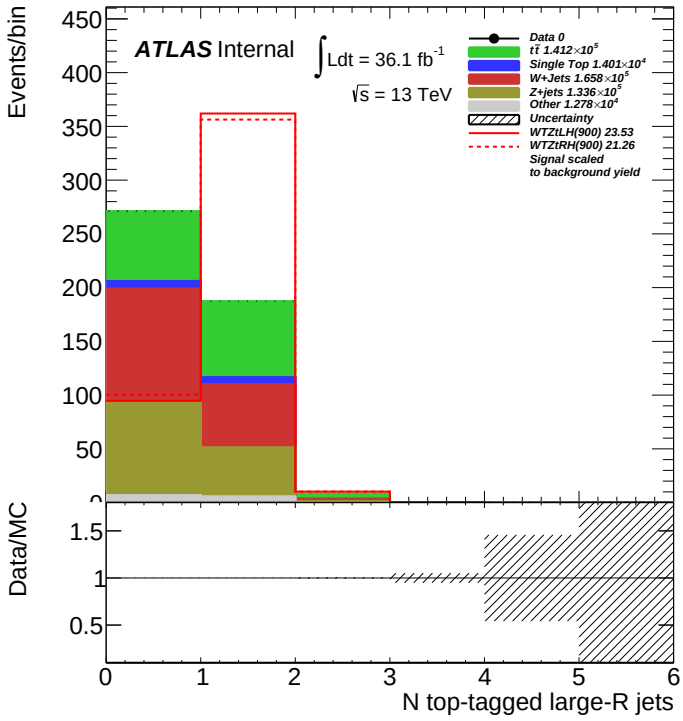

Figure 6.16: Multiplicity of top-tagged large-R jets for signal and SM background after the pre-selection.

6.19. This cut is used to suppress background events due to the mis-reconstructed $E_{\mathrm{T}}^{\mathrm{miss}}$, which comes mostly from the multijet events. Events with mis-reconstructed $E_{\mathrm{T}}^{\mathrm{miss}}$ tend to be asymmetric with respect to $E_{\mathrm{T}}^{\mathrm{miss}}$ and $p_{\mathrm{T}}(J)$, i.e. having values of the asymmetry Ω smaller than zero. This is because the mis-reconstruction is caused by fluctuations in the $p_{\mathrm{T}}(J)$ which are likely to be smaller than the $p_{\mathrm{T}}(J)$ itself. The cut at > -0.3 is obtained by varying the selection point from -0.5 to 0.0 and record the value that gives the best expected exclusion limit.

Optimization based on $E_{\mathrm{T}}^{\mathrm{miss}}$ mis-reconstruction

Another way to reduce the multijet background is to apply a cut on the minimum $\Delta\phi$ between $E_{\mathrm{T}}^{\mathrm{miss}}$ and any anti-$k_t(R = 0.4)$ calorimeter jet with $|\eta| < 2.5$ due to the fact that events from this background tend to have a small azimuthal difference between jets and $E_{\mathrm{T}}^{\mathrm{miss}}$. The distribution of $\Delta\phi_{\mathrm{min}}(E_{\mathrm{T}}^{\mathrm{miss}}, j)$ for the MC signal and background samples after the pre-selection and cuts a) to d) is shown in Figure 6.20. As before, the cut value is determined by choosing the value that gives the best expected exclusion limit, which is 1.0.

This cut is also found to reduce the mis-modeling of $E_{\mathrm{T}}^{\mathrm{miss}}$ due to the dead tile-calorimeter modules. In addition to the reduction of multi-jet contribution in the

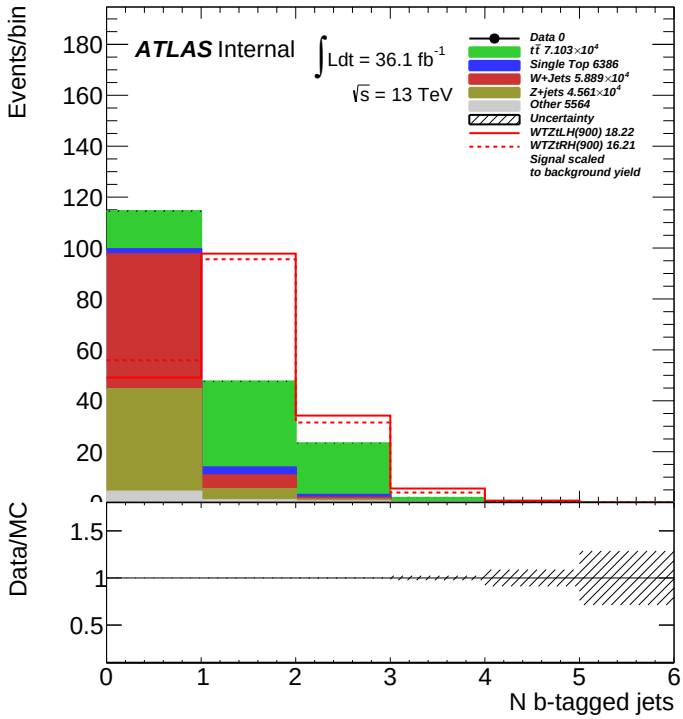

Figure 6.17: The distribution of the number of b-tagged track jets for signal and SM background after applying the pre-selection and cut a).

signal region this cut was found to also reduce the $E_{\mathrm{T}}^{\mathrm{miss}}$ miss-modeling due to dead tile-calorimeter modules.

Optimization based on number of forward jets (for the VLT production)

For the scenario of the VLT production, the events are require to have at least one forward jet, in addition to the pre-selection and selections a) to e). The distribution of the number of forward jets is shown in Figure 6.21. As expected for the signal most events contain one or more forward jets while the majority of background events contains zero.

The cutflow is displayed in Table 6.5 showing the event yield for signal and total background without the multijet contribution after the pre-selection and all the cuts mentioned above.

6.2.3 Background estimation

As we can see from Tables 6.9 and 6.10, the background in the signal region is dominated by $t\bar{t}$. Processes with a smaller contribution are the W+jets and Z+jets. In order to check if the kinematic variables in these samples are well modeled, control regions that

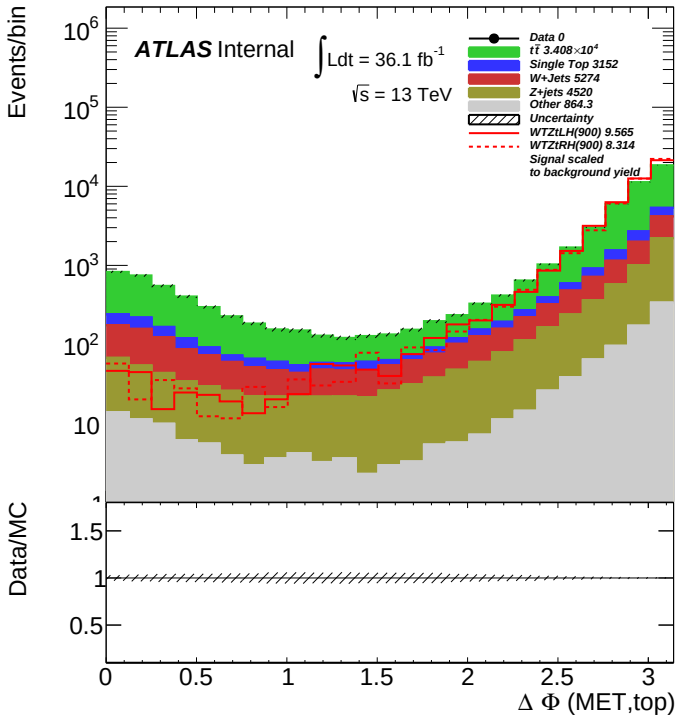

Figure 6.18: Distribution of $\Delta\phi((E_{\mathrm{T}}^{\mathrm{miss}}, J)$ for signal and SM background after applying the pre-selection and cuts a) and b).

are orthogonal to the signal region and enriched in the background events are defined for these processes. The other backgrounds have negligible contribution in the signal region including single-top, $t\bar{t}$, diboson and multijet events. However, the multijet process does play an important role in the $t\bar{t}$ control region and therefore is estimated using a data-driven method, as described below. A validation region for the multijet events is also defined in order to check the estimation of the multijet events. The definition of the $t\bar{t}$ control region is defined in the following section, and the V+jets control regions are presented afterwards, followed by the estimation of the multijet background.

$t\bar{t}$ Control Region

The $t\bar{t}$ control region is required to have two b-tagged track jets instead of one since there is a pair of top quarks. In addition, the cut on $\Delta\phi(E_{\mathrm{T}}^{\mathrm{miss}}, J)$ is flipped to reduce the contribution from the signal events. Furthermore, events with minimal $\Delta\phi$ less than 0.2 are excluded to reduce the contamination coming from the multijet events. Since this cut in the signal region is also used to suppress the effects of the dead modules of the ATLAS tile calorimeter, an additional way to handle the additional background from the defective tiles is needed.

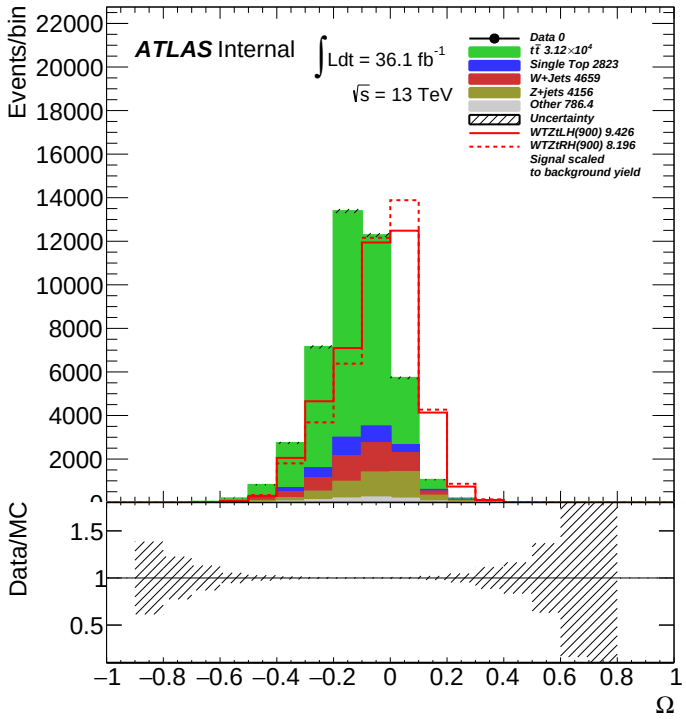

Figure 6.19: Distribution of the asymmetry between and the p_{T} of the top-tagged large-R jet for signal and SM background after applying the pre-selection and cuts a) - c).

Therefore, a veto on events containing calorimeter jets located closely in ΔR to the masked modules in the regions of $(\phi, \eta) = (-12 \cdot \frac{2\pi}{64}, 0.5)$ and $(\phi, \eta) = (5 \cdot \frac{2\pi}{64}, -0.5)$ is applied. The veto-regions have been defined with respect to the agreement between healthy (not affected) $E_{\mathrm{T}}^{\mathrm{miss}}$ properties and the affected $E_{\mathrm{T}}^{\mathrm{miss}}$ after applying different definitions, respectively.

The distributions of the transverse mass M_{T} and other variables are shown in Figures 6.25 and 6.31. We can see a good agreement between the number of events from the MC backgrounds and data.

An additional study concerning the composition of the $t\bar{t}$ background is done to verify the similarity of the $t\bar{t}$ process in the signal and $t\bar{t}$ control region. The compositions in both regions are compared to the truth information from the Monte Carlo samples and the results are shown in Table 6.6. We can see that the largest composition part of the $t\bar{t}$ events is the semi-leptonic component ($\sim$94%) and there is no sigficance difference between these compositions in the signal region and the $t\bar{t}$ control region.

V+jets Control Region

The V+jets control regions are obtained using the same selections as these on the signal region except that an additional veto on the b-tagged track jets is applied. The fractions

	WTZtLH ($\frac{S}{\sqrt{B}}$)	WTZtRH ($\frac{S}{\sqrt{B}}$)	total background
pre-selection	23.67 ± 0.23 (0.034)	21.61 ± 0.14 (0.031)	474750 ± 780
n(top-tagged large-R jet J)= 1	18.34 ± 0.20 (0.042)	16.48 ± 0.12 (0.038)	190690 ± 470
n(b-tagged track jet)= 1	9.65 ± 0.14 (0.044)	8.415 ± 0.086 (0.039)	47800 ± 190
$\Delta\Phi(MET, J) > \pi/2$	9.56 ± 0.14 (0.046)	8.344 ± 0.086 (0.040)	43859 ± 190
$\Omega > -0.3$	9.05 ± 0.14 (0.045)	7.917 ± 0.083 (0.040)	40000 ± 180
$\Delta\Phi_{\min}(MET, j) > 1.0$	5.89 ± 0.11 (0.050)	5.602 ± 0.070 (0.044)	16420 ± 120
n(forward jet)> 0	4.70 ± 0.10 (0.062)	4.082 ± 0.060 (0.054)	5751 ± 65

Table 6.5: Table displaying the event yields after the cuts a) - f) for signal and total background without the multijet contribution. The uncertainty accounts for the statistical uncertainty of the MC simulation events

	signal region				
	semi-leptonic	di-leptonic			all-hadronic
	0.941 ± 0.010	0.0581 ± 0.0026			0.0013 ± 0.0007
		e	μ	τ	
e	0.160 ± 0.004	0.0038 ± 0.0008	-	-	-
μ	0.243 ± 0.005	0.0053 ± 0.0007	0.0016 ± 0.0005	-	-
τ	0.539 ± 0.008	0.0183 ± 0.0015	0.0126 ± 0.0012	0.0165 ± 0.0014	-
	$t\bar{t}$ control region				
	semi-leptonic	di-leptonic			all-hadronic
	0.939 ± 0.014	0.0576 ± 0.0034			0.0031 ± 0.0014
		e	μ	τ	
e	0.188 ± 0.006	0.0034 ± 0.0007	-	-	-
μ	0.225 ± 0.007	0.0055 ± 0.0010	0.0019 ± 0.0005	-	-
τ	0.530 ± 0.010	0.0159 ± 0.0016	0.0116 ± 0.0014	0.0192 ± 0.0023	-

Table 6.6: Composition of the $t\bar{t}$ background decay processes in signal and control regions as fractions with respect to total amount of events.

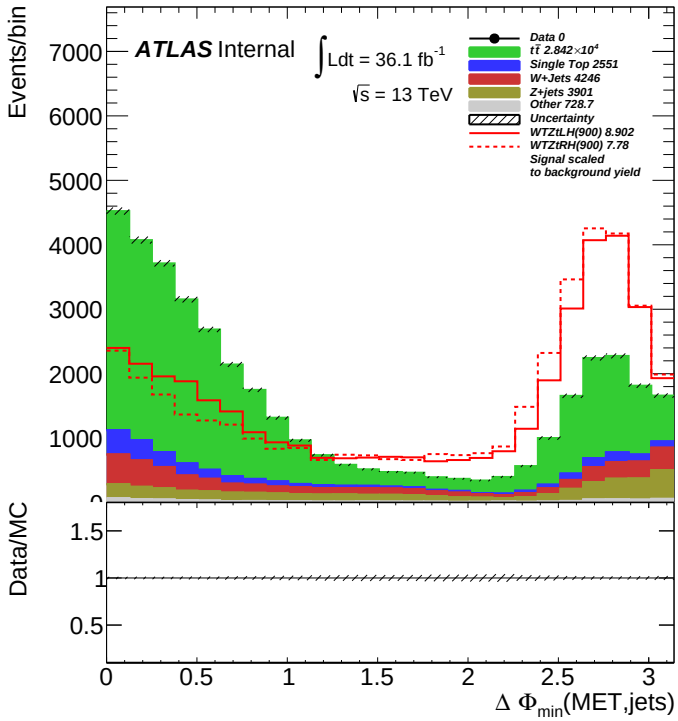

Figure 6.20: Distribution of the minimal $\Delta\phi$ between ($E_{\mathrm{T}}^{\mathrm{miss}}$ and any anti-$k_t(R = 0.4)$ calorimeter jet for signal and SM background after applying the pre-selection and cuts a) - d).

of the jet flavor composition and the decay channel are shown in Table 6.7 separately for W+jets and Z+jets. The contribution of either W+jets or Z+jets is comparable in each signal and control region. The fractions of the V-boson decay modes are comparable in the signal and control regions whereas the jet flavor composition differs because different b-jet multiplicities are used to distinguish between the region, respectively.

The distributions of the reconstructed transverse mass M_T and other observables for the signal and backgrounds are shown in Figures 6.26 and 6.32.

Estimation of Multijet Background Using a Data-Driven Approach

The multijet background plays an important role in the study of the $t\bar{t}$ control region, and its contribution is also calculated in the signal and the V+jets control region. The ABCD method (82) is used to estimate the amount and distribution of the multijet events. Designated estimation regions (**B,C,D**) are defined and used to extract information about the shape and normalization of the multijet contribution and the information is then propagated to the evaluation region (**A**). These estimation regions need to be orthogonal to the evaluation region and are obtained by applying cuts on two variables which are chosen in order to be largely uncorrelated between each other and

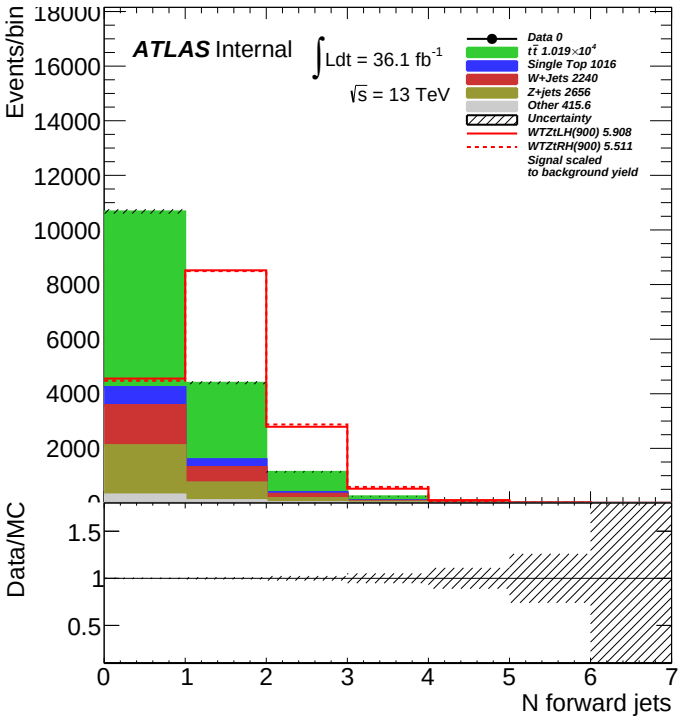

Figure 6.21: Distribution of the forward jets for signal and SM background after applying the pre-selection and cuts a) - e).

	SR(Fwd. Jet)	SR	$t\bar{t}$ CR	V+Jets CR	Multi-jet VR
W + light	20,27	22,17	0,00	68,02	4,13
W + c	40,39	42,05	5,34	28,44	11,37
W + b	39,33	35,78	94,66	3,54	84,5
$W \to e\nu_e$	22,09	20,83	22,16	19,46	19,58
$W \to \mu\nu_\mu$	24,22	24,75	18,53	25,16	22,30
$W \to \tau\nu_\tau$	53,69	54,43	59,31	55,38	58,12
Z + light	15,19	17,16	0,00	69,75	3,14
Z + c	38,66	38,17	4,42	26,31	8,91
Z + b	46,15	44,67	95,58	3,94	87,95
$Z \to ee$	0,00	0,00	0,00	0,00	0,43
$Z \to \mu\mu$	0,58	0,48	0,64	0,53	0,86
$Z \to \tau\tau$	1,88	1,75	3,25	1,85	9,30
$Z \to \nu\nu$	97,54	97,77	96,10	97,62	89,40
$\frac{W\text{+jets}}{Z\text{+jets}}$	90,54	84,35	106,06	103,76	161,88

Table 6.7: Fractions of additional jet flavor and vector-boson decay process composition in the different signal and control regions in percent points [%]. The fractions are given with respect to the total amount of event in the different signal and control regions, respectively, but separately for either W+jets or Z+jets

with respect to the $M_{\mathrm{T}}(E_{\mathrm{T}}^{\mathrm{miss}}, \mathrm{top})$. The denifition of each these regions is illustrated in Figure 6.22.

The results of this method are examined in a multijet validation region, which is required to have the asymmetry Ω between $E_{\mathrm{T}}^{\mathrm{miss}}$ and p_{T} of the top-tagged large-R jet above -0.3, a selection that is inverted compared to that in the signal region, in order to make the validation region orthogonal to the signal region. Whereas the cut on the minimal $\Delta\phi$ between $E_{\mathrm{T}}^{\mathrm{miss}}$ and any jet is kept the same as in the signal region. The distributions of some chosen variables in the regions A, B, C and D are shown in Figure 6.24 and 6.23 in the signal region with and without additional forward jets requirement. The distributions in the $t\bar{t}$, multi-jet and V+jets control regions are shown in Figures 6.25, 6.27 and 6.26.

The shape of the multijet distribution is estimated as the difference between the binned data and MC background distributions in the shape-estimation region (B). Afterwards, the normalization is estimated as the fraction of the overall event yield in estimation region C over D. The normalization is applied as an overall scale-factor to the binned multijet distribution taken from region B. The outcome of this procedure is then used as the estimated multijet distribution in evaluation region A. The estimated multi-jet distribution has the following ith bin content in evaluation region A:

$$\mathrm{Content}_i^A = (\mathrm{Data}_i^B - \mathrm{MC}_i^B) \cdot \frac{\mathrm{Integral}_{\mathrm{Data\ -\ MC}}^C}{\mathrm{Integral}_{\mathrm{Data\ -\ MC}}^D}\,. \tag{6.2}$$

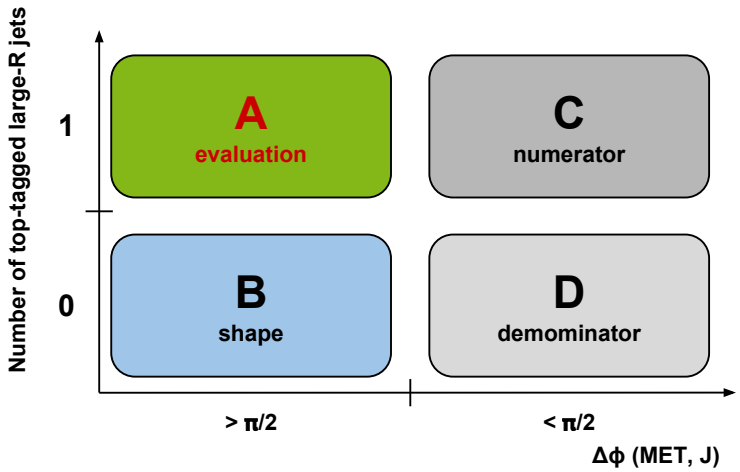

Figure 6.22: Different regions define for the data-driven multi-jet estimate using the ABCD-method.

Figure 6.27 shows that the background prediction in the evaluation region tends to be overestimated. In order to mitigate this effect random large-R jets are chosen instead of the leading large-R jet in case that no top-tagged jet is found. This approach is found to improve both the overall normalization as well as the shape of the estimated multijet distribution.

The estimated multijet contribution in the multi-jet validation region is still slightly overestimated by about 10-15%, but completely covered modeling and propagated statistical uncertainties affecting the estimated multi-jet background and a multi-jet closure uncertainty, which are described in Section 6.4.2 .

The overall estimated multijet shape, however, seems to be well modeled which can be seen in all the control regions and the multijet validation region. In addition, the multijet contribution is negligibly small in the signal region and V+jets control regions, hence the main contribution of the estimated multijet contribution which enters the binned likelihood fit comes from the $t\bar{t}$ control region.

6.2.4 Observable distributions and expected yields

The definitions of all of the different regions are summarized in Table 6.8. The expected event yields for the VLT signal and background processes are shown in Table 6.9 in the signal region with and without the additional forward jet requirement and the control regions. The expected event yields are shown for the dark matter signal and background processes in Table 6.10.

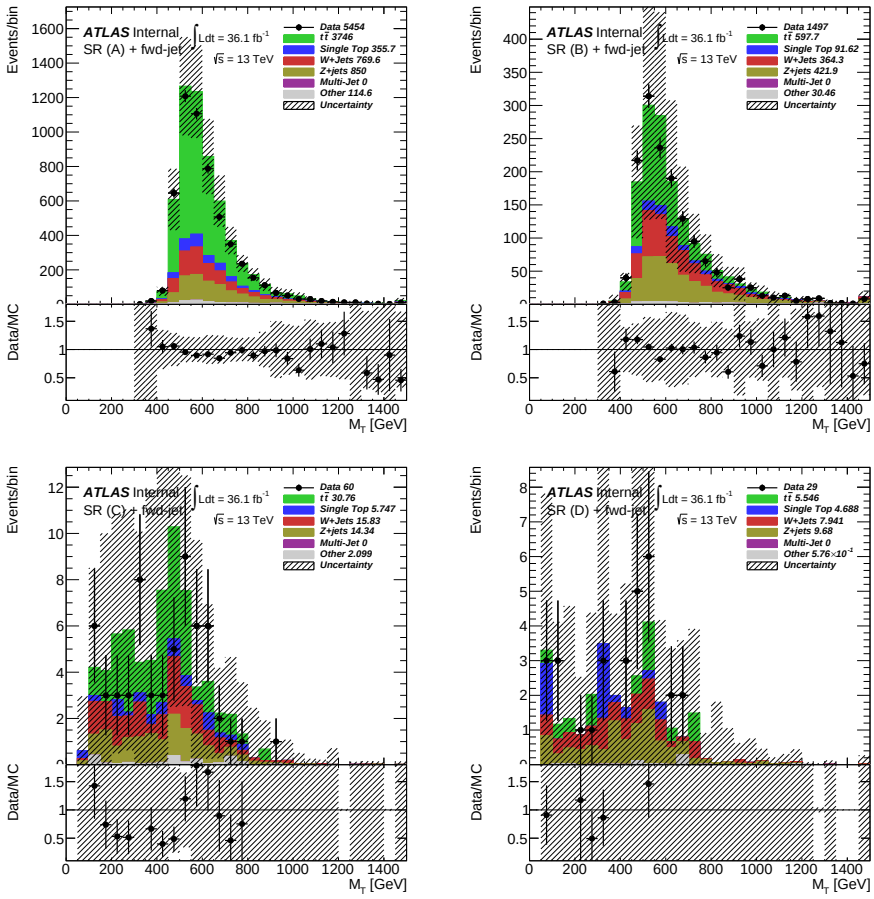

Figure 6.23: Distributions of the transverse mass M_T for the different regions of the ABCD method in the signal region with additional forward jet requirement. The uncertainties cover both systematic (object and modeling) and statistic contributions.

Selections	SR	$t\bar{t}$ CR	V+Jets CR	Multi-jet VR
Num. leptons (e,μ)	$= 0$	$= 0$	$= 0$	$= 0$
MET	> 200 GeV	> 200 GeV	> 200 GeV	> 200 GeV
Num. large-R jets($p_T > 250$ GeV)	≥ 1	≥ 1	≥ 1	≥ 1
Num. top-tagged jets (80%)	≥ 1	≥ 1	≥ 1	≥ 1
$\Delta\Phi(MET$, top jet)	$> \frac{\pi}{2}$	$> \frac{\pi}{2}$	$> \frac{\pi}{2}$	$> \frac{\pi}{2}$
Num. b-tagged track-jets (70%)	$= 1$	≥ 2	$= 0$	$= 1$
Veto jet (masked tile-calo)	-	applied	-	-
$\Omega = \frac{MET - p_T(J)}{MET + p_T(J)}$	> 0.3	> 0.3	> 0.3	< 0.3
$\Delta\Phi_{\min}(MET$, calo jets)	> 1.0	$0.2 < \Delta\Phi_{\min} < 1.0$	> 1.0	-
Num. forwards jets (VLT)	≥ 1	≥ 1	≥ 1	≥ 1

Table 6.8: Summary of the definition of the control, validation and signal regions.

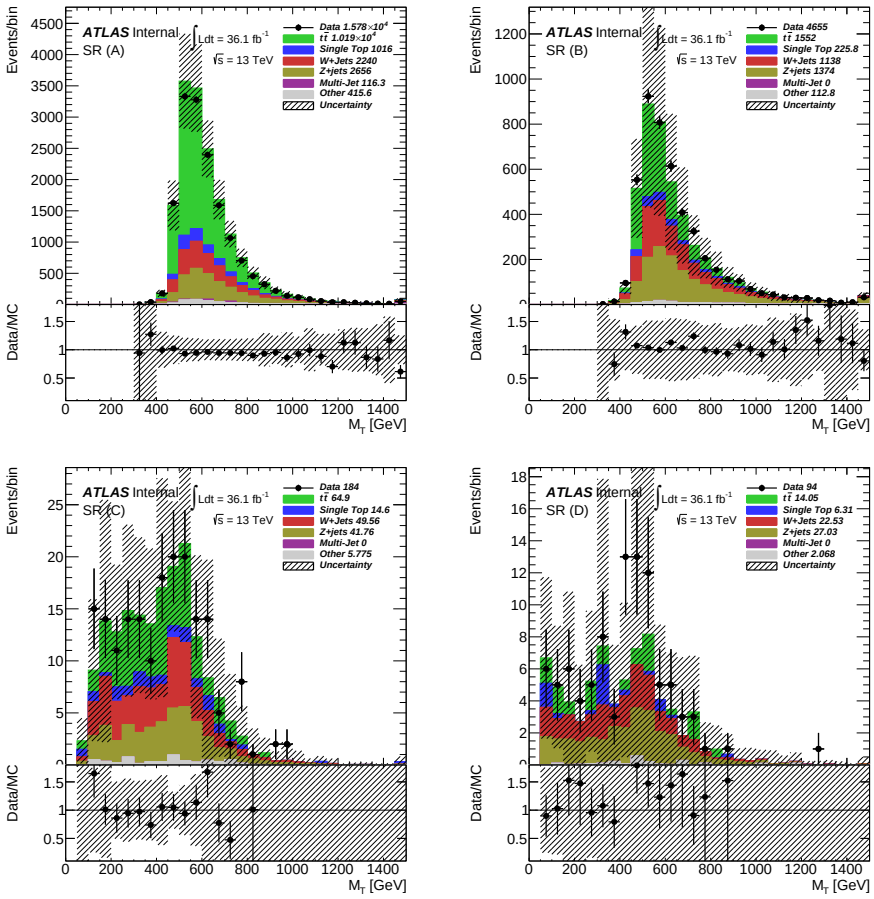

Figure 6.24: Distributions of the transverse mass M_T for the different regions of the ABCD method in the signal region without additional forward jet requirement. The uncertainties cover both systematic (object and modeling) and statistic contributions.

	SR(Fwd. Jet)	SR	$t\bar{t}$ CR	V+Jets CR	Multi-jet VR
$t\bar{t}$	3746.14 ± 53.22 ± 1170.71	10187.47 ± 87.09 ± 2721.97	6979.81 ± 75.76 ± 1837.16	6067.23 ± 67.52 ± 1707.94	2786.90 ± 50.12 ± 872.37
Single Top	355.75 ± 11.11 ± 83.71	1015.82 ± 18.81 ± 222.97	273.87 ± 9.86 ± 66.23	888.05 ± 18.02 ± 223.35	272.46 ± 9.49 ± 73.96
W+Jets	769.55 ± 20.16 ± 294.13	2239.95 ± 38.56 ± 862.62	147.15 ± 12.13 ± 79.36	28470.36 ± 177.90 ± 10710.20	419.64 ± 20.49 ± 164.26
Z+Jets	849.96 ± 29.16 ± 348.37	2655.56 ± 51.54 ± 1084.55	138.73 ± 11.78 ± 75.48	27437.99 ± 165.65 ± 10466.03	259.23 ± 16.10 ± 132.16
Other	114.62 ± 4.70 ± 30.47	415.55 ± 8.68 ± 103.24	95.64 ± 1.53 ± 34.47	2731.51 ± 24.94 ± 699.94	58.40 ± 2.13 ± 15.65
Multi-Jet	0	116.27 ± 121.23	959.78 ± 654.12	0	14191.47 ± 2940.99
Total bkg.	5836.02 ± 65.07 ± 1626.11	16630.62 ± 110.25 ± 4183.15	8594.98 ± 78.27 ± 2048.84	65595.15 ± 254.15 ± 19029.36	17988.11 ± 57.32 ± 3130.15
Data	5454	15781	8493	62304	16095
Data/Bkg.	0.93 ± 0.26	0.95 ± 0.24	0.99 ± 0.25	0.95 ± 0.28	0.90 ± 0.16
WTZt 900LH	111.59 ± 1.60 ± 19.80	145.02 ± 1.80 ± 25.70	21.01 ± 0.67 ± 5.21	76.10 ± 1.28 ± 16.49	13.30 ± 0.56 ± 3.71
WTZt 1200LH	51.13 ± 0.73 ± 8.91	66.01 ± 0.84 ± 11.67	9.23 ± 0.33 ± 2.34	34.99 ± 0.61 ± 7.99	10.69 ± 0.33 ± 2.45
WTZt 1600LH	16.35 ± 1.23 ± 3.08	20.48 ± 0.26 ± 3.86	2.58 ± 0.09 ± 0.63	10.25 ± 0.20 ± 3.24	4.86 ± 0.14 ± 0.98

Table 6.9: Event yields in signal and control regions for the different VLT signal mass points and background processes.

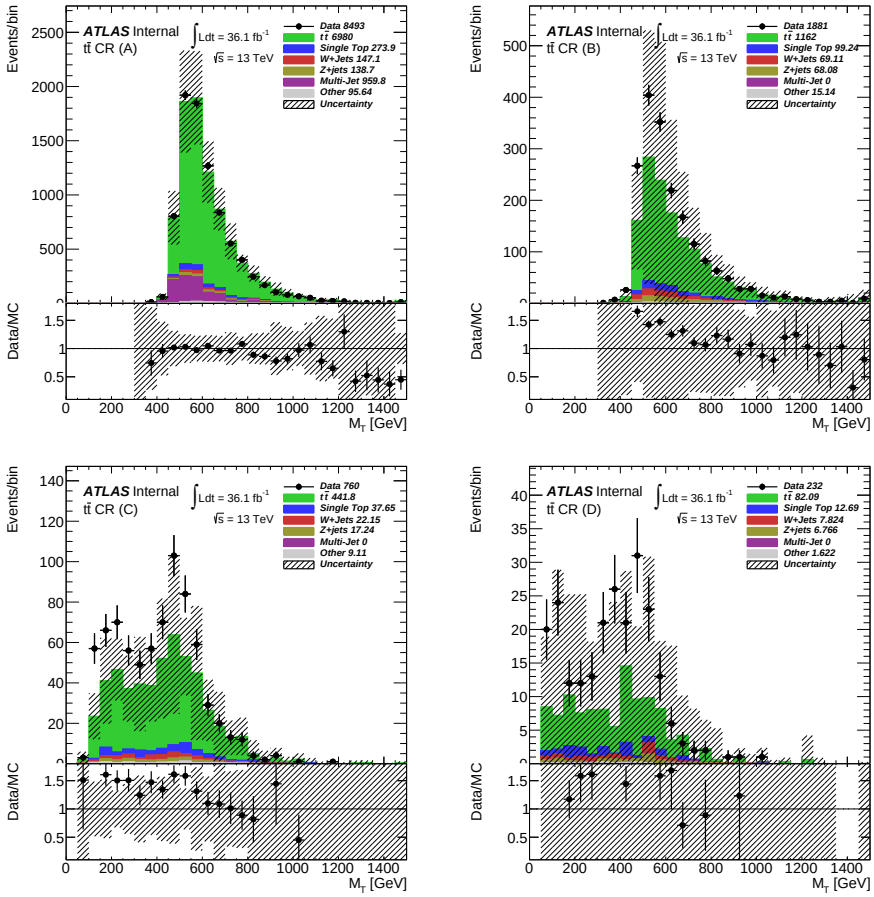

Figure 6.25: Distributions of the transverse mass M_T for the different regions of the ABCD method in the $t\bar{t}$ control region. The uncertainties cover both systematic (object and modeling) and statistic contributions.

	SR	$t\bar{t}$ CR	V+Jets CR	Multi-jet VR
$t\bar{t}$	10187.47 ± 87.09 ± 2721.97	6979.81 ± 75.76 ± 1837.16	6067.23 ± 67.52 ± 1707.94	2786.90 ± 50.12 ± 872.37
Single Top	1015.82 ± 18.81 ± 222.97	273.87 ± 9.86 ± 66.23	888.05 ± 18.02 ± 223.35	272.46 ± 9.49 ± 73.96
W+Jets	2239.95 ± 38.56 ± 862.62	147.15 ± 12.13 ± 79.36	28470.36 ± 177.90 ± 10710.20	419.64 ± 20.49 ± 164.26
Z+Jets	2655.56 ± 51.54 ± 1084.55	138.73 ± 11.78 ± 75.48	27437.99 ± 165.65 ± 10466.03	259.23 ± 16.10 ± 132.16
Other	415.55 ± 8.68 ± 103.24	95.64 ± 1.53 ± 34.47	2731.51 ± 24.94 ± 699.94	58.40 ± 2.13 ± 15.65
Multi-Jet	116.27 ± 121.23	959.78 ± 654.12	0	14191.47 ± 2940.99
Total bkg.	16630.62 ± 110.25 ± 4183.15	8594.98 ± 78.27 ± 2048.84	65595.15 ± 254.15 ± 19029.36	17988.11 ± 57.32 ± 3130.15
Data	15781	8493	62304	16095
Data/Bkg.	0.95 ± 0.24	0.99 ± 0.25	0.95 ± 0.28	0.90 ± 0.16
DM res.(m_Φ=1,m_χ=0.01)GeV	11260.78 ± 74.81 ± 1255.25	55.80 ± 5.58 ± 11.51	8084.18 ± 64.13 ± 1496.60	82.81 ± 6.74 ± 16.70
DM res.(m_Φ=2,m_χ=0.01)GeV	468.98 ± 2.98 ± 83.79	4.83 ± 0.56 ± 1.16	348.52 ± 2.67 ± 84.19	2.62 ± 0.21 ± 0.43
DM res.(m_Φ=3,m_χ=0.01)GeV	39.31 ± 0.27 ± 32.59	1.08 ± 0.09 ± 0.19	41.82 ± 0.30 ± 37.28	0.14 ± 0.02 ± 0.02
DM res.(m_Φ=4,m_χ=0.01)GeV	5.03 ± 0.04 ± 33.92	0.06 ± 0.01 ± 0.46	7.96 ± 0.05 ± 68.03	0.02 ± 0.00 ± 0.01
DM res.(m_Φ=5,m_χ=0.01)GeV	0.89 ± 0.01 ± 7.04	0.01 ± 0.00 ± 0.07	1.89 ± 0.01 ± 19.78	$0.00 \pm 0.00^{+0.00}_{-0.00}$
DM non-res. (m_Φ=1,m_χ=0.001)GeV	2090.29 ± 22.26 ± 285.12	29.00 ± 3.30 ± 5.79	1600.20 ± 18.67 ± 317.03	36.61 ± 2.62 ± 7.80
DM non-res. (m_Φ=1.5,m_χ=0.001)GeV	396.39 ± 3.89 ± 58.60	4.83 ± 0.56 ± 1.16	305.79 ± 3.44 ± 67.88	5.74 ± 0.46 ± 1.10
DM non-res. (m_Φ=2,m_χ=0.001)GeV	94.67 ± 0.92 ± 15.07	1.08 ± 0.09 ± 0.19	75.18 ± 0.83 ± 17.44	1.33 ± 0.11 ± 0.33
DM non-res. (m_Φ=2.5,m_χ=0.001)GeV	28.32 ± 0.28 ± 4.73	0.37 ± 0.04 ± 0.09	22.35 ± 0.25 ± 6.10	0.34 ± 0.03 ± 0.09
DM non-res. (m_Φ=3,m_χ=0.1)GeV	9.79 ± 0.07 ± 1.66	0.12 ± 0.01 ± 0.03	14.62 ± 0.06 ± 2.02	0.11 ± 0.01 ± 0.03

Table 6.10: Event yields in signal and control regions for the different DM signal and background processes.

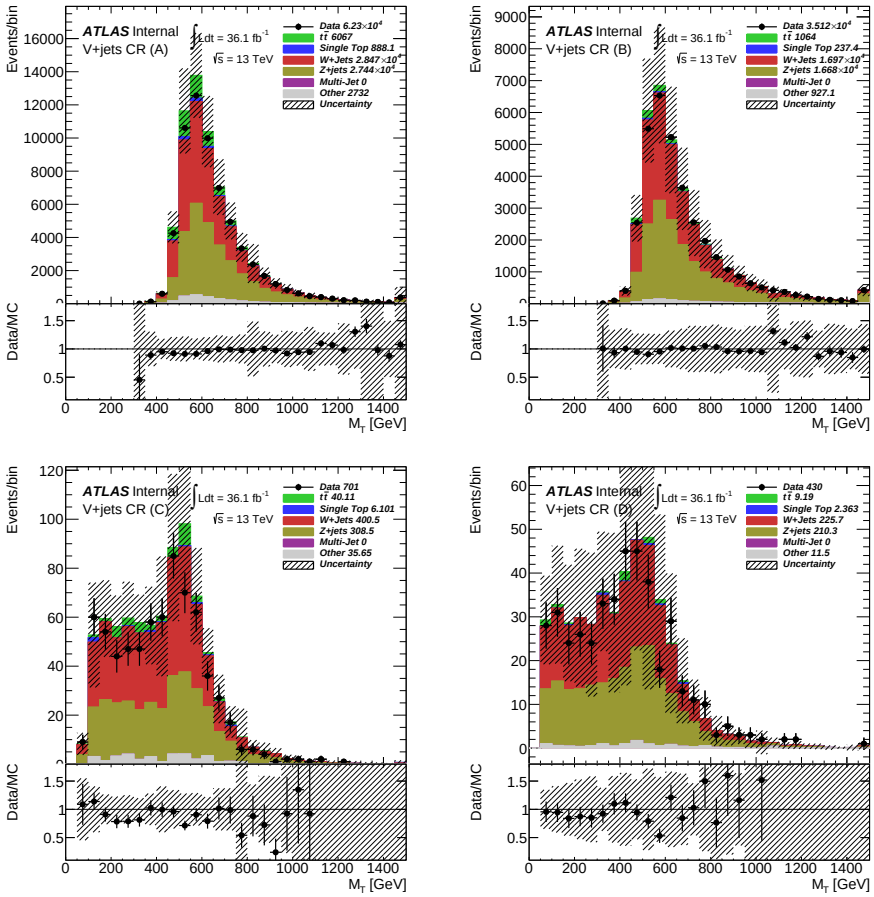

Figure 6.26: Distributions of the transverse mass M_T for the different regions of the ABCD method in the V+jets control region. The uncertainties cover both systematic (object and modeling) and statistic contributions.

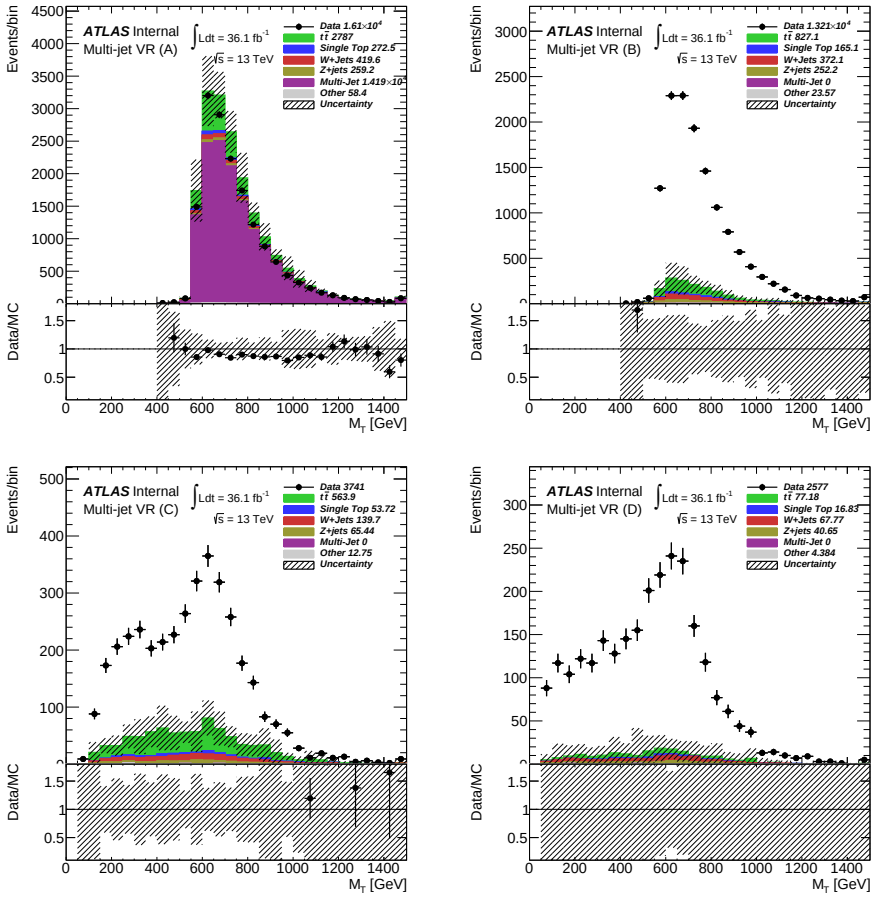

Figure 6.27: Distributions of the transverse mass m_T for the different regions of the ABCD method in the multi-jet control region. The uncertainties cover both systematic (object and modeling) and statistic contributions.

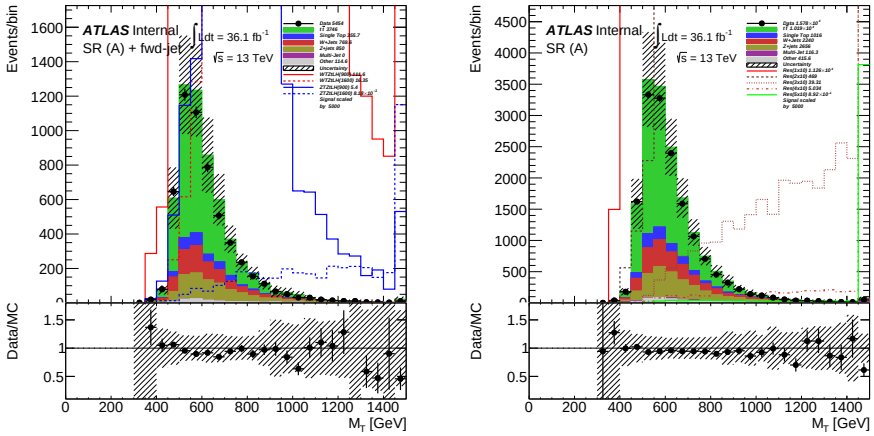

Figure 6.28: Distributions of the transverse mass m_T in the signal region with(left) and without(right) additional forward jet requirement. The uncertainties cover both systematic (object and modeling) and statistic contributions.

6.3 Data blinding policy

A data blinding policy is adopted in order to avoid biases when optimizating the event selections. The strategy, agreed between the analysis team, Editorial Board and HQT conveners, is to not look at the data events in the signal regions for both channels. The optimization of the analysis is done considering only expected exclusion limits obatined using only the MC simulation events. As described in Chapter 7.

1. Closure tests: perform $S + B$ fits in the signal plus control regions using pseudo-datasets build from Monte Carlo for these cases:

   (a) enhancement of the dominant backgrounds;

   (b) injection of a signal with $\mu = 1$.

2. Perform the full unblinding by looking at all the results of the fit.

   After performing and presenting these checks, on January 8th 2018 the team was allowed by the HQT subgroup conveners to unblind the analysis.

6.4 Systematic uncertainties

Systematic uncertainties, coming from various sources, can affect both the overall yield and shape of the variables used in the fit for the statistical analysis. In this section, the uncertainties considered in this analysis are described. They can be classified into two groups: detector-related uncertainties and uncertainties of background modeling. All sources of systematic uncertainties are included as nuisance parameters in the fit, and are evaluated by using the tools provided by the CP groups.

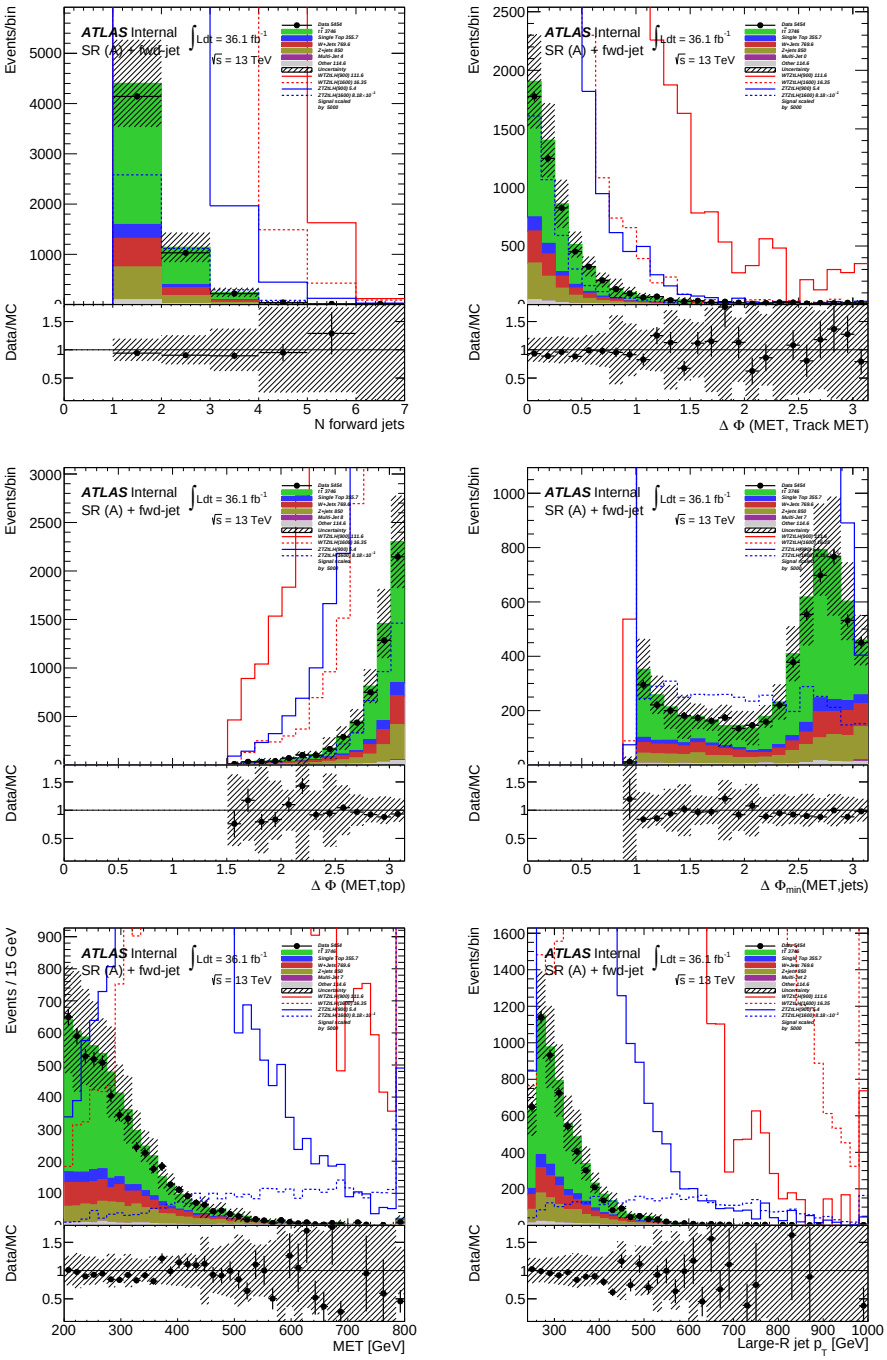

Figure 6.29: Distributions of the number of forward jets, $\Delta\phi((E_{\mathrm{T}}^{\mathrm{miss}}, \mathrm{Track}\ (E_{\mathrm{T}}^{\mathrm{miss}})$, $\Delta\phi((E_{\mathrm{T}}^{\mathrm{miss}}, \mathrm{Top})$, $\Delta\phi((E_{\mathrm{T}}^{\mathrm{miss}}, \mathrm{jet})$, ($E_{\mathrm{T}}^{\mathrm{miss}}$ and top-tagged large-R jet p_{T} in the signal region. Showing the signal region with forward jet requirement. The uncertainties cover both systematic (object and modeling) and statistic contributions.

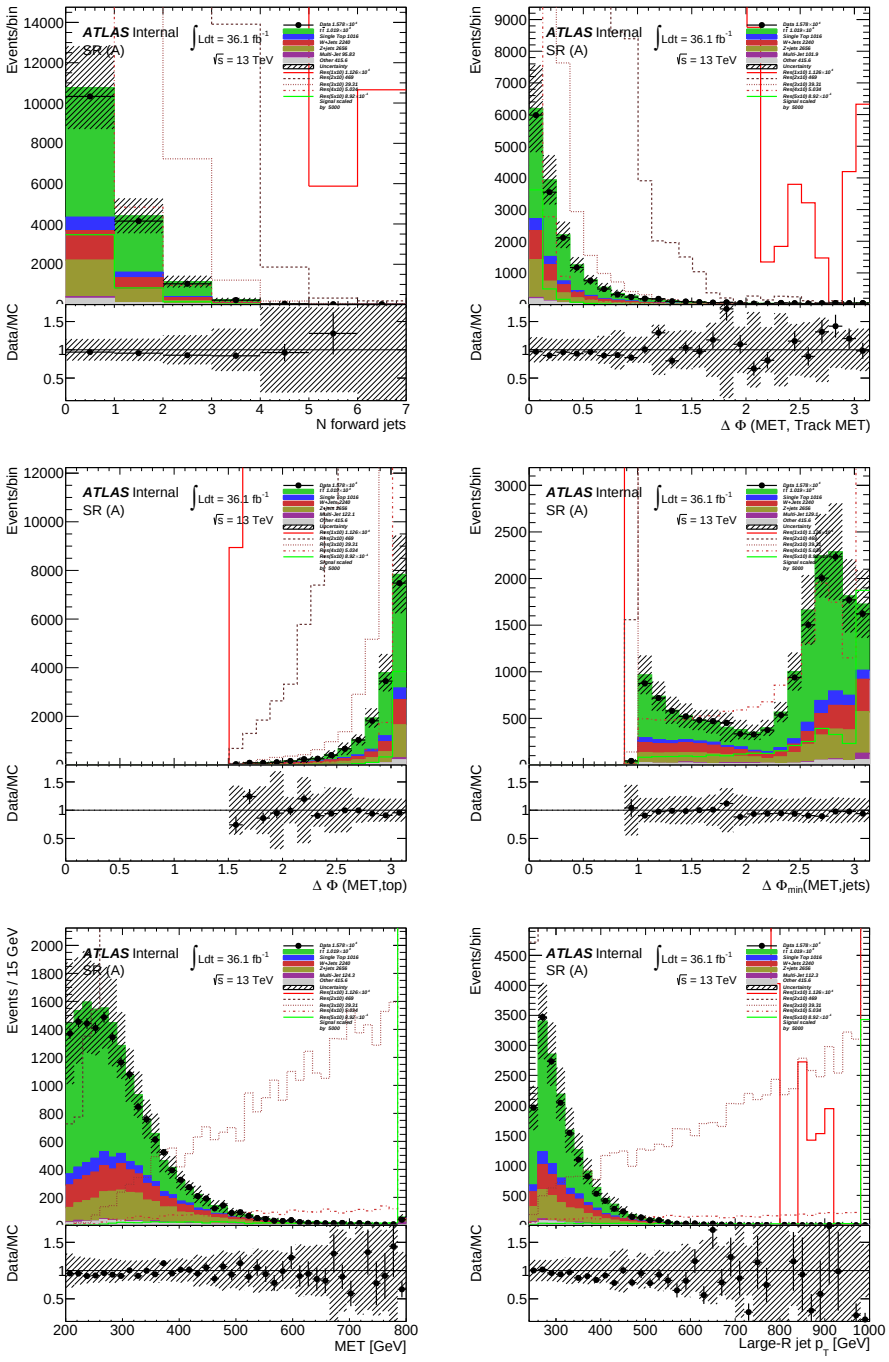

Figure 6.30: Distributions of the number of forward jets, $\Delta\phi((E_{\mathrm{T}}^{\mathrm{miss}}, \mathrm{Track}\ (E_{\mathrm{T}}^{\mathrm{miss}})$, $\Delta\phi((E_{\mathrm{T}}^{\mathrm{miss}}, \mathrm{Top})$, $\Delta\phi((E_{\mathrm{T}}^{\mathrm{miss}}, \mathrm{jet})$, ($E_{\mathrm{T}}^{\mathrm{miss}}$ and top-tagged large-R jet p_{T} in the signal region. Showing the signal region without forward jet requirement. The uncertainties cover both systematic (object and modeling) and statistic contributions.

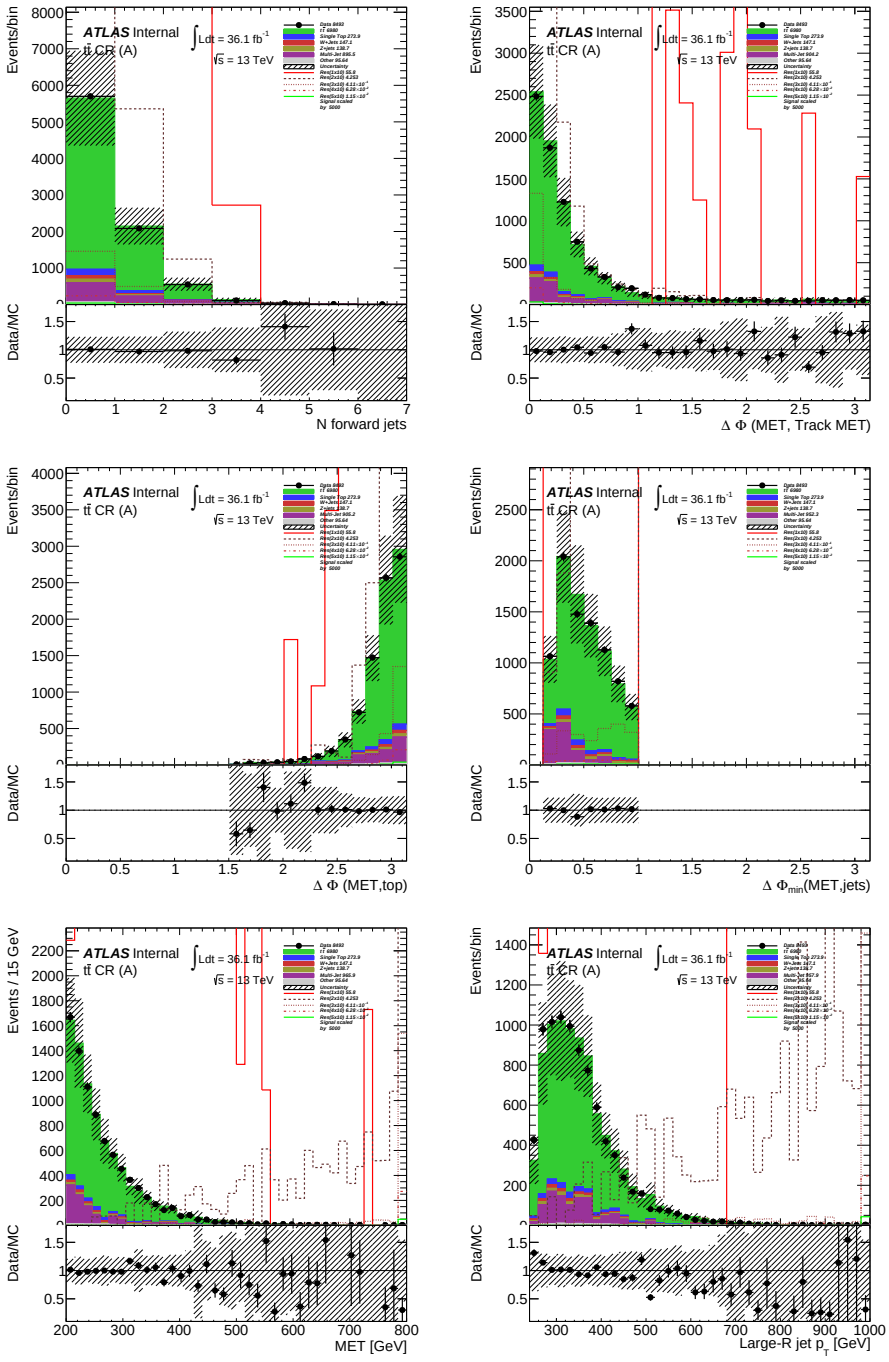

Figure 6.31: Distributions of the number of forward jets, $\Delta\phi((E_{\mathrm{T}}^{\mathrm{miss}}, \mathrm{Track}\ (E_{\mathrm{T}}^{\mathrm{miss}})$, $\Delta\phi((E_{\mathrm{T}}^{\mathrm{miss}}, \mathrm{Top})$, $\Delta\phi((E_{\mathrm{T}}^{\mathrm{miss}}, \mathrm{jet})$, ($E_{\mathrm{T}}^{\mathrm{miss}}$ and top-tagged large-R jet p_{T} in the $t\bar{t}$ control region. The uncertainties cover both systematic (object and modeling) and statistic contributions.

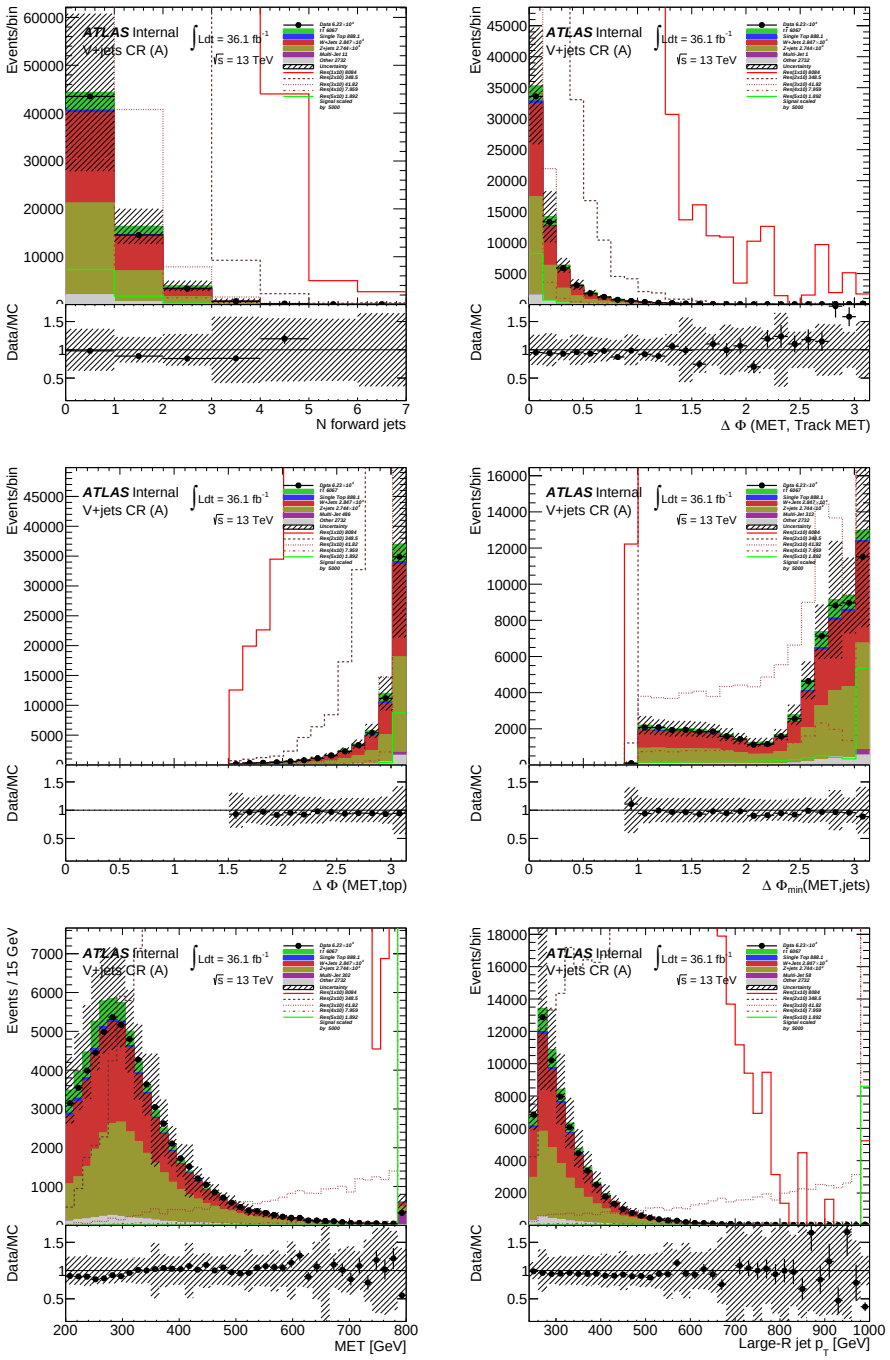

Figure 6.32: Distributions of the number of forward jets, $\Delta\phi((E_{\mathrm{T}}^{\mathrm{miss}}, \mathrm{Track}\ (E_{\mathrm{T}}^{\mathrm{miss}})$, $\Delta\phi((E_{\mathrm{T}}^{\mathrm{miss}}, \mathrm{Top})$, $\Delta\phi((E_{\mathrm{T}}^{\mathrm{miss}}, \mathrm{jet})$, ($E_{\mathrm{T}}^{\mathrm{miss}}$ and top-tagged large-R jet p_{T} in the V+jets control region. The uncertainties cover both systeatic (object and modeling) and statistic contributions.

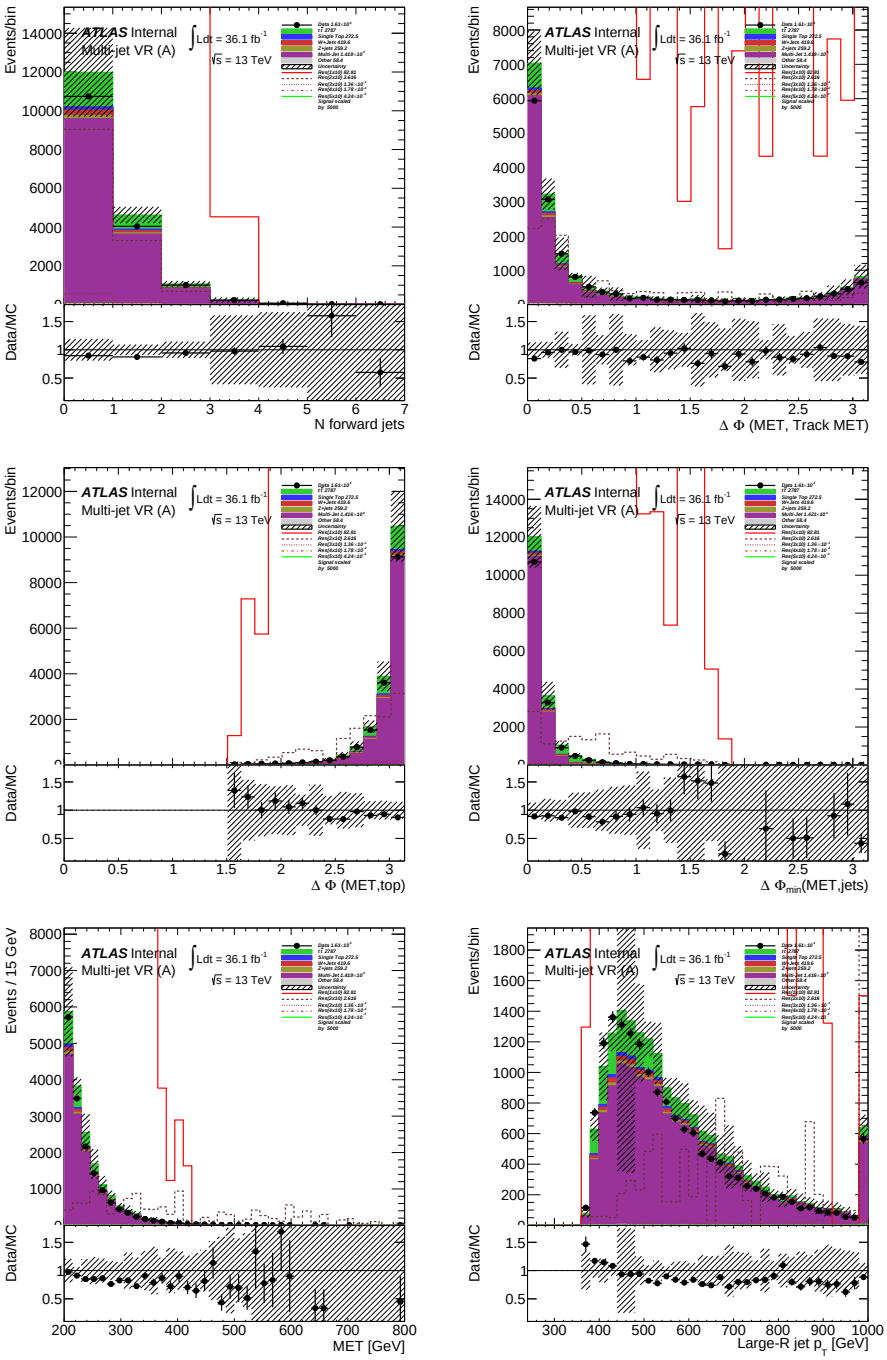

Figure 6.33: Distributions of the number of forward jets, $\Delta\phi((E_{\mathrm{T}}^{\mathrm{miss}}, \mathrm{Track}\ (E_{\mathrm{T}}^{\mathrm{miss}})$, $\Delta\phi((E_{\mathrm{T}}^{\mathrm{miss}}, \mathrm{Top})$, $\Delta\phi((E_{\mathrm{T}}^{\mathrm{miss}}, \mathrm{jet})$, ($E_{\mathrm{T}}^{\mathrm{miss}}$ and top-tagged large-R jet p_{T} in the multi-jet validation region. The uncertainties cover both systematic (object and modeling) and statistic contributions.

The detector-related uncertainties are described in Section 6.4.1, and the uncertainties of background modeling are discussed in Section 6.4.2. Then Sections 6.4.3 and 6.4.4 show the impact of the systematic uncertainties in each region for all the processes, for both leptonic and hadronic channels, respectively.

6.4.1 Detector-related uncertainties

Luminosity

The event yields of the MC simulation samples are normalized to the recorded data using the total integrated luminosity. To account for its uncertainty, an overall variation of 2.1%, corresponding to the combined luminosity error for the 2015 and 2016 data is applied to all MC processes. It is derived, following a methodology similar to that detailed in (88), from a calibration of the luminosity scale using x-y beam-separation scans performed in August 2015 and May 2016.

Electron and muon uncertainties

Differences between data and simulation in the reconstruction, identification, isolation and trigger efficiencies of leptons are taken into account by applying scale factors to the MC samples derived using tag-and-probe techniques on $Z \rightarrow \ell^+\ell^- (\ell = e, \mu)$ events and simulated samples. The scale factors have associated uncertainties which are propagated as corrections to the event weight using specific tools. In the case of muons, these uncertainties include two components, a statistical and a systematic uncertainties associated to the efficiency derivations. The impact of the lepton energy scale and resolution uncertainty on the selected sample is evaluated by scaling the p_{T} of all leptons up or down by 1σ and re-applying the event selection. Additional uncertainties which include variations in the p_{T} smearing in the ID and MS are considered for muons.

Missing Transverse Momentum

The missing transverse momentum is calculated using physics objects as described in Section 4.4. Apart from the uncertainties associated with the reconstructed components, uncertainties related with soft terms in the calculation (such as the modeling of the the underlying event and in particular its impact on the scale and resolution of th unclustered energy) are considered. These are taken into account by including variations in the energy scale and smearing according to the resolution uncertainty in the parallel and perpendicular direction to the p_{T}-hard plane.

Jet Energy Scale (JES)

A precise knowledge about the JES is needed for various purposes such as event selections based on kinematic properties of jets and the reconstruction of other variables and objects based on the properties of jets. The JES is calibrated using MC simulations and data taken during LHC runs. A large set of up to 75 nuisance parameters

derived in bins of jet p_{T} and η as well as other information, accounting for different effects on the JES are combined into a couple of two sided systematic variation related to η inter-calibration, jet flavor composition and response, b-jets, detector modeling, statistics, non-closure, punch trough losses and several pile-up properties. Also the effect of single high p_{T} particles is described. Large radius jets are calibrated using also MC and measured LHC data as well as measurement of the calorimeter response with respect to track information in the$r$-track double ratio procedure. Different effects are considered like basic efficiency, MC modeling uncertainties, statistics and tracking uncertainties to provide two sided systematic variations.

Jet energy resolution (JER)

The JER is important for all purposes which require precise energy separation of different jets, and might affect the acceptance of applied selections based on the properties of jets. The JER uncertainty has been measured in Run 1 data in bins of jet p_{T} and η in comparison to the MC prediction. Di-jet events are used to determine a one sided systematic variation and the provided one sided systematic is symmetrized by simple considering the up variation magnitude to be equal to the down variation magnitude.

Jet vertex tagger (JVT)

Information of the JVT can be used to suppress jets resulting from soft energetic radiation. Uncertainties on the JVT are provided as a two sided variation covering the differences in JVT efficiency measured in data and MC simulation, respectively, based on the scale factors derived in Z+jets events. The impact of statistical uncertainties and residual pile-up contamination in the used datasets are combined in the uncertainty on these scale factors which are applied to jets with $p_{\mathrm{T}} > 60$ GeV.

b-tagging

Systematic uncertainties related to the b-tagging efficiency and the mis-tag rate are associated to either the anti-k_t calorimeter jets with $R = 0.4$ or to the anti-k_t track jets with $R = 0.2$ using the officially recommended eigenvector variations. These variations have been derived and are applied on the ntuple level in bins of jet η, p_{T} and jet flavor, separated into jets originating from b, c or light quarks. A set of six(five), three(four) and sixteen(seventeen) independent and almost uncorrelated scale factors are applied to the different calorimeter(track-jet) favors b-jets, c-jets and light-jets.

6.4.2 Modeling uncertainties

Trigger turn-on

An $E_{\mathrm{T}}^{\mathrm{miss}}$ cut is applied at the beginning of the $E_{\mathrm{T}}^{\mathrm{miss}}$ trigger for the hadronic channel. In order to account for the potential efficiency loss due to residual turn-on effects a 2% overall uncertainty is applied. The corresponding $E_{\mathrm{T}}^{\mathrm{miss}}$ trigger efficiency as a function

of $E_{\mathrm{T}}^{\mathrm{miss}}$ can be found in Figure 3 of (89). In the leptonic channel, the lepton p_{T} cut applied is well above the trigger efficiency turn-on and this uncertainty is not applied.

Lepton-veto uncertainties

Since a veto on the reconstructed electrons and muons is applied in the hadronic channel, the impact of different lepton object uncertainties on the number of reconstructed leptons is evaluated. For this purpose the lepton veto is dropped and the relative variation of different object uncertainties is evaluated. This is than propagated as a relative overall and symmetric uncertainty for each region separately.

Cross-section uncertainties

MC samples are typically generated at given cross-section for the respective process determined at leading order and hence the normalization of each background contribution underlies theory uncertainties due to the cross-section approximation. Uncertainties on the LO or NLO cross-sections used to generate background MC samples are taken from NNLO cross-section calculations. The following two-sided uncertainties are used for different background processes as an overall uncertainty:

- $t\bar{t}$: (+5.58, -6.11)%,
  - Squared sum of: scale (90), PDf+α_S (91) and mass uncertainties (90, 92).
- $t\bar{t}$+X : (+13.3, -11.98)% for $t\bar{t}$+W and (+10.38, -11.97)% for $t\bar{t}$+Z and $t\bar{t}$+$\ell\ell$,
- V+jets : (+5.0, -5.0)% for W+jets and Z+jets (84),
- Single top : (+3.62, -3.15)% in the s-channel (top) (85), (+3.97, -3.36)% in the t-channel (top), (+5.02, -4.46)% in the t-channel (anti-top) (86) and (+5.3, -5.3)% in the Wt-channel (87),
- Di-bosons : (+6.0, -6.0)% (84).

$t\bar{t}$ modeling uncertainties

In order to account for the mis-modeling of the $t\bar{t}$ background (especially in the high p_{T} large-R jet modeling) different modeling uncertainties are considered. This is of particular importance since $t\bar{t}$ is the main background contribution to both SRs with and without additional forward jet requirement.

To estimate the impact of different hard scattering generators the difference between the nominal Powheg+Pythia8 samples and an aMcAtNlo+Pythia8 variation sample is used and to also account for the impact of different fragmentation and hadronization models the difference between the nominal and a Powheg+Herwig7 variation sample is used. In both cases the difference is used as a symmetric up and down variation.

To model the effect of additional radiation a set of two POWHEG+PYTHIA8 samples is used which are generated with different factorization and renormalization scale ($\times 2$ and $\times 0.5$) and modified NLO radiation (hdamp parameter = $1.5 \times m_{\text{top}}$, $3.0 \times m_{\text{top}}$).

The impact of different PDF set and internal scale variations has been tested (NNPDF3.0: used in the nominal samples,MMHT,CT14) and all variations are reasonably modeled by the combined PDF4LHC30 PDF set and its internal scale variations. The envelope of the maximal up and down variations with respect to the nominal distribution are taken as a two-sided uncertainty.

V+jets modeling uncertainties

To account for differences in both the Z+jets and the W+jets background prediction due to different particle and shower generation the nominal SHERPA 2.2.1 V+jets samples are compared to V+jets variation samples generated using MADGRAPH+PYTHIA8. While Sherpa uses $\max(H_{\text{T}}, p_{\text{T}}(Z))$ to divide the samples into different slices based on their kinematics only, the MADGRAPH+PYTHIA8 samples use the H_{T} property for the same purpose, for all W+boson decay channels, as well as for Z-boson decay into two electrons or two muons. For Z-boson decay to two taus or two neutrinos the number of additionally produced truth particles is used. The difference between the nominal and the variation sample is used as both the up and down variation uncertainty. The impact of different renormalization and factorization scales, varied between various combinations of the following values [0.5/0.5, 0.5/1, 1/0.5, 1/1, 1/2, 2/1, 2/2] is estimated by evaluation of the SHERPA 2.2.1 internal weights. The envelope of maximal and minimal variation compared to the nominal distribution are used as a two-sided uncertainty. The impact of different PDF sets are evaluated in the same way as for the internal scale variation, by using the envelope of maximal and minimal variation as a two-sided uncertainty.

In the hadronic channel the difference between the heavy jet flavor contributions in the different regions, as well as the need to account for potential mis-modeling of this quantity, is considered by including a heavy flavor (HF) uncertainty. The systematic variations are created by scaling the events which contain a jet ghost-associated to a b-meson by $\pm$ 50%. The difference with respect to the nominal samples are used as a symmetric and two-sides uncertainty.

Large-R jet resolution uncertainties

The expected resolution uncertainties of the three properties of the large-R jets, the reconstructed jet mass, the transverse jet momentum p_{T} and the n-subjettiness ratio substructure variable τ_{32}^{wta}, are derived by randomly smearing the respective jet property within 20% of a Gaussian function with a standard deviations σ derived from a Gaussian fit to the response function ($\frac{\text{reco}}{\text{truth}}$) of the jet property. The smeared jet properties are propagated through the analysis selection requirements and all three jet properties are treated as fully uncorrelated.

In the case of the large-R jet mass and p_{T} the fitted response functions are derived

in five bins of the jet p_{T} [200,500,750,1000,1250,$>$ 1250] GeV and four bins of $\frac{\mathrm{mass}}{p_T}$ [$<$ 0.2 , 0.2, 0.4, $>$ 0.4] using a set of $Z' \to t\bar{t}$ samples. In the case of large-R jet τ_{32}^{wta} a single fit to the response function taken from the MC prediction in the signal region is performed.

Multijet closure uncertainty for the ABCD method in the hadronic channel

In the hadronic channel a closure uncertainty of the ABCD method on the multi-jet contribution is derived in the multi-jet validation region and then propagated to different regions. It is derived using the ABCD method to derive the estimated multi-jet contribution using either POWHEG+PYTHIA8 di-jet samples in the different multi-jet estimation regions or just considering the nominal multi-jet prediction in the multi-jet validation region provided by these samples. The relative difference is derived in bins of the considered distribution and applied as a relative symmetric up and down variation.

Reweighting closure

A set of signal samples with different values of the mediator mass, the DM particle mass, the mediator-DM particle coupling and the mediator-SM particle coupling are generated using a reweighting technique based on generator-level variables, as explained in Section 7.5. Those samples will be used to extract two-dimensional exclusion regions. While the shape distributions at reconstructed level is well modeled by the reweighted samples, there are small differences in the normalisation which is not fully covered by the statistical uncertainty. To account for these discrepancies, an extra source of uncertainty is used when performing the signal plus background fits to data with the reweighted samples. This uncertainty is estimated as an overall normalisation factor. Given the studies done, the following values are used:

- Non-resonant model: $\pm 6\%$
- Resonant model: $\pm 25\%$

6.4.3 Rate variations in the single-lepton channel

The relative systematic uncertainties on the predicted event yields after the fit in the signal region evaluated for the non-resonant signal ($m(v_{\mathrm{met}}) = 1000$ GeV) and background processes are listed in Table 6.11. The values combine the electron and muon channels. The relative systematic uncertainties on the predicted rates in the two control regions used to constrain the W+jets and $t\bar{t}$ background rates are listed in Tables 6.12 and 6.13, respectively.

6.4.4 Rate variations in the hadronic channel

The relative systematic uncertainties on the predicted event yields in the signal region evaluated for the VLT signal processes are shown in Table 6.15 and the background

	non-$t\bar{t}$	Non resonant, m(v_{met}) = 1000 GeV	$t\bar{t}$
Electron SF ID	1.16 / -1.16	0.71 / -0.71	0.646 / -0.646
Electron SF reco	0.118 / -0.118	0.129 / -0.129	0.12 / -0.12
Electron SF isol.	0.804 / -0.804	0.662 / -0.662	0.28 / -0.28
Electron SF trigger.	0.123 / -0.123	0.0961 / -0.0961	0.102 / -0.102
Muon ID	-0.238 / 0.238	0.00254 / -0.00254	-0.273 / 0.273
Muon MS	0.824 / -0.824	0.0245 / -0.0245	0.0603 / -0.0603
Muon sagitta resbias	0 / 0	8.68e-07 / 8.68e-07	0 / 0
Muon sagitta rho	0 / 0	8.68e-07 / 8.68e-07	0 / 0
Muon scale	0 / 0	-0.0241 / 0.0241	-0.179 / 0.179
Muon SF ID	0.554 / -0.554	0.526 / -0.526	0.436 / -0.436
Muon SF isol.	0.0944 / -0.0944	0.0968 / -0.0968	0.0882 / -0.0882
Muon SF isol. stat.	0.0193 / -0.0193	0.0192 / -0.0192	0.0155 / -0.0155
Muon SF ID. stat.	0.0831 / -0.0831	0.0789 / -0.0789	0.0777 / -0.0777
Muon SF ttva	0.0356 / -0.0356	0.0347 / -0.0347	0.0325 / -0.0325
Muon SF ttva stat.	0.0357 / -0.0357	0.0335 / -0.0335	0.0333 / -0.0333
Muon SF low p_T	0 / 0	8.68e-07 / 8.68e-07	0 / 0
Muon SF low p_T stat.	0 / 0	8.68e-07 / 8.68e-07	0 / 0
Muon SF trigger	0.432 / -0.432	0.411 / -0.411	0.412 / -0.412
Muon SF trigger stat.	0.238 / -0.238	0.241 / -0.241	0.246 / -0.246
E_T^{miss} scale	-0.275 / 0.275	-0.645 / 0.645	-0.809 / 0.809
E_T^{miss} resolution perp.	-8.51 / 8.51	-0.625 / 0.625	-0.485 / 0.485
E_T^{miss} resolution para.	-9.64 / 9.64	-0.589 / 0.589	-0.492 / 0.492
JES punchthrough (AF)	0 / 0	8.68e-07 / 8.68e-07	0 / 0
AFII non closure	0 / 0	0.442 / -0.442	0 / 0
Jet Energy Resolution	-7.36 / 7.36	-1.93 / 1.93	-3.28 / 3.28
JES single part. high p_T	0 / 0	8.68e-07 / 8.68e-07	0 / 0
JES pile-up rho topo.	-1.89 / 1.89	-1.69 / 1.69	-3.44 / 3.44
JES pile-up p_T term	1.32 / -1.32	-0.0817 / 0.0817	-0.577 / 0.577
JES pile-up offset npv	-1.22 / 1.22	-0.242 / 0.242	-0.637 / 0.637
JES pile-up offset mu	0.0919 / -0.0919	0.0635 / -0.0635	0.278 / -0.278
JES flavor response	2.81 / -2.81	0.991 / -0.991	1.64 / -1.64
JES flavor composition	-6.37 / 6.37	-4.09 / 4.09	-5.66 / 5.66
JES EIC total stat.	-2.05 / 2.05	-0.289 / 0.289	-0.596 / 0.596
JES EIC total non-closure	-1.75 / 1.75	-0.315 / 0.315	-0.452 / 0.452
JES EIC total modelling	-2.09 / 2.09	-1.01 / 1.01	-1.74 / 1.74
JES Eff. NP 8	-0.00167 / 0.00168	-0.0355 / 0.0355	-0.0644 / 0.0644
JES Eff. NP 7	-0.0177 / 0.0177	-0.0131 / 0.0131	0.0683 / -0.0683
JES Eff. NP 6	0.0217 / -0.0217	-0.0676 / 0.0676	-0.155 / 0.155
JES Eff. NP 5	-0.00484 / 0.00484	0.0468 / -0.0468	0.12 / -0.12
JES Eff. NP 4	-0.015 / 0.015	0.00731 / -0.00731	0.0323 / -0.0323
JES Eff. NP 3	0.0215 / -0.0215	-0.0457 / 0.0457	-0.0771 / 0.0771
JES Eff. NP 2	2.4 / -2.4	0.241 / -0.241	0.455 / -0.455
JES Eff. NP 1	-1.85 / 1.85	-1.01 / 1.01	-2.1 / 2.1
B-jet energy scale	1.26 / -1.26	0.2 / -0.2	0.0382 / -0.0382
B-tag(70) eff. b EV 1	-2.54 / 2.54	-2.55 / 2.55	-2.8 / 2.8
B-tag(70) eff. b EV 2	-3.24 / 3.24	-4.48 / 4.48	-4.2 / 4.2
B-tag(70) eff. b EV 3	-2.77 / 2.77	-4.3 / 4.3	-3.69 / 3.69
B-tag(70) eff. b EV 4	-2.83 / 2.83	-4.22 / 4.22	-3.58 / 3.58
B-tag(70) eff. b EV 5	-2.82 / 2.82	-4.24 / 4.24	-3.59 / 3.59
B-tag(70) eff. b EV 6	-2.82 / 2.82	-4.24 / 4.24	-3.6 / 3.6
B-tag(70) eff. c EV 1	-0.109 / 0.109	0.00355 / -0.00355	0.0808 / -0.0808
B-tag(70) eff. c EV 2	-1.09 / 1.09	-0.00754 / 0.00754	0.0572 / -0.0572
B-tag(70) eff. c EV 3	-1.11 / 1.11	-0.011 / 0.011	0.0841 / -0.0841
B-tag(70) eff. l. EV 1	-1.23 / 1.23	-0.0723 / 0.0723	-0.0231 / 0.0231
B-tag(70) eff. l. EV 2	-1.18 / 1.18	-0.0297 / 0.0297	-0.0588 / 0.0588
B-tag(70) eff. l. EV 3	-0.758 / 0.758	-0.0371 / 0.0371	-0.0406 / 0.0406
B-tag(70) eff. l. EV 4	-0.741 / 0.741	-0.033 / 0.033	-0.0733 / 0.0733
B-tag(70) eff. l. EV 5	-0.749 / 0.749	-0.0316 / 0.0316	-0.0756 / 0.0756
B-tag(70) eff. l. EV 6	-0.715 / 0.715	-0.0266 / 0.0266	-0.0881 / 0.0881
B-tag(70) eff. l. EV 7	-0.742 / 0.742	-0.0317 / 0.0317	-0.0851 / 0.0851
B-tag(70) eff. l. EV 8	-0.646 / 0.646	-0.029 / 0.029	-0.0816 / 0.0816
B-tag(70) eff. l. EV 9	-0.828 / 0.828	-0.0282 / 0.0282	-0.0793 / 0.0793
B-tag(70) eff. l. EV 10	-0.908 / 0.908	-0.0245 / 0.0245	-0.0893 / 0.0893
B-tag(70) eff. l. EV 11	-0.945 / 0.945	-0.0239 / 0.0239	-0.0856 / 0.0856
B-tag(70) eff. l. EV 12	-0.936 / 0.936	-0.0212 / 0.0212	-0.0813 / 0.0813
B-tag(70) eff. l. EV 13	-1.02 / 1.02	-0.0211 / 0.0211	-0.0787 / 0.0787
B-tag(70) eff. l. EV 14	-1.02 / 1.02	-0.0219 / 0.0219	-0.0801 / 0.0801
B-tag(70) eff. l. EV 15	-1.02 / 1.02	-0.0223 / 0.0223	-0.0796 / 0.0796
B-tag(70) eff. l. EV 16	-1.01 / 1.01	-0.0224 / 0.0224	-0.0803 / 0.0803
B-tag(70) XTR	0.0977 / -0.0977	0.195 / -0.195	0.0303 / -0.0303
B-tag(70) XTR CHRM	0.098 / -0.098	8.68e-07 / 8.68e-07	-0.0313 / 0.0313
Pile-up	-5.52 / 5.52	0.555 / -0.555	-1.47 / 1.47
Jet-vertex-tagger	0.0698 / -0.0698	-0.038 / 0.038	-0.252 / 0.252
non-$t\bar{t}$ cross-section	7.37 / -7.37	0 / 0	0 / 0
Luminosity	2.1 / -2.1	2.1 / -2.1	2.1 / -2.1
Energy scale	0.35 / -0.35	0.138 / -0.138	0.621 / -0.621
Energy resolution	0.206 / -0.206	0.027 / -0.027	-0.101 / 0.101
t-channel radiation	0 / 0	0 / 0	0 / 0
t-channel generator	0 / 0	0 / 0	0 / 0
t-channel parton shower	0 / 0	0 / 0	0 / 0
Wt-channel DS	-13.7 / 13.7	0 / 0	0 / 0
$t\bar{t}$ cross-section	0 / 0	0 / 0	5.58 / -6.11
$t\bar{t}$ radiation	0 / 0	0 / 0	3.26 / -3.26
$t\bar{t}$ generator	0 / 0	0 / 0	-31.8 / 31.8
$t\bar{t}$ parton shower	0 / 0	0 / 0	3.75 / -3.75
$t\bar{t}$ PDF variation	0 / 0	0 / 0	1.09 / -1.09

Table 6.11: Relative variations (up/down) on the background event yields in the SR. The rate variations for the non-resonant signal model with $m(v_{\text{met}}) = 1000$ GeV are also shown. They combine the electron and muon channels, and are quoted in per cent.

	non-$t\bar{t}$	Non resonant, $m(v_{met}) = 1000$ GeV	$t\bar{t}$
Electron SF ID	0.279 / -0.279	0.297 / -0.297	0.272 / -0.272
Electron SF reco	0.0515 / -0.0515	0.0782 / -0.0782	0.0514 / -0.0514
Electron SF isol.	0.0577 / -0.0577	0.077 / -0.077	0.0521 / -0.0521
Electron SF trigger.	0.111 / -0.111	0.111 / -0.111	0.115 / -0.115
Muon ID	-0.136 / 0.136	-1.22 / 1.22	0.0352 / -0.0352
Muon MS	-0.188 / 0.188	0 / 0	-0.00491 / 0.00491
Muon sagitta resbias	0 / 0	0 / 0	0 / 0
Muon sagitta rho	0 / 0	0 / 0	0 / 0
Muon scale	-0.155 / 0.155	0 / 0	-0.00366 / 0.00366
Muon SF ID	0.307 / -0.307	0.341 / -0.341	0.327 / -0.327
Muon SF isol.	0.089 / -0.089	0.0966 / -0.0966	0.102 / -0.102
Muon SF isol. stat.	0.00645 / -0.00645	0.00704 / -0.00704	0.00693 / -0.00693
Muon SF ID. stat.	0.0816 / -0.0816	0.0762 / -0.0762	0.0923 / -0.0923
Muon SF ttva	0.0234 / -0.0234	0.0187 / -0.0187	0.0328 / -0.0328
Muon SF ttva stat.	0.0914 / -0.0914	0.0365 / -0.0365	0.039 / -0.039
Muon SF low p_T	0 / 0	0 / 0	0 / 0
Muon SF low p_T stat.	0.0509 / -0.0509	0 / 0	0 / 0
Muon SF trigger	0.131 / -0.131	0.43 / -0.43	0.48 / -0.48
Muon SF trigger stat.	3.55 / -3.55	0.311 / -0.311	0.281 / -0.281
E_T^{miss} scale	-1.08 / 1.08	3.87 / -3.87	0.214 / -0.214
E_T^{miss} resolution perp.	-9.97 / 9.97	0 / 0	-0.0626 / 0.0626
E_T^{miss} resolution para.	-9.75 / 9.75	2.66 / -2.66	0.0644 / -0.0644
JES punchthrough (AF)	0 / 0	0 / 0	0 / 0
AFII non closure	0 / 0	-2.97 / 2.97	0 / 0
Jet Energy Resolution	-9.67 / 9.67	-9.74 / 9.74	-2.58 / 2.58
JES single part. high p_T	0 / 0	0 / 0	0 / 0
JES pile-up rho topo.	0.71 / -0.71	0.59 / -0.59	-2.98 / 2.98
JES pile-up p_T term	0.882 / -0.882	-3.04 / 3.04	-0.449 / 0.449
JES pile-up offset npv	2.27 / -2.27	-3.04 / 3.04	-0.578 / 0.578
JES pile-up offset mu	-0.421 / 0.421	-3.04 / 3.04	0.2 / -0.2
JES flavor response	1.48 / -1.48	-0.899 / 0.899	2.38 / -2.38
JES flavor composition	-0.969 / 0.969	-0.874 / 0.874	-8.1 / 8.1
JES EIC total stat.	0.626 / -0.626	3.04 / -3.04	-0.61 / 0.61
JES EIC total non-closure	-0.0672 / 0.0672	3.04 / -3.04	-0.298 / 0.298
JES EIC total modelling	2.1 / -2.1	4.46 / -4.46	-1.97 / 1.97
JES Eff. NP 8	0.0246 / -0.0246	-0.00173 / 0.00173	-0.0489 / 0.0489
JES Eff. NP 7	0.602 / -0.602	0.00189 / -0.00189	0.0106 / -0.0106
JES Eff. NP 6	-0.125 / 0.125	0.00143 / -0.00143	-0.12 / 0.12
JES Eff. NP 5	-0.569 / 0.569	-0.00161 / 0.00161	0.0787 / -0.0787
JES Eff. NP 4	0.754 / -0.754	-0.00163 / 0.00163	0.0718 / -0.0718
JES Eff. NP 3	-0.874 / 0.874	0.00757 / -0.00757	-0.102 / 0.102
JES Eff. NP 2	0.915 / -0.915	-3.05 / 3.05	0.515 / -0.515
JES Eff. NP 1	-1.34 / 1.34	2.37 / -2.37	-1.98 / 1.98
B-jet energy scale	1.22 / -1.22	3.03 / -3.03	0.789 / -0.789
B-tag(70) eff. b EV 1	-5.96 / 5.96	-4.13 / 4.13	-5.51 / 5.51
B-tag(70) eff. b EV 2	-7.48 / 7.48	-6.01 / 6.01	-7.7 / 7.7
B-tag(70) eff. b EV 3	-6.25 / 6.25	-5.37 / 5.37	-6.3 / 6.3
B-tag(70) eff. b EV 4	-6.38 / 6.38	-5.56 / 5.56	-6.23 / 6.23
B-tag(70) eff. b EV 5	-6.39 / 6.39	-5.61 / 5.61	-6.31 / 6.31
B-tag(70) eff. b EV 6	-6.39 / 6.39	-5.61 / 5.61	-6.3 / 6.3
B-tag(70) eff. c EV 1	0.545 / -0.545	0.684 / -0.684	0.0998 / -0.0998
B-tag(70) eff. c EV 2	-0.123 / 0.123	-1.32 / 1.32	-0.183 / 0.183
B-tag(70) eff. c EV 3	0.0924 / -0.0924	-1.47 / 1.47	-0.127 / 0.127
B-tag(70) eff. l. EV 1	1.15 / -1.15	-5.96 / 5.96	-0.26 / 0.26
B-tag(70) eff. l. EV 2	0.251 / -0.251	-7.28 / 7.28	-0.221 / 0.221
B-tag(70) eff. l. EV 3	-0.829 / 0.829	-6.62 / 6.62	-0.194 / 0.194
B-tag(70) eff. l. EV 4	-2.22 / 2.22	-8.28 / 8.28	-0.252 / 0.252
B-tag(70) eff. l. EV 5	-2.24 / 2.24	-8.07 / 8.07	-0.253 / 0.253
B-tag(70) eff. l. EV 6	-2.42 / 2.42	-7.66 / 7.66	-0.287 / 0.287
B-tag(70) eff. l. EV 7	-2.39 / 2.39	-8.28 / 8.28	-0.28 / 0.28
B-tag(70) eff. l. EV 8	-2.36 / 2.36	-7.94 / 7.94	-0.274 / 0.274
B-tag(70) eff. l. EV 9	-2.34 / 2.34	-8.13 / 8.13	-0.258 / 0.258
B-tag(70) eff. l. EV 10	-2.33 / 2.33	-9.21 / 9.21	-0.269 / 0.269
B-tag(70) eff. l. EV 11	-2.3 / 2.3	-9.27 / 9.27	-0.27 / 0.27
B-tag(70) eff. l. EV 12	-2.36 / 2.36	-9.16 / 9.16	-0.266 / 0.266
B-tag(70) eff. l. EV 13	-2.34 / 2.34	-9.21 / 9.21	-0.266 / 0.266
B-tag(70) eff. l. EV 14	-2.31 / 2.31	-9.32 / 9.32	-0.266 / 0.266
B-tag(70) eff. l. EV 15	-2.32 / 2.32	-9.32 / 9.32	-0.266 / 0.266
B-tag(70) eff. l. EV 16	-2.33 / 2.33	-9.34 / 9.34	-0.266 / 0.266
B-tag(70) XTR	0.107 / -0.107	0.814 / -0.814	0.0572 / -0.0572
B-tag(70) XTR CHRM	0.0659 / -0.0659	0 / 0	0.0883 / -0.0883
Pile-up	-0.388 / 0.388	-10.3 / 10.3	-1.23 / 1.23
Jet-vertex-tagger	0.166 / -0.166	0.0974 / -0.0974	-0.11 / 0.11
non-$t\bar{t}$ cross-section	8.6 / -8.6	0 / 0	0 / 0
Luminosity	2.1 / -2.1	2.1 / -2.1	2.1 / -2.1
Energy scale	-0.616 / 0.616	0 / 0	-0.0417 / 0.0417
Energy resolution	-0.631 / 0.631	0 / 0	0.0518 / -0.0518
t-channel radiation	0.427 / -0.427	0 / 0	0 / 0
t-channel generator	7.31 / -7.31	0 / 0	0 / 0
t-channel parton shower	-3.62 / 3.62	0 / 0	0 / 0
Wt-channel DS	-4.54 / 4.54	0 / 0	0 / 0
$t\bar{t}$ cross-section	0 / 0	0 / 0	5.58 / -6.11
$t\bar{t}$ radiation	0 / 0	0 / 0	1.88 / -1.88
$t\bar{t}$ generator	0 / 0	0 / 0	-15.6 / 15.6
$t\bar{t}$ parton shower	0 / 0	0 / 0	-1.02 / 1.02
$t\bar{t}$ PDF variation	0 / 0	0 / 0	1.04 / -1.04

Table 6.12: Relative variations (up/down) on the background event yields in the TCR. The rate variations for the non-resonant signal model with $m(v_{\text{met}}) = 1000$ GeV are also shown. They combine the electron and muon channels, and are quoted in per cent.

	non-$t\bar{t}$	Non resonant, $m(v_{met}) = 1000$ GeV	$t\bar{t}$
Electron SF ID	0.25 / -0.25	0.233 / -0.233	0.284 / -0.284
Electron SF reco	0.0397 / -0.0397	0.0484 / -0.0484	0.052 / -0.052
Electron SF isol.	0.0454 / -0.0454	0.0694 / -0.0694	0.0531 / -0.0531
Electron SF trigger.	0.111 / -0.111	0.119 / -0.119	0.117 / -0.117
Muon ID	0.138 / -0.138	0.346 / -0.346	0.00214 / -0.00214
Muon MS	-0.0295 / 0.0295	0.295 / -0.295	-0.0089 / 0.0089
Muon sagitta resbias	0 / 0	0 / 0	0 / 0
Muon sagitta rho	-6.9e-06 / 6.9e-06	0 / 0	0 / 0
Muon scale	-0.153 / 0.153	0.0624 / -0.0624	0.00233 / -0.00233
Muon SF ID	0.359 / -0.359	0.355 / -0.355	0.331 / -0.331
Muon SF isol.	0.108 / -0.108	0.11 / -0.11	0.101 / -0.101
Muon SF isol. stat.	0.00713 / -0.00713	0.00703 / -0.00703	0.00694 / -0.00694
Muon SF ID. stat.	0.0956 / -0.0956	0.0984 / -0.0984	0.0914 / -0.0914
Muon SF ttva	0.0219 / -0.0219	0.0343 / -0.0343	0.0304 / -0.0304
Muon SF ttva stat.	0.0525 / -0.0525	0.0415 / -0.0415	0.0383 / -0.0383
Muon SF low p_T	1.38e-05 / -1.38e-05	0 / 0	0 / 0
Muon SF low p_T stat.	-0.267 / 0.267	0 / 0	0 / 0
Muon SF trigger	-0.0573 / 0.0573	0.52 / -0.52	0.473 / -0.473
Muon SF trigger stat.	2.07 / -2.07	0.3 / -0.3	0.274 / -0.274
E_T^{miss} scale	-1.34 / 1.34	0.843 / -0.843	0.312 / -0.312
E_T^{miss} resolution perp.	-7.14 / 7.14	3.07 / -3.07	0.0056 / -0.0056
E_T^{miss} resolution para.	-6.41 / 6.41	0.778 / -0.778	0.482 / -0.482
JES punchthrough (AF)	0 / 0	0 / 0	0 / 0
AFII non closure	0 / 0	0.385 / -0.385	0 / 0
Jet Energy Resolution	-5.62 / 5.62	-6.61 / 6.61	-2.15 / 2.15
JES single part. high p_T	1.38e-05 / -1.38e-05	0 / 0	0 / 0
JES pile-up rho topo.	3.22 / -3.22	-1.92 / 1.92	-6.38 / 6.38
JES pile-up p_T term	-0.0875 / 0.0875	-0.31 / 0.31	-0.669 / 0.669
JES pile-up offset npv	1.6 / -1.6	0.196 / -0.196	-0.929 / 0.929
JES pile-up offset mu	0.86 / -0.86	1.13 / -1.13	0.594 / -0.594
JES flavor response	-1.54 / 1.54	1.61 / -1.61	2.48 / -2.48
JES flavor composition	3.68 / -3.68	-4.24 / 4.24	-8.07 / 8.07
JES EIC total stat.	0.626 / -0.626	-0.972 / 0.972	-1.19 / 1.19
JES EIC total non-closure	-1.16 / 1.16	0.00407 / -0.00407	-0.364 / 0.364
JES EIC total modelling	0.55 / -0.55	-1.48 / 1.48	-2.82 / 2.82
JES Eff. NP 8	0.122 / -0.122	-0.0634 / 0.0634	-0.108 / 0.108
JES Eff. NP 7	0.0998 / -0.0998	-0.125 / 0.125	-0.0455 / 0.0455
JES Eff. NP 6	0.141 / -0.141	-0.215 / 0.215	-0.263 / 0.263
JES Eff. NP 5	-0.208 / 0.208	0.208 / -0.208	0.23 / -0.23
JES Eff. NP 4	0.192 / -0.192	-0.129 / 0.129	0.0135 / -0.0135
JES Eff. NP 3	-0.158 / 0.158	0.0599 / -0.0599	-0.197 / 0.197
JES Eff. NP 2	-0.437 / 0.437	0.47 / -0.47	1.03 / -1.03
JES Eff. NP 1	2.13 / -2.13	-1.96 / 1.96	-4.07 / 4.07
B-jet energy scale	0.524 / -0.524	-0.266 / 0.266	-0.901 / 0.901
B-tag(70) eff. b EV 1	-1.22 / 1.22	-2.81 / 2.81	-2.6 / 2.6
B-tag(70) eff. b EV 2	-1.42 / 1.42	-3.85 / 3.85	-3.84 / 3.84
B-tag(70) eff. b EV 3	-1.17 / 1.17	-3.08 / 3.08	-3.17 / 3.17
B-tag(70) eff. b EV 4	-1.22 / 1.22	-3.07 / 3.07	-3.06 / 3.06
B-tag(70) eff. b EV 5	-1.22 / 1.22	-3.11 / 3.11	-3.11 / 3.11
B-tag(70) eff. b EV 6	-1.22 / 1.22	-3.11 / 3.11	-3.11 / 3.11
B-tag(70) eff. c EV 1	1.94 / -1.94	0.0707 / -0.0707	0.0266 / -0.0266
B-tag(70) eff. c EV 2	1.19 / -1.19	0.0525 / -0.0525	-0.0754 / 0.0754
B-tag(70) eff. c EV 3	1.96 / -1.96	0.0539 / -0.0539	-0.0771 / 0.0771
B-tag(70) eff. l. EV 1	-7.78 / 7.78	-0.304 / 0.304	-0.047 / 0.047
B-tag(70) eff. l. EV 2	-4.82 / 4.82	-0.322 / 0.322	-0.0479 / 0.0479
B-tag(70) eff. l. EV 3	-4.3 / 4.3	-0.194 / 0.194	-0.0346 / 0.0346
B-tag(70) eff. l. EV 4	-4.4 / 4.4	-0.182 / 0.182	-0.0472 / 0.0472
B-tag(70) eff. l. EV 5	-4.34 / 4.34	-0.185 / 0.185	-0.0479 / 0.0479
B-tag(70) eff. l. EV 6	-5.09 / 5.09	-0.173 / 0.173	-0.0533 / 0.0533
B-tag(70) eff. l. EV 7	-4.83 / 4.83	-0.174 / 0.174	-0.0529 / 0.0529
B-tag(70) eff. l. EV 8	-4.98 / 4.98	-0.179 / 0.179	-0.0504 / 0.0504
B-tag(70) eff. l. EV 9	-4.61 / 4.61	-0.208 / 0.208	-0.0498 / 0.0498
B-tag(70) eff. l. EV 10	-4.77 / 4.77	-0.191 / 0.191	-0.052 / 0.052
B-tag(70) eff. l. EV 11	-4.86 / 4.86	-0.193 / 0.193	-0.0511 / 0.0511
B-tag(70) eff. l. EV 12	-4.74 / 4.74	-0.182 / 0.182	-0.0514 / 0.0514
B-tag(70) eff. l. EV 13	-4.8 / 4.8	-0.172 / 0.172	-0.0514 / 0.0514
B-tag(70) eff. l. EV 14	-4.83 / 4.83	-0.171 / 0.171	-0.0512 / 0.0512
B-tag(70) eff. l. EV 15	-4.82 / 4.82	-0.174 / 0.174	-0.0513 / 0.0513
B-tag(70) eff. l. EV 16	-4.81 / 4.81	-0.179 / 0.179	-0.0513 / 0.0513
B-tag(70) XTR	0.0523 / -0.0523	0.0141 / -0.0141	0.0204 / -0.0204
B-tag(70) XTR CHRM	0.00331 / -0.00331	0 / 0	0.0183 / -0.0183
Pile-up	1.73 / -1.73	3.46 / -3.46	-1.42 / 1.42
Jet-vertex-tagger	-0.0121 / 0.0121	-0.0655 / 0.0655	-0.284 / 0.284
non-$t\bar{t}$ cross-section	7.21 / -7.21	0 / 0	0 / 0
Luminosity	2.1 / -2.1	2.1 / -2.1	2.1 / -2.1
Energy scale	0.208 / -0.208	0.00949 / -0.00949	-0.0995 / 0.0995
Energy resolution	0.0936 / -0.0936	0.0545 / -0.0545	0.013 / -0.013
t-channel radiation	0.106 / -0.106	0 / 0	0 / 0
t-channel generator	-0.0511 / 0.0511	0 / 0	0 / 0
t-channel parton shower	0.35 / -0.35	0 / 0	0 / 0
Wt-channel DS	-0.895 / 0.895	0 / 0	0 / 0
$t\bar{t}$ cross-section	0 / 0	0 / 0	5.58 / -6.11
$t\bar{t}$ radiation	0 / 0	0 / 0	0.685 / -0.685
$t\bar{t}$ generator	0 / 0	0 / 0	-11.7 / 11.7
$t\bar{t}$ parton shower	0 / 0	0 / 0	1.98 / -1.98
$t\bar{t}$ PDF variation	0 / 0	0 / 0	0.977 / -0.977

Table 6.13: Relative variations (up/down) on the background event yields in WCR. The rate variations for the non-resonant signal model with $m(v_{\text{met}}) = 1000$ GeV are also shown. They combine the electron and muon channels, and are quoted in per cent.

processes are listed in Tables 6.14 and 6.16. The relative systematic uncertainties for background processes in the three control regions used to constrain the $t\bar{t}$, multijet and V+jets background rates are listed in Tables 6.19, 6.20 and 6.21, respectively. The sample properties for the DM processes in the signal region without the additional forward jet requirement are listed in Tables 6.17 and 6.18.

	$t\bar{t}$	Single Top	W+Jets	Z+jets	Other
Trigger turn on uncertainty	+2.00/-2.00	+2.00/-2.00	+2.00/-2.00	+2.00/-2.00	+2.00/-2.00
$t\bar{t}$ hard scatter gen.	+8.12/–	–	–	–	–
$t\bar{t}$ fragm./hadr. model	–/-15.04	–	–	–	–
$t\bar{t}$ add. radiation	+1.89/-1.89	–	–	–	–
$t\bar{t}$ PDF	+4.99/-4.99	–	–	–	–
$t\bar{t}$ cross-section	+5.58/-6.11	–	–	–	–
$t\bar{t}$+W cross-section	–	–	–	–	+0.91/-0.82
$t\bar{t}$+Z cross-section	–	–	–	–	–/-8.90
$t\bar{t}$+ll cross-section	–	–	–	–	+0.08/-0.10
Single top cross-section	–	+3.62/-3.15	–	–	–
Di-bosons cross-section	–	–	–	–	+0.73/-0.73
Z+jets generator	–	–	–	–/-0.17	–
Z+jets heavy flavor	–	–	–	+27.44/-27.44	–
Z+jets internal scale	–	–	–	+6.02/-6.02	–
Z+jets PDF	–	–	–	+6.56/-6.56	–
W+jets generator	–	–	+0.86/-0.86	–	–
W+jets heavy flavor	–	–	+23.20/-23.20	–	–
W+jets internal scale	–	–	+5.22/-5.22	–	–
W+jets PDF	–	–	+8.58/-8.58	–	–
V+jets cross-section	–	–	+5.00/-5.00	+5.00/-5.00	–
Energy resolution	+0.01/-0.06	~ 0	+0.07/–	–	~ 0/-0.02
Energy scale	+0.03/-0.02	–/-0.06	+0.06/-0.02	–	+0.02/-0.01
Jet energy resolution	+4.15/–	+4.89/–	+4.65/–	+4.55/–	+5.34/–
B-jet energy scale	+0.06/-0.38	–/-0.74	–/-0.12	+0.04/~ 0	+0.16/–
JES Eff. NP 1	+2.04/-2.56	+2.66/-2.57	+1.86/-2.03	+2.70/-2.55	+2.34/-3.10
JES Eff. NP 2	+0.08/-0.04	+0.29/-0.25	+0.13/-0.28	+0.29/-0.34	+0.62/-1.18
JES Eff. NP 3	+0.15/-0.40	+0.22/-0.06	+0.18/-0.25	+0.08/-0.09	+0.04/-0.06
JES Eff. NP 4	+0.09/-0.11	+0.15/-0.11	+0.04/-0.15	+0.05/-0.14	+0.14/-0.13
JES Eff. NP 5	+0.13/-0.27	+0.15/-0.13	–/-0.27	+0.04/-0.03	+0.04/-0.19
JES Eff. NP 6	+0.01/-0.23	+0.14/–	+0.02/-0.14	+0.07/-0.14	+0.11/-0.10
JES Eff. NP 7	+0.05/-0.32	+0.21/-0.12	–/-0.15	+0.06/-0.15	+0.17/-0.16
JES Eff. NP 8	+0.01/-0.18	+0.08/-0.03	–/-0.15	+0.02/-0.03	~ 0
JES EIC modeling	+3.24/-3.73	+3.54/-3.91	+2.56/-2.82	+3.96/-4.01	+3.57/-4.67
JES EIC non-closure	+1.52/-2.20	+1.27/-2.26	+1.25/-1.98	+1.85/-1.76	+1.92/-2.65
JES EIC total stat.	+0.60/-0.69	+0.73/-0.79	+0.18/-0.73	+0.87/-0.71	+0.91/-1.40
JES flavor composition	+4.56/-5.15	+4.27/-3.89	+4.09/-4.24	+5.78/-5.89	+4.74/-6.23
JES flavor response	+1.34/-2.07	+1.68/-1.60	+1.54/-1.13	+1.94/-1.96	+1.96/-2.17
JES pile-up offset mu	+0.49/-0.51	–/-0.90	+0.75/-1.13	+0.74/-0.48	+0.41/-1.70
JES pile-up offset npv	+0.45/-0.65	+0.70/-1.49	+0.42/-0.51	+0.92/-1.02	+1.05/-1.16
JES pile-up p_T term	–/-0.45	+0.05/-0.19	+0.06/-0.17	+0.14/-0.20	+0.26/-0.32
JES pile-up rho topo.	+1.94/-2.71	+1.30/-2.50	+2.19/-2.59	+3.32/-3.35	+2.89/-3.46
JES punchthrough	+0.03/–	+0.06/–	+0.01/–	~ 0	~ 0
FatJet r-track baseline	+8.90/-9.12	+11.30/-7.71	+7.63/-8.82	+8.53/-7.89	+6.69/-8.36
FatJet r-track modeling	+3.19/-3.06	+3.95/-2.79	+3.50/-3.23	+3.55/-3.64	+2.49/-2.58
FatJet r-track total stat.	+0.41/-0.32	+0.71/-0.16	+0.47/-0.22	+0.32/-0.40	+0.26/-0.41
FatJet r-track tracking	+2.67/-2.26	+3.57/-1.93	+2.29/-2.31	+2.69/-2.49	+1.87/-1.68
FatJet p_T resolution	+10.40/-10.40	+10.71/-10.71	+4.60/-4.60	+6.93/-6.93	+7.93/-7.93
FatJet mass resolution	+3.95/-3.95	+5.26/-5.26	+8.45/-8.45	+8.83/-8.83	+5.14/-5.14
FatJet τ_{32}^{wta} resolution	+16.80/16.80	+18.73/-18.73	+23.42/-23.42	-0.23.20/+23.20	-19.57/+19.57
MET resolution para.	–/-0.71	–/-0.87	–/-0.10	–/-0.20	–/-0.08
MET resolution perp.	–/-0.73	–/-0.77	–/-0.23	–/-0.43	–/-0.10
MET scale	+0.50/-0.80	+1.07/-0.69	+0.59/-0.08	+0.12/-0.18	+0.16/–
B-tag(70) XTR	+0.02/-0.02	~ 0	+0.20/-0.20	+0.26/-0.26	+0.20/-0.20
B-tag(70) XTR charm	+0.14/-0.14	+0.15/-0.15	+0.16/-0.16	~ 0	+0.12/-0.12
B-tag(70) eff. b EV 1	+3.03/-2.98	+1.99/-1.98	+1.45/-1.43	+1.32/-1.31	+2.48/-2.47
B-tag(70) eff. b EV 2	+1.17/-1.18	+1.12/-1.15	+0.43/-0.44	+0.67/-0.69	+0.07/-0.11
B-tag(70) eff. b EV 3	~ 0	+0.06/-0.06	+0.03/-0.03	~ 0	+0.13/-0.13
B-tag(70) eff. b EV 4	+0.17/-0.17	+0.18/-0.18	+0.05/-0.05	+0.07/-0.07	+0.02/-0.02
B-tag(70) eff. b EV 5	+0.02/-0.02	+0.02/-0.02	+0.02/-0.02	+0.02/-0.02	+0.02/-0.02
B-tag(70) eff. c EV 1	+0.31/-0.32	+0.33/-0.33	+0.87/-0.87	+0.61/-0.61	+1.06/-1.06
B-tag(70) eff. c EV 2	+0.21/-0.21	+0.05/-0.04	+4.74/-4.77	+4.35/-4.39	+4.98/-5.07
B-tag(70) eff. c EV 3	+0.04/-0.04	+0.08/-0.08	+0.18/-0.17	+0.20/-0.20	+0.43/-0.43
B-tag(70) eff. c EV 4	+0.02/-0.02	+0.02/-0.02	+0.19/-0.19	+0.22/-0.22	+0.30/-0.30
B-tag(70) eff. l EV 1	+1.78/-1.75	+1.61/-1.61	+8.05/-8.33	+5.87/-6.29	+2.01/-2.13
B-tag(70) eff. l EV 2	+0.90/-0.90	+0.80/-0.80	+0.10/-0.10	+0.07/-0.08	+0.43/-0.43
B-tag(70) eff. l EV 3	+0.09/-0.09	+0.12/-0.12	+1.12/-1.13	+0.67/-0.67	+0.37/-0.38
B-tag(70) eff. l EV 4	+0.62/-0.62	+0.59/-0.58	+1.88/-1.86	+1.56/-1.55	+0.92/-0.91
B-tag(70) eff. l EV 5	+0.04/-0.04	+0.03/-0.03	+0.03/-0.03	+0.02/-0.02	+0.03/-0.03
B-tag(70) eff. l EV 6	+0.09/-0.09	+0.12/-0.12	+0.64/-0.63	+0.49/-0.49	+0.33/-0.33
B-tag(70) eff. l EV 7	+0.04/-0.04	+0.07/-0.07	+0.08/-0.08	+0.06/-0.07	+0.07/-0.07
B-tag(70) eff. l EV 8	~ 0	+0.03/-0.03	+0.36/-0.36	+0.31/-0.31	+0.04/-0.04
B-tag(70) eff. l EV 9	+0.06/-0.06	+0.07/-0.07	+0.31/-0.31	+0.30/-0.30	+0.17/-0.17
B-tag(70) eff. l EV 10	+0.04/-0.04	+0.04/-0.04	+0.17/-0.17	+0.20/-0.20	+0.03/-0.03
B-tag(70) eff. l EV 11	+0.03/-0.03	+0.03/-0.03	+0.07/-0.07	~ 0	+0.01/-0.01
B-tag(70) eff. l EV 12	+0.02/-0.02	+0.02/-0.02	+0.03/-0.03	~ 0	+0.02/-0.02
B-tag(70) eff. l EV 13	+0.01/-0.01	~ 0	+0.03/-0.03	~ 0	~ 0
B-tag(70) eff. l EV 14	+0.01/-0.01	~ 0	~ 0	~ 0	~ 0
B-tag(70) eff. l EV 15	~ 0	~ 0	~ 0	~ 0	~ 0
B-tag(70) eff. l EV 16	~ 0	~ 0	~ 0	~ 0	~ 0
B-tag(70) eff. l EV 17	–	–	–	–	–
Pile-up	+1.16/-1.30	+2.79/-2.22	+5.28/-2.90	+4.54/-3.61	+4.20/-4.20
Jet-vertex-tagger	+0.18/-0.24	+0.16/-0.21	+0.15/-0.20	+0.17/-0.21	+0.26/-0.29
Luminosity	+3.20/-3.20	+3.20/-3.20	+3.20/-3.20	+3.20/-3.20	+3.20/-3.20
Lepton veto uncertainty	+3.18/-3.18	+4.33/-4.33	+2.89/-2.89	+0.22/-0.22	+2.45/-2.45
Statistical	+1.42/ − 1.42	+3.12/ − 3.12	+2.62/ − 2.62	+3.43/ − 3.43	+4.10/ − 4.10

Table 6.14: Relative variations (up/down) on the background event yields in the signal region with additional forward jet requirement of the hadronic channel in percent.

	WTZtLH(900)	WTZtLH(1200)	WTZtLH(1600)	ZTZtLH(900)	ZTZtLH(1200)	ZTZtLH(1600)
Trigger turn on uncertainty	+2.00/-2.00	+1.98/-2.02	+1.92/-2.08	+2.00/-2.00	+1.97/-2.03	+1.86/-2.13
Energy resolution	∼ 0	–/-0.03	–/-0.18	–/-0.02	–/-0.09	–/-0.27
Energy scale	–/-0.02	–/-0.05	–/-0.16	+0.02/–	–/-0.07	–/-0.27
Jet energy resolution	+0.83/–	+0.62/-0.02	+0.39/-0.08	–/-1.04	–/-0.15	+1.04/-0.14
B-jet energy scale	–/-0.03	+0.05/-0.06	∼ 0/-0.10	+0.03/–	+0.14/∼ 0	–/-0.21
JES Eff. NP 1	+0.88/-0.68	+0.62/-0.59	+0.63/-0.76	+0.33/-0.78	+0.68/-0.49	+0.26/-0.06
JES Eff. NP 2	+0.38/-0.34	+0.16/-0.17	+0.17/-0.43	–/-0.35	+0.13/–	∼ 0/-0.18
JES Eff. NP 3	+0.07/∼ 0	+0.03/–	–/-0.17	–/-0.18	+0.12/∼ 0	–/-0.32
JES Eff. NP 4	+0.03/∼ 0	+0.06/-0.03	–/-0.10	–/-0.14	+0.02/-0.02	–/-0.39
JES Eff. NP 5	+0.01/–	+0.02/-0.03	–/-0.10	–/-0.18	+0.06/-0.07	–/-0.27
JES Eff. NP 6	+0.11/-0.05	+0.08/-0.04	–/-0.20	–/-0.14	–/-0.12	–/-0.19
JES Eff. NP 7	+0.13/-0.06	+0.09/∼ 0	–/-0.20	–/-0.15	+0.04/-0.07	–/-0.29
JES Eff. NP 8	+0.02/∼ 0	∼ 0	–/-0.13	–/-0.08	–/-0.04	–/-0.32
JES EIC modeling	+1.20/-1.32	+1.34/-0.93	+1.25/-1.39	+0.76/-1.30	+1.02/-1.25	+1.03/-0.57
JES EIC non-closure	+0.72/-0.50	+0.67/-0.48	+0.53/-0.71	+0.08/-0.40	+0.50/-0.47	+0.43/-0.48
JES EIC total stat.	+0.44/-0.36	+0.28/-0.27	+0.33/-0.44	–/-0.27	+0.20/-0.09	+0.01/-0.06
JES flavor composition	+1.40/-1.26	+1.32/-0.93	+1.09/-1.18	+0.56/-1.10	+1.04/-1.18	+0.52/-0.56
JES flavor response	+0.55/-0.36	+0.17/-0.33	+0.56/-0.61	+0.03/-0.09	+0.36/-0.25	+0.09/-0.03
JES pile-up offset mu	+0.27/-0.31	+0.32/-0.22	+0.34/-0.49	+0.35/-0.56	+0.30/-0.27	+0.25/-0.13
JES pile-up offset npv	+0.38/-0.03	–/-0.32	+0.13/-0.33	∼ 0/-0.13	+0.16/-0.09	–/-0.51
JES pile-up p_T term	+0.16/-0.04	+0.09/-0.12	+0.02/-0.16	+0.09/-0.20	+0.22/-0.11	+0.08/-0.19
JES pile-up rho topo.	+1.04/-0.89	+0.73/-0.63	+0.71/-0.75	+0.43/-0.57	+0.72/-0.49	+0.36/-0.29
JES punchthrough	+0.01/∼ 0	–/-0.04	–/-0.16	∼ 0	–/-0.05	–/-0.25
FatJet r-track baseline	+2.15/-2.74	+1.04/-0.80	+0.45/-0.96	+0.72/-2.26	+0.53/-0.98	+0.83/–
FatJet r-track modeling	+1.22/-1.26	+0.79/-0.84	+0.56/-0.81	+0.66/-0.72	+0.51/-0.55	+0.38/-0.11
FatJet r-track total stat.	+0.16/-0.05	–/-0.02	–/-0.16	+0.27/∼ 0	–/-0.13	+0.03/-0.08
FatJet r-track tracking	+0.55/-0.84	+0.21/-0.28	+0.07/-0.46	+0.42/-0.78	+0.28/-0.37	+0.13/–
FatJet p_T resolution	+0.49/–	–/-0.52	–/-0.68	+1.50/–	–/-0.23	+0.47/-0.14
FatJet mass resolution	+3.45/–	+3.06/-0.02	+2.83/-0.08	+2.08/–	+2.36/-0.03	+2.56/-0.14
FatJet τ_{32}^{wta} resolution	–/-16.71	–/-16.63	–/-18.01	–/-11.74	–/-13.46	–/-13.52
MET resolution para.	–/-0.03	–/-0.05	–/-0.15	–/-0.06	+0.04/-0.03	–/-0.19
MET resolution perp.	+0.05/–	–/-0.02	–/-0.19	–/-0.12	–/-0.13	–/-0.19
MET scale	+0.04/∼ 0	∼ 0/-0.02	–/-0.22	+0.02/-0.30	+0.06/-0.08	–/-0.14
B-tag(70) XTR	+0.02/-0.02	+0.11/-0.15	–/-0.17	+0.07/-0.07	+0.14/-0.20	+0.31/-0.58
B-tag(70) XTR charm	+0.03/-0.03	+0.01/-0.06	–/-0.16	+0.10/-0.10	+0.05/-0.11	–/-0.27
B-tag(70) eff. b EV 1	+1.06/-1.05	+0.66/-0.72	+0.69/-0.87	+4.08/-4.12	+4.13/-4.22	+4.02/-4.32
B-tag(70) eff. b EV 2	+1.29/-1.33	+1.39/-1.49	+0.97/-1.21	+0.67/-0.75	+1.17/-1.35	+1.40/-1.83
B-tag(70) eff. b EV 3	∼ 0	+0.11/-0.15	+0.06/-0.22	+0.38/-0.38	+0.32/-0.38	+0.13/-0.40
B-tag(70) eff. b EV 4	+0.09/-0.09	–/-0.05	–/-0.16	+0.04/-0.04	–/-0.05	–/-0.27
B-tag(70) eff. b EV 5	∼ 0	–/-0.05	–/-0.16	+0.03/-0.03	–/-0.05	–/-0.27
B-tag(70) eff. c EV 1	+0.34/-0.34	+0.24/-0.28	+0.07/-0.23	+0.69/-0.68	+0.59/-0.64	+0.32/-0.60
B-tag(70) eff. c EV 2	+0.79/-0.79	+1.16/-1.20	+1.15/-1.33	+0.87/-0.85	+1.14/-1.20	+1.45/-1.73
B-tag(70) eff. c EV 3	+0.01/-0.01	+0.10/-0.14	+0.09/-0.25	∼ 0	+0.03/-0.08	+0.07/-0.34
B-tag(70) eff. c EV 4	+0.04/-0.04	+0.07/-0.12	+0.04/-0.21	+0.06/-0.06	+0.06/-0.11	–/-0.27
B-tag(70) eff. l EV 1	+1.36/-1.34	+1.44/-1.47	+1.70/-1.80	+2.29/-2.12	+2.03/-2.07	+2.16/-2.38
B-tag(70) eff. l EV 2	+0.63/-0.62	+0.72/-0.76	+0.63/-0.79	+1.13/-1.11	+1.05/-1.09	+0.90/-1.16
B-tag(70) eff. l EV 3	+0.11/-0.10	+0.10/-0.15	+0.07/-0.24	+0.17/-0.17	+0.19/-0.24	+0.05/-0.32
B-tag(70) eff. l EV 4	+0.43/-0.43	+0.54/-0.58	+0.38/-0.55	+0.83/-0.82	+0.84/-0.89	+0.59/-0.85
B-tag(70) eff. l EV 5	+0.03/-0.03	∼ 0/-0.05	–/-0.16	+0.05/-0.05	+0.02/-0.07	–/-0.27
B-tag(70) eff. l EV 6	+0.07/-0.07	+0.09/-0.13	–/-0.16	+0.12/-0.12	+0.12/-0.17	∼ 0/-0.27
B-tag(70) eff. l EV 7	+0.04/-0.04	+0.04/-0.09	–/-0.16	+0.05/-0.05	+0.04/-0.09	–/-0.27
B-tag(70) eff. l EV 8	∼ 0	∼ 0/-0.05	–/-0.16	+0.03/-0.03	–/-0.05	–/-0.27
B-tag(70) eff. l EV 9	+0.05/-0.05	+0.04/-0.08	–/-0.16	+0.10/-0.10	+0.05/-0.10	–/-0.27
B-tag(70) eff. l EV 10	+0.05/-0.05	+0.02/-0.07	–/-0.16	+0.10/-0.10	+0.06/-0.12	–/-0.27
B-tag(70) eff. l EV 11	+0.03/-0.03	+0.01/-0.06	–/-0.16	+0.04/-0.04	∼ 0/-0.06	–/-0.27
B-tag(70) eff. l EV 12	+0.04/-0.04	∼ 0/-0.05	–/-0.16	+0.05/-0.05	+0.02/-0.07	–/-0.27
B-tag(70) eff. l EV 13	∼ 0	–/-0.05	–/-0.16	+0.01/-0.01	–/-0.05	–/-0.27
B-tag(70) eff. l EV 14	+0.02/-0.02	–/-0.05	–/-0.16	+0.02/-0.02	–/-0.05	–/-0.27
B-tag(70) eff. l EV 15	∼ 0	–/-0.05	–/-0.16	∼ 0	–/-0.05	–/-0.27
B-tag(70) eff. l EV 16	∼ 0	–/-0.05	–/-0.16	∼ 0	–/-0.05	–/-0.27
B-tag(70) eff. l EV 17	–	–/-0.05	–/-0.16	–	–/-0.05	–/-0.27
Pile-up	+0.77/-0.23	+0.24/-0.89	–/-0.47	+0.98/-1.84	+0.70/-0.38	+0.20/-1.61
Jet-vertex-tagger	+0.12/-0.16	+0.10/-0.18	–/-0.21	+0.17/-0.23	+0.19/-0.30	–/-0.34
Luminosity	+3.20/-3.20	+3.18/-3.22	+3.12/-3.28	+3.20/-3.20	+3.17/-3.23	+3.06/-3.33
Lepton veto uncertainty	+0.10/-0.10	+0.10/-0.14	+0.04/-0.21	+0.23/-0.21	+0.25/-0.27	+0.14/-0.40
Statistical	+1.43/ − 1.43	+1.42/ − 1.42	+1.41/ − 1.41	+1.79/ − 1.79	+2.03/ − 2.03	+2.09/ − 2.09

Table 6.15: Relative variations (up/down) on the VLT signal event yields in the signal region with additional forward jet requirement of the hadronic channel in percent.

	$t\bar{t}$	Single Top	W+Jets	Z+jets	Other
Trigger turn on uncertainty	+2.00/-2.00	+2.00/-2.00	+2.00/-2.00	+2.00/-2.00	+2.00/-2.00
$t\bar{t}$ hard scatter gen.	–/-2.07	–	–	–	–
$t\bar{t}$ fragm./hadr. model	–/-6.86	–	–	–	–
$t\bar{t}$ add. radiation	+4.87/-4.87	–	–	–	–
$t\bar{t}$ PDF	+9.92/-9.92	–	–	–	–
$t\bar{t}$ cross-section	+5.58/-6.11	–	–	–	–
$t\bar{t}$+W cross-section	–	–	–	–	+0.87/-0.78
$t\bar{t}$+Z cross-section	–	–	–	–	–/-6.63
$t\bar{t}$+ll cross-section	–	–	–	–	+0.07/-0.08
Single top cross-section	–	+3.62/-3.15	–	–	–
Di-bosons cross-section	–	–	–	–	+0.84/-0.84
Z+jets generator	–	–	–	+6.12/–	–
Z+jets heavy flavor	–	–	–	+27.80/-27.80	–
Z+jets internal scale	–	–	–	+8.65/-8.65	–
Z+jets PDF	–	–	–	+7.30/-7.30	–
W+jets generator	–	–	+2.37/-2.37	–	–
W+jets heavy flavor	–	–	+23.30/-23.30	–	–
W+jets internal scale	–	–	+8.32/-8.32	–	–
W+jets PDF	–	–	+7.14/-7.14	–	–
V+jets cross-section	–	–	+5.00/-5.00	+5.00/-5.00	–
Energy resolution	∼ 0/-0.04	∼ 0/-0.02	+0.04/-0.01	∼ 0	–/-0.04
Energy scale	+0.02/-0.02	–/-0.04	+0.07/-0.02	–	∼ 0/-0.02
Jet energy resolution	–/-0.15	+2.69/–	–/-0.27	–/-0.45	+0.29/–
B-jet energy scale	+0.33/-0.36	+0.19/-0.34	–/-0.10	+0.02/-0.04	+0.08/-0.04
JES Eff. NP 1	+0.28/-0.29	+0.09/–	+0.19/-0.07	–/-0.12	+0.03/-0.08
JES Eff. NP 2	+0.40/-0.41	+0.38/-0.18	+0.18/-0.24	+0.14/-0.12	+0.03/-0.10
JES Eff. NP 3	+0.19/-0.23	+0.22/-0.15	+0.04/-0.14	+0.10/-0.06	+0.01/-0.03
JES Eff. NP 4	+0.05/-0.12	+0.08/-0.02	+0.08/-0.19	∼ 0/-0.02	+0.07/-0.05
JES Eff. NP 5	+0.15/-0.24	+0.21/-0.10	+0.02/-0.18	+0.06/-0.04	+0.03/-0.10
JES Eff. NP 6	–/-0.04	+0.05/-0.02	∼ 0/-0.04	+0.01/∼ 0	∼ 0
JES Eff. NP 7	+0.02/-0.11	+0.10/–	–/-0.09	+0.01/∼ 0	+0.02/-0.03
JES Eff. NP 8	–/-0.11	+0.02/-0.02	–/-0.12	+0.02/-0.01	∼ 0
JES EIC modeling	+0.24/-0.32	+0.27/-0.13	+0.31/-0.13	∼ 0/-0.12	+0.10/-0.03
JES EIC non-closure	–/-0.14	+0.05/-0.01	∼ 0/-0.11	∼ 0	+0.05/-0.15
JES EIC total stat.	+0.11/-0.22	+0.36/–	+0.04/-0.18	+0.07/-0.04	+0.08/-0.06
JES flavor composition	+0.60/-0.91	+1.19/-0.77	+0.95/-0.36	–/-0.56	+0.65/-0.70
JES flavor response	+0.11/-0.33	+0.33/-0.21	+0.44/-0.28	–/-0.39	+0.16/-0.08
JES pile-up offset mu	+0.14/-0.05	+0.20/-0.22	+0.11/-0.05	+0.04/-0.02	+0.01/-0.03
JES pile-up offset npv	+0.24/-0.21	–/-0.21	+0.04/-0.11	+0.05/-0.06	+0.11/–
JES pile-up p_T term	–/-0.28	–/-0.14	+0.07/-0.18	–/-0.06	+0.15/-0.14
JES pile-up rho topo.	+0.77/-0.83	+0.69/-0.82	+0.51/-0.28	–/-0.44	+0.13/-0.29
JES punchthrough	∼ 0	+0.02/–	+0.01/–	∼ 0	∼ 0
FatJet r-track baseline	+9.81/-9.76	+10.58/-8.93	+9.20/-9.19	+8.16/-8.49	+7.59/-8.18
FatJet r-track modeling	+3.45/-3.30	+3.59/-3.40	+3.73/-3.63	+3.48/-3.64	+3.52/-2.91
FatJet r-track total stat.	+0.36/-0.33	+0.49/-0.24	+0.56/-0.41	+0.34/-0.43	+0.24/-0.38
FatJet r-track tracking	+2.91/-2.75	+2.93/-2.62	+2.75/-2.63	+2.63/-2.56	+2.54/-2.22
FatJet p_T resolution	+3.94/-3.94	+5.18/-5.18	+8.66/-8.66	+8.28/-8.28	+6.80/-6.80
FatJet mass resolution	+12.10/-12.10	+11.40/-11.40	+7.22/-7.22	+7.44/-7.44	+7.86/-7.86
FatJet τ_{32}^{wta} resolution	-16.50/+16.50	-18.10/+1.810	-24.10/+24.10	-23.50/+23.50	-20.70/+20.70
MET resolution para.	–/-0.47	–/-0.27	+0.04/–	∼ 0	–/-0.14
MET resolution perp.	–/-0.51	–/-0.35	–/-0.02	–/-0.14	–/-0.12
MET scale	+0.44/-0.51	+0.46/-0.41	+0.39/–	+0.06/-0.03	+0.05/–
B-tag(70) XTR	+0.01/-0.01	∼ 0	+0.21/-0.21	+0.24/-0.24	+0.21/-0.21
B-tag(70) XTR charm	+0.15/-0.15	+0.19/-0.18	+0.05/-0.05	∼ 0	+0.03/-0.03
B-tag(70) eff. b EV 1	+3.31/-3.26	+2.03/-2.03	+1.54/-1.52	+1.29/-1.28	+2.53/-2.52
B-tag(70) eff. b EV 2	+1.10/-1.11	+0.97/-1.00	+0.42/-0.43	+0.65/-0.66	+0.25/-0.30
B-tag(70) eff. b EV 3	+0.04/-0.04	+0.08/-0.08	+0.02/-0.03	+0.03/-0.03	+0.15/-0.16
B-tag(70) eff. b EV 4	+0.17/-0.17	+0.17/-0.17	+0.06/-0.06	+0.07/-0.07	+0.02/-0.02
B-tag(70) eff. b EV 5	+0.02/-0.02	+0.02/-0.02	+0.02/-0.02	+0.01/-0.01	+0.02/-0.02
B-tag(70) eff. c EV 1	+0.31/-0.31	+0.35/-0.35	+0.70/-0.69	+0.62/-0.61	+1.01/-1.01
B-tag(70) eff. c EV 2	+0.19/-0.19	+0.09/-0.08	+4.89/-4.93	+4.12/-4.17	+5.55/-5.66
B-tag(70) eff. c EV 3	∼ 0	+0.09/-0.09	+0.17/-0.17	+0.20/-0.20	+0.45/-0.45
B-tag(70) eff. c EV 4	+0.02/-0.02	∼ 0	+0.19/-0.19	+0.19/-0.19	+0.31/-0.31
B-tag(70) eff. l EV 1	+1.77/-1.74	+1.42/-1.43	+7.59/-7.96	+6.34/-6.68	+2.42/-2.51
B-tag(70) eff. l EV 2	+0.86/-0.85	+0.81/-0.80	∼ 0/-0.01	+0.03/-0.03	+0.35/-0.35
B-tag(70) eff. l EV 3	+0.12/-0.12	+0.09/-0.09	+1.06/-1.07	+0.71/-0.72	+0.22/-0.23
B-tag(70) eff. l EV 4	+0.59/-0.59	+0.61/-0.61	+1.65/-1.63	+1.60/-1.58	+1.08/-1.08
B-tag(70) eff. l EV 5	+0.03/-0.03	+0.03/-0.03	+0.03/-0.03	+0.02/-0.02	+0.03/-0.03
B-tag(70) eff. l EV 6	+0.09/-0.09	+0.10/-0.10	+0.60/-0.60	+0.51/-0.51	+0.31/-0.31
B-tag(70) eff. l EV 7	+0.04/-0.04	+0.05/-0.05	+0.05/-0.05	+0.08/-0.08	∼ 0
B-tag(70) eff. l EV 8	∼ 0	∼ 0	+0.29/-0.29	+0.31/-0.32	+0.14/-0.14
B-tag(70) eff. l EV 9	+0.06/-0.06	+0.04/-0.04	+0.32/-0.32	+0.31/-0.31	+0.21/-0.21
B-tag(70) eff. l EV 10	+0.04/-0.04	+0.06/-0.06	+0.12/-0.12	+0.16/-0.16	+0.08/-0.08
B-tag(70) eff. l EV 11	+0.03/-0.03	+0.03/-0.03	+0.03/-0.03	+0.02/-0.02	+0.01/-0.01
B-tag(70) eff. l EV 12	+0.03/-0.03	+0.03/-0.03	+0.04/-0.04	+0.01/-0.01	∼ 0
B-tag(70) eff. l EV 13	∼ 0	+0.01/-0.01	∼ 0	∼ 0	∼ 0
B-tag(70) eff. l EV 14	+0.02/-0.02	+0.01/-0.01	∼ 0	∼ 0	∼ 0
B-tag(70) eff. l EV 15	∼ 0	∼ 0	∼ 0	∼ 0	∼ 0
B-tag(70) eff. l EV 16	∼ 0	∼ 0	∼ 0	∼ 0	∼ 0
B-tag(70) eff. l EV 17	–	–	∼ 0	∼ 0	–
Pile-up	+0.26/-0.27	+0.28/-0.41	+0.72/-0.74	+0.85/-1.03	+1.68/-1.13
Jet-vertex-tagger	+0.21/-0.28	+0.15/-0.20	+0.11/-0.16	+0.16/-0.19	+0.18/-0.22
Luminosity	+3.20/-3.20	+3.20/-3.20	+3.20/-3.20	+3.20/-3.20	+3.20/-3.20
Lepton veto uncertainty	+0.32/-0.32	+0.43/-0.43	+0.31/-0.31	+0.01/-0.01	+0.25/-0.25
Statistical	$+0.85/-0.85$	$+1.85/-1.85$	$+1.72/-1.72$	$+1.94/-1.94$	$+2.09/-2.09$

Table 6.16: Relative variations (up/down) on the background event yields in the signal region without additional forward jet requirement of the hadronic channel in percent.

	DM res.(m_Φ=4, m_χ=0.01)TeV	DM res.(m_Φ=1, m_χ=0.2)TeV	DM res.(m_Φ=5, m_χ=0.2)TeV	DM nonres.(m_Φ=1, m_χ=0.001)TeV	DM nonres.(m_Φ=1.5, m_χ=0.001)TeV
Trigger turn on uncertainty	+2.00/-2.00	+2.00/-2.00	+2.00/-2.00	+2.00/-2.00	+2.00/-2.00
Energy resolution	–	–	–	–	–
Energy scale	–	–	–	–	–
Jet energy resolution	–/-0.11	–/-0.06	–/-0.07	–/-0.11	–/-0.09
B-jet energy scale	∼ 0	–/-0.03	∼ 0	+0.02/∼ 0	–/-0.04
JES Eff. NP 1	+0.08/-0.08	+0.10/-0.11	–/-0.16	+0.09/–	–/-0.16
JES Eff. NP 2	+0.05/-0.07	–/-0.02	–/-0.04	+0.02/-0.04	–/-0.10
JES Eff. NP 3	+0.01/-0.02	–/-0.01	+0.02/-0.02	–/-0.02	∼ 0
JES Eff. NP 4	+0.03/-0.03	∼ 0	+0.02/-0.02	+0.01/–	∼ 0/-0.03
JES Eff. NP 5	+0.02/-0.02	∼ 0/-0.03	+0.01/∼ 0	+0.02/-0.01	–/-0.03
JES Eff. NP 6	∼ 0	∼ 0	∼ 0	–/-0.01	∼ 0
JES Eff. NP 7	∼ 0/-0.02	∼ 0	∼ 0	–/-0.02	–/-0.02
JES Eff. NP 8	∼ 0/-0.01	–/-0.03	∼ 0	∼ 0	–/-0.02
JES EIC modeling	+0.07/-0.12	+0.11/-0.16	+0.04/-0.09	+0.05/-0.04	∼ 0/-0.17
JES EIC non-closure	+0.03/-0.04	–/-0.04	–/-0.06	+0.06/–	–/-0.12
JES EIC total stat.	+0.03/-0.04	+0.04/-0.02	+0.02/-0.04	+0.02/-0.04	–/-0.09
JES flavor composition	+0.26/-0.35	+0.26/-0.31	+0.16/-0.34	+0.25/-0.26	+0.06/-0.28
JES flavor response	+0.09/-0.15	+0.11/-0.12	+0.03/-0.15	+0.10/-0.03	–/-0.22
JES pile-up offset mu	+0.02/-0.04	+0.02/-0.01	–/-0.04	+0.05/–	–/-0.09
JES pile-up offset npv	+0.04/-0.08	+0.05/-0.03	–/-0.13	+0.07/–	–/-0.15
JES pile-up p_T term	+0.05/-0.04	+0.07/-0.08	+0.03/-0.08	+0.05/∼ 0	–/-0.10
JES pile-up rho topo.	+0.09/-0.20	+0.13/-0.11	+0.06/-0.20	+0.10/-0.03	–/-0.20
JES punchthrough	–	∼ 0	–	–	∼ 0
FatJet r-track baseline	+0.35/-0.30	+1.56/-1.56	+0.69/-0.72	+2.35/-3.03	+2.11/-2.25
FatJet r-track modeling	+0.20/-0.13	+1.01/-0.86	+0.28/-0.31	+1.08/-1.18	+0.91/-0.98
FatJet r-track total stat.	+0.21/-0.17	+0.08/-0.05	+0.55/-0.48	+0.16/-0.12	+0.16/-0.07
FatJet r-track tracking	+0.20/-0.12	+0.54/-0.34	+0.35/-0.33	+0.70/-0.72	+0.53/-0.62
FatJet p_T resolution	-0.15/+0.15	+0.46/-0.46	-0.04/+0.04	+2.64/-2.64	+2.18/-2.18
FatJet mass resolution	+2.17/-2.17	+2.24/-2.24	+2.21/-2.21	+2.38/-2.38	+2.01/-2.01
FatJet τ_{32}^{wta} resolution	-23.43/+23.43	-10.00/+10.00	-25.04/+25.04	-12.01/+12.01	-11.88/+11.88
MET resolution para.	+0.01/–	∼ 0	∼ 0	∼ 0	∼ 0
MET resolution perp.	∼ 0	–/-0.04	∼ 0	+0.01/–	+0.04/–
MET scale	∼ 0	–/-0.02	∼ 0	+0.03/–	+0.01/-0.02
B-tag(70) XTR	+0.07/-0.09	+0.04/-0.04	+0.11/-0.13	+0.08/-0.08	+0.11/-0.11
B-tag(70) XTR charm	∼ 0	∼ 0	∼ 0	∼ 0	∼ 0
B-tag(70) eff. b EV 1	+1.11/-1.10	+0.69/-0.68	+0.64/-0.63	+0.50/-0.50	+0.61/-0.60
B-tag(70) eff. b EV 2	+2.51/-2.52	+1.93/-1.93	+2.02/-2.04	+1.98/-1.98	+1.98/-1.99
B-tag(70) eff. b EV 3	+0.09/-0.09	+0.29/-0.29	+0.04/-0.04	+0.21/-0.21	+0.21/-0.21
B-tag(70) eff. b EV 4	∼ 0	+0.21/-0.21	+0.02/-0.02	+0.17/-0.17	+0.15/-0.15
B-tag(70) eff. b EV 5	+0.02/-0.02	∼ 0	+0.02/-0.02	+0.02/-0.02	+0.01/-0.01
B-tag(70) eff. c EV 1	+0.14/-0.14	+0.45/-0.45	+0.18/-0.18	+0.50/-0.49	+0.47/-0.47
B-tag(70) eff. c EV 2	+1.17/-1.17	+0.37/-0.37	+0.88/-0.89	+0.50/-0.51	+0.45/-0.44
B-tag(70) eff. c EV 3	+0.23/-0.23	+0.02/-0.02	+0.20/-0.20	∼ 0	∼ 0
B-tag(70) eff. c EV 4	+0.14/-0.14	+0.02/-0.02	+0.12/-0.12	+0.04/-0.04	+0.03/-0.03
B-tag(70) eff. l EV 1	+0.52/-0.49	+1.03/-1.02	+0.13/-0.10	+1.46/-1.45	+1.60/-1.58
B-tag(70) eff. l EV 2	+0.57/-0.57	+0.55/-0.55	+0.60/-0.60	+0.71/-0.71	+0.75/-0.74
B-tag(70) eff. l EV 3	+0.04/-0.04	+0.10/-0.10	+0.08/-0.08	+0.12/-0.12	+0.16/-0.16
B-tag(70) eff. l EV 4	+0.48/-0.48	+0.45/-0.45	+0.47/-0.46	+0.53/-0.52	+0.55/-0.54
B-tag(70) eff. l EV 5	+0.02/-0.02	+0.02/-0.02	+0.05/-0.05	+0.03/-0.03	+0.04/-0.04
B-tag(70) eff. l EV 6	+0.04/-0.04	+0.08/-0.08	+0.05/-0.05	+0.08/-0.08	+0.09/-0.09
B-tag(70) eff. l EV 7	∼ 0	+0.03/-0.03	∼ 0	+0.02/-0.02	+0.04/-0.04
B-tag(70) eff. l EV 8	∼ 0	∼ 0	∼ 0	+0.02/-0.02	∼ 0
B-tag(70) eff. l EV 9	+0.06/-0.06	+0.06/-0.06	+0.07/-0.07	+0.07/-0.07	+0.06/-0.06
B-tag(70) eff. l EV 10	+0.05/-0.05	+0.05/-0.05	+0.06/-0.06	+0.06/-0.06	+0.07/-0.07
B-tag(70) eff. l EV 11	+0.03/-0.03	+0.02/-0.02	+0.02/-0.02	+0.03/-0.03	+0.03/-0.03
B-tag(70) eff. l EV 12	+0.02/-0.02	+0.02/-0.02	+0.02/-0.02	+0.04/-0.04	+0.03/-0.03
B-tag(70) eff. l EV 13	∼ 0	∼ 0	∼ 0	∼ 0	∼ 0
B-tag(70) eff. l EV 14	∼ 0	∼ 0	∼ 0	+0.02/-0.02	+0.01/-0.01
B-tag(70) eff. l EV 15	∼ 0	∼ 0	∼ 0	∼ 0	∼ 0
B-tag(70) eff. l EV 16	∼ 0	∼ 0	∼ 0	∼ 0	∼ 0
B-tag(70) eff. l EV 17	∼ 0	–	∼ 0	–	–
Pile-up	+0.25/-0.77	+0.19/–	+0.25/-0.49	+0.59/-0.51	+0.20/-0.49
Jet-vertex-tagger	+0.02/-0.05	+0.07/-0.10	+0.02/-0.05	+0.12/-0.15	+0.12/-0.15
Luminosity	+3.20/-3.20	+3.20/-3.20	+3.20/-3.20	+3.20/-3.20	+3.20/-3.20
Lepton veto uncertainty	+0.00/-0.00	+0.00/-0.00	+0.00/-0.00	+0.00/-0.00	+0.00/-0.00
Statistical	+0.78/ − 0.78	+0.68/ − 0.68	+0.86/ − 0.86	+1.06/ − 1.06	+0.98/ − 0.98

Table 6.17: Relative variations (up/down) on the DM signal event yields in the signal region without additional forward jet requirement of the hadronic channel in percent.

	DM nonres.(m_Φ=2, m_χ=0.001)TeV	DM nonres.(m_Φ=2.5, m_χ=0.001)TeV	DM nonres.(m_Φ=3, m_χ=0.001)TeV	DM res.(m_Φ=2, m_χ=0.1)TeV	DM res.(m_Φ=3)TeV m_χ=0.1)TeV
Trigger turn on uncertainty	+2.00/-2.00	+2.00/-2.00	+2.00/-2.00	+2.00/-2.00	+2.00/-2.00
Energy resolution	–	–	–	–	–
Energy scale	–	–	–	–	–
Jet energy resolution	–/-0.40	+0.13/–	+0.07/–	–/-0.06	–/-0.08
B-jet energy scale	+0.04/–	+0.02/∼ 0	+0.01/–	+0.02/∼ 0	–/-0.02
JES Eff. NP 1	–/-0.03	+0.13/-0.04	+0.03/-0.03	+0.11/-0.07	+0.01/-0.07
JES Eff. NP 2	+0.02/-0.03	+0.05/–	∼ 0	+0.05/-0.02	+0.01/-0.01
JES Eff. NP 3	+0.04/–	+0.05/–	∼ 0	+0.01/∼ 0	∼ 0/-0.02
JES Eff. NP 4	+0.02/–	+0.07/–	∼ 0	–/-0.01	∼ 0/-0.01
JES Eff. NP 5	+0.03/-0.01	+0.06/–	+0.02/∼ 0	∼ 0/-0.03	–/-0.01
JES Eff. NP 6	+0.03/–	+0.02/–	∼ 0	∼ 0	∼ 0
JES Eff. NP 7	+0.03/-0.02	+0.06/–	+0.01/–	–/-0.02	∼ 0/-0.01
JES Eff. NP 8	∼ 0/-0.01	+0.05/–	∼ 0	∼ 0	∼ 0
JES EIC modeling	+0.04/-0.04	+0.16/-0.03	+0.09/-0.04	+0.11/-0.04	+0.03/-0.11
JES EIC non-closure	+0.08/–	+0.06/–	+0.02/–	+0.03/-0.03	–/-0.07
JES EIC total stat.	+0.04/–	+0.06/∼ 0	+0.03/–	+0.02/-0.05	+0.02/-0.04
JES flavor composition	+0.12/-0.43	+0.38/-0.31	+0.30/-0.15	+0.26/-0.19	+0.18/-0.31
JES flavor response	+0.08/-0.07	+0.16/-0.06	+0.09/-0.04	+0.14/-0.14	+0.06/-0.13
JES pile-up offset mu	∼ 0/-0.01	+0.12/–	+0.01/-0.02	–/-0.03	–/-0.03
JES pile-up offset npv	+0.03/–	+0.03/∼ 0	+0.06/∼ 0	+0.06/-0.04	–/-0.06
JES pile-up p_T term	+0.02/-0.02	+0.08/-0.01	+0.04/-0.03	+0.09/-0.04	∼ 0/-0.04
JES pile-up rho topo.	+0.05/-0.15	+0.16/-0.02	+0.12/-0.04	+0.17/-0.10	+0.05/-0.14
JES punchthrough	+0.02/–	∼ 0	∼ 0	∼ 0	∼ 0
FatJet r-track baseline	+2.28/-2.41	+2.10/-2.83	+1.83/-2.48	+2.07/-2.42	+1.84/-2.01
FatJet r-track modeling	+0.99/-1.07	+0.97/-1.25	+0.82/-1.10	+0.94/-1.19	+0.81/-0.96
FatJet r-track total stat.	+0.14/-0.14	+0.11/-0.17	+0.09/-0.11	+0.15/-0.11	+0.11/-0.09
FatJet r-track tracking	+0.77/-0.62	+0.65/-1.00	+0.51/-0.71	+0.71/-0.56	+0.48/-0.56
FatJet p_T resolution	+2.22/-2.22	+2.08/-2.08	+1.87/-1.87	-0.26/+0.26	-0.21/+0.21
FatJet mass resolution	+2.55/-2.55	+2.42/-2.42	+2.08/-2.08	+1.88/-1.88	+1.69/-1.69
FatJet τ_{32}^{wta} resolution	-12.59/+12.59	-12.37/+12.37	-12.46/+12.46	-17.03/+17.03	-21.15/+21.15
MET resolution para.	–/-0.02	+0.01/–	+0.05/–	+0.05/–	∼ 0
MET resolution perp.	+0.02/–	+0.04/–	+0.04/–	+0.07/–	+0.02/–
MET scale	∼ 0	+0.04/–	+0.02/–	+0.02/–	+0.02/-0.02
B-tag(70) XTR	+0.10/-0.10	+0.13/-0.13	+0.13/-0.13	+0.11/-0.12	+0.15/-0.15
B-tag(70) XTR charm	∼ 0	–	∼ 0	∼ 0	∼ 0
B-tag(70) eff. b EV 1	+0.62/-0.62	+0.54/-0.53	+0.62/-0.61	+0.66/-0.65	+0.71/-0.70
B-tag(70) eff. b EV 2	+2.06/-2.06	+1.99/-1.99	+2.06/-2.06	+2.11/-2.11	+2.11/-2.11
B-tag(70) eff. b EV 3	+0.18/-0.18	+0.17/-0.17	+0.18/-0.18	+0.19/-0.19	+0.15/-0.15
B-tag(70) eff. b EV 4	+0.14/-0.14	+0.15/-0.15	+0.14/-0.14	+0.16/-0.16	+0.14/-0.14
B-tag(70) eff. b EV 5	+0.01/-0.01	+0.02/-0.02	+0.01/-0.01	+0.01/-0.01	+0.01/-0.01
B-tag(70) eff. c EV 1	+0.43/-0.42	+0.45/-0.44	+0.44/-0.44	+0.41/-0.41	+0.44/-0.44
B-tag(70) eff. c EV 2	+0.71/-0.71	+0.55/-0.56	+0.67/-0.68	+0.65/-0.65	+0.64/-0.64
B-tag(70) eff. c EV 3	+0.07/-0.07	+0.03/-0.03	+0.04/-0.04	+0.06/-0.06	+0.04/-0.04
B-tag(70) eff. c EV 4	+0.06/-0.06	+0.05/-0.05	+0.06/-0.06	+0.06/-0.06	+0.06/-0.06
B-tag(70) eff. l EV 1	+1.35/-1.35	+1.38/-1.38	+1.20/-1.16	+1.41/-1.38	+1.30/-1.28
B-tag(70) eff. l EV 2	+0.71/-0.71	+0.70/-0.69	+0.72/-0.71	+0.70/-0.70	+0.73/-0.73
B-tag(70) eff. l EV 3	+0.16/-0.16	+0.11/-0.11	+0.09/-0.08	+0.11/-0.10	+0.13/-0.13
B-tag(70) eff. l EV 4	+0.58/-0.57	+0.48/-0.48	+0.53/-0.53	+0.52/-0.51	+0.61/-0.60
B-tag(70) eff. l EV 5	+0.02/-0.02	+0.03/-0.03	+0.01/-0.01	+0.03/-0.03	+0.03/-0.03
B-tag(70) eff. l EV 6	+0.11/-0.11	+0.08/-0.08	+0.11/-0.11	+0.09/-0.09	+0.10/-0.10
B-tag(70) eff. l EV 7	+0.05/-0.05	+0.03/-0.03	+0.04/-0.04	+0.05/-0.05	+0.03/-0.03
B-tag(70) eff. l EV 8	∼ 0	∼ 0	+0.03/-0.03	+0.02/-0.02	+0.03/-0.03
B-tag(70) eff. l EV 9	+0.06/-0.06	+0.07/-0.07	+0.08/-0.08	+0.07/-0.07	+0.07/-0.07
B-tag(70) eff. l EV 10	+0.07/-0.07	+0.07/-0.07	+0.08/-0.08	+0.07/-0.07	+0.06/-0.06
B-tag(70) eff. l EV 11	+0.03/-0.03	+0.03/-0.03	+0.03/-0.03	+0.03/-0.03	+0.03/-0.03
B-tag(70) eff. l EV 12	+0.04/-0.04	+0.03/-0.03	+0.04/-0.04	+0.03/-0.03	+0.03/-0.03
B-tag(70) eff. l EV 13	∼ 0	∼ 0	∼ 0	∼ 0	∼ 0
B-tag(70) eff. l EV 14	+0.01/-0.01	+0.01/-0.01	+0.01/-0.01	∼ 0	+0.01/-0.01
B-tag(70) eff. l EV 15	∼ 0	∼ 0	∼ 0	∼ 0	∼ 0
B-tag(70) eff. l EV 16	∼ 0	∼ 0	∼ 0	∼ 0	∼ 0
B-tag(70) eff. l EV 17	∼ 0	∼ 0	∼ 0	∼ 0	∼ 0
Pile-up	+0.46/–	+0.42/–	+0.33/-0.53	+1.00/-0.65	+0.14/-0.15
Jet-vertex-tagger	+0.12/-0.15	+0.09/-0.13	+0.12/-0.15	+0.11/-0.14	+0.10/-0.14
Luminosity	+3.20/-3.20	+3.20/-3.20	+3.20/-3.20	+3.20/-3.20	+3.20/-3.20
Lepton veto uncertainty	+0.00/-0.00	+0.00/-0.00	+0.00/-0.00	+0.00/-0.00	+0.00/-0.00
Statistical	+0.97/ − 0.97	+0.97/ − 0.97	+0.70/ − 0.70	+0.96/ − 0.96	+0.63/ − 0.63

Table 6.18: Relative variations (up/down) on the DM signal event yields in the signal region without additional forward jet requirement of the hadronic channel in percent.

	$t\bar{t}$	Single Top	W+Jets	Z+jets	Other
Trigger turn on uncertainty	+2.00/-2.00	+2.00/-2.00	+2.00/-2.00	+2.00/-2.00	+2.00/-2.00
$t\bar{t}$ hard scatter gen.	–/-7.50	–	–	–	–
$t\bar{t}$ fragm./hadr. model	–/-9.52	–	–	–	–
$t\bar{t}$ add. radiation	+2.81/-2.81	–	–	–	–
$t\bar{t}$ PDF	+9.72/-9.72	–	–	–	–
$t\bar{t}$ cross-section	+5.58/-6.11	–	–	–	–
$t\bar{t}$+W cross-section	–	–	–	–	+2.58/-2.33
$t\bar{t}$+Z cross-section	–	–	–	–	–/-44.37
$t\bar{t}$+ll cross-section	–	–	–	–	+0.22/-0.25
Single top cross-section	–	+3.62/-3.15	–	–	–
Di-bosons cross-section	–	–	–	–	+4.23/-4.23
Z+jets generator	–	–	–	+32.72/–	–
Z+jets heavy flavor	–	–	–	+40.90/-40.90	–
Z+jets internal scale	–	–	–	+2.19/-2.19	–
Z+jets PDF	–	–	–	+7.95/-7.95	–
W+jets generator	–	–	+33.00/-33.00	–	–
W+jets heavy flavor	–	–	+39.00/-39.00	–	–
W+jets internal scale	–	–	+3.11/-3.11	–	–
W+jets PDF	–	–	+7.99/-7.99	–	–
V+jets cross-section	–	–	+5.00/-5.00	+5.00/-5.00	–
Energy resolution	+0.01/-0.01	–	+0.05/–	–	–/-0.02
Energy scale	+0.02/-0.02	–	–/-0.10	–	~ 0
Jet energy resolution	+0.55/–	+1.88/–	+1.23/–	+0.35/–	+0.22/–
B-jet energy scale	+0.19/-0.19	+0.29/-0.21	+0.78/-0.37	+0.46/-0.51	+0.50/~ 0
JES Eff. NP 1	+1.36/-1.09	+1.23/-0.17	+1.53/-2.28	+0.92/-2.12	+0.82/-0.56
JES Eff. NP 2	+0.93/-0.99	+1.75/–	+0.70/-0.82	+0.90/-0.89	+1.22/-0.61
JES Eff. NP 3	+0.59/-0.68	+0.99/-0.22	+0.01/-0.61	+0.50/-0.62	+0.52/-0.47
JES Eff. NP 4	–/-0.14	+0.34/-0.26	+0.03/-0.43	–/-0.16	+0.02/–
JES Eff. NP 5	+0.05/-0.18	+0.34/–	+0.01/-0.37	+0.05/-0.10	+0.14/-0.28
JES Eff. NP 6	+0.11/-0.14	~ 0/-0.07	–/-0.09	+0.10/-0.16	+0.15/-0.04
JES Eff. NP 7	+0.07/-0.12	+0.02/-0.06	–/-0.26	+0.11/-0.15	–/-0.07
JES Eff. NP 8	+0.17/-0.24	+0.22/–	–/-0.14	+0.10/-0.23	+0.16/-0.18
JES EIC modeling	+0.70/-0.83	+1.28/–	+1.33/-2.16	+0.34/-1.57	+0.63/-0.57
JES EIC non-closure	+0.31/-0.41	+1.06/–	–/-0.52	+0.34/-0.35	+0.76/-0.41
JES EIC total stat.	+0.25/-0.39	+1.08/–	+0.05/-0.61	+0.39/-0.36	+0.41/-0.10
JES flavor composition	+2.46/-2.17	+4.24/-1.76	+4.11/-3.77	+1.91/-3.25	+2.16/-1.58
JES flavor response	+0.90/-1.00	+1.37/-0.70	+1.35/-1.15	+0.25/-1.61	+0.85/-0.18
JES pile-up offset mu	+0.13/-0.03	+0.28/-0.02	–/-0.47	–/-0.74	+0.08/–
JES pile-up offset npv	+0.31/-0.32	+0.85/–	+0.69/-0.72	+0.14/-0.47	+0.20/-0.10
JES pile-up p_T term	+0.83/-0.75	+1.58/-0.54	+0.53/-1.33	+0.98/-0.64	+1.04/-0.67
JES pile-up rho topo.	+1.43/-1.12	+1.83/-0.49	+2.44/-2.88	+1.01/-2.42	+1.09/-0.72
JES punchthrough	+0.02/–	–	+0.16/–	+0.01/–	–/-0.02
FatJet r-track baseline	+2.16/-2.16	+4.65/-3.42	+2.19/-3.38	+4.33/-3.71	+1.51/-1.71
FatJet r-track modelling	+0.82/-0.67	+1.99/-1.70	+1.23/-2.11	+2.48/-2.04	+0.80/-0.71
FatJet r-track total stat.	+0.09/–	+0.16/–	–/-0.14	+0.12/-0.15	+0.03/-0.10
FatJet r-track tracking	+0.04/-0.06	+1.48/–	–/-1.28	+0.85/-0.21	+0.05/-0.09
FatJet p_T resolution	-8.06/+8.06	+1.31/-1.31	-1.86/+1.86	+0.24/-0.24	-0.49/+0.49
FatJet mass resolution	+3.31/-3.31	+7.69/-7.69	+8.02/-8.02	+9.09/-9.09	+3.73/-3.73
FatJet τ_{32}^{wta} resolution	-16.30/+16.30	-22.40/+22.40	-24.10/+24.10	-22.30/+22.30	-13.00/+13.00
MET resolution para.	–/-0.79	–/-0.52	–/-0.65	–/-1.03	–/-0.84
MET resolution perp.	–/-0.84	–/-1.00	–/-0.76	–/-0.92	–/-0.58
MET scale	+0.92/-0.75	+1.46/-1.37	+0.64/-0.58	+0.23/-0.79	+0.72/-0.67
B-tag(70) XTR	+0.10/-0.10	+0.28/-0.28	+0.34/-0.35	+0.33/-0.33	+0.15/-0.15
B-tag(70) XTR charm	+0.04/-0.04	+0.25/-0.25	+0.60/-0.60	+0.02/-0.02	+0.05/-0.05
B-tag(70) eff. b EV 1	+0.93/-0.91	+0.66/-0.65	+1.09/-1.07	+0.86/-0.84	+0.92/-0.90
B-tag(70) eff. b EV 2	+3.59/-3.53	+3.65/-3.59	+2.94/-2.90	+3.03/-2.99	+3.13/-3.10
B-tag(70) eff. b EV 3	+0.67/-0.67	+0.60/-0.59	+0.49/-0.49	+0.48/-0.48	+0.50/-0.50
B-tag(70) eff. b EV 4	+0.46/-0.46	+0.37/-0.37	+0.35/-0.34	+0.29/-0.29	+0.38/-0.38
B-tag(70) eff. b EV 5	+0.03/-0.03	+0.03/-0.03	+0.05/-0.05	+0.05/-0.05	+0.05/-0.05
B-tag(70) eff. c EV 1	+0.54/-0.53	+0.96/-0.95	+1.19/-1.19	+0.61/-0.61	+0.70/-0.69
B-tag(70) eff. c EV 2	+0.74/-0.74	+2.17/-2.13	+3.13/-2.97	+2.95/-2.79	+1.13/-1.12
B-tag(70) eff. c EV 3	+0.02/-0.02	+0.23/-0.23	+0.21/-0.22	+0.09/-0.09	+0.02/-0.02
B-tag(70) eff. c EV 4	~ 0	+0.11/-0.11	+0.12/-0.12	+0.12/-0.12	+0.03/-0.03
B-tag(70) eff. l EV 1	+0.70/-0.74	+0.21/-0.03	+5.55/-5.06	+3.39/-3.00	+0.22/-0.03
B-tag(70) eff. l EV 2	+0.68/-0.68	+0.73/-0.72	+0.17/-0.18	+0.30/-0.30	+0.85/-0.84
B-tag(70) eff. l EV 3	+0.08/-0.08	+0.15/-0.14	+0.80/-0.78	+0.39/-0.39	+0.04/-0.05
B-tag(70) eff. l EV 4	+0.56/-0.55	+0.74/-0.75	+1.31/-1.34	+1.08/-1.05	+0.99/-0.97
B-tag(70) eff. l EV 5	+0.03/-0.03	+0.04/-0.04	+0.02/-0.02	+0.03/-0.03	+0.04/-0.04
B-tag(70) eff. l EV 6	+0.14/-0.13	+0.20/-0.20	+0.52/-0.52	+0.40/-0.40	+0.22/-0.22
B-tag(70) eff. l EV 7	+0.04/-0.04	+0.06/-0.06	+0.01/-0.01	+0.10/-0.10	+0.04/-0.04
B-tag(70) eff. l EV 8	+0.02/-0.02	+0.02/-0.02	+0.20/-0.20	~ 0	+0.07/-0.07
B-tag(70) eff. l EV 9	+0.09/-0.09	+0.12/-0.12	+0.35/-0.35	+0.18/-0.18	+0.12/-0.12
B-tag(70) eff. l EV 10	+0.09/-0.09	+0.05/-0.05	+0.22/-0.22	+0.04/-0.05	+0.12/-0.12
B-tag(70) eff. l EV 11	+0.04/-0.04	+0.03/-0.03	+0.04/-0.04	+0.03/-0.03	+0.05/-0.05
B-tag(70) eff. l EV 12	+0.05/-0.05	+0.03/-0.03	+0.03/-0.03	+0.05/-0.05	+0.04/-0.04
B-tag(70) eff. l EV 13	~ 0	~ 0	+0.02/-0.02	~ 0	+0.02/-0.02
B-tag(70) eff. l EV 14	+0.02/-0.02	+0.02/-0.02	+0.02/-0.02	+0.02/-0.02	+0.02/-0.02
B-tag(70) eff. l EV 15	~ 0	~ 0	~ 0	~ 0	~ 0
B-tag(70) eff. l EV 16	~ 0	~ 0	~ 0	~ 0	~ 0
B-tag(70) eff. l EV 17	–	~ 0	–	–	–
Pile-up	+0.44/-0.30	+1.82/–	+1.54/-2.50	+0.72/-0.20	+0.24/-0.03
Jet-vertex-tagger	+0.11/-0.16	+0.15/-0.20	+0.15/-0.19	+0.22/-0.25	+0.19/-0.24
Luminosity	+3.20/-3.20	+3.20/-3.20	+3.20/-3.20	+3.20/-3.20	+3.20/-3.20
Lepton veto uncertainty	+0.20/-0.20	+0.23/-0.23	+0.18/-0.18	+0.01/-0.01	+0.22/-0.22
Statistical	+1.09/ − 1.09	+3.60/ − 3.60	+8.24/ − 8.24	+8.49/ − 8.49	+1.60/ − 1.60

Table 6.19: Relative variations (up/down) on the background event yields in the $t\bar{t}$ control region of the hadronic channel in percent.

	$t\bar{t}$	Single Top	W+Jets	Z+jets	Other
Trigger turn on uncertainty	+2.00/-2.00	+2.00/-2.00	+2.00/-2.00	+2.00/-2.00	+2.00/-2.00
$t\bar{t}$ hard scatter gen.	–/-9.87	–	–	–	–
$t\bar{t}$ fragm./hadr. model	–/-4.35	–	–	–	–
$t\bar{t}$ add. radiation	+1.44/-1.44	–	–	–	–
$t\bar{t}$ PDF	+12.80/-12.80	–	–	–	–
$t\bar{t}$ cross-section	+5.58/-6.11	–	–	–	–
$t\bar{t}$+W cross-section	–	–	–	–	+2.91/-2.62
$t\bar{t}$+Z cross-section	–	–	–	–	–/-28.08
$t\bar{t}$+ll cross-section	–	–	–	–	+0.26/-0.30
Single top cross-section	–	+3.62/-3.15	–	–	–
Di-bosons cross-section	–	–	–	–	+0.90/-0.90
Z+jets generator	–	–	–	+41.39/–	–
Z+jets heavy flavor	–	–	–	+18.20/-18.20	–
Z+jets internal scale	–	–	–	+2.27/-2.27	–
Z+jets PDF	–	–	–	+8.82/-8.82	–
W+jets generator	–	–	+24.20/-24.20	–	–
W+jets heavy flavor	–	–	+14.50/-14.50	–	–
W+jets internal scale	–	–	+2.76/-2.76	–	–
W+jets PDF	–	–	+11.50/-11.50	–	–
V+jets cross-section	–	–	+5.00/-5.00	+5.00/-5.00	–
Energy resolution	–/-0.06	–	–/-0.02	+0.02/–	–
Energy scale	–/-0.03	–	~ 0	~ 0	~ 0
Jet energy resolution	–/-1.70	+0.84/–	–/-0.23	+1.46/–	–/-4.41
B-jet energy scale	+0.09/-0.08	+0.39/–	+0.06/-0.11	+0.12/~ 0	+0.23/–
JES Eff. NP 1	–/-1.36	+1.00/–	–/-1.32	+0.85/–	–/-1.93
JES Eff. NP 2	–/-1.03	+0.34/-1.03	+0.33/-0.77	+0.32/–	+0.21/-0.74
JES Eff. NP 3	–/-0.25	+0.11/-0.15	–/-0.79	+0.55/–	+0.43/-0.68
JES Eff. NP 4	+0.22/-0.66	+0.07/-0.34	–/-0.61	+0.68/–	–/-0.87
JES Eff. NP 5	–/-0.71	+0.50/-0.27	–/-0.53	+0.52/–	–/-0.39
JES Eff. NP 6	+0.12/-0.16	+0.63/-0.19	–/-0.34	+0.41/–	–/-0.64
JES Eff. NP 7	–/-0.05	–/-0.34	–/-0.42	+0.32/–	–/-0.74
JES Eff. NP 8	+0.13/–	+0.15/-0.18	–/-0.35	+0.36/–	+0.06/-0.23
JES EIC modeling	–/-1.17	+1.24/–	–/-0.52	+0.75/–	+0.20/-0.42
JES EIC non-closure	~ 0/-0.71	+0.80/-1.16	+0.23/-0.38	+0.93/–	–/-1.31
JES EIC total stat.	–/-0.50	+0.31/-0.66	–/-0.18	+0.18/-0.03	–/-0.80
JES flavor composition	–/-2.35	+0.39/-1.61	+0.62/-1.34	+0.62/-0.27	–/-3.10
JES flavor response	–/-1.26	+1.21/-0.29	–/-0.47	+0.46/–	–/-1.07
JES pile-up offset mu	–/-0.38	+0.52/-0.62	–/-0.77	+0.31/–	+0.04/-1.75
JES pile-up offset npv	–/-1.01	–/-0.21	–/-0.75	+0.11/-0.02	–/-0.58
JES pile-up p_T term	–/-0.48	+1.64/–	–/-0.31	+0.36/–	+0.07/-0.41
JES pile-up rho topo.	–/-1.44	+1.17/-0.45	–/-1.21	+0.92/-0.59	–/-1.99
JES punchthrough	+0.07/-0.09	+0.08/-0.01	+0.11/–	+0.09/-0.02	–/-0.03
FatJet r-track baseline	+2.65/-1.68	+2.60/-3.10	+2.23/-2.50	+2.68/-2.23	–/-1.81
FatJet r-track modelling	+2.43/-2.41	+3.10/-3.70	+1.81/-2.15	+1.98/-2.18	+0.88/-1.64
FatJet r-track total stat.	+0.45/-0.27	+0.14/-0.74	+0.17/-0.33	+0.23/-0.26	+0.18/-0.19
FatJet r-track tracking	+4.92/-4.81	+4.36/-4.77	+3.47/-3.83	+4.03/-3.33	+3.12/-4.43
FatJet p_T resolution	+4.58/-4.58	+14.10/-14.10	+9.27/-9.27	+8.64/-8.64	+7.22/-7.22
FatJet mass resolution	+24.50/-24.50	+19.00/-19.00	+17.30/-17.30	+16.50/-16.50	+21.50/-21.50
FatJet τ_{32}^{wta} resolution	-15.90/+15.90	-24.80/+24.80	-31.00/+31.00	-33.70/+33.70	-11.40/+11.40
MET resolution para.	–/-0.12	+0.78/–	–/-0.13	+0.68/–	–/-0.63
MET resolution perp.	+0.22/–	+0.04/–	+0.31/–	–/-0.14	–/-0.87
MET scale	+0.31/-0.42	+1.73/–	+0.33/-0.02	+0.37/-0.03	+0.63/-0.38
B-tag(70) XTR	+0.52/-0.53	+0.81/-0.81	+0.73/-0.73	+0.58/-0.58	+0.14/-0.15
B-tag(70) XTR charm	+0.24/-0.24	+0.14/-0.14	+0.75/-0.75	+0.39/-0.40	+0.21/-0.21
B-tag(70) eff. b EV 1	+4.30/-4.44	+3.11/-3.15	+1.11/-1.11	+1.08/-1.08	+3.86/-3.87
B-tag(70) eff. b EV 2	+3.00/-3.33	+1.81/-2.02	+0.28/-0.32	+0.32/-0.37	+1.81/-1.95
B-tag(70) eff. b EV 3	+0.23/-0.23	+0.04/-0.03	+0.01/-0.01	+0.02/-0.02	+0.23/-0.23
B-tag(70) eff. b EV 4	+0.07/-0.07	+0.12/-0.12	+0.03/-0.03	+0.02/-0.02	+0.08/-0.08
B-tag(70) eff. b EV 5	+0.02/-0.02	+0.01/-0.01	+0.01/-0.01	+0.02/-0.02	+0.02/-0.02
B-tag(70) eff. c EV 1	+0.09/-0.09	+0.15/-0.15	+1.66/-1.66	+1.18/-1.19	+0.55/-0.55
B-tag(70) eff. c EV 2	+1.52/-1.51	+1.29/-1.30	+5.84/-6.05	+4.98/-5.15	+1.30/-1.43
B-tag(70) eff. c EV 3	+0.16/-0.16	+0.21/-0.21	+0.68/-0.68	+0.61/-0.61	+0.10/-0.10
B-tag(70) eff. c EV 4	+0.13/-0.13	+0.11/-0.11	+0.42/-0.42	+0.35/-0.36	+0.04/-0.04
B-tag(70) eff. l EV 1	+1.94/-1.93	+1.15/-0.96	+7.92/-8.49	+7.87/-8.31	+0.77/-0.70
B-tag(70) eff. l EV 2	+0.94/-0.93	+0.69/-0.69	+0.71/-0.70	+0.74/-0.73	+1.12/-1.11
B-tag(70) eff. l EV 3	+0.13/-0.13	+0.18/-0.17	+0.96/-0.98	+0.94/-0.95	+0.36/-0.35
B-tag(70) eff. l EV 4	+0.67/-0.67	+0.62/-0.63	+2.32/-2.29	+2.26/-2.23	+1.39/-1.38
B-tag(70) eff. l EV 5	+0.04/-0.04	~ 0	~ 0	+0.01/-0.01	+0.04/-0.04
B-tag(70) eff. l EV 6	+0.10/-0.10	+0.09/-0.09	+0.41/-0.41	+0.33/-0.33	+0.21/-0.21
B-tag(70) eff. l EV 7	+0.03/-0.03	+0.02/-0.02	+0.32/-0.32	+0.37/-0.37	+0.19/-0.19
B-tag(70) eff. l EV 8	+0.03/-0.03	+0.06/-0.06	+0.45/-0.45	+0.47/-0.47	+0.33/-0.33
B-tag(70) eff. l EV 9	+0.10/-0.10	+0.13/-0.13	+0.13/-0.14	+0.18/-0.18	+0.31/-0.31
B-tag(70) eff. l EV 10	+0.08/-0.08	+0.07/-0.07	+0.07/-0.07	+0.04/-0.03	+0.04/-0.04
B-tag(70) eff. l EV 11	+0.04/-0.04	+0.02/-0.02	+0.10/-0.10	+0.06/-0.06	+0.02/-0.02
B-tag(70) eff. l EV 12	+0.04/-0.04	~ 0	~ 0	~ 0	+0.12/-0.12
B-tag(70) eff. l EV 13	~ 0	~ 0	~ 0	+0.02/-0.02	+0.01/-0.01
B-tag(70) eff. l EV 14	+0.02/-0.02	+0.02/-0.02	+0.07/-0.07	+0.07/-0.07	+0.04/-0.04
B-tag(70) eff. l EV 15	~ 0	+0.02/-0.02	+0.03/-0.03	+0.04/-0.04	~ 0
B-tag(70) eff. l EV 16	~ 0	~ 0	+0.01/-0.01	+0.01/-0.01	~ 0
B-tag(70) eff. l EV 17	–	–	~ 0	~ 0	~ 0
Pile-up	+1.24/-0.98	+2.28/-3.05	+0.02/-0.03	+0.46/-0.19	+1.96/-2.62
Jet-vertex-tagger	+0.11/-0.16	+0.06/-0.11	+0.10/-0.15	+0.11/-0.14	+0.16/-0.21
Luminosity	+3.20/-3.20	+3.20/-3.20	+3.20/-3.20	+3.20/-3.20	+3.20/-3.20
Lepton veto uncertainty	+4.52/-4.52	+0.60/-0.60	+0.51/-0.51	+0.20/-0.20	+0.53/-0.53
Statistical	$+1.80/-1.80$	$+3.48/-3.48$	$+4.88/-4.88$	$+6.21/-6.21$	$+3.65/-3.65$

Table 6.20: Relative variations (up/down) on the background event yields in the multijet validation region of the hadronic channel in percent.

	$t\bar{t}$	Single Top	W+Jets	Z+jets	Other
Trigger turn on uncertainty	+2.00/-2.00	+2.00/-2.00	+2.00/-2.00	+2.00/-2.00	+2.00/-2.00
$t\bar{t}$ hard scatter gen.	–/-2.61	–	–	–	–
$t\bar{t}$ fragm./hadr. model	–/-3.48	–	–	–	–
$t\bar{t}$ add. radiation	+2.39/-2.39	–	–	–	–
$t\bar{t}$ PDF	+10.20/-10.20	–	–	–	–
$t\bar{t}$ cross-section	+5.58/-6.11	–	–	–	–
$t\bar{t}$+W cross-section	–	–	–	–	+0.07/-0.06
$t\bar{t}$+Z cross-section	–	–	–	–	–/-0.47
$t\bar{t}$+ll cross-section	–	–	–	–	∼ 0
Single top cross-section	–	+3.62/-3.15	–	–	–
Di-bosons cross-section	–	–	–	–	+1.42/-1.42
Z+jets generator	–	–	–	+19.08/–	–
Z+jets heavy flavor	–	–	–	+3.99/-3.99	–
Z+jets internal scale	–	–	–	+12.80/-12.80	–
Z+jets PDF	–	–	–	+14.30/-14.30	–
W+jets generator	–	–	+25.20/-25.20	–	–
W+jets heavy flavor	–	–	+3.69/-3.69	–	–
W+jets internal scale	–	–	+11.10/-11.10	–	–
W+jets PDF	–	–	+12.60/-12.60	–	–
V+jets cross-section	–	–	+5.00/-5.00	+5.00/-5.00	–
Energy resolution	+0.02/-0.01	+0.07/∼ 0	+0.02/–	∼ 0	+0.04/–
Energy scale	∼ 0	+0.07/-0.05	+0.03/-0.03	∼ 0	∼ 0
Jet energy resolution	+0.08/–	+0.37/–	+0.03/–	–/-0.10	+0.05/–
B-jet energy scale	+0.41/-0.11	–/-0.18	∼ 0	∼ 0	∼ 0
JES Eff. NP 1	+0.27/-0.01	–/-0.28	+0.05/-0.09	+0.03/-0.05	–/-0.11
JES Eff. NP 2	+0.35/-0.29	+0.26/-0.50	+0.22/-0.21	+0.10/-0.12	+0.06/-0.09
JES Eff. NP 3	+0.25/-0.13	+0.22/-0.31	+0.12/-0.13	+0.04/-0.07	+0.07/-0.05
JES Eff. NP 4	+0.07/-0.09	+0.05/-0.06	+0.04/-0.07	+0.02/-0.04	+0.04/–
JES Eff. NP 5	+0.21/-0.19	+0.14/-0.17	+0.08/-0.10	+0.04/-0.08	+0.07/-0.09
JES Eff. NP 6	∼ 0	+0.10/-0.06	+0.02/-0.03	+0.02/-0.01	∼ 0
JES Eff. NP 7	+0.07/-0.13	+0.09/–	+0.02/-0.02	∼ 0	+0.04/-0.02
JES Eff. NP 8	+0.03/-0.05	+0.01/-0.04	+0.03/-0.02	∼ 0/-0.03	+0.01/-0.05
JES EIC modeling	+0.43/-0.19	+0.45/-0.20	+0.05/-0.15	+0.04/-0.11	+0.10/-0.13
JES EIC non-closure	+0.21/∼ 0	–/-0.29	+0.06/–	+0.04/-0.06	+0.04/-0.06
JES EIC total stat.	+0.19/-0.10	–/-0.18	+0.09/-0.06	+0.03/-0.06	∼ 0
JES flavor composition	+0.98/-0.54	+0.20/-0.29	+0.54/-0.46	+0.11/-0.16	+0.34/-0.63
JES flavor response	+0.19/-0.09	–/-0.22	+0.10/-0.09	+0.01/-0.10	+0.07/-0.08
JES pile-up offset mu	–/-0.14	–/-0.16	–/-0.10	∼ 0/-0.03	–/-0.07
JES pile-up offset npv	+0.29/–	–/-0.30	∼ 0/-0.01	–/-0.09	+0.04/-0.06
JES pile-up p_T term	+0.06/–	+0.02/∼ 0	+0.05/-0.04	–/-0.02	+0.02/-0.02
JES pile-up rho topo.	+0.79/-0.46	–/-0.61	+0.13/-0.17	–/-0.05	+0.11/-0.19
JES punchthrough	–	+0.02/–	∼ 0	∼ 0	∼ 0
FatJet r-track baseline	+11.57/-10.67	+11.06/-10.17	+10.16/-10.03	+9.67/-8.98	+8.88/-8.80
FatJet r-track modelling	+4.18/-3.94	+3.86/-3.33	+4.56/-4.60	+4.27/-4.08	+3.82/-3.93
FatJet r-track total stat.	+0.36/-0.46	+0.50/-0.36	+0.40/-0.48	+0.36/-0.37	+0.37/-0.32
FatJet r-track tracking	+3.71/-3.40	+2.95/-2.75	+3.09/-3.18	+2.95/-2.91	+3.08/-2.71
FatJet p_T resolution	+13.20/-13.20	+11.40/-11.40	+8.50/-8.50	+08.09/-8.09	+8.49/-8.49
FatJet mass resolution	+5.09/-5.09	+7.15/-7.15	+11.00/-11.00	+11.10/-11.10	+8.06/-8.06
FatJet τ_{32}^{wta} resolution	-17.70/+17.70	-20.70/+20.70	-23.00/+23.00	-23.20/+23.20	-23.10/+23.10
MET resolution para.	–/-0.49	–/-0.19	–/-0.08	–/-0.04	–/-0.13
MET resolution perp.	–/-0.55	+0.06/–	–/-0.09	–/-0.07	∼ 0
MET scale	+0.48/-0.43	+0.39/–	+0.11/-0.11	+0.03/-0.07	+0.04/-0.03
B-tag(70) XTR	+0.08/-0.08	+0.15/-0.15	+0.03/-0.03	+0.03/-0.03	+0.06/-0.06
B-tag(70) XTR charm	+0.21/-0.21	+0.20/-0.20	+0.14/-0.14	+0.01/-0.01	+0.10/-0.10
B-tag(70) eff. b EV 1	+7.12/-6.88	+5.11/-5.01	+0.22/-0.21	+0.28/-0.28	+0.38/-0.36
B-tag(70) eff. b EV 2	+2.61/-2.61	+2.28/-2.26	+0.06/-0.06	+0.13/-0.13	+0.16/-0.16
B-tag(70) eff. b EV 3	+0.97/-0.96	+0.59/-0.59	+0.02/-0.02	+0.03/-0.03	+0.05/-0.05
B-tag(70) eff. b EV 4	+0.29/-0.29	+0.18/-0.18	∼ 0	∼ 0	+0.01/-0.01
B-tag(70) eff. b EV 5	+0.02/-0.02	+0.02/-0.02	∼ 0	∼ 0	∼ 0
B-tag(70) eff. c EV 1	+0.18/-0.18	+0.07/-0.07	+0.13/-0.13	+0.26/-0.26	+0.21/-0.21
B-tag(70) eff. c EV 2	+1.03/-1.04	+1.05/-1.04	+0.40/-0.40	+0.48/-0.48	+1.33/-1.32
B-tag(70) eff. c EV 3	+0.04/-0.04	+0.07/-0.07	+0.03/-0.03	+0.03/-0.03	+0.09/-0.09
B-tag(70) eff. c EV 4	+0.06/-0.06	+0.07/-0.07	+0.04/-0.04	+0.03/-0.03	+0.09/-0.09
B-tag(70) eff. l EV 1	+2.01/-1.97	+1.49/-1.46	+2.23/-2.18	+2.14/-2.10	+2.07/-2.02
B-tag(70) eff. l EV 2	+0.83/-0.82	+0.72/-0.71	+0.95/-0.94	+0.91/-0.90	+0.75/-0.74
B-tag(70) eff. l EV 3	+0.16/-0.16	+0.16/-0.16	+0.14/-0.14	+0.20/-0.20	+0.18/-0.18
B-tag(70) eff. l EV 4	+0.51/-0.51	+0.55/-0.55	+0.58/-0.57	+0.62/-0.62	+0.42/-0.42
B-tag(70) eff. l EV 5	+0.03/-0.03	+0.03/-0.03	+0.04/-0.04	+0.04/-0.04	+0.03/-0.03
B-tag(70) eff. l EV 6	+0.07/-0.07	+0.10/-0.09	+0.09/-0.09	+0.10/-0.10	+0.05/-0.05
B-tag(70) eff. l EV 7	+0.05/-0.05	+0.06/-0.06	+0.06/-0.06	+0.06/-0.06	+0.05/-0.05
B-tag(70) eff. l EV 8	+0.02/-0.02	+0.02/-0.02	+0.02/-0.02	+0.01/-0.01	+0.02/-0.02
B-tag(70) eff. l EV 9	+0.05/-0.05	+0.05/-0.05	+0.06/-0.06	+0.07/-0.07	+0.04/-0.04
B-tag(70) eff. l EV 10	+0.05/-0.05	+0.04/-0.04	+0.06/-0.06	+0.06/-0.06	+0.05/-0.05
B-tag(70) eff. l EV 11	+0.03/-0.03	+0.03/-0.03	+0.04/-0.04	+0.04/-0.04	+0.03/-0.03
B-tag(70) eff. l EV 12	+0.04/-0.04	+0.04/-0.04	+0.05/-0.05	+0.04/-0.04	+0.03/-0.03
B-tag(70) eff. l EV 13	∼ 0	∼ 0	∼ 0	∼ 0	∼ 0
B-tag(70) eff. l EV 14	+0.02/-0.02	+0.01/-0.01	+0.02/-0.02	+0.02/-0.02	+0.01/-0.01
B-tag(70) eff. l EV 15	∼ 0	∼ 0	∼ 0	∼ 0	∼ 0
B-tag(70) eff. l EV 16	∼ 0	∼ 0	∼ 0	∼ 0	∼ 0
B-tag(70) eff. l EV 17	–	–	∼ 0	∼ 0	∼ 0
Pile-up	+1.06/-0.77	+2.88/-1.85	+1.22/-1.17	+0.60/-0.57	+0.96/-0.43
Jet-vertex-tagger	+0.18/-0.25	+0.15/-0.20	+0.07/-0.12	+0.10/-0.13	+0.08/-0.11
Luminosity	+3.20/-3.20	+3.20/-3.20	+3.20/-3.20	+3.20/-3.20	+3.20/-3.20
Lepton veto uncertainty	+0.32/-0.32	+0.37/-0.37	+0.30/-0.30	+0.01/-0.01	+0.26/-0.26
Statistical	+1.11/ − 1.11	+2.03/ − 2.03	+0.62/ − 0.62	+0.60/ − 0.60	+0.91/ − 0.91

Table 6.21: Relative variations (up/down) on the background event yields in the V+jet control region of the hadronic channel in percent.

7

Results

This last chapter of the analysis first describes the general statistical formalism based on the frequentist approach we use in experimental particle physics in order to make a statement of either discovery or exclusion of new physics at a certain confidence level. Then the results for the leptonic and hadronic channels are presented, respectively. A statistical combination of these two channels is done for the non-resonant DM model. Two-dimensional excluded regions on the parameter space are also described. Finally, conclusions are made for this analysis.

7.1 The statistical formalism

We know that in a hypothesis testing, we can only choose to reject or accept the null hypothesis, based on the result of the test. Therefore, in order to claim discovery, we need to construct a physics model which only includes the known SM processes, corresponding to the background-only hypothesis. In order to calculate the exlcusion limit, we need a physics model that describes both the background and the new physics signal, corresponding to the nominal signal hypothesis.

To construct the test statistic for the hypothesis testing, let us first consider the distribution of a variable which provides the most discriminatory power of signal over background (e.g. $E_{\mathrm{T}}^{\mathrm{miss}}$ for the leptonic channel, and $m_{\mathrm{T}}(E_{\mathrm{T}}^{\mathrm{miss}}, J)$ for the hadronic channel). The expected number of events in the ith bin of the distribution is given by

$$n_i^{obs} = \mu s_i + b_i, \tag{7.1}$$

where s_i and b_i are the expected event yields for siganl and background in the i-th bin, respectively. The signal strength μ, is defined as the ratio of the signal cross-section to the theoretical signal cross-section. The value $\mu = 0$ corresponds the background-only hypothesis while $\mu = 1$ represents the nominal hypothesis. Since we are dealing with a simple event-counting experiment, the event yields will follow the Poisson distribution. In addition, by assuming that all the bins are statistically independent, we can express

the probality, or likelihood, of observing n^{obs} events in total as:

$$L(n^{obs}|\mu) = \prod_{i=1}^{N} \frac{(\mu s_i + b_i)^{n_i^{obs}}}{n_i^{obs}!} \exp^{-(\mu s_i + b_i)}, \tag{7.2}$$

where n_i^{obs} is the number of observed events in the i-th bin and N is the total number of bins.

The uncertainties described in Section 6.4, which account for the variations of the event counts, are incorporated into the likelihood function as nuisance parameters $\boldsymbol{\theta}$. When the signal and background yields are fitted to data, each nuiance parameter θ_i is constrained by a Gaussian distribution or a log-normal distribution. The mean θ_i^0 and the standard deviation σ_{θ_i} are determined through some dedicated auxiliary measurements.

The new likelihood function, incorporating the nuiance parameters representing the uncertainties, is given by:

$$L(n^{obs}|\mu, \boldsymbol{\theta}) = \prod_{i=1}^{N} \frac{(\mu s_i(\boldsymbol{\theta}) + b_i(\boldsymbol{\theta}))^{n_i^{obs}}}{n_i^{obs}!} \exp^{-(\mu s_i(\boldsymbol{\theta}) + b_i(\boldsymbol{\theta}))}. \tag{7.3}$$

In order to construct the test statistic, we introduce the so-called profile likelihood ratio, which is defined as:

$$\lambda(\mu) = \frac{L(\mu, \hat{\hat{\boldsymbol{\theta}}}(\mu))}{L(\hat{\mu}, \hat{\boldsymbol{\theta}})}, \tag{7.4}$$

where $\hat{\hat{\boldsymbol{\theta}}}(\mu)$ is the conditional maximum-likelihood (ML) estimator of $\boldsymbol{\theta}$, which is the value of $\boldsymbol{\theta}$ that maximizes L given a specific value of μ. $\hat{\mu}$ and $\hat{\boldsymbol{\theta}}$ are the ML estimators of μ and $\boldsymbol{\theta}$, the values that maximize L unconditionally. The test statistic for discovery, under the background-only hypothesis, corresponding to $\mu = 0$, is definded as:

$$q_0 = \begin{cases} -2\ln\lambda(0), & \hat{\mu} \geq 0, \\ 0, & \hat{\mu} < 0. \end{cases} \tag{7.5}$$

Since new physics only leads to an increase in the number of observed events, q_0 is 0 for $\hat{\mu} < 0$. Similarly, the test statistic for exclusion limit, under the nomial signal hypotheses including both new physics signal and background ($s + b$ hypothesis) is defined as:

$$q_\mu = \begin{cases} -2\ln\lambda(\mu), & \hat{\mu} \leq \mu, \\ 0, & \hat{\mu} > \mu. \end{cases} \tag{7.6}$$

Since we want to establish upper limits of the signal strength μ, $\hat{\mu} > \mu$ is not taken as part of the rejection region of the test.

Figure 7.1 shows the probability density functions (PDFs) of the test statistic q_0 under the background-only hypothesis, and q_μ under the $s + b$ hypothesis where the former is denoted by $f(q|b) = f(q_0|b)$ and the latter is denoted by $f(q|s+b) = f(q_\mu|s+$

b). For a given observed q^{obs}, the disagreement between the data and hypothesis is described by the p-value which is defined as the probability of observing a test result that is as extreme as the observed result, assuming the hypothesis is true. A small enough p-value means there is enough incompatibility between the data and hypothesis such that we can reject the hypothesis. Based on this definition, we can express the p-value under the background-only hypothesis, p_b and the p-value under the $s + b$ hypothesis, p_{s+b} as:

$$p_b = \int_{-\infty}^{q^{obs}} f(q|b)dq, \tag{7.7}$$

$$p_{s+b} = \int_{q^{obs}}^{\infty} f(q|s+b)dq. \tag{7.8}$$

The significance of the test Z, is defined such that a Gaussian distributed variable found the number of Z standard deviations above the mean has an upper-tail probability equal to the p-value. That is,

$$Z = \Phi^{-1}(1-p), \tag{7.9}$$

where Φ^{-1} stands for the inverse of the cumulative distribution of the Gaussian distribution. In the experimental particle physics community, a test under the background-only hypothesis with a significance of Z above 3 is said to observe the evidence for the existence of new physics, and a test Z above 5 is said to have a discovery, which corresponds to a p-value of 2.87×10^{-7}.

For the purpose of setting exclusion limits, we say that we may exclude a signal model at a confidence level $1 - \alpha = 95\%$ if $p_{s+b} < \alpha = 0.05$. However, in the region where the experiment has little sensitivity, which means the distributions of q_0 and q_μ are highly overlapped with each other, as illustrated in the right plot in Figure 7.1, we tend to get a small value of p_{s+b} and therefore it is more likely to reject the signal hypothesis. A new quantity CL_s is introduced to solve this problem, which is defined as:

$$\mathrm{CL}_s = \frac{p_{s+b}}{1-p_b}. \tag{7.10}$$

As a result, for the region of little sensitivity, p_b is close to 1, and this prevents CL_s to become too small. In addition, since $1 - p_b \leq 1$, then $\mathrm{CL}_s \geq p_{s+b}$, hence upper limits computed with the CL_s method are always conservative.

As deduced from the Wald's and Wilk's theorem (14), q_0 and q_μ follow a χ^2-distribution with one degree of freedom if we have many events, which is referred to as asymptotic formula. Based on the asymptotic formula, the Asimov data set is defined as the data set for which all the Asimov observed quantities are equal to their expected values. The Asimov data set is used, instead of the MC simulation events, to estimate the distribution of the test statistic and optimize the study in order to have the best significance or exclusion limits, which decrease the computational demand significantly. In this analysis, Asimov data sets are used to optimize the exclusion limits for both channels before looking at the real data.

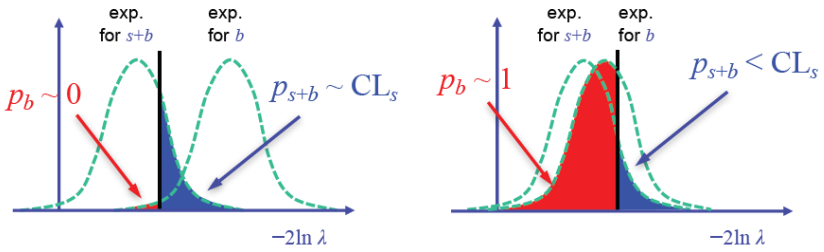

Figure 7.1: Illustration of the CL_s method on cases of well seperated distributions of the test statistic q for the s+b and b hypothesis (left) and in case if largely overlapping distributions (right)

7.2 Likelihood fit in the leptonic channel

In order to test for the presence of the dark matter particles or the VLT a simultaneous fit in the signal and control regions is performed. For the leptonic channel, the distribution of the $E_{\mathrm{T}}^{\mathrm{miss}}$ in the signal region (Figure 7.2) and the number of events in the control regions are used in the fit. In addition, the electron channel and muon channel are combined together for the fit.

Since all other backgrounds except $t\bar{t}$ have very small contribution in the signal region, they are merged together as the non-$t\bar{t}$ process in order to use a binned likelihood which could utilize the shape information from the $E_{\mathrm{T}}^{\mathrm{miss}}$ distribution and also make the fit stable. The normalization uncertainties of the backgrounds are propagated to the non-$t\bar{t}$ background according to their composition in each region.

When performing the fit, the favored fitted nuisance parameter values will differ from the original values, which are provided either from the theoretical predictions or the auxiliary measurements. In this case, we say that the nuisance parameter is pulled. The pull of a nuisance parameter is defined as $(\theta_{\mathrm{fitted}} - \theta_0)/\Delta\theta$, where θ_{fitted} is the fitted value of the nuisance parameter which maximizes the likelihood, θ_0 is the original value and $\Delta\theta$ is the prior uncertainty on the nuisance parameter.

In the rest of this section, the fit using the DM signal sample with $m(v_{\mathrm{met}})$ is used for illustration. Negligible differences are seen for the samples with other mass points of the vector mediator considered. Figure 7.3 shows the pulls of the nuisance parameters with their constraints. The statistical model fit behaves well as most pulls are centered around zero. Several nuisance parameters related to the modeling of $t\bar{t}$ have the largest pulls but are still within the 1σ range. For each nuisance parameter, its impact on the shift of the signal strength, is evaluated by repeating the fit with the NP fixed to the values that are 1σ away from the pre-fit and post-fit expected values, respectively. A pruning process is applied to remove the systematic uncertainties which have an impact less than 1% on either normalization or shape, in order to make the fit stable. The ranking of these NPs, according to their impact on the shift of the signal strength, is shown in Figure 7.3. The leading sources of uncertainties come from the simulation

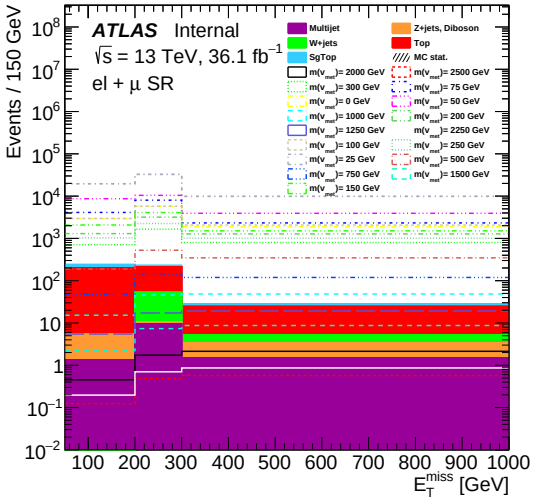

Figure 7.2: Expected signal (non-resonant model) and backgrounds $E_{\mathrm{T}}^{\mathrm{miss}}$ distribution in the signal region defined by $|\eta| < 1.8$ and $m_{\mathrm{T}} > 240GeV$.

statistics in the first two bins of the $E_{\mathrm{T}}^{\mathrm{miss}}$ distribution in the SR is due to the limited number of events we have available, the modeling of the $t\bar{t}$ and the single top t-channel processes.

Figures 7.4 and 7.5 show the post-fit distributions of a selection of kinematic variables in the signal region for the electron and muon channels separately. Three non-resonant DM signal models with $m(v_{\mathrm{met}}) = 200$, 500 and 1500 GeV are also shown. Table 7.1 shows the fitted event yields for the non-resonant DM signal models with $m(v_{\mathrm{met}}) = 1$ and 2 TeV and other backgrounds in the signal region and control regions. No significant excess above the SM is found in the signal region, therefore the expected and observed 95% CL upper limits on the production cross-section are derived based on the procedure and configuration explained in Section 7.1, as a function of the mass of the vector mediator for the non-resonant model, which are illustrated in Figure 7.6.

The results for the DM resonant model and VLT production, which are not competitive with the hadronic channel, and thus will not be used in the combination.

7.3 Likelihood fit in the hadronic channel

A similar likelihood fit and limit setting approach, as described in Section 7.1, is applied in the hadronic channel. For the leptonic channel, the distributions of the M_{T} in the signal region and the control regions are used in the fit. In addition to the non-resonant DM scenario, we also need to make the same study on the resonant DM and VLT cases for the hadronic channel. In order to take into consideration the differences in the kinematics of the various signal models, especially the different ranges of mass points, the binning of the M_{T} is studied to optimize the limit. In the case of the DM models,

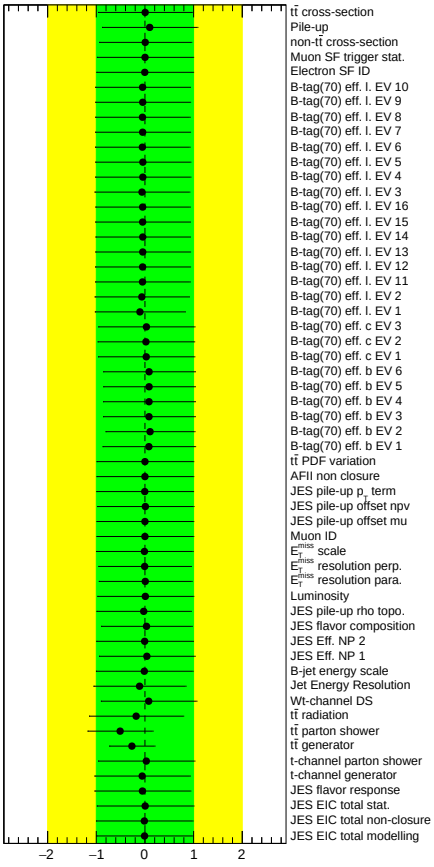

Figure 7.3: Pull plot of the floating parameters in the simultaneous likelihood fit to data.

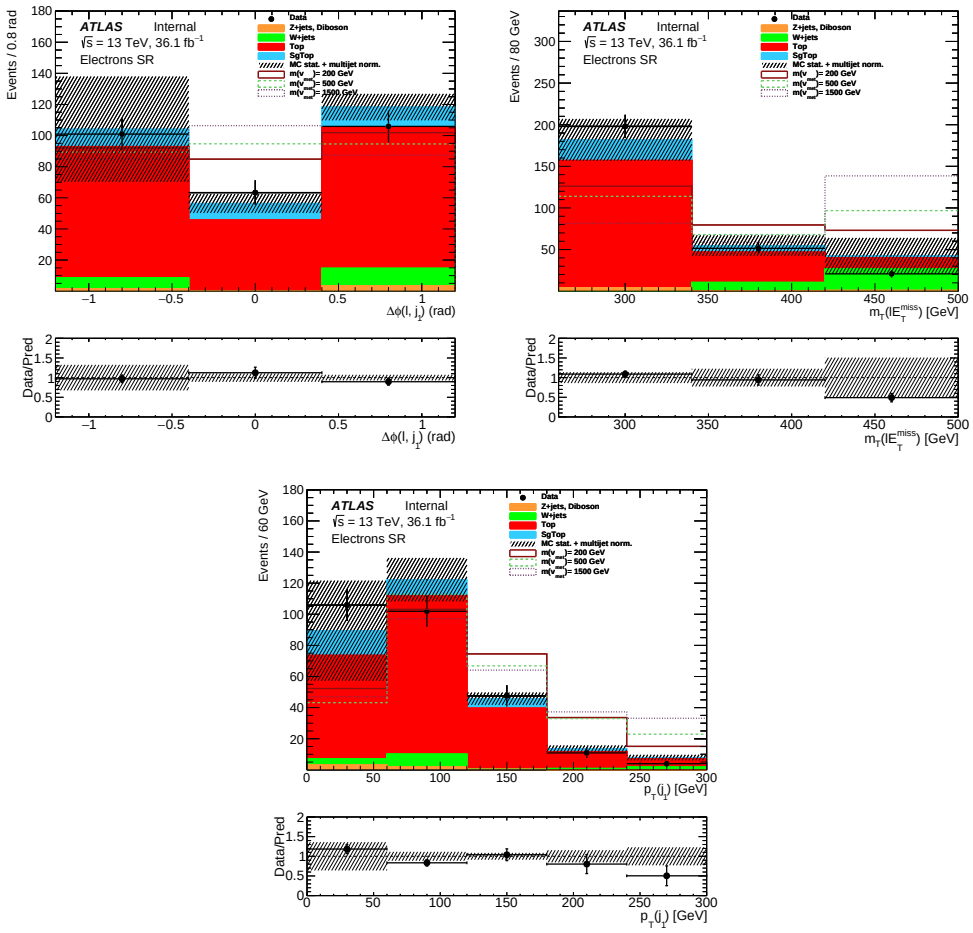

Figure 7.4: The post-fit distributions of the $E_{\mathrm{T}}^{\mathrm{miss}}$, m_{T} and jet p_{T} variables in the SR for the electron channel. Three non-resonant signal models with $m(v_{\mathrm{met}}) = 200$, 500 and 1500 GeV are also shown, normalised to the total expected background yields. The uncertainty band includes the simulation statistics contribution and a 50% normalisation uncertainty for the data-driven multijet background.

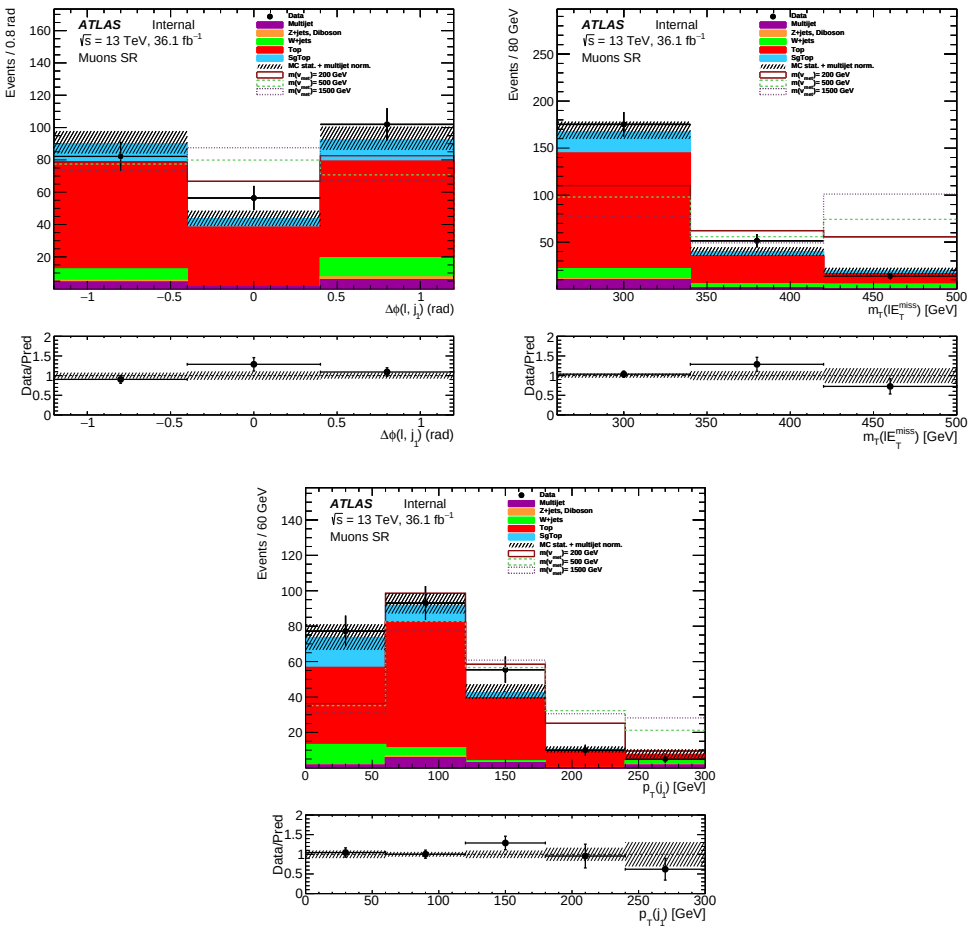

Figure 7.5: The post-fit distributions of the $\Delta\phi(l, j)$, m_{T} and jet p_{T} variables in the SR for the muon channel. Three non-resonant signal models with $m(v_{\mathrm{met}}) = 200$, 500 and 1500 GeV are also shown, normalised to the total expected background yields. The uncertainty band includes the simulation statistics contribution and a 50% normalisation uncertainty for the data-driven multijet background.

	SR	TCR	WCR
NR $(v_{met}) = 1$ TeV	165 ± 23	1.02 ± 0.47	20.2 ± 2.8
NR $(v_{met}) = 2$ TeV	1 ± 0	0 ± 0	4 ± 0
$t\bar{t}$	5797 ± 51	1441 ± 27	1683 ± 30
Single top	4218 ± 40	6111 ± 48	4242 ± 40
W+jets	41074 ± 1714	1091 ± 67	7088 ± 705
Z+jets	1087 ± 182	91 ± 10	169 ± 74
Other	1147 ± 38	0 ± 8	181 ± 18
Total backgrounds	53322 ± 1725	8734 ± 88	13364 ± 711
Data	57273	8440	12825

Table 7.1: The post-fit event yields in the electron channel in the control, validation and signal regions. The uncertainties include the statistical uncertainty of the MC simulation events and the systematic uncertainties.

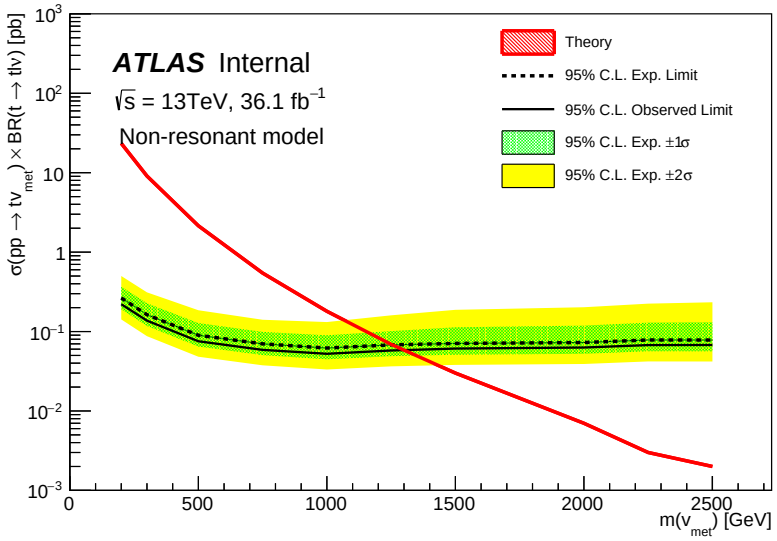

Figure 7.6: Expected 95% CL upper limits on the production cross-section for the non-resonant model in the leptonic channel. The mass of the DM particle is $m_\chi = 1$ GeV while the coupling constant between the massive invisible vector boson and the top quark is $a = 0.2$.

due to the limited statistics in the higher M_{T} region for the $t\bar{t}$ MC samples, the last bin is chosen to start a 1 TeV. Furthermore, in order to improve the limits obtained after the binned likelihood fit, the last bin is split up for the SR to create a larger bin

granularity in the higher M_{T} region. The following binning configurations have been chosen :

- VLT (CRs and SR) : [300, 600, 750, 900, 1000, 3000],
- DM (CRs) : [300, 750, 900, 1000, 3000],
- DM (SR) : [300, 750, 900, 1000, 1450, 3000].

In the rest of this section, the non-resonant DM model with $m(v_{\mathrm{met}}) = 1$ TeV, the resonant DM model with $m_{\phi} = 1$ TeV, and the VLT model with $m_{\mathrm{VLT}} = 900$ GeV are chosen for the illustrations of the pulls, the ranking of uncertainties and the post-fit distributions of the variables. Figure 7.7 shows the pull plots for these three scenarios. We can see that the statistical model fit behaves well and only a few NPs are pulled within the 1σ range, which correspond to the $t\bar{t}$ hard scattering generator and large-R jet τ_{32}^{wta} to compensate for slight discrepancies between data and MC predictions mainly driven by the large number of $t\bar{t}$ events, suffering from the top quark p_{T} mis-modeling effect described above. The impact of the uncertainties on the signal strength is also evaluated and shown in Figure 7.8, similar to that in the leptonic channel.

Figures 7.9 and 7.10 show the pre-fit and post-fit distribution of M_{T} in the signal and the control regions, for the VLT model and DM models where the non-resonant DM model with $m(v_{\mathrm{met}}) = 1$ TeV is shown. Table 7.2 shows the fitted event yields for the sinal and background processes in the signal region and control regions. No significant excess above the SM is found in the signal region, therefore the expected and observed 95% CL upper limits on the production cross-section are derived based on the procedure and configuration explained in Section 7.1, as a function of the mass of the vector mediator for the non-resonant model, as a function of the mass of the scalar particle for the renonant DM model and as a function of the mass of the VLT model, which are illustrated in Figures 7.11, 7.12 and 7.13.

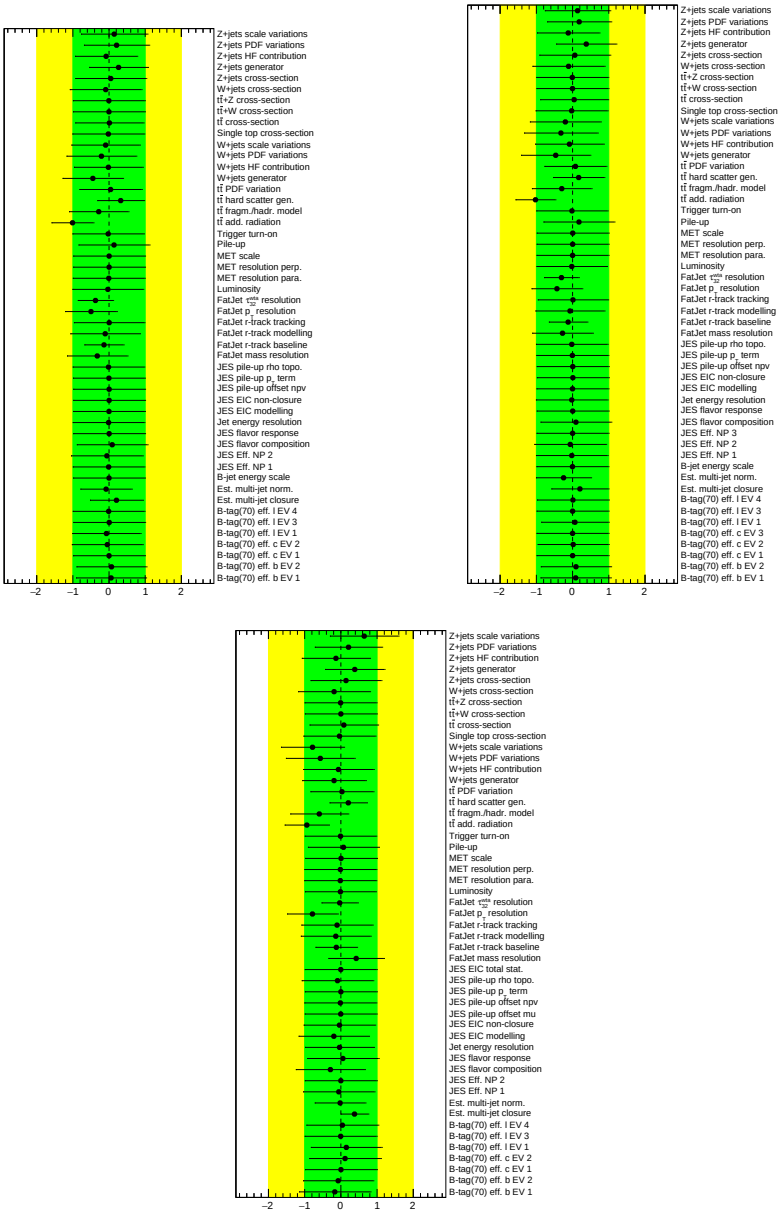

Figure 7.7: Pull on nuisance parameters after the binned likelihood fit to data in the control regions only and under the background only hypothesis. Showing the described properties for the VLT binning (left) and the DM binning (right).

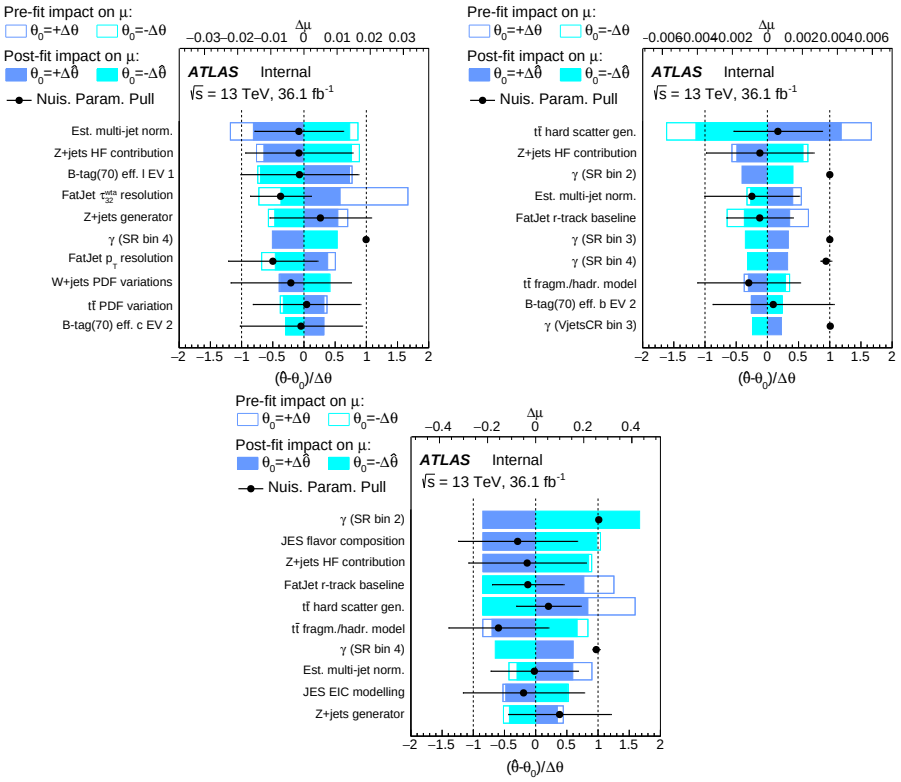

Figure 7.8: Ten systematics ordered by impact on the signal strength during the binned likely hood fit before and after the fit for different signal processes: DM non-resonant with $m_\phi = 1$ TeV (top-left), DM resonant with $m_\phi = 1$ TeV (top-right), WTZt with $m_{\mathrm{VLT}} = 0.9$ TeV, $c^{\mathrm{Zt}} = 0.5$ (bottom). The fit is performed to the unblinded signal region to data.

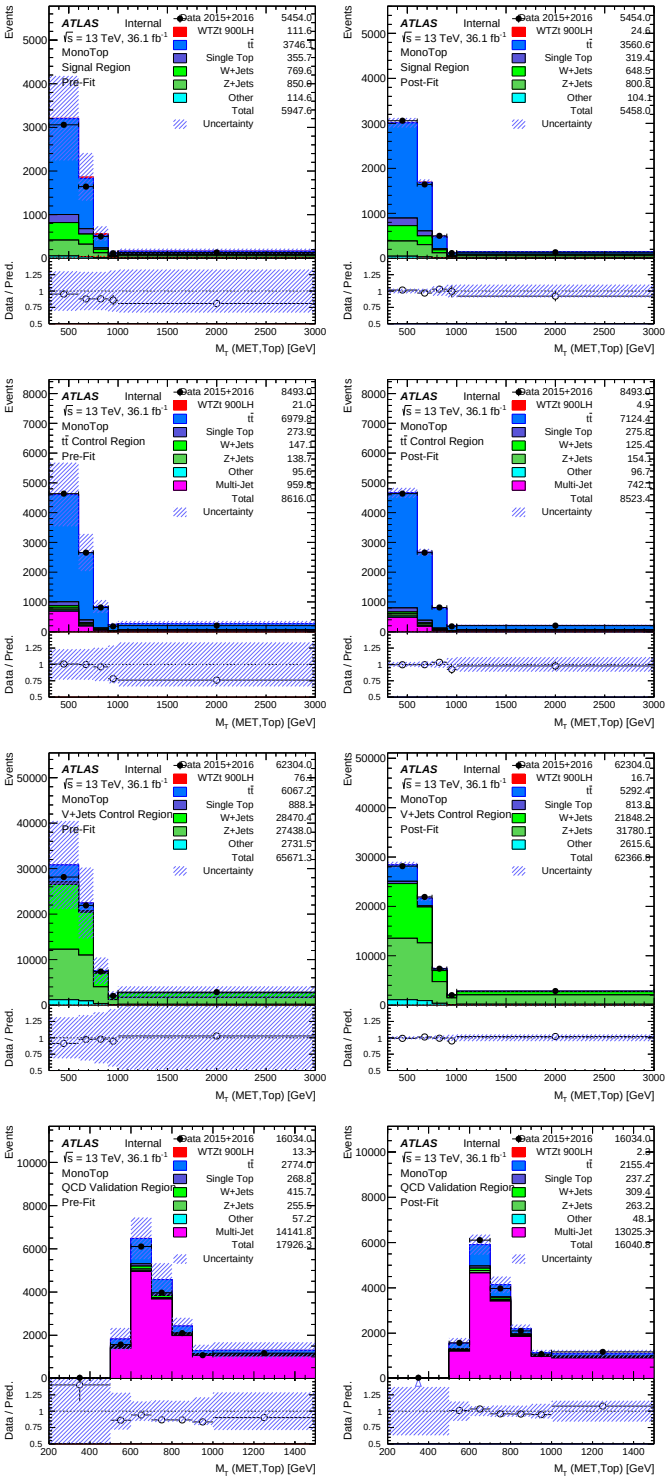

Figure 7.9: Pre- and post-fit plots in signal and control regions after the binned likelihood fit in CRs only to data under the background only hypothesis. The plots shown represent the VLT binning and the signal region with additional forward jet requirement.

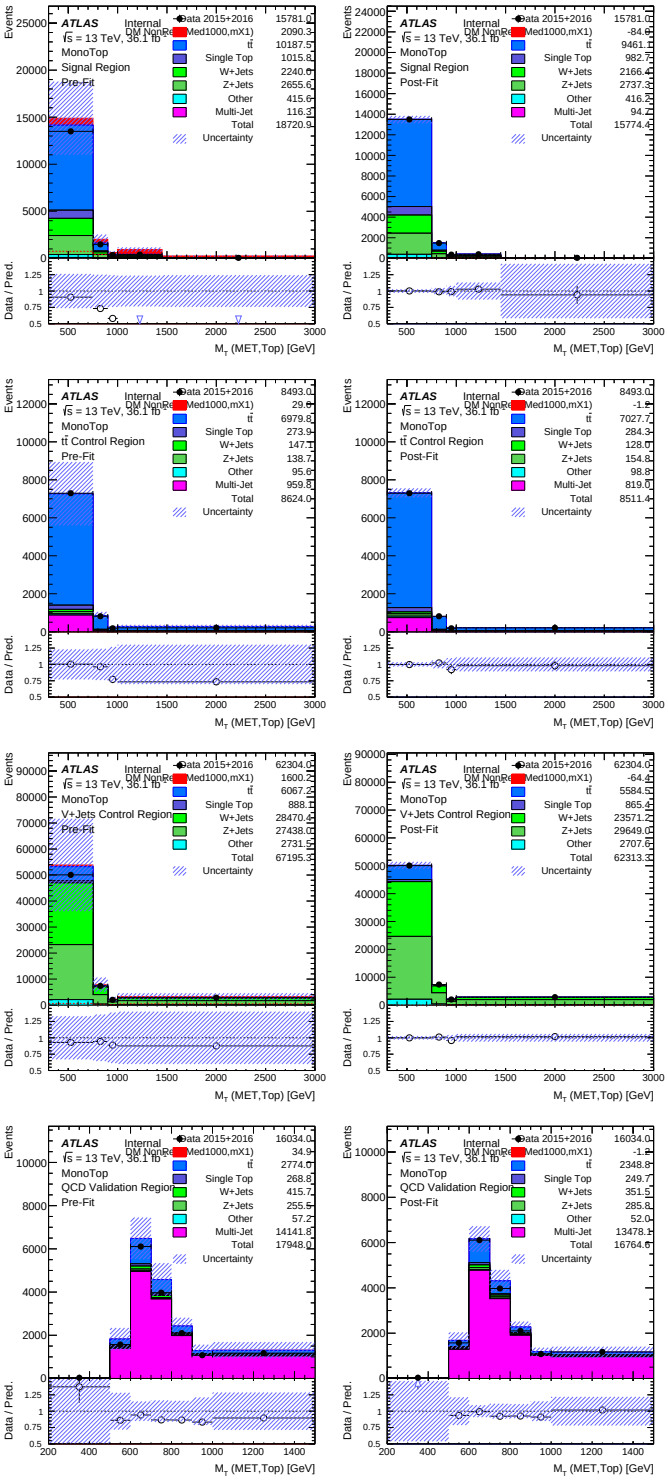

Figure 7.10: Pre- and post-fit plots in signal and control regions after the binned likelihood fit in CRs only to data under the background only hypothesis. The plots shown represent the DM binning and the signal region without additional forward jet requirement.

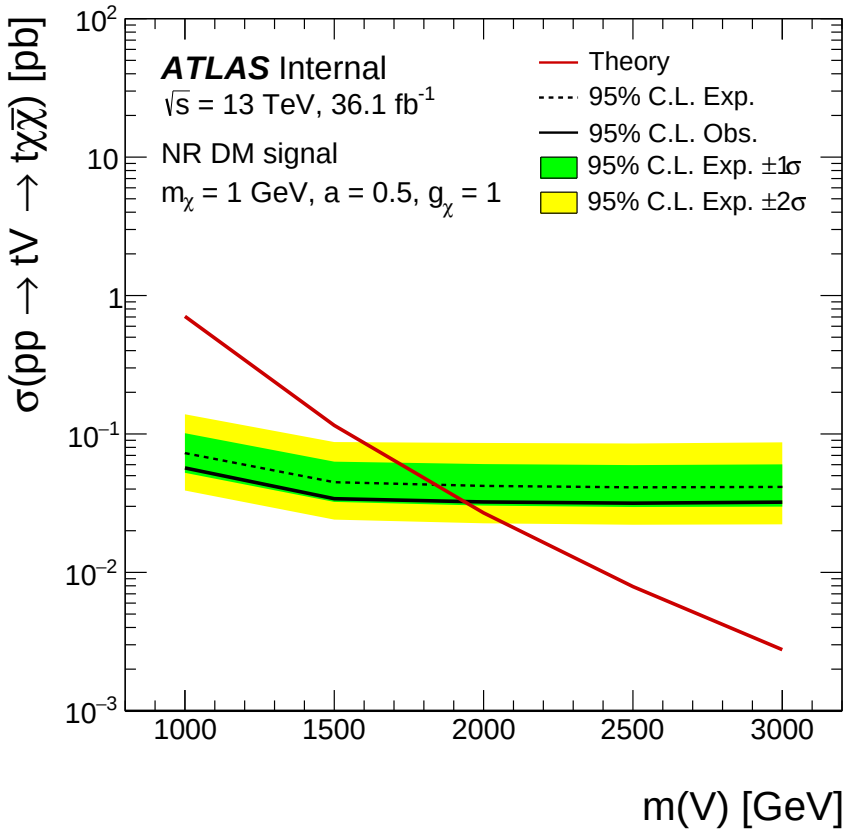

Figure 7.11: Expected and observed 95% CLs on cross-section × branching ratio for different mass points of the non-resonant DM model.

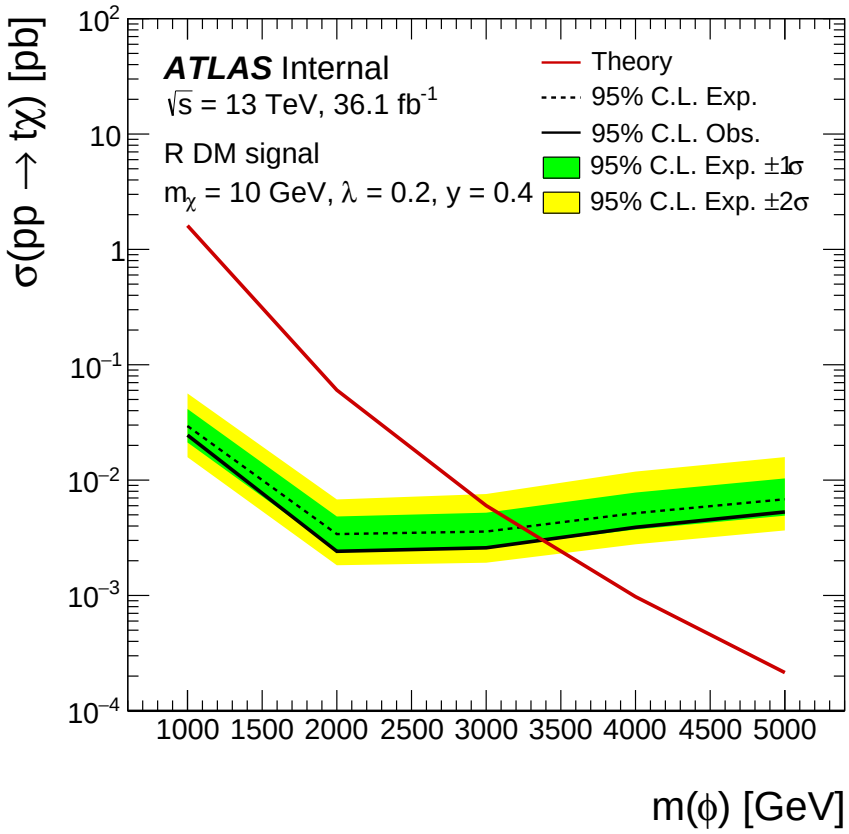

Figure 7.12: Expected and observed 95% CLs on cross-section × branching ratio for different mass points of the resonant DM model.

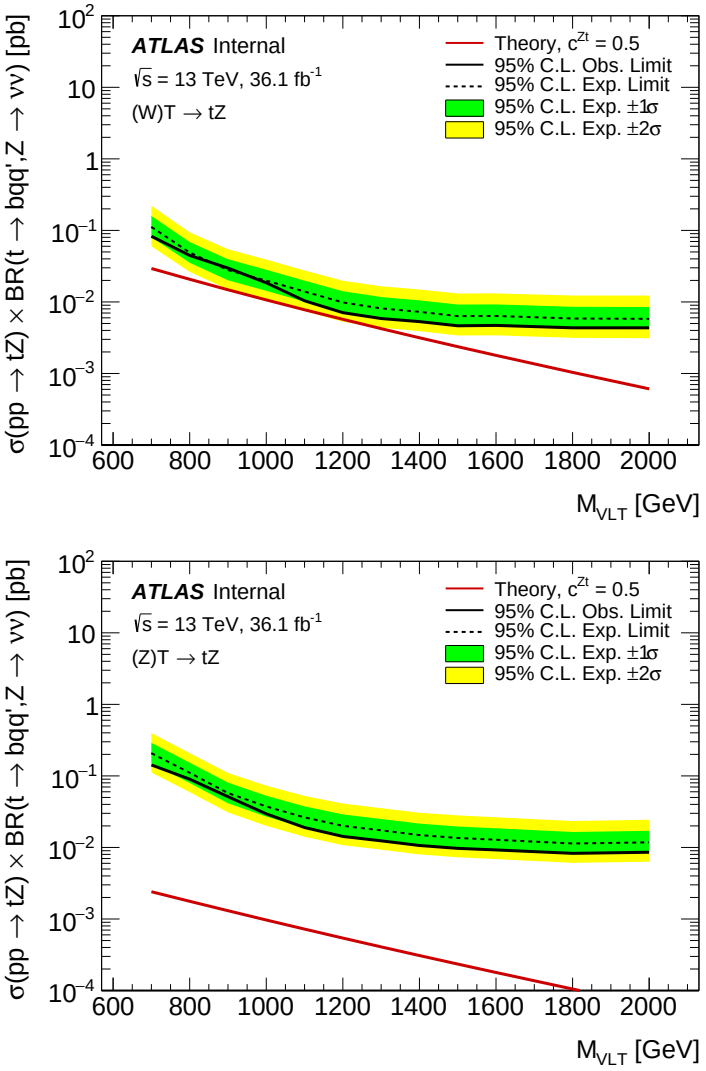

Figure 7.13: Expected and observed 95% CLs on cross-section × branching ratio for different mass points determined at a coupling parameter of $c^{Zt} = 0.5$ of the resonant VLT model produced via the exchange of a W-boson(top) and Z-boson(bottom).

	SR	TCR	WCR
NR (v_{met}) = 1 TeV	165 ± 23	1.02 ± 0.47	20.2 ± 2.8
NR (v_{met}) = 2 TeV	1 ± 0	0 ± 0	4 ± 0
$t\bar{t}$	5797 ± 51	1441 ± 27	1683 ± 30
Single top	4218 ± 40	6111 ± 48	4242 ± 40
W+jets	41074 ± 1714	1091 ± 67	7088 ± 705
Z+jets	1087 ± 182	91 ± 10	169 ± 74
Other	1147 ± 38	0 ± 8	181 ± 18
Total backgrounds	53322 ± 1725	8734 ± 88	13364 ± 711
Data	57273	8440	12825

Table 7.2: The post-fit event yields in the electron channel in the control, validation and signal regions. The uncertainties include the statistical uncertainty of the MC simulation events and the systematic uncertainties.

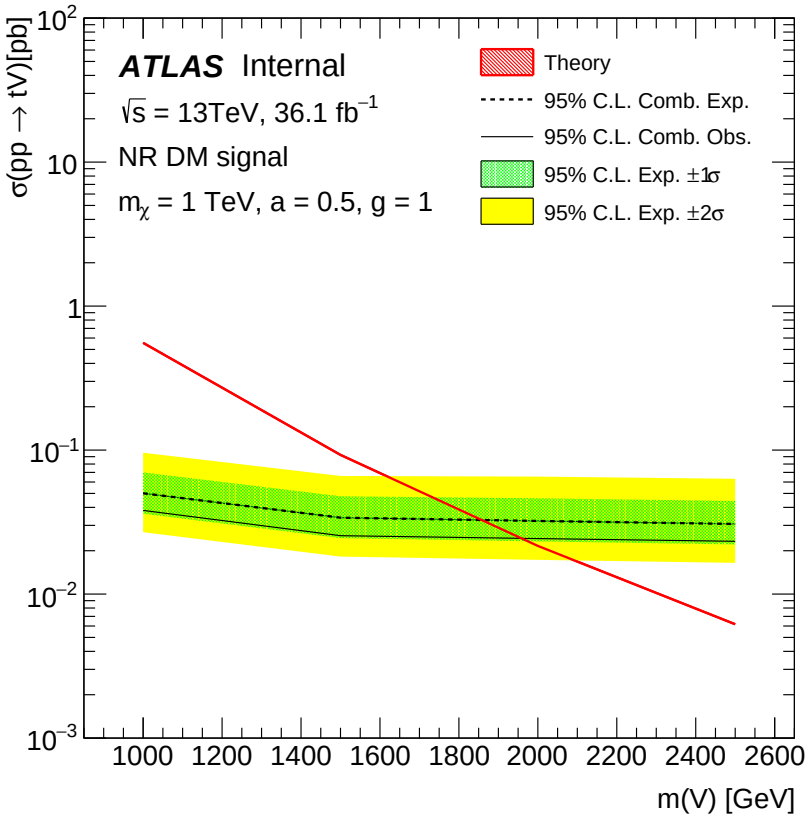

Figure 7.14: Expected and observed 95% CLs on cross-section for different mass points of the non-resonant DM model after the combined likelihood fit in lepton plus hadron channels.

7.4 Statistical combination of the results for the non-resonant DM model

Since the expected sensitivities of the lepton and hadron channels for the non-resonant Dark Matter model are comparable (*c.f.* Figure 7.6 and 7.11), the inputs in the signal and control regions used for this model in both channels will be combined in a single likelihood fit to data. The expected and observed 95% CL upper limits on the production cross-section are shown in Figure 7.14.

7.5 Two-dimensinal exclusion regions

We also calculate the two-dimensional exclusion regions in the plane formed by the mediator mass, the DM particle mass, and the couplings between the mediator, the DM particle and the SM fermions. In order to have smooth contours in the plane, we need many samples with different mass points or couplings while we only have a few

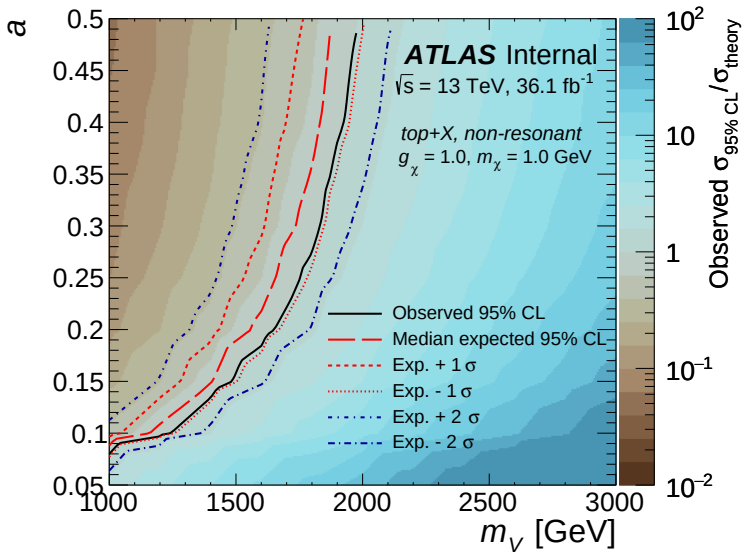

Figure 7.15: The ratios of the observed and expected 95% C.L. upper limits on the signal cross section to the predicted signal cross sections for the non-resonant model in the (a,m_V) plane.

of them. It is not viable to request the production of all these samples. Therefore a resampling technique is adopted in order to get the distribution of the variable of interest for these samples. First, we request a fully simulated and reconstructed sample with rich statistics, e.g. 10 times the number of events available in a current sample, which is called the benchmark sample. Then we generate samples with a variety of mass points and couplings up to the generator level which are called the test samples. We derive bin-by-bin weights by comparing the distribution of the variable of interest, such as $E_{\mathrm{T}}^{\mathrm{miss}}$ between the benchmark sample and the test samples at generator level. Then we apply the weights on the distribution of $E_{\mathrm{T}}^{\mathrm{miss}}$ from the benchmark sample at the reconstructed level in order to get the distribution of $E_{\mathrm{T}}^{\mathrm{miss}}$ for these test samples. This technique is validated using the fully simulated and reconstructed signal samples used in this analysis. The systematic uncertainty introduced by this technique on the signal normalization, is estimated from dedicated MC samples to be 10% for the non-resonant DM model and 25% for the resonant DM model.

The observed and expected 95% CL limit contours for the signal strength $\sigma^{\mathrm{obs}}/\sigma^{\mathrm{th}}$ are shown in Figures 7.15, 7.16, and 7.17 for the non-resonant model, where $\sigma_{95\%\ \mathrm{CL}}$ is the observed limit on the model cross section at a given point of the parameter space and σ_{theory} is the predicted cross section in the model at the same point. In the scenario of the resonant DM model, Figures7.18, 7.19 show the observed and expected 95% CL limit contours for the signal strength $\sigma^{\mathrm{obs}}/\sigma^{\mathrm{th}}$.

The reduced sensitivity to the single VLT production (*c.f.* Figure 7.13) implies that there is also a reduced sensitivity to the corresponding coupling. This can be seen in Figure 7.20a, which shows the expected and observed 95% CL upper limits on c_W,

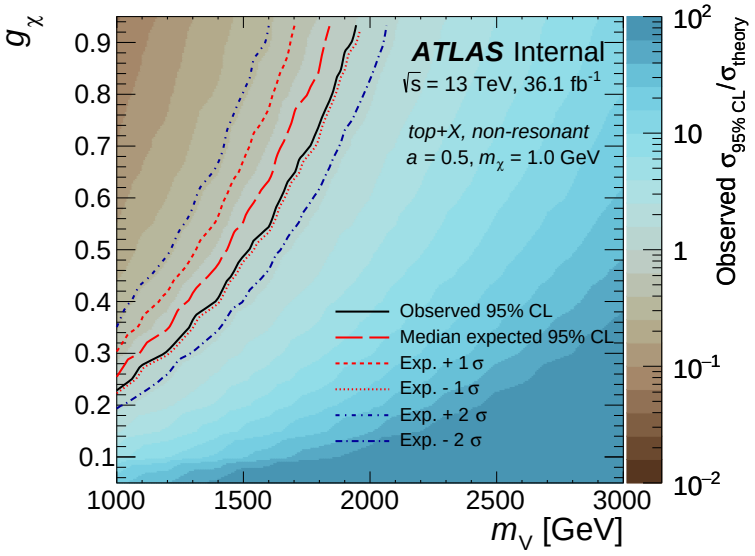

Figure 7.16: The ratios of the observed and expected 95% C.L. upper limits on the signal cross section to the predicted signal cross sections for the non-resonant model in the (g_χ,m_V) plane.

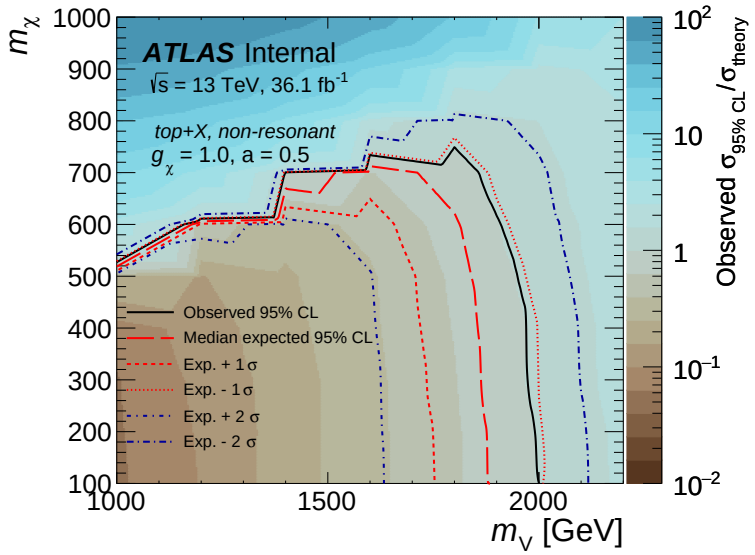

Figure 7.17: The ratios of the observed and expected 95% C.L. upper limits on the signal cross section to the predicted signal cross sections for the non-resonant model in the (m_χ,m_V) plane.

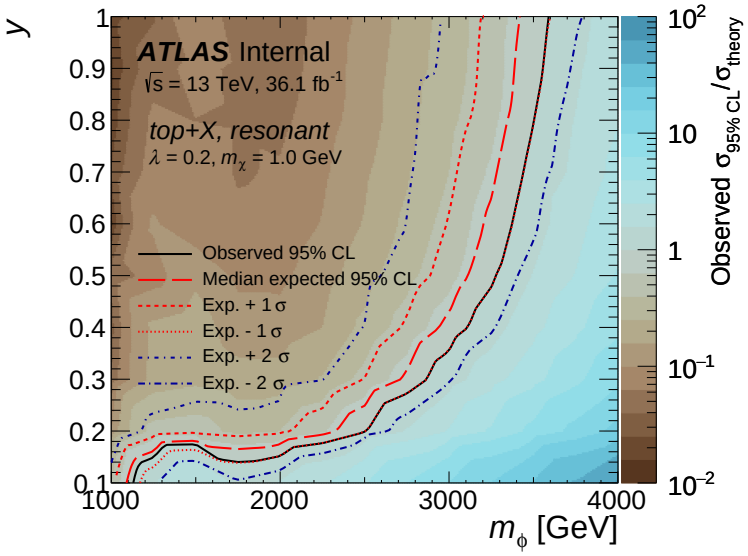

Figure 7.18: The ratios of the observed and expected 95% C.L. upper limits on the signal cross section to the predicted signal cross sections for the resonant model in the (y,m_ϕ) plane.

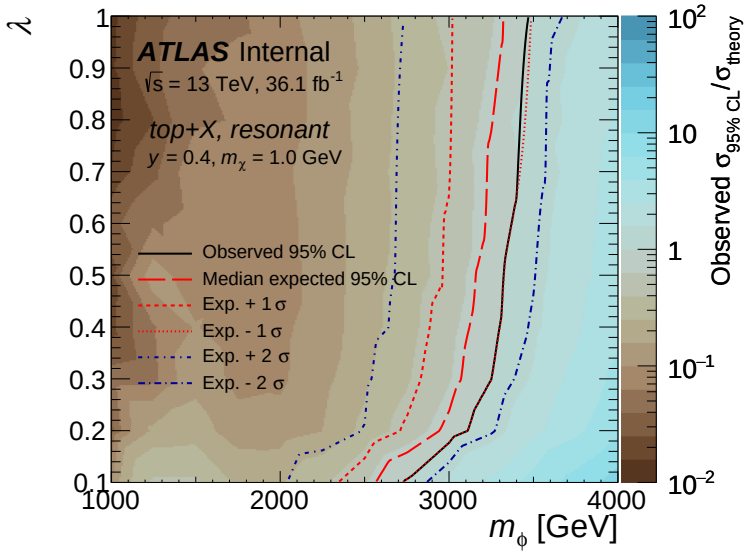

Figure 7.19: The ratios of the observed and expected 95% C.L. upper limits on the signal cross section to the predicted signal cross sections for the resonant model in the (λ,m_ϕ) plane.

taken as the quadratic sum of the left- and right-handed couplings $c_{L,W}$ and $c_{R,W}$, as a function of the VLT mass. Nonetheless, the sensitivity remains approximately constant for masses up to 1.4 TeV. A singlet T, which corresponds to a BR to Zt of $\approx 25\%$ over the mass range studied in this analysis, was assumed. The obtained limits on c_W can also be translated into expected and observed 95% CL upper limits for the mixing angle of a singlet T with the SM top quark, as shown in Figure 7.20b.

7.6 Conclusions

There are still many questions that remain unanswered by the SM. Such as the so-called hierarchy problem, that is why the Higgs mass is so much smaller than the Planck mass, which can be explained via Supersymmetry and other BSM models which introduce the vector like quarks. The SM also does not explain the dark matter, which is confirmed to exist by several cosmological experiments.

This thesis describes the search for the dark matter particles and the VLT in the final states with large $E_{\mathrm{T}}^{\mathrm{miss}}$ and a single top-quark, from the proton-proton collisions at LHC at $\sqrt{s} = 13$ TeV, using the data collected by the ATLAS detector in 2015 and 2016 which corresponds to a total integrated luminosity of 36.1 fb^{-1}. Since the data agree to within measurement uncertainties with the SM, 95% CL upper limits are set on the production cross-section of the three scenarios we consider: the non-resonant and resonant DM models and the VLT model with the VLT decaying into $tZ(\rightarrow \nu\bar{\nu})$. For the DM production in the resonant scenario, masses of the a new vectorial particle coupling to the DM candidate up to 2 TeV are excluded at 95% CL for $m_\chi = 1$ TeV, $g_\chi = 1.0$ and $a = 0.5$, while in the resonant case, masses of the new scalar coupling to the DM up to 3.5 TeV are excluded at 95% CL for $m_\chi = 1$ TeV, $y = 0.4$ and $\lambda = 0.2$. For the production of T singlets, couplings of these new quarks to top-quarks and W bosons, c_W, above 0.7 are excluded for $m_{\mathrm{T}} = 1.4$ TeV and below. These limits are also interpreted in terms of the two-dimensional excluded regions on the parameter space considered in the BSM models.

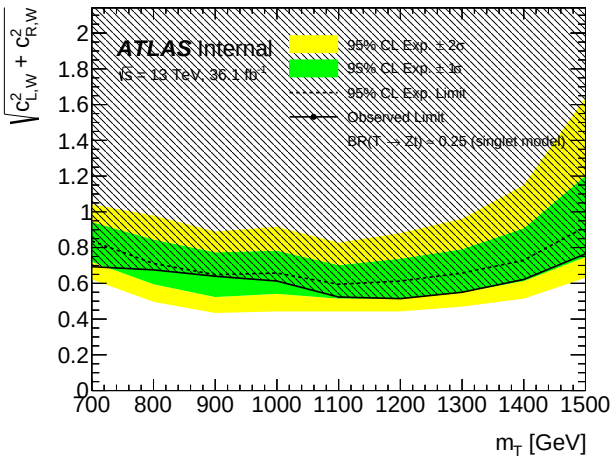

(a)

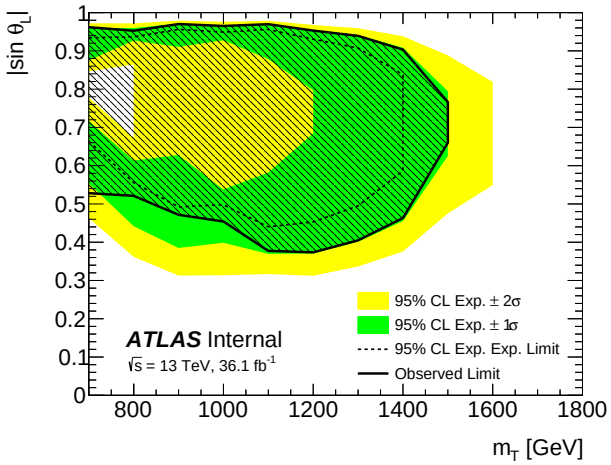

(b)

Figure 7.20: Expected and observed 95% CL limits from the combination of the single-production channels on (a) the coupling of the T quark to SM particles, $c_W = \sqrt{c_{L,W}^2 + c_{R,W}^2}$ assuming a singlet T, corresponding to a BR of $\approx 25\%$; and (b) the absolute value of $\sin(\theta_L)$, with θ_L being the mixing angle of a singlet T with the SM top quark. The shaded area corresponds to the observed exclusion at 95% CL.

References

[1] F.Hasert et al, *Search for elastic muon-neutrino electron scattering*, Phys. Lett. B **46** (1973), 121 1

[2] F.Hasert et al, *Observation of neutrino-like interactions without muon or electron in the gargamelle neutrino experiment*, Phys. Lett. B **46** (1973), 138 1

[3] UA1 Collaboration, *Experimental Observation of Isolated Large Transverse Energy Electrons with Associated Missing Energy at* $\sqrt{s}$ *= 540-GeV*, Phys.Lett. B **122** (1983), 103 1

[4] UA2 Collaboration, *Observation of Single Isolated Electrons of High Transverse Momentum in Events with Missing Transverse Energy at the CERN* $p\bar{p}$ *Collider*, Phys. Lett. B, **122** (1983):476. 1

[5] UA1 Collaboration, *Experimental Observation of Lepton Pairs of Invariant Mass Around 95 GeV/*c^2 *at the CERN SPS Collider*, Lett. B, **126** (1983):398. 1

[6] ATLAS Collaboration, *Observation of a new particle in the search for the Standard Model Higgs boson with the ATLAS detector at the LHC*, Phys. Lett. B **716** (2012), 1, arXiv:1207.7214 [hep-ex] 1

[7] CMS Collaboration, *Observation of a new boson at a mass of 125 GeV with the CMS experiment at the LHC*, Phys. Lett. B **716** (2012), 30, arXiv:1207.7235 [hep-ex]. 1

[8] , *Baryon asymmetry*, `https://en.wikipedia.org/wiki/Baryon_asymmetry`. 1

[9] F. Zwicky, *Spectral displacement of extra galactic nebulae*, Helv.Phys., **6** (1933):110. 1

[10] A. Refregier, *Weak Gravitational Lensing by Large-Scale Structure*, Ann.Rev.Astron.Astrophys., **41** (2003):645. 1

[11] J. A. Tyson, G. P. Kochanski, and I. P. Dell'Antonio, *Detailed Mass Map of CL0024+1654 from Strong Lensing*, Astrophys. J., **498** (1998):L107. 1

[12] E. Komatsu et al, *Seven-Year Wilkinson Microwave Anisotropy Probe (WMAP) Observations: Cosmological Interpretation*, Astrophys. J., **192** (2011): 18. 1

[13] Super-Kamiokande Collaboration, *Evidence for oscillation of atmospheric neutrinos*, Phys.Rev.Lett. 81 (1998) 1562, arXiv:hep-ex/9807003 [hep-ex]. 1, 2

[14] M.Peskin and D.Schroeder, *An Introduction To Quantum Field Theory*, Westview Press, 1995. 1, 4, 6, 101

[15] *Figure of Standard Model*, `https://en.wikipedia.org/wiki/Standard_Model/media/File:Standard_Model_of_Elementary_Particles.svg`. vii, 2

[16] N. Arkani-Hamed, A. Cohen, E. Katz and A. Nelson, *The littlest Higgs*, JHEP **07** (2002) 34, arXiv: 0206021 [hep-ph]. 6

[17] M. Schmaltz and D. Tucker-Smith, *Little Higgs Theories*, Ann. Rev. Nucl. Part. Sci. **55** (2005) 229, arXiv: 0502182 [hep-ph]. 6

[18] D. B. Kaplan, H. Georgi and S. Dimopoulos, *Composite Higgs scalars*, Physics Letters B **136** (1984) 187. 6

[19] K. Agashe, R. Contino and A. Pomarol, *The minimal composite Higgs model*, Nucl. Phys. B **719** (2005) 165, arXiv: 0412089 [hep-ph]. 6

[20] J. Andrea, B. Fuks and F. Maltoni, *Monotops at the LHC*, Phys. Rev. D **84** (2011) 074025, arXiv: 1106.6199 [hep-ph]. vii, 7, 9

[21] J.-L. Agram et al., *Monotop phenomenology at the Large Hadron Collider*, Phys.Rev. D **89** (2014) 014028, arXiv: 1311.6478 [hep-ph]. 9

[22] I. Boucheneb et al., *Revisiting monotop production at the LHC*, JHEP **1501** (2015) 017, arXiv: 1407.7529 [hep-ph]. 9

[23] J. Wang, C. S. Li, D. Y. Shao and H. Zhang, *Search for the signal of monotop production at the early LHC*, Phys. Rev. D **86** (2012) 034008, arXiv: 1109.5963 [hep-ph]. 9

[24] K. G. Begeman, A. H. Broeils, and R. H. Sanders, *Extended rotation curves of spiral galaxies: Dark haloes and modified dynamics*, Mon. Not. Roy. Astron. Soc. **249** (1991) 523. vii, 8

[25] Space Telescope Science Institute, *v1.0 Data products for Epoch 1 of Abell 370*, Public data, 2016. `http://www.stsci.edu/hst/campaigns/frontier-fields/`. vii, 8, 9

[26] D. Abercrombie et al.,

[27] , (2015), ed. by A. Boveia, C. Doglioni, S. Lowette, S. Malik and S. Mrenna, arXiv: 1507.00966 [hep-ex]. 9

[28] ATLAS Collaboration, *Search for dark matter and other new phenomena in events with an energetic jet and large missing transverse momentum using the ATLAS detector*, JHEP **01** (2018) 126, arXiv: 1711.03301 [hep-ex].

[29] CMS Collaboration, *Search for dark matter produced with an energetic jet or a hadronically decaying W or Z boson at $\sqrt{s}$ = 13 TeV*, JHEP **07** (2017) 014, arXiv: 1703.01651 [hep-ex]. 7

[30] ATLAS Collaboration, *Search for dark matter produced in association with bottom or top quarks in $\sqrt{s}$ = 13 TeV pp collisions with the ATLAS detector*, Eur. Phys. J. C **78** (2018) 18, arXiv: 1710.11412 [hep-ex]. 7

[31] ATLAS Collaboration, *Search for top-squark pair production in final states with one lepton, jets, and missing transverse momentum using 36 fb^{-}1 of $\sqrt{s}$ = 13 TeV pp collision data with the ATLAS detector*, JHEP **06** (2018) 108, arXiv: 1711.11520 [hep-ex]. 7

[32] ATLAS Collaboration, *Search for dark matter at $\sqrt{s}$ = 13 TeV in final states containing an energetic photon and large missing transverse momentum with the ATLAS detector*, Eur. Phys. J. C **77** (2017) 393, arXiv: 1704.03848 [hep-ex]. 7

[33] CMS Collaboration, *Search for new physics in the monophoton final state in proton-proton collisions at $\sqrt{s}$ = 13 TeV*, JHEP **10** (2017) 073, arXiv: 1706.03794 [hep-ex]. 7

[34] CMS Collaboration, *Search for dark matter produced with an energetic jet or a hadronically decaying W or Z boson at $\sqrt{s}$ = 13 TeV*, JHEP **07** (2017) 014, arXiv: 1703.01651 [hep-ex]. 7

[35] ATLAS Collaboration, *Search for dark matter in events with a hadronically decaying vector boson and missing transverse momentum in pp collisions at $\sqrt{s}$ = 13 TeV with the ATLAS detector*, JHEP **10** (2018) 180, arXiv: 1807.11471 [hep-ex]. 7

[36] ATLAS Collaboration, *Search for an invisibly decaying Higgs boson or dark matter candidates produced in association with a Z boson in pp collisions at $\sqrt{s}$ = 13 TeV with the ATLAS detector*, Phys. Lett. B **776** (2018) 318, arXiv: 1708.09624 [hep-ex]. 7

[37] ATLAS Collaboration, *Search for Dark Matter Produced in Association with a Higgs Boson Decaying to $b\bar{b}$ using 36 fb^{-1} of pp collisions at $\sqrt{s}$ = 13 TeV with the ATLAS Detector*, Phys. Rev. Lett. **119** (2017) 181804, arXiv: 1707.01302 [hep-ex]. 7

[38] ATLAS Collaboration, *Search for dark matter in association with a Higgs boson decaying to two photons at $\sqrt{s}$ = 13 TeV with the ATLAS detector*, Phys. Rev. D **96** (2017) 112004, arXiv: 1706.03948 [hep-ex]. 7

[39] CMS Collaboration, *Search for associated production of dark matter with a Higgs boson decaying to $b\bar{b}$ or $\gamma\gamma$ at $\sqrt{s}$ = 13 TeV*, JHEP **10** (2017) 180, arXiv: 1703.05236 [hep-ex]. 7

[40] CMS Collaboration, *Search for dark matter produced in association with a Higgs boson decaying to $\gamma\gamma$ or $\tau^+\tau^-$ at $\sqrt{s}$ = 13 TeV*, JHEP **09** (2018) 046, arXiv: 1806.04771 [hep-ex]. 7
7

[41] P. Bryant and L. Evans, *LHC Machine*, JINST, **3**:S08001, 2008. 11

[42] ATLAS Collaboration, *Luminosity Public Results*, ATLAS public plots.
`https://twiki.cern.ch/twiki/bin/view/AtlasPublic/LuminosityPublicResultsRun2`
vii, 13

[43] ATLAS Collaboration, *The ATLAS Experiment at the CERN Large Hadron Collider*. JINST, **3** (2008): S08003. vii, viii, 16, 18, 19, 20, 21, 22, 23, 24, 26

[44] Inspirehep public page.
`https://twiki.cern.ch/twiki/bin/view/AtlasPublic/LuminosityPublicResultsRun2`.
vii, 17

[45] ATLAS Collaboration, *The ATLAS Level-1 Topological Trigger performance in Run 2*. J. Phys. Conf. Ser. **898**, no.3, 032037. 25

[46] ATLAS Collaboration, *The ATLAS Simulation Infrastructure*, Eur. Phys. J. C **70** (2010) 823, arXiv: 1005.4568 [hep-ex]. 40

[47] ATLAS Collaboration, *Performance of the Fast ATLAS Tracking Simulation (FATRAS) and the 1763 ATLAS Fast Calorimeter Simulation (FastCaloSim) with single particles*, ATL-SOFT-PUB-2014-01, 2014,
`https://cds.cern.ch/record/1669341`. 40

[48] J. Alwall et al., *The automated computation of tree-level and next-to-leading order differential cross sections, and their matching to parton shower simulations*, JHEP **07** (2014) 079, axXiv: 1405.0301 [hep-ph]. 40

[49] R. D. Ball et al., *Parton distributions for the LHC Run II*, JHEP **04** (2015) 040, arXiv: 1410.8849 [hep-ph]. 40

[50] T. Sjostrand, S. Mrenna and P. Skands, *A brief introduction to PYTHIA 8.1*, Comput. Phys. Commun. **178** (2008) 852, arXiv: 0710.3820 [hep-ph]. 40

[51] ATLAS Collaboration, *ATLAS Run 1 Pythia8 tunes*, ATL-PHYS-PUB-2014-021, 2014,
`https://cds.cern.ch/record/1966419`. 40

[52] R. D. Ball et al., *Parton distributions with LHC data*, Nucl. Phys. B **867** (2013) 244, arXiv: 1207.1303 [hep-ph]. 40

[53] O. Matsedonskyi, G. Panico and A. Wulzer, *On the interpretation of Top Partners searches*, JHEP **12** (2014) 097, arXiv: 1409.0100 [hep-ph]. 41

[54] P. Nason, *A new method for combining NLO QCD with shower Monte Carlo algorithms*, JHEP **11** (2004) 040, arXiv: hep-ph/0409146. 42

[55] S. Frixione, P. Nason and C. Oleari, *Matching NLO QCD computations with parton shower simulations: the POWHEG method*, JHEP **11** (2007) 070, arXiv: 0709.2092 [hep-ph]. 42

[56] S. Alioli, P. Nason, C. Oleari and E. Re, *general framework for implementing NLO calculations in shower Monte Carlo programs: the POWHEG BOX*, JHEP **06** (2010) 043, arXiv: 1002.2581 [hep-ph]. 42

[57] S. Frixione, P. Nason and G. Ridolfi, *A positive-weight next-to-leading-order Monte Carlo for heavy flavour hadroproduction*, JHEP **09** (2007) 126, arXiv: 0707.3088 [hep-ph]. 42

[58] R. Frederix, E. Re and P. Torrielli, *Single-top t-channel hadroproduction in the four-flavour scheme with POWHEG and aMC@NLO*, JHEP **09** (2012) 130, arXiv: 1207.5391 [hep-ph]. 42

[59] E. Re, *Single-top Wt-channel production matched with parton showers using the POWHEG method*, Eur. Phys. J. C **71** (2011) 1547, arXiv: 1009.2450 [hep-ph]. 42

[60] S. Alioli, P. Nason, C. Oleari and E. Re, *NLO single-top production matched with shower in POWHEG: s- and t-channel contributions*, JHEP **09** (2009) 111, arXiv: 0907.4076 [hep-ph], Erratum: JHEP **02** (2010) 011. 42

[61] T. Sjöstrand, S. Mrenna and P. Z. Skands, *PYTHIA 6.4 physics and manual*, JHEP **05** (2006) 026, arXiv: hep-ph/0603175. 42

[62] H.-L. Lai et al., *New parton distributions for collider physics*, Phys. Rev. D **82** (2010) 074024, arXiv: 1007.2241 [hep-ph]. 42

[63] J. Pumplin et al., *New Generation of Parton Distributions with Uncertainties from Global QCD Analysis*, JHEP **07** (2002) 012, arXiv: hep-ph/0201195. 42

[64] P. Z. Skands, *Tuning Monte Carlo generators: The Perugia tunes*, Phys. Rev. D **82** (2010) 074018, arXiv: 1005.3457 [hep-ph]. 42

[65] T. Gleisberg et al., *Event generation with SHERPA 1.1*, JHEP **02** (2009) 007, arXiv: 0811.4622 [hep-ph]. 42

[66] T. Gleisberg and S. Höche, *Comix, a new matrix element generator*, JHEP **12** (2008) 039, arXiv: 0808.3674 [hep-ph]. 42

[67] F. Cascioli, P. Maierhofer and S. Pozzorini, *Scattering Amplitudes with Open Loops*, Phys. Rev. Lett. **108** (2012) 111601, arXiv: 1111.5206 [hep-ph]. 42

[68] S. Schumann and F. Krauss, *A Parton shower algorithm based on Catani-Seymour dipole factorisation*, JHEP **03** (2008) 038, arXiv: 0709.1027 [hep-ph]. 42

[69] S. Höche, F. Krauss, M. Schönherr and F. Siegert, *QCD matrix elements + parton showers: The NLO case*, JHEP **04** (2013) 027, arXiv: 1207.5030 [hep-ph]. 42

[70] R. D. Ball et al., *Parton distributions for the LHC Run II*, JHEP **04** (2015) 040, arXiv: 1410.8849 [hep-ph]. 42

[71] ATLAS Collaboration, *Measurement of the Z/γ^* boson transverse momentum distribution in pp collisions at $\sqrt{s}$ = 7 TeV with the ATLAS detector*, JHEP **09** (2014) 145, arXiv: 1406.3660 [hep-ex]. 42

[72] M. Czakon and A. Mitov, *Top++: A program for the calculation of the top-pair cross-section at hadron colliders*, Comput. Phys. Commun. **185** (2014) 2930, arXiv: 1112.5675 [hep-ph]. 42

[73] S. Catani, L. Cieri, G. Ferrera, D. de Florian and M. Grazzini, *Vector Boson Production at Hadron Colliders: A Fully Exclusive QCD Calculation at Next-to-Next-to-Leading Order*, Phys. Rev. Lett. **103** (2009) 082001, arXiv: 0903.2120 [hep-ph]. 42

[74] ATLAS Collaboration, *Electron efficiency measurements with the ATLAS detector using the 2015 LHC proton–proton collision data*, ATLAS-CONF-2016-024, 2016, `https://cds.cern.ch/record/2157687` viii, 27, 29

[75] W. Lampl et al., *Calorimeter Clustering Algorithms: Description and Performance*, ATL-LARG-PUB-2008-002, 2008. 27

[76] T. G. Cornelissen, M. Elsing, I. Gavrilenko, J. F. Laporte, W. Liebig, M. Limper, K. Nikolopoulos, A. Poppleton, and A. Salzburger, *The global χ^2 track fitter in ATLAS*, J. Phys. Conf. Ser. **119** (2008) 032013. 28

[77] ATLAS Collaboration, *Improved electron reconstruction in ATLAS using the Gaussian Sum Filter-based model for bremsstrahlung*, ATLAS-CONF-2012-047, 2012, `http://cdsweb.cern.ch/record/1449796`. 28

[78] ATLAS Collaboration, *Electron efficiency measurements with the ATLAS detector using the 2012 LHC proton–proton collision data*, ATLAS-CONF-2014-032, 2014, `http://cdsweb.cern.ch/record/1706245`. 28

[79] ATLAS Collaboration, *Electron and photon energy calibration with the ATLAS detector using LHC Run 1 data*, Eur. Phys. J. C, **74**:3071, 2014 28

[80] ATLAS Collaboration, *Muon reconstruction performance of the ATLAS detector in protonproton collision data at $\sqrt{s}$ =13 TeV*, Eur. Phys. J. **C76** (2016) 292, arXiv:1603.05598 [hep-ex]. viii, 30, 31, 32

[81] M. Cacciari, G. P. Salam and G. Soyez, *The Anti-k(t) jet clustering algorithm*, JHEP **04** (2008) 063, arXiv: 0802.1189 [hep-ph]. 31

[82] ATLAS Collaboration, *Jet energy scale measurements and their systematic uncertainties in proton-proton collisions at $\sqrt{s}$ = 13 TeV with the ATLAS detector*, Phys. Rev. **D96** (2017) 072002, arXiv:1703.09665 [hep-ex]. viii, 33, 34, 35, 67

[83] ATLAS Collaboration, *Performance of b-jet identification in the ATLAS experiment*, J. Instrum., **11**, P04008 (2016), viii, 36, 37, 38

[84] J Butterworth et al., *Single Boson and Diboson Production Cross Sections in pp Collisions at sqrts=7 TeV*, tech. rep. ATL-COM-PHYS-2010-695, CERN, 2010 84

[85] N. Kidonakis, *NNLL resummation for s-channel single top quark production*, Phys. Rev. **D81** (2010) 054028, arXiv: 1001.5034 [hep-ph]. 84

[86] N. Kidonakis, *Next-to-next-to-leading-order collinear and soft gluon corrections for t-channel single top quark production*, Phys. Rev. **D83** (2011) 091503, arXiv: 1103.2792 [hep-ph]. 84

[87] N. Kidonakis, *Two-loop soft anomalous dimensions for single top quark associated production with a W- or H-*, Phys. Rev. **D82** (2010) 054018, arXiv: 1005.4451 [hep-ph]. 84

[88] ATLAS Collaboration, *Luminosity determination in pp collisions at $\sqrt{s}$ = 8 TeV using the ATLAS detector at the LHC*, Eur. Phys. J. C **76** (2016) 653, arXiv: 1608.03953 [hep-ex]. 82

[89] J.-F. Arguin et al., *Search for gluino-mediated stop and sbottom pair production in events with b-jets and large missing transverse momentum*, tech. rep. ATL-COM-PHYS-2016-1592,
`https://cds.cern.ch/record/2231120`. 84

[90] M. Czakon, P. Fiedler and A. Mitov, *Total Top-Quark Pair-Production Cross Section at Hadron Colliders Through O(4/S)*, Phys. Rev. Lett. **110** (2013) 252004, arXiv: 1303.6254 [hep-ph]. 84

[91] M. Botje et al., *The PDF4LHC Working Group Interim Recommendations*, arXiv: 1101.0538 [hep-ph]. 84

[92] U. Langenfeld, S. Moch and P. Uwer, *New results for t anti-t production at hadron colliders, Proceedings, 17th International Workshop on Deep-Inelastic Scattering and Related Subjects (DIS 2009): Madrid, Spain, April 26-30, 2009*, arXiv: 0907.2527 [hep-ph]. 84